Structure and Function of Multivalent Supramolecular Aggregates

Inaugural-Dissertation

to obtain the academic degree

Doctor rerum naturalium (Dr.rer.nat.)

submitted to the Department of Biology, Chemistry and Pharmacy

of Freie Universität Berlin

by

Svenja Christina Ehrmann

2019

The following work was carried out within the research group of Prof. Dr. Rainer Haag from June 2015 until April 2019 at the Institute of Chemistry and Biochemistry of the Freie Universität Berlin.

1. Reviewer: Prof. Dr. Rainer Haag, Freie Universität Berlin, Germany

2. Reviewer: Prof. Dr. Egbert Willem Meijer, Technische Universiteit Eindhoven, The Netherlands

Date of defense: 16.05.2019

Contents

I. Introduction **1**

1. Introduction and Outline **3**

2. Fundamentals **5**

2.1. Supramolecular aggregation in water 5

2.1.1. Self-assembly of amphiphilic structures in water 5

2.1.2. Supramolecular polymers 10

2.2. Cryo-TEM and its application in the analysis of supramolecular assemblies . 18

2.2.1. Introduction to cryo-TEM 18

2.2.2. Cryo-TEM - structural analysis of supramolecular and biological samples 24

2.3. Functional supramolecular aggregates and polymers 29

2.3.1. Carbohydrate recognition processes, the glycocalyx, and multivalency 29

2.3.2. Synthetic supramolecular architectures with (multivalent) biological function 32

3. Scientific Aim **38**

II. Results and discussion **39**

4. Synthesis and characterisation of new BTA-based amphiphiles with polyglycerol-based dendritic head groups **41**

4.1. Introduction 41

4.2. Results and discussion 43

4.2.1. Synthesis 43

4.2.2. Properties of BTA-C_{16}-G1 in aqueous solution 44

4.2.3. Ultrastructure analysis of nBTA and BTA-C_{16}-G1 50

4.2.4. Discussion 58

4.3. Conclusion and Outlook 60

4.4. Experimental section and Supplementary Information 62

4.4.1. Synthetic procedures 65

5. Structural analysis of BTA-based supramolecular copolymers **75**

5.1. Introduction 75

5.2. Results and Discussion 78

5.2.1. Ultrastructure investigation of copolymer system nBTA/dBTA 78

5.2.2. Investigation of the supramolecular copolymerisation of BTA and BTA-C_{16}-G1 . . . 82
5.2.3. Comparison of both copolymer systems and discussion . . . 92
5.3. Conclusion . . . 93
5.4. Methods and Materials . . . 95

6. BTA-based amphiphiles for multivalent pathogen inhibition 97
6.1. Introduction . . . 97
6.2. Self-assembly of BTA-mannose and BTA-EG_4-mannose . . . 98
6.3. Biological function . . . 106
6.3.1. Ligand binding . . . 106
6.3.2. Perspective - Towards multivalent pathogen binding with BTA polymers 111
6.4. Conclusions . . . 113
6.5. Methods and Materials . . . 115

7. Multivalently functionalised vesicles for ligand-receptor recognition 118
7.1. Introduction . . . 118
7.2. Results and Discussion . . . 121
7.2.1. Synthesis . . . 121
7.2.2. Physicochemical characterisation . . . 121
7.2.3. Lectin binding . . . 128
7.3. Conclusion . . . 138
7.4. Supplementary Information . . . 139
7.4.1. Methods and Materials . . . 139
7.4.2. Synthetic procedures . . . 142
7.4.3. Synthesis of Ad_2Man_8 . . . 142

8. Abstract 146

9. Zusammenfassung 148

III. Appendix 151

A. Acknowledgement/Danksagung 153

B. Curriculum Vitae 157

C. List of Publications 159

D. NMR spectra 161

Bibliography 177

Part I.

Introduction

1 Introduction and Outline

Multivalent supramolecular interactions are prevalent in nature. By the combination of multiple weak interactions, strong and highly specific interactions can be generated, which still remain reversible. Moreover, by organising multivalent binding partners in a supramolecular fashion, as for example glycoconjugates at the cell surface, these systems are highly adaptive towards an optimal structural organisation due to the inherent dynamic and reversible nature of non-covalent bonds. It is thus desirable to design new multivalent biofunctional materials, such as inhibitors of pathogens, based on supramolecular scaffolds in order to mimic and maintain flexibility, as well as adaptivity within these functional materials. However, fundamental understanding of the supramolecular architectures with regard to stability, structure and dynamics is required in order to rationally design materials with desired functions. The present work contributes to a deeper understanding of structure and function of supramolecular aggregates and polymers with a view to the application of such structures as multivalent binders to biological lectin receptors.

In **Chapter 2**, fundamental aspects of supramolecular chemistry, non-covalent interactions and supramolecular polymers are discussed. Furthermore, an introduction to cryogenic transmission electron microscopy is given as one major technique to analyse the structure of supramolecular systems. Third, examples of functional supramolecular aggregates are given with respect to multivalent carbohydrate interactions.

In **Chapter 4**, the synthesis of new BTA-based molecules, functionalised with glycerol-based dendrons is reported. The aggregation in a one-dimensional supramolecular polymers is investigated, as well as the detailed structure of the polymers by cryo-TEM. In addition, the structure of a supramolecular polymer based on a BTA with linear PEG chains is studied and both structures are compared.

In **Chapter 5**, the influence of copolymer formation between linear and dendritic functionalised BTAs on the structure and dynamics of supramolecular polymers is studied. To this end, the ultrastructure of the polymers at nanometre scale is investigated by cryo-TEM.

In **Chapter 6** the assembly of two monosaccharide-functionalised BTAs is investigated, as well as the relationship between structure and monomer ratio in copolymers. The accessibility of the monosaccharides at the supramolecular polymers for lectin binding is investigated

with two different protein receptors, in combination with a study on the influence of structure and carbohydrate concentration on efficient binding.

In **Chapter 7**, a toolbox approach based on supramolecular cyclodextrin vesicles for multivalent ligand-receptor recognition is investigated. Here, the synthesis of dendritic glyco- and sulphateconjugates is reported, as well as the analysis of the supramolecular decoration of the vesicles with these conjugates. Furthermore, the binding to multivalent lectin receptors, as well as to bacteria is tested including an analysis on the relationship between ligand concentration and clustering of the binding affinities.

2 Fundamentals

2.1. Supramolecular aggregation in water

Self-assembled structures in aqueous solution are omnipresent in nature. Without phospholipids assembled to cell membranes, the double-helix of the DNA held together by hydrogen bonds, assembled proteins or polysaccharides in the cytoskeleton and extracellular matrix, and non-covalent recognition processes, life would not be possible. All these structures in nature fulfil specific tasks or enable function due to highly specific interactions. Moreover, due to the reversible nature of non-covalent interactions, these supramolecular assemblies are adaptive to changing environments or external stimuli. The field of supramolecular chemistry aims at the understanding of the underlying principles. Furthermore, the obtained findings have been utilised to design and synthesise (bio-)functional supramolecular aggregates and polymers.

This chapter gives a short introduction into general aspects of self-assembly processes of amphiphiles in water, driven by non-covalent interactions, the packing parameter, and dendritic head group architectures. Furthermore, supramolecular polymers, their polymerisation mechanisms and selected examples of natural and synthetic one-dimensional supramolecular polymers and copolymers are addressed.

2.1.1. Self-assembly of amphiphilic structures in water

In general, amphiphilic structures contain of a polar, ionic or non-ionic, head group and a hydrophobic tail. Dissolved in water, amphiphiles assemble in supramolecular aggregates due to the hydrophobic effect and may additionally be held together by non-covalent interactions, such as hydrogen binding, π-π-interactions, and electrostatic interactions. In most cases, a combination of more than one interaction is involved. The hydrophobic effect induces the compartmentalisation of hydrophobic moieties in water. Through this, the interface between hydrophobic areas and water is decreased, minimizing the enthalpic costs of solubilising the aggregates. In addition, hydration water is released, which is entropically favourable.[1,2] Electrostatic, or coulomb interactions are the strongest among all non-covalent interactions

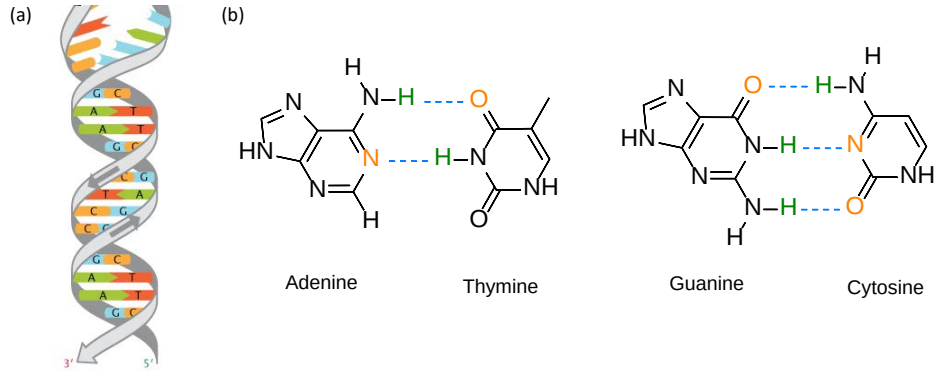

Figure 2.1.: (a) DNA double helix and (b) complementary DNA nucleic base pairs forming multiple H-bonds (blue) between hydrogen atoms (green) and electronegative hydrogen bond acceptors (orange). Part (a) reprinted from Ref. 7 with permission.

and are formed between positive and negative ions. However, water as a highly polar solvent weakens this interaction by solvating charged groups. Here, a sequence of multiple binding sites (multivalent binding) or shielding in a hydrophobic pocket helps to enable a strong overall bond formation.[3,4] Between aromatic, uncharged moieties, π-π interactions can be formed as special case of van der Waals interactions. In this case, the strength depends on the size of the aromatic system. Hydrogen bonds (H-bonds) are probably the most important interaction in supramolecular aggregation. H-bonds are directional dipol-dipol interactions between a hydrogen atom, bound to a more electronegative atom, and an acceptor group comprising an electron-withdrawing atom. A prominent example of H-bonds in nature is the DNA double-helix.[5,6] Multiple H-bonds are formed between complementary nucleic base pairs, such as Adenine - Thymine and Guanine - Cytosine, as shown in Fig. 2.1, whereby, both helix strands are held together.

The morphology of supramolecular assemblies is highly diverse and affected by a lot of variables, including the geometry of amphiphiles, concentration, temperature, purity of the samples and many more. A model for the prediction of the shape of a supramolecular aggregate with respect to the geometry of the amphiphile is based on the work of Israelachvili in 1976, who introduced the so-called packing parameter P:

$$P = \frac{V_0}{a_e \cdot l_0}. \tag{2.1}$$

This model considers a classical surfactant comprising a hydrophilic head group and a hydrophobic tail.[8–10] The packing parameter includes the surfactant tail volume V_0, the equilibrium area per molecule a_e, as well as the surfactant tail length l_0. The equilibrium area a_e refers to the transition region between the polar and hydrophobic parts of the molecule and

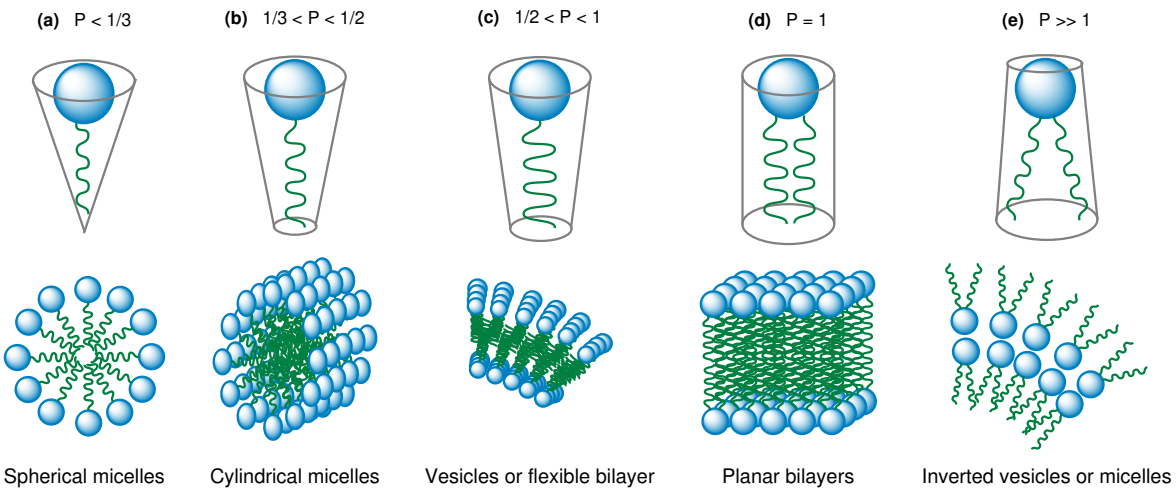

Figure 2.2.: Schematic depiction of the packing parameter concept. The packing parameter reflects the shape of amphiphiles and predicts the geometry of the aggregate. With increasing parameter from (a) to (e), the morphology is passing a transition from spherical micelles towards bilayered and inverse micellar structures.

is mainly influenced by the nature of the head group. A packing parameter of less than 1/3 predicts the formation of spherical micelles,. With increasing values of the packing parameters, a transition from spherical micelles to cylindrical micelles, vesicles and planar bilayers is obtained, as schematically and generalised depicted in Fig. 2.2. Values greater than 1 imply inverse vesicle or inverse micelle formation.

Although this model considers a basic composition of amphiphiles, comprising one hydrophilic head group and a hydrophobic tail, it helps also in understanding other amphiphile architectures and their aggregation behaviour, such as bola-amphiphiles with two head groups or amphiphiles with even more complex compositions, such as amphiphiles with dendritic head groups.

Amphiphiles with dendritic head groups and their aggregates in water have gained much attention in recent years and are considered as a special class within the wide field of amphiphiles and surfactants.[11–13] The design of dendritic amphiphiles can be diverse, as shown in Fig. 2.3(b), and the large number of terminal groups allows for facile multiple functionalisations and versatile applications.[13] In particular, glycerol-based dendrons are of great interest for biomedical applications, as they are non-ionic, highly water soluble, biocompatible, and exhibit a large number of reactive groups in the periphery.[14–17] Furthermore, glycerol is available in large scale as industrial side product and the synthesis of oligoglycerol compounds is straightforward, both industrial and in the laboratory scale.[18–22] Thus, glycerol-based dendrons have been applied as polar head groups of amphiphilic structures, studied in terms of

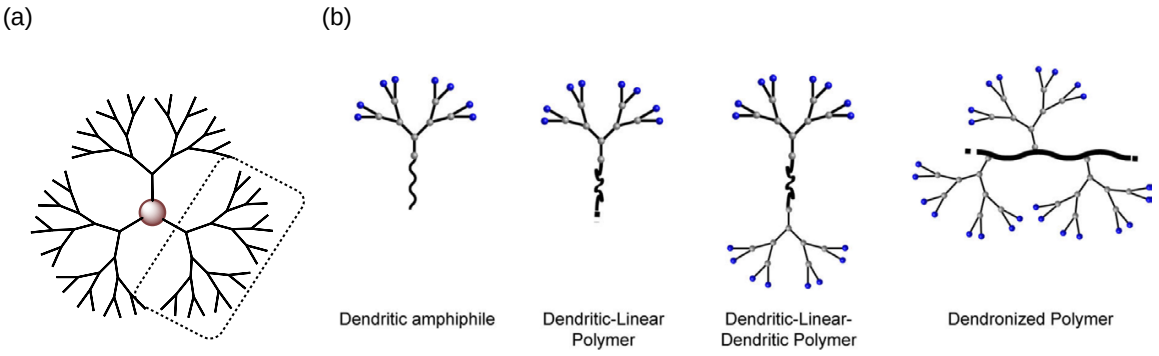

Figure 2.3.: (a) Schematic depiction of a dendrimer, consisting of branched dendrons (dashed rectangle). (b) Illustration of different dendritic amphiphile architectures. Reprinted and modified with permission from Ref. 11 . Copyright 2016 American Chemical Society.

their aggregation behaviour, and functionalised and applied as biofunctional material.[11] Dendritic amphiphiles with spatially low demanding hydrophobic tails assemble often in small spherical micelles. These spherical micelles are often structurally dynamic and the exact assembly geometry of the amphiphile cannot be determined. However, there are some prominent examples reported of dendritic amphiphiles forming structurally persistent micelles. Böttcher *et al.* reported on the structure of persistent micelles of ionic[23] and nonionic[24] dendritic amphiphiles. In both cases, cryo-TEM experiments and subsequent image analysis and processing revealed highly ordered micellar aggregates of a defined number of amphiphiles, as shown in Fig. 2.4 for the case of a nonionic, glycerol-based, dendritic amphiphile.[24]

By changing the geometry of amphiphiles, a variety of assembly morphologies including rods, fibres, vesicles, sheets, etc. have been obtained.[11] Among the diverse types of aggregation, one-dimensional aggregation needs directed interactions such as π-π-interactions or H-bonds in combination to the hydrophobic interactions.[25] Urner *et al.* reported on dendritic, glycerol-based bola-amphiphiles comprising a photo-switchable azo-benzene moiety. Here, different aggregation morphologies for the trans and cis state of the azo-benzene were obtained, *i.e.*, only in the trans state aggregation in tape-like structures occurred, whereas molecules of the cis state did not assemble into supramolecular structures.[26]

Various studies show the impact of the size relation between hydrophobic and hydrophilic compartment of the amphiphile on the aggregate morphology. By varying the head group size, as well as the lipophilic chains, Thota *et al.* were able to engineer the morphology of assemblies including micelles, worm-like micelles, and vesicles.[27] Recently, C3-symmetric 1,3,5-benzenetricarboxamide-based amphiphiles (BTA) were functionalised with generation 1 (G1) polyglycerol-based dendrons as hydrophilic head groups.[28] Disc-shaped BTA am-

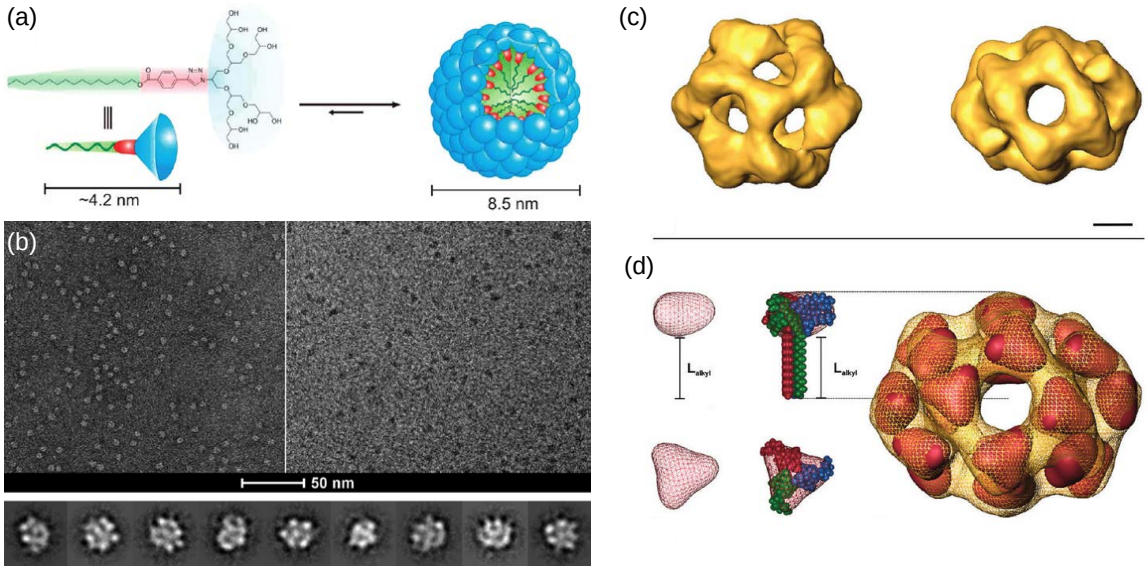

Figure 2.4.: Example of nonionic dendritic amphiphiles assembled in a structurally persistent spherical micelle. (a) Schematic depiction of chemical structure and assembly of glycerol-based amphiphile. (b) Cryo-TEM images, showing spherical micelles with 8-9 nm in diameter. Bottom row gallery shows representative class sum images after image processing and classification, representing views in different spatial orientations. (c) Surface representation of three-dimensional reconstruction in top and side view. (d) Building blocks of three amphiphiles assemble into the shown structure. Altogether, 20 building blocks contribute to the final structure. Reprinted and adapted with permission from Ref. 24. Copyright 2010 American Chemical Society

phiphiles are known to assembly in one-dimensional aggregates by intermolecular H-bonds (*vide infra*). However, the reported dendritic functionalised BTA assembled in spherical micelles due to the large and polar head groups. The immediate influence of the head group size on the morphology was as well shown in a study on amphiphilic cyclodextrins (CD).[29] The amphiphilic functionalisation of CDs with alkyl chains and glycerol-based dendrons lead to the formation of different morphologies depending on the generation (size) of the dendron. Functionalisation with G1-Dendrons resulted in the formation of multi-layered vesicles, as revealed by cryo-TEM. In contrast, worm-like structures were observed for functionalisation of CDs with bigger G2-dendrons, hence, following the concept of Israelachvili.[8]
In sum, this small selection of studies shows the high diversity of dendritic amphiphiles and their aggregates, of which (poly)glycerol-based dendritic amphiphiles are one sub-category. In the next section supramolecular polymers are addressed.

2.1.2. Supramolecular polymers

Polymers are ubiquitously present in our life. Since the pioneering work of Berzelius and Staudinger in the last century, polymers are defined as macromolecules consisting of monomeric repeating units, which are covalently connected to each other. Synthetic polymers, have been intensively studied regarding their unique chemical and physical properties. Furthermore, they have been applied as advanced materials in various fields of, *e.g.*, electronics, coatings, clothes, elastomers, and many more. Besides synthetic polymers, also natural polymers are omnipresent. Cellulose, starch, proteins and the DNA are all made of connected monomeric repeating units.
In the last two decades, supramolecular polymers have gained increasing attention.[3,30–35] In supramolecular polymers, the repeating units are not covalently linked to each other, but via non-covalent interactions. Whereas the hydrophobic effect causes the self-assembly itself, directional secondary interactions, such as H-bonds or aromatic interactions define the spatial direction of the polymeric growth. The directional growth of the structures, as well as the high resulting molecular weight, differentiates supramolecular polymers from other types of supramolecular assembly. Depending on the binding geometries, polymerisation in one, two or three dimensions can be achieved. In the framework of the present work, the focus has been put on one-dimensional supramolecular polymers.
In this section, a short introduction into the mechanisms of supramolecular polymerisation is given, along with selected examples of natural and synthetic supramolecular polymers as well as copolymers. Functional supramolecular polymers are discussed later in this chapter

in section 2.3.

Two major polymerisation mechanisms can be distinguished in the supramolecular polymerisation of one-dimensional aggregates, *i.e.*, isodesmic and cooperative polymerisation, which can be compared to step growth and chain growth polymerisation, respectively, in covalent polymerisation.[32] During an isodesmic polymerisation, supramolecular polymers are growing by monomer addition with a non-varying association constant K, as shown in Fig. 2.5(a). The affinity of a monomer to the growing polymer chain is independent of the chain length and no critical concentration or temperature has to be reached. As a consequence, a high total concentration of monomers and a high binding constant of the non-covalent bond are needed to achieve a high degree of polymerisation, otherwise only moderate degrees of polymerisation and high polydispersities are obtained.

In a cooperative polymerisation, (at least) two different polymerisation phases can be distinguished, *i.e.*, the nucleation and the elongation phase with two different association constants K_n and K_e, as it is schematically depicted in Fig. 2.5(b). In the initial phase, a nucleus of two or more monomers has to be formed, before the polymer starts growing in the elongation phase. Here, a critical concentration of assembled monomers has to be surpassed. The nucleation process can be classified as nucleated or downhill, depending on an increase or decrease of the Gibbs free energy, during the nucleus formation. Effects that induce the cooperativity can be subdivided into structural or electronic, or are caused by the hydrophobic effect.

Examples of supramolecular one-dimensional polymers can be also found at the cellular level. For example, myosin and actin filaments are supramolecular linear polymers based on globular proteins and assemble in a nucleation elongation mechanism activated by ATP binding to the monomeric proteins. Both can be found for example in the cytoskeleton of muscle cells, enabling the contraction of muscle cells by interaction of both filamentous structures under energy consumption mediated by ATP. Furthermore, actin filaments contribute together with microtubules and intermediate filaments to the structural stability of the cytoskeleton, to the cell motility, and the translation of environmental forces to signals in the cell.[36] Another supramolecular polymer found at the cell level is the amyloid fibre. Amyloid fibres are aggregated unfolded proteins in a cross-β-sheet structure. During conformational changes, proteins may unfold and fold back again to globular soluble aggregates. Additionally, proteins may unfold due to misfunction. If these unfolded proteins aggregate, they become insoluble and deposit, which can lead to amylidosis, which is nowadays associated among others with Alzheimer's disease and type II diabetes.[37] The unfolded protein β-sheets arrange in reverse directions and assemble into one-dimensional fibrils, as shown in Fig. 2.6(b). Fitzpatrick *et*

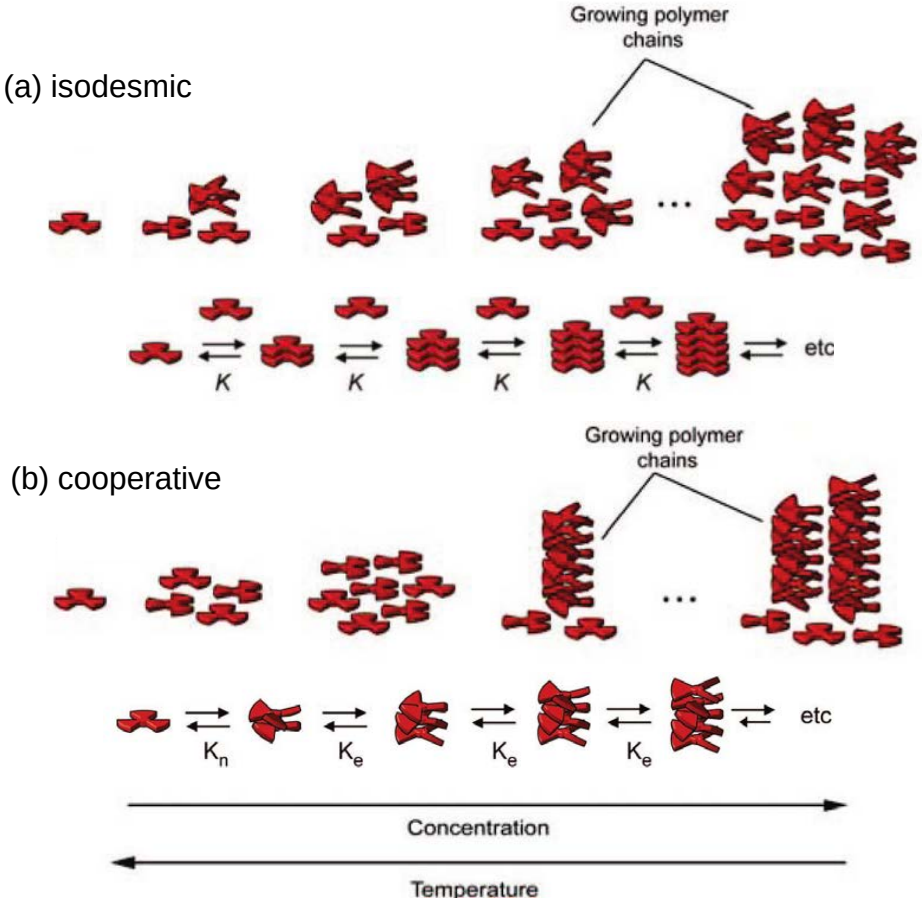

Figure 2.5.: Schematic representation of supramolecular polymerisation mechanisms: (a) isodesmic polymerisation with constant equilibrium constant K independent of the polymer chain length (b) cooperative polymerisation with K_n and K_e describing different intermolecular equilibrium constants in the nucleation and elongation phase. Adapted with permission from Ref. 32. Copyright 2009 American Chemical Society.

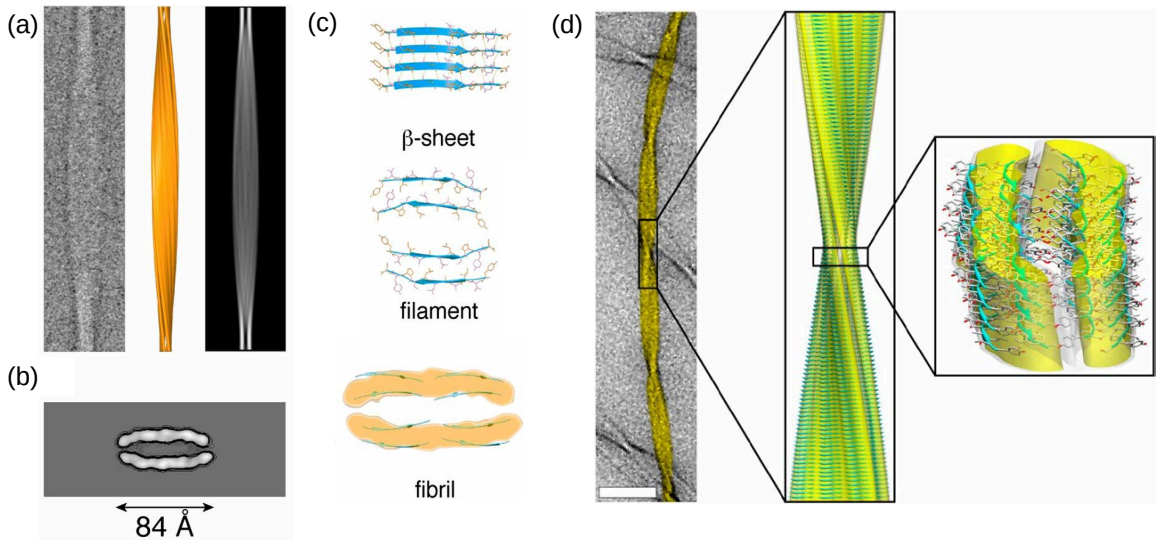

Figure 2.6.: (a) Representative cryo-EM class sum image after MSA, surface representation of the 3D reconstruction and the fibril back projection of a 11-residue peptide [TTR(105-115)] amyloid fibril. (b) Contoured cross-section of the amyloid fibril. (c) Hierarchy of increasing structural complexity during the peptide self-assembly. (d) Combined representation of TEM image, cryo-TEM reconstruction and magic angle spinning NMR atomic-resolution structure of the amyloid fibril. Reprinted and adapted with permission from Ref. 38. Copyright 2013 National Academy of Science.

al. investigated the polymer structure and molecular organisation in a amyloid fibril of an 11-residue peptide at atomic resolution by the combination of several microscopy techniques and NMR, including cryo-TEM combined with multivariate statistical analysis (MSA).[38] The analysed structural organisation of β-sheets and reconstructed 3D fibril structure and cross-section are shown in Fig. 2.6.

The dynamics of the formed amyloid supramolecular polymers were investigated by hydrogen-deuterium exchange (HDX) experiments.[39] This technique is a powerful tool to probe the stability and dynamics of supramolecular polymers in general. By dilution of respective samples in D_2O, the exchange of hydrogen atoms with deuterium is monitored by time-dependent mass spectrometry experiments. Hydrogen atoms subjected to the surrounding water are exchange-labile and promptly replaced by deuterium, due to the high surrounding concentration of D_2O. Contrarily, hydrogen atoms contributing to stable H-bonds or located in hydrophobic, solvent-shielded compartments, are exchanged only gradually or not at all. Therefore, the rate of HDX tells about the dynamics of supramolecular aggregates and the persistence of H-bonds and hydrophobic pockets. For amyloid fibres, it was found that the aggregates dissociate and reassemble at the time scale of days, which opens the field for spe-

cific therapeutic approaches.[39]

Inspired by supramolecular polymers in nature and the intriguing properties of some supramolecular polymers in bulk and organic media[31,40], such as mechanical robustness, self-healing, and electronic conductivity, the interest of stable supramolecular polymers in water increased over the past decades. In particular, the application of stable, yet adaptive supramolecular polymers in biological systems is targeted. As above introduced, several non-covalent interactions can be utilised when designing and synthesising supramolecular aggregates. In the following, the focus is set to H-bonds as predominant directional binding motif.

Inspired by the H-bond motifs in DNA, Meijer *et al.* introduced in 1997 a synthetic supramolecular polymer based on the 2-ureido-4-pyrimidone (UPy) motif.[41] During the assembly of bifunctional UPy-monomers, four H-bonds are formed between the self-complementary monomers, contributing to a strong interconnection, which enabled the growth of supramolecular polymers with a high molecular weight. Albeit a variety of supramolecular polymers based on the UPy motif with a large number of different kinds of monomers were synthesised in bulk and in organic solvent[31], the direct transfer into aqueous media was not possible, as H-bonds are generally weakened in water. Therefore, in order to ensure stable H-bond formation, the UPy-based monomers were functionalised in an amphiphilic fashion. Hydrophobic alkyl chains next to the UPy motifs built a hydrophobic domain, hence, shielding and stabilising the H-bonds, whereas hydrophilic PEG chains provided water solubility.[42] Several further functionalisations with bioactive moieties or peptides have been investigated since then, including their application as hydrogels to mimic the extracellular matrix.[43]

Water-soluble supramolecular polymers based on a 1,3,5-benzenetricarboxamide (BTA) motif were first reported by the Meijer group.[44,45] In general, by functionalisation of the central benzene core via amide bond formation with identical side chains, C_3-symmetric molecules are obtained, which are discotic through the stiff and planar BTA motif in the center.[46] By amphiphilic functionalisation of the side chains, comprising a hydrophobic unit and a hydrophilic water-soluble linear tetra(ethyleneglycol) chain, BTAs can assemble in micrometre long, one-dimensional fibrous stacks in water through compartmentalisation of the hydrophobic and hydrophilic domains in a cooperative nucleation-growth mechanism, as schematically shown in Figs. 2.7(a) and (b). Between the stacked molecules, intermolecular H-bonds at the amide groups are formed [*cf.* Fig. 2.7(c)], which are stabilised in a hydrophobic pocket, induced by for instance hydrophobic alkyl chains. Here, the strength of the hydrophobic pocket and thus, the stabilisation of the H-bonds is influenced by the length of the hydrophobic chains.

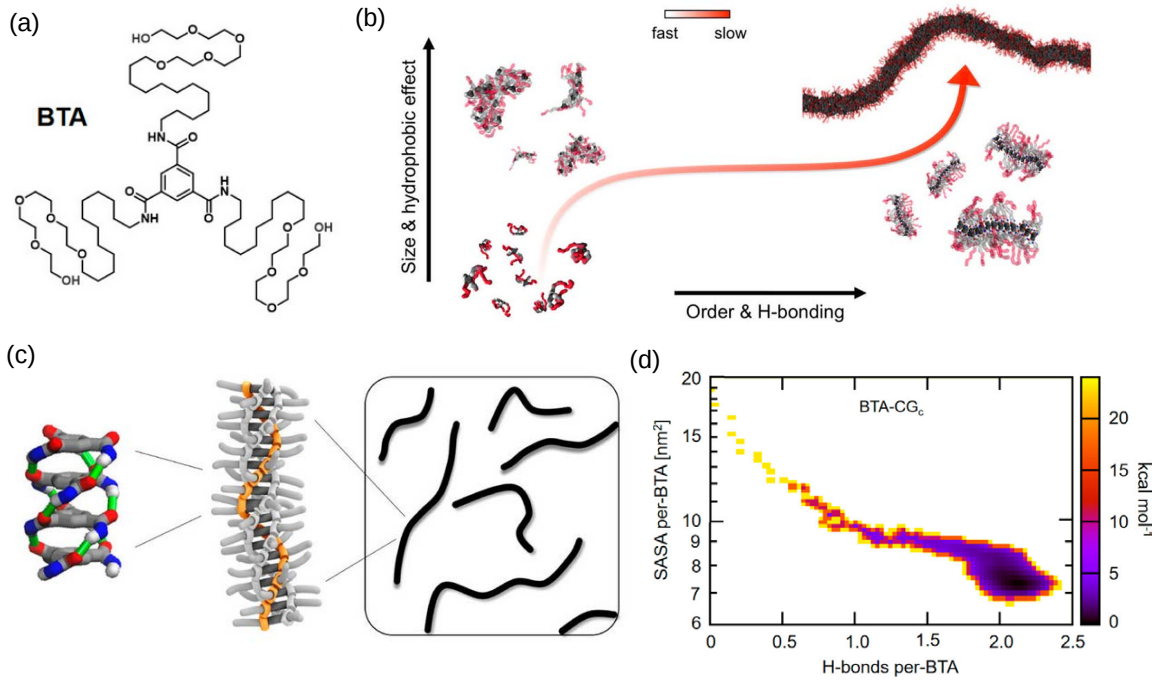

Figure 2.7.: (a) Chemical structure of water-soluble BTA with C_{12} alkyl chain and tetra(ethyleneglycol) modification. (b) Schematic depicting of nucleation-elongation polymerisation mechanism with a slow nucleus formation by hydrophobic interactions and subsequent order amplification including cooperative fibre growth by directional H-bonds. (c) Core-core stacking and H-bond formation between BTA monomers leading to helical fibre growth. (d) Solvent accessible surface area and self-assembly free-energy as a function of H-bonds per BTA. Reprinted and modified with permission from Ref. 48. Copyright 2017 American Chemical Society.

Additionally, more complex hydrophobic units including aromatic moieties, fluorocarbons, peptides or ionic groups have been investigated.[44,47] In order to obtain one-dimensional aggregates, the sizes of hydrophobic and hydrophilic units need to be in balance. If, on the contrary, this balance is disturbed, spherical micelles are obtained instead, as the hydrogen bonds cannot be formed or stabilised sufficiently.[28,45]

Several recent experimental and theoretical approaches investigated the stability of the supramolecular stack and the dynamics within polymers based on a water-soluble BTA monomers. Garzoni *et al.* investigated the importance of intermolecular H-bonds in the polymer for the stability of long stacks. For the initial nucleus formation of few monomers, only the hydrophobic effect is involved, whereas intermolecular H-bonds are crucial for the cooperative self-assembly in oligomers and the growth of ordered fibres, as it was shown by comparing ester and amide-based monomers in molecular dynamics simulations.[49] Course-grained simulations indicated the presence of two H-bonds per BTA in saturated polymers with H-bond

strength similar to those obtained in peptidic structures, as shown in Fig. 2.7(d).[48] By HDX experiments the dynamic monomer exchange with the bulk was shown. Solvent-accessible protons at the surface of the polymer are exchanged immediately upon dilution of the polymer in D_2O, whereas protons contributing to H-bonds are stabilised and additionally shielded in the hydrophobic domain formed by alkyl chains. However, exchange of these protons was observed over a time-scale of days, revealing the constant and dynamic exchange of monomers with the bulk enabled by the reversible nature of non-covalent bonds.[50] Simulation studies in water are not straight forward, due to the surrounding interactions with water, however, recent developments in simulation models and their application to BTA-based polymers revealed further insights in the interactions at monomer level. Using a combined approach of coarse-grained (CG), molecular dynamics (MD), and well-tempered metadynamics (WT-MetaD) simulations, a multi-step process for the monomer exchange in water soluble BTA supramolecular polymers could be identified.[51] At hot spots of decreased order along the supramolecular fibre, monomers leave the stack and diffuse along the surface, before dissociating to the water. Reincorporation of monomers from water follows the same step-like mechanism at dynamic hot spots. Strengthening the core-interaction by additional hydrophobic moieties resulted in a slower exchange process of the monomer to the fibre surface. These finding are highly interesting, as they help to understand structure-function relationships in supramolecular polymers, in particular with a view to tunable adaptivity to multivalent biological systems. A further option to modify properties of supramolecular polymers are multi-component systems, so-called supramolecular copolymers, which will be briefly introduced in the next paragraph.

Supramolecular copolymers are, just like their covalent counterparts, build of more than one component. Since the first example of a supramolecular copolymer in 1990 by Lehn and co-workers[52], consisting of two complementary components that form three H-bonds per dimerisation, the research field is experiencing growing attention. Both, fundamentally, as well as from a material science point of view, this class of polymers is highly interesting, as it opens the possibility to tune structure and function of supramolecular polymers by altering the composition of the copolymer. In a recent perspective[53], Adelizzi and co-authors summarised general principles and examples of supramolecular copolymerisation, of which some are reflected below.

The most basic approach to design a supramolecular (one-dimensional) copolymer is to combine two kinds of monomers, of which both bear two identical binding sites, which are complementary to the binding sites of the second monomer type. Both are not able to polymerise

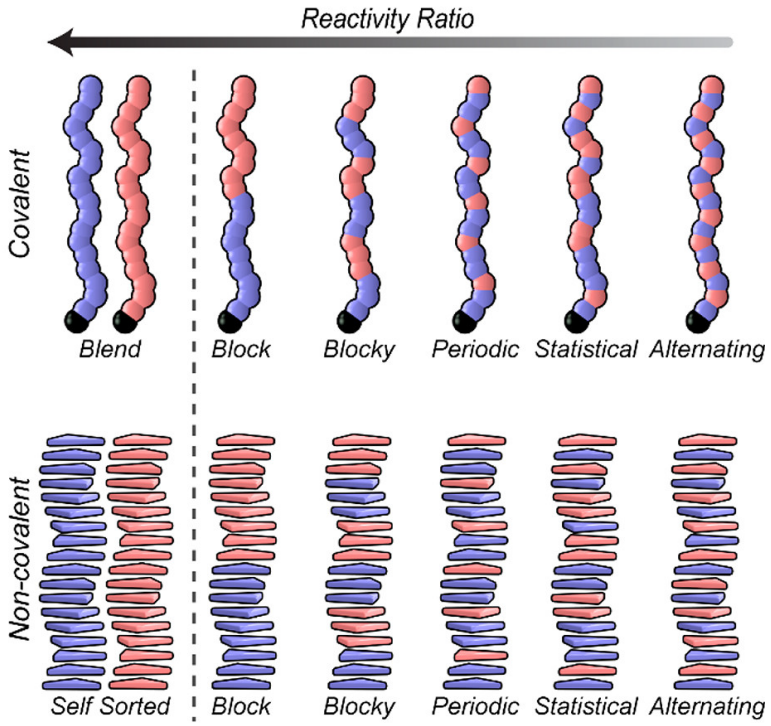

Figure 2.8.: Comparison of covalent and supramolecular copolymers in terms of monomer sequence microstructure. Adapted with permission from Ref. 53. Copyright 2019 American Chemical Society.

on their own, but through organisation in an alternating sequence the complementary binding sites interact non-covalently and thus, the supramolecular polymer is growing. Just like covalent copolymers, their supramolecular counterparts can be classified by the sequence of monomers in self-sorted, (di-)block, blocky (multi-block), periodic, random, or alternating copolymers. In Fig. 2.8, a schematic depiction of these classes is shown and directly compared to covalent copolymers. However, the design and predictability of the copolymer composition is difficult, due to the reversible nature of the bonds and the dynamics of supramolecular aggregates. One approach to predict and estimate the microstructure of copolymers is to compare thermodynamics of bond formations between two similar monomers (homo-aggregation) and two different monomers (hetero-aggregation). By relating both energy changes to each other, a reactivity ratio is obtained. This ratio indicates, if monomers preferentially interact with a monomer of the same kind (self-sorting/block) or the other kind (random, alternating).[53,54] In addition, solvent effects[55,56], temperature changes, impurities[57], etc. upset the balance easily and influence the (co-)polymerisation process. Thus, non-covalent synthesis strategies have to be employed and constantly refined.[58,59]

For multicomponent BTA supramolecular polymers, several studies have been conducted.

Albertazzi and co-workers reported on the spatiotemporal control of monomer distribution along the copolymer by clustering positively charged monomers with a negatively charged recruiter in a stack together with neutral monomers.[60] Furthermore, by mixing BTAs with linear and dendritic headgroups, Thota *et al.* were able to tune the monomer exchange dynamics as a function of the monomer ratio.[28] Both studies show nicely the adaptivity of supramolecular copolymers trough the reversible nature of bonds and the constant dynamic exchange of monomers with the bulk. Investigating relationships of structure, function, and dynamics with regard to monomer ratios, external stimuli, and multivalent receptors is in particular interesting for the application in biological systems in terms of ligand-clustering at multivalent receptors for instance.

However, the thorough characterisation of supramolecular copolymers is highly challenging. Due to the adaptivity and flexibility of the system, hardly any invasive characterisation technique can be applied. Thus, it remains challenging to analyse the copolymer composition at molecular level. Therefore, in most cases, a combination of spectroscopic (UV, Fluorescence, CD) and microscopic (AFM, TEM) techniques, as well as mass spectrometry[50], super resolution fluorescence microscopy[61] (STED, STORM) and computational simulations[62] is applied. In recent years, the technological progress in cryogenic transmission electron microscopy (cryo-TEM) led to remarking insights in the structure to both, synthetic, as well as natural macromolecules. Thus, this technique is introduced in the next section in further detail.

2.2. Cryo-TEM and its application in the analysis of supramolecular assemblies

2.2.1. Introduction to cryo-TEM

Cryogenic transmission electron microscopy (cryo-TEM) has become a central method for investigating the structure of supramolecular assemblies. Atomic resolution in TEM is nowadays easily obtained of crystalline structures in material science, however, high spatial resolution and sufficient contrast can be only achieved at high magnification and thus high electron doses. In contrast, for biologically samples or organic supramolecular structures, radiation sensitivity plays an additional key role, as these compounds are destroyed by illumination upon inelastic scattering with highly energetic electrons.[63]

Techniques to overcome the problem of radiation sensitivity traditionally include the chemical fixation and staining of sample solutions on the specimen grids. Hereby, a heavy metal

salt, *e.g.* uranyl acetate or phosphotungstic acid salts, is added during the specimen preparation. Upon drying, the salt coats the sample. In this way, the sample is fixated and able to resist the high vacuum within the microscope. Additionally, the heavy metal atoms around the sample increase the obtained image contrast due to the strong scattering of electrons at heavy metal atoms (*vide infra*). This techniques is referred to as "negative staining". However, using this method, the sample is measured in a dried state, hence, artefacts and morphology changes induced during the drying process or by interactions of the sample with the stain cannot be excluded and the original native state of the sample in solution is not accessible for imaging. Therefore, cryo-fixation techniques were developed. In this approach, a thin solution film with a thickness of only few hundred nanometres is generated on holey specimen grids, which is then frozen in liquid ethane. By the high thermal conductivity of liquid ethane, water freezes with a high cooling rate into an amorphous (vitrous) state, thus, becoming transparent for the electron beam, which enables the investigation of the embedded biological or supramolecular structures in their quasi native state by using phase contrast imaging techniques. Subsequently, the sample is measured in the microscope at liquid nitrogen temperatures, at which the amorphous ice layer is stable to the vacuum conditions in the electron microscope against evaporation and crystallisation.[63,64]

These days, cryo-TEM is commonly and routinely used for the characterisation of organic supramolecular structures in aqueous solution with resolutions of one to two nanometres. Higher resolutions are achieved depending on the degree of order of the specimen. For structurally persistent structures, such as proteins, averaging techniques can be applied, enabeling the structure elucidation at near-atomic resolution. However, a low degree of order, as often obtained for supramolecular structures, is resolution-limiting. Low-dose techniques are applied in order to minimise the dose that is subjected to the area of interest and, hence, minimise radiation induced damage. However, organic supramolecular structures mainly consist of low molecular weight atoms such as C, H, N, or O, which induce only minor contrast in comparison to the surrounding ice.

In order to enhance contrast, phase contrast imaging conditions are applied. Furthermore, contrast-enhancing phase plates have been recently developed for standard usage.[65] Both, fundamentals on contrast in TEM, as well as the principles of phase plates are addressed in the next paragraphs.

Each electron wave is characterised by its frequency, amplitude, and phase. In general, these three properties or the change of these properties can be used to image and characterise an object that the electron wave was interacting with. In the most basic approach to image a

sample in TEM, only the bare intensity/number of scattered electrons in a given spatial region in the image plan is measured. This is referred to as amplitude contrast. Amplitude contrast originates from elastic scattering of electrons, which is the interaction of electrons with the positively charged nucleus of an atom while conserving momentum and energy. Here, the deflection depends on the speed of the electrons (acceleration voltage), the distance between electron and nucleus, as well as the atomic number. For light atoms, only minor deflection is observed and all scattered electrons contribute to the image. Therefore, no spatial variation in intensity is measured and, thus, no or only negligible amplitude contrast is present. In contrast, scattering of electrons at atoms with a high atomic number leads to a high deflection, so that the electrons are trapped at the objective/contrast aperture in the back focal plane of the objective lens. Consequently, these electrons do no contribute to image generation, thus, making objects visible by their absence. In sum, sufficient amplitude contrast can be only observed for atoms with a high atomic number. This effect is used in negative-stain TEM.
Besides elastic scattering, also so-called inelastic scattering of the electrons does occur. Here, beam electrons interact with the electrons in the atom's shell. During this process, momentum and energy are not conserved as some of the beam electrons' energy is absorbed by the shell electrons. This leads to a distinct distribution of energies of the electrons after passing the sample/specimen. Due to the energy dependence of diffraction (so-called chromatic aberration), electrons with different energy are imaged to different focal planes, resulting in increased noise and contrast loss in the images. Thus, energy filter that separate inelastic and elastic scattered electrons are used in high-resolution applications to overcome this issue and enhance contrast.[66]
While imaging a sample, only the absolute square-value of the electromagnetic wave in the image plane is measured. Thus, only the amplitude of the electron wave contributes to the image generation and the phase of the wave is discarded. As described above, this is referred to as amplitude contrast. However, the phase information can give additional valuable insights to the sample and can be also used to induce image contrast. This is especially important for samples with light atoms, such as C, H, N, O, where amplitude contrast can be neglected. In general, the scattered electrons experience a phase change while passing through a sample compared to an unscattered electron. Let

$$\Psi_i = \Psi_0 \sin(2\pi\, kz) \tag{2.2}$$

be the wave function of the initial electron beam with amplitude Ψ_0, frequency k, and position z. After passing the sample, the phase of the electron is changed by ϕ, thus, the wave function

now reads as

$$\Psi_a = \Psi_0 \, \sin\left(2\pi \, kz + \phi\right), \tag{2.3}$$

which can be rewritten using trigonometric relationships as

$$\Psi_a = \Psi_0 \, \sin\left(2\pi \, kz\right) \cos\left(\phi\right) + \Psi_0 \, \cos\left(2\pi \, kz\right) \sin\left(\phi\right). \tag{2.4}$$

For small ϕ and using

$$\cos\left(\phi\right) = \sin\left(\phi + \frac{\pi}{2}\right), \tag{2.5}$$

the above expression can be simplified as

$$\Psi_a = \Psi_0 \, \sin\left(2\pi \, kz\right) + \Psi_0 \phi \, \sin\left(2\pi \, kz + \frac{\pi}{2}\right) \tag{2.6}$$

$$= \Psi_i + i \, \Psi_{sc}. \tag{2.7}$$

Thus, the scattered wave can be seen as a superposition of the initial electron wave plus a contribution from the scattered wave Ψ_{sc}. Both waves are orthogonal to each other, reflecting the phase shift of $\frac{\pi}{2}$ of Ψ_{sc}. This situation is shown in Fig. 2.9(a). From this figure, also the minor influence of a phase shift on the amplitude contrast can be seen, as the difference between

$$\left|\Psi_i\right|^2 \qquad \text{and} \qquad \left|\Psi_a\right|^2 = \left|\Psi_i + i \, \Psi_{sc}\right|^2 \tag{2.8}$$

is negligible.

To overcome the problem of a faint phase contrast in TEM, the difference between $\left|\Psi_i\right|^2$ and $\left|\Psi_a\right|^2$ has to be enlarged. A possible approach to maximise the difference is to induce an additional phase shift of $\frac{\pi}{2}$ to Ψ_{sc}. This scenario is depicted in Fig. 2.9(b) and (c). As the phase shift can be positive or negative, two resulting situations can be obtained. In case of an additional $-\frac{\pi}{2}$ phase shift, Ψ_{sc} adds to Ψ_i, whereas the opposite is observed for a phase shift of $+\frac{\pi}{2}$. These phase variations cause a change in the amplitude in the resulting wave, thus, leading to different absolute square values and a measurable amplitude contrast. This effect is referred to as positive or negative phase contrast, respectively.

In order to induce this additional phase shift, mainly two different approaches can be followed, of which the first includes defocussing the objective lens and the second the use of a phase plate.

As shown above, the small phase shift induced by an object does not induce amplitude contrast, hence, the object would not appear in the image. However, the spherical aberration C_s

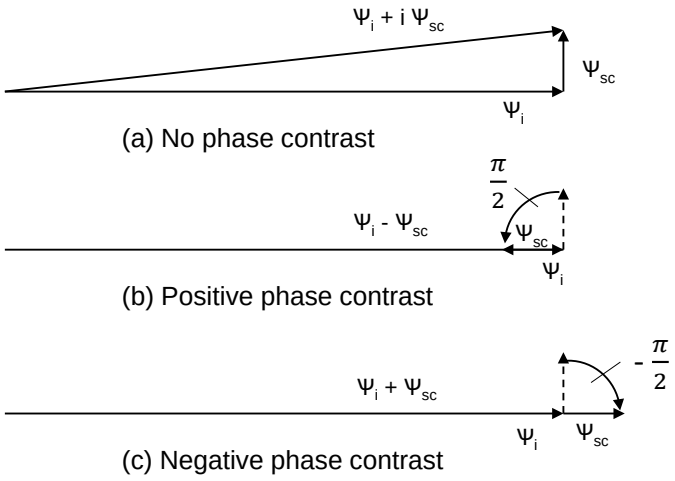

Figure 2.9.: (a) Orthogonal superposition of initial wave amplitude Ψ_i and scattered amplitude Ψ_{sc}. (b) An additional phase shift by $\frac{\pi}{2}$ induces positive phase shift (c) An additional phase shift by $-\frac{\pi}{2}$ results in negative phase shift. Image adapted from Ref. 67

.

of the objective lens induces small additional phase shifts, which are caused by imperfections of the lens itself. By this aberration effect, waves refracted at a curved lens surface experience different phase shifts and are thus not focused in the same point. The phase shift χ is a function of the spatial frequency k and is given by

$$\chi(k) = 2k^4 C_s \lambda^3 - \Delta z k^2 \lambda \pi \tag{2.9}$$

with the wavelength of the electron λ and the defocus Δz. The resulting contrast as a function of k is then described via the contrast transfer function CTF

$$CTF(k) = 2\sin(\chi) \tag{2.10}$$

$$= \sin\left(\frac{\pi}{2}\left[C_s\lambda^3 k^4 + \frac{1}{2}\Delta z \lambda k^2\right]\right). \tag{2.11}$$

As can be inferred from Eq. (2.11), the obtained contrast is oscillating, following the sine function and depends on C_s, λ, and Δz. Due to limited coherency of the illumination, the CTF gets attenuated for high spatial frequencies. At the zero-crossings of the function, no information is gained in the images for this particular spatial frequency. As C_s is specific for the instrument and λ is fixed during the measurement, the obtained contrast can be modulated by the defocus Δz. With increasing values of Δz, the first zero-crossing is shifted towards low spatial frequencies, whereby informations of comparably large objects (nanometre scale), which are relevant in supramolecular or biological applications, are obtained with good contrast. However, this high contrast is accompanied with a decreasing resolution at high

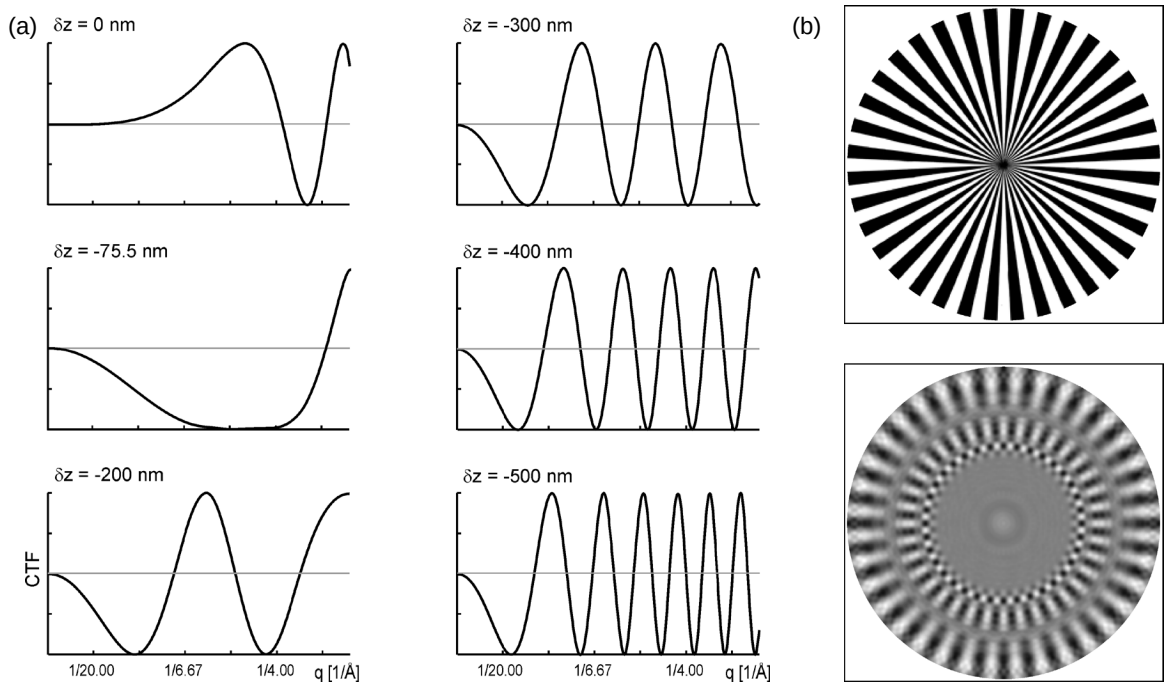

Figure 2.10.: (a) Undampened contrast transfer functions (CTFs) of a TEM with U_B = 160 kV and C_s = 2 mm with increasing defocus values δz . δz = -75.5 nm corresponds to the Scherzer focus with a large range of spatial frequencies transferred with high contrast. (b) Upper image: Siemens star test image providing a graphical object with a continuous decrease of spacings from the periphery towards the center. Bottom image: Test image convoluted with a CTF of a TEM at δz = -300 nm (*cf.* left panel), illustrating the contrast reversals at spatial frequencies corresponding to zero-crossings in the CTF. Reprinted and modified with permission from Ref. 63. Copyright 2012, John Wiley and Sons.

spatial frequencies and artefacts induced by frequent changes of the sign of the contrast.[66,67] In Fig. 2.10(a), CTFs with increasing defocus values are depicted, showing the shift of the first zero-crossing towards smaller spatial frequencies. This Fig. 2.10(b) illustrates the impact of the zero-crossings and sign-reversals in the CTF. In this specific test image (Siemens star), the spacing between the black and white stripes decreases towards the center. After convolution with a CTF at a certain defocus value, the sign of the contrast changes frequently at spacings corresponding to the respective zero-crossings in the CTF. By this illustration, artefacts and misinterpretations resulting from contrast sign-reversals can be vividly understood.

A second option to induce additional phase shift, are so-called phase plates. In light microscopy, the insertion of a Zernike phase plate leads to the desired phase shift of the scattered light. By adjusting the thickness of this plate, the value of the induced phase shift can be tuned. In contrast, the central beam passes through a hole and remains unmodulated, which results in a phase difference between scattered and central beam. The introduction of

a Zernike phase plate has also been tried in electron microscopy. However, difficulties such as induced contamination, charging, and a resulting short life-time of the phase plate prevented this element from being widely applied.[68]

In 2014, however, Danev and Baumeister introduced the Volta phase plate. In this approach, a thin carbon film is inserted in the beam path in the back focal plane. In Fig. 2.11, all three microscope set-ups are depicted. Upon irradiation of the carbon film with the central diffraction beam, a negative volta potential is build up just above the surface of the film. The volta potential results from changes of the inner and surface potential of the carbon film and increases with accumulating dose. Although the exact processes that lead to the presence of the beam-induced potential are not fully understood, changes in the surface chemistry and local reduction were proposed. Through this beam-induced potential, the electrons of the central beam experience an additional phase shift compared to the scattered electrons. If this phase shift is $\frac{\pi}{2}$, a maximum phase contrast is observed as shown above. As the potential varies with increasing dose, also the phase shift changes over time. Thus, the phase shift has to be measured regularly and if the shift exceeds around 0.7π, the position at the phase plate needs to be changed. At the new position, again, a potential is generated. In addition, the previous positions regenerates over time, which leads to a long lifetime of the Volta phase plate.[65]

By using a phase plate, additional defocus is no longer needed and images can be in principle recorded directly in focus. As a result, no CTF zero-crossings over a large spectrum of spatial frequencies are present. Thus, defocus induced artefacts and multiple sign reversals in the CTF are avoided. However, for practical reasons, a slight defocus of a few hundreds of nanometres is usually applied today in phase plate imaging conditions.[69,70]

2.2.2. Cryo-TEM - structural analysis of supramolecular and biological samples

The importance of cryo-TEM for structural analysis was appreciated only recently. In 2017, the Nobel prize in chemistry was awarded to Jacques Dubochet, Joachim Frank, and Richard Henderson for *"developing cryo-electron microscopy for the high-resolution structure determination of biomolecules in solution"*.[71,72] Jacquet Dubochet developed in his pioneering work the cryogenic sample preparation through vitrification in liquid ethane.[73,74] Richard Henderson laid the foundations of the analysis of biological macromolecules, such as proteins, with atomic resolution with his seminal works on electron crystallography.[75]

Joachim Frank laid the foundations with his work on reconstructing single particles by image processing techniques.[76] Single-particle cryo-TEM is based on the 3D reconstruction of

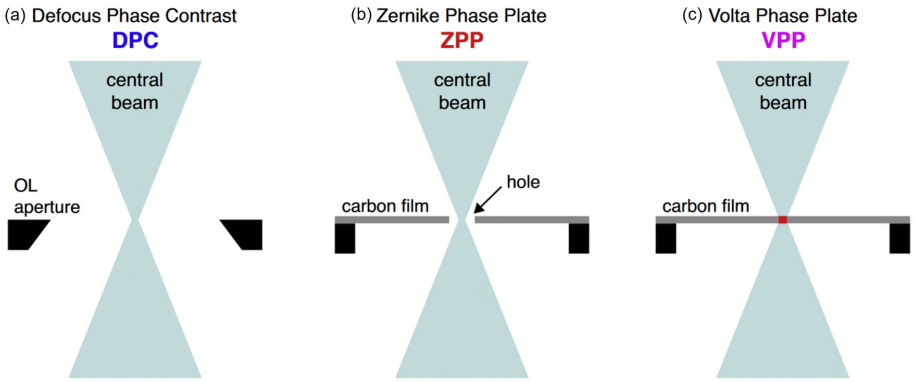

Figure 2.11.: Different imaging modes using (a) an objective lense aperture for defocus phase contrast, (b) a Zernike phase plate with a small central hole in the middle of a thin carbon film, and (c) a continuous thin carbon film, a so-called Volta phase plate. Both phase plate modifications aim for an additional phase shift of either the scattered or central beam to gain phase contrast. Reprinted and modified from Ref. 70, with permission from Elsevier Ltd.

2D images of randomly oriented protein molecules. In this context, multivariate statistical analysis (MSA) was used by Frank and van Heel in order to classify particles on the basis of their orientation or heterogeneous samples in terms of recurring motifs.[77] The analysis of heterogeneous samples is especially interesting for supramolecular aggregates, as often a variety of morphologies is present. Furthermore, by this technique, the signal-to-noise ratio is improved by combining images of identical features, which is highly beneficial for the structural analysis at nanometre scale. An introduction to MSA is thus given in the next paragraphs.

Multivariate statistical analysis (MSA) is a well-established method used to identify similarities in a large heterogeneous data set of images and cluster these images subsequently.[77–79] It is also frequently used to enable the reconstruction of three-dimensional structures from two-dimensional images, which is in general not trivial due to the loss of image information by projection onto the image plane. Here, MSA can be used to classify and cluster these different projections into distinct sum images, which each exhibit a better signal-to-noise ratio than the single images and allow a reconstruction of the three-dimensional object.[80]

In this work, multivariate statistical analysis was used for image classification and ultrastructure analysis. In a first step, the data set is prepared for the subsequent analysis. Here, a set of i images from the respective structure is created by well-chosen excerpts from the recorded cryo-TEM images. Special care is taken to exclude contaminants and other artefacts from these excerpts. In the following, these cut-outs are then rotated and translated

by cross-correlation methods in such a way that the respective structures are aligned with respect to one or multiple reference images. Afterwards, each image i is represented in an n-dimensional coordinate system or hyper space, respectively, where n reflects the number of pixels in each image. For a specific image i, the coordinate value along a certain axis n is given by the grey value of the pixel n in this image. In the following multivariate statistical analysis, which can be also understood as a principal component analysis, the data points in the n-dimensional coordinate system are described in a new coordinate basis with a drastically reduced number of vectors. The procedure is as follows: The first basis vector is chosen in such a way that the vector points along the direction of the highest variance in the data cloud. This approach is based on the idea that the direction of highest variance reflects a major difference between all the images. Next, the second basis vector is chosen orthogonal to the first one and points in the direction of the second highest variance. By repeating this step several times, a new basis set of vectors is created. These vectors are referred to as eigenvectors, which can be also be represented with eigenimages of the data set. Similar to the eigenvectors of a coordinate system, the eigenimages reflect the basis to construct the images of the data set. Using the new coordinate system, which is build from the calculated eigenvectors, the images are classified in such a way that the variance between images of the same class is minimized. These classes then reflect recurring structural similarities. Here, different algorithms and approaches can be applied. First, in the hierarchical approach, the number of classes equals the number of images in the beginning. Subsequently, images are merged in combined classes according to a variance criterion. A second option is the so-called partitional algorithm. Here, the final number of classes is pre-defined by the operator and the images are classified iteratively, until an optimal distribution is achieved. This method is relatively fast, however, the level of sensitivity, as well as the accuracy of this analysis, highly depends on the manual selection of the number of considered eigenvectors, eigenimages and resulting classes, which might be adjusted iteratively. Finally, after completed classification, all aligned images of one class are averaged, thus, creating class sum images.[63,80] In the following paragraphs prominent examples of structural investigations of supramolecular and biological systems are introduced.

Together with constant technical developments regarding direct electron detectors, software, faster readout and computing times, the implementation of autoloaders in the instrument set-up, and many more, cryo-TEM has become a powerful technique for the structural analysis of supramolecular and biological samples in aqueous solution, partly with near-atomic resolution, over the past decades. Just recently, the helical assembly of the Ebola virus nu-

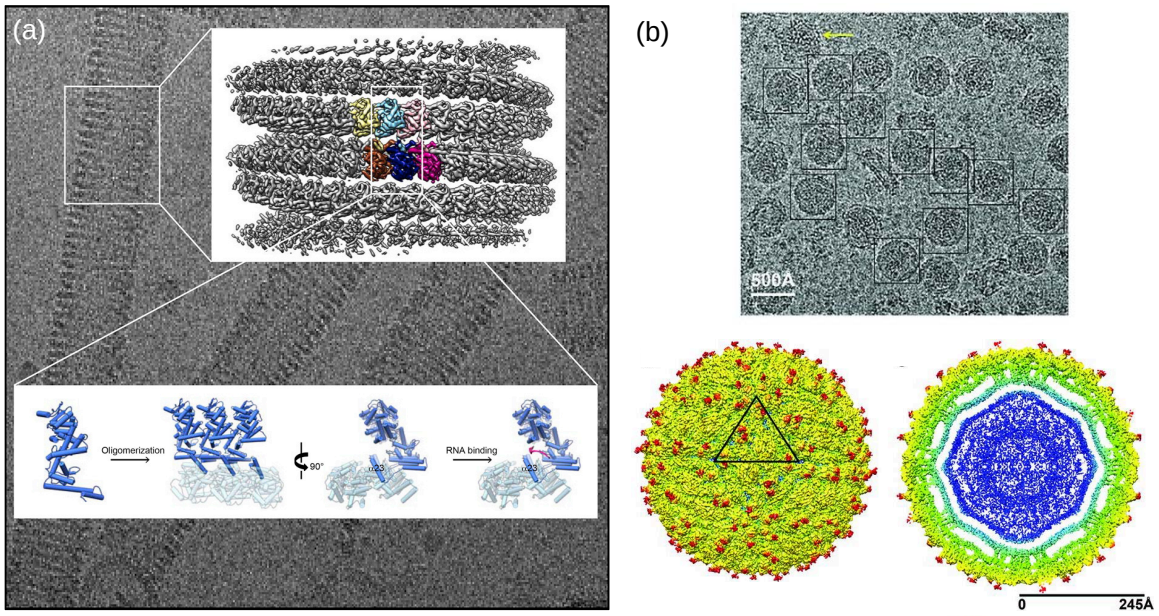

Figure 2.12.: (a) Left-handed helical reconstruction of the Ebola virus nucleoprotein from cryo-TEM images, revealing the assembly of the proteins in the viral nucleocapsid. Reprinted with permission from Ref. 81 Copyright 2018 Elsevier Inc. (b) High-resolution reconstruction of the mature Zika virus by cryo-TEM. The upper image shows a representative cryo-TEM image, the images below are a surface-shaded and a cross-section depiction of virus. Reprinted and adapted with permission from Ref. 83. Copyright 2016, American Association for the Advancement of Science.

cleoprotein, forming the viral nucleocapsid, was revealed using cryo-TEM at a resolution of 3.6 Å, as shown in Fig. 2.12(a).[81,82] By the high-resolution analysis of biological structure, a better mechanistic understanding of RNA replication processes was gained, paving the way for future anti-viral drug developments. Likewise, in 2018, the structure of the mature Zika virus was reported at a resolution of 3.1 Å, which is depicted in Fig. 2.12(b).[83,84] Through this study, possible binding pockets for anti-viral compounds or vaccines could be identified. Besides these stunning examples for structural analysis of biological samples, cryo-TEM is also increasingly used for the structural analysis of supramolecular aggregates.[64,85,86] However supramolecular structures often lack the precise identical arrangement in a variety of samples. Thus, the application of averaging techniques is limited to supramolecular aggregates with persistent and repeatedly occurring structural motifs.[23,24,87] One prominent example is the elucidation of a stacked bilayer helical structure of self-assembled N-octyl-D-gluconamide by Böttcher *et al.*.[88]. N-octyl-D-gluconamide is a chiral amphiphile, comprising a single alkyl chain and a sugar-based gluconamide head group [*cf.* Fig. 2.13(a)]. The compound dissolves in water above temperature of 68°C and a gel is formed upon cooling. Cryo-TEM images

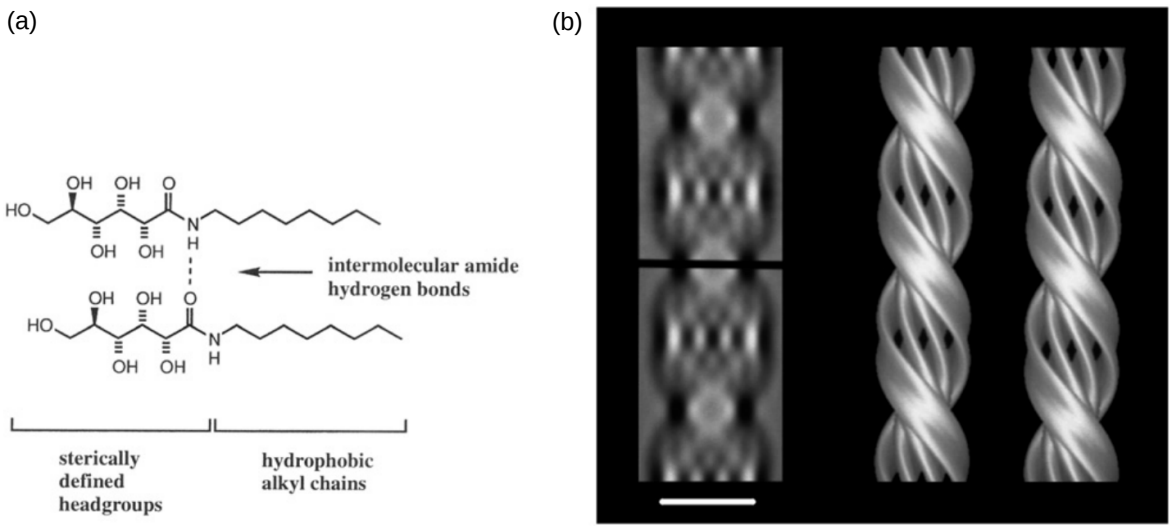

Figure 2.13.: (a) Chemical structure of n-octyl-D-gluconamide. (b) Clockwise from top left: Average of 100 aligned cut-outs of cryo-TEM images showing one repeating unit. 3D reconstruction of the left-handed helix of stacked bilayers, depicted as stereo image. Back projection of the 3D reconstruction confirming the good agreement between obtained experimental data and reconstruction. Reprinted with permission from Ref. 85 Copyright 2014 Elsevier B.V..

of the gel showed the presence of long, fibrous aggregates with a inner periodic structure. Therefore, hundreds of cut-outs comprising one repeating unit were extracted, aligned in vertical orientation and classified by MSA. By subsequent reconstruction in 3D, the complex supramolecular structure comprising a helically twisted stack of bilayers was revealed. In Fig. 2.13(b), the average of aligned cryo-TEM images is shown, including the 3D reconstruction and its back projection to 2D. A left-handedness of the helix was elucidated by tungsten shadowing experiments.

Subsequent studies showed that this special and complex structure is part of a morphology transition process, starting from spherical micelles, over the obtained helical bilayer structures towards tubes and crystals.[63,85] This transition process occured within a time scale of several hours as revealed by time-dependent sample preparations. These findings underline and highlight the complex structural processes that take place during supramolecular aggregation, which are highly sensitive to a variety of conditions, including temperature, time, and the sample preparation process in general. Thus, care has to be taken in regards of sample preparation and subsequent analysis in order to obtain reproducible and comparable results.

As mentioned above, supramolecular aggregates are often structurally divers, *i.e.*, more than one morphology of the same sample is present at the same time. Thus, averaging or single-

particle approaches might not help for the structural elucidation of assemblies, especially in 3D. Here, cryogenic electron tomography (cryo-ET) has gained increasing attention lately.[80] 2D images of one specific structure within the whole sample are recorded in several projection angles. Subsequently, the images are combined, aligned towards each other and, hence, a reconstruction of the structure in (almost) 3D can be obtained. Furthermore, by the combination of several images of the same area, the signal-to-noise ratio is improved. However, care must be taken with regard to the electron dose subjected to a single area.
Taken together, cryo-TEM in combination with image processing or tomography techniques, enables the direct structural characterisation of supramolecular and biological samples (in 3D) in their native environment at high-resolution. In addition, the detailed elucidation of structure paves the way for a better understanding of the interplay between function and properties of these samples.

2.3. Functional supramolecular aggregates and polymers

2.3.1. Carbohydrate recognition processes, the glycocalyx, and multivalency

Carbohydrate recognition is a fundamental process in nature and the underlying biochemical processes. Interactions of carbohydrates with other carbohydrates or proteins regulate a multitude of processes, including cell-cell recognition, immune responses, inflammation and adhesion.[89] However, the supramolecular interactions between carbohydrates and proteins or lectins are usually weak. In order to strengthen the binding, nature utilises the concept of multivalency. Through the combination of multiple weak interactions, an overall strong binding is achieved, which is more than the sum of its individual components, but still reversible.[90] A multivalent interaction is defined as an interaction between an m-valent receptor and an n-valent ligand, whereas m and n are larger than one. The enhancement of the binding constant of a multivalent binding [K_{multi}] between a multivalent ligand to a multivalent receptor compared to the binding constant [K_{mono}] between a monovalent ligand to a multivalent receptor is reflected by the enhancement factor β, introduced by Whitesides *et al.*.[91] This factor includes already underlying effects as the symmetry effect[92] or cooperativity, which is often negative in multivalent systems.[93,94] One of the main contribution to the high dissociation constants K_D of multivalent systems is the decreased dissociation rate k_{off} in multivalent systems. The association rate k_{on}, however, was shown to be often similar to those of analogous monovalent systems, as this rate is mostly diffusion-limited.[90,95] The thermodynamic and kinetic processes which are involved in multivalent binding are often

complex and include not only the binding of the ligand to the receptor itself, but also the size and shape of the scaffold[96], the influence of linkers or spatial distributions of ligands. Furthermore, effects like local concentration[97], ligand clusters[98], statistical rebinding, and steric shielding[99,100] have to be taken into account.[101]

At the surface of cells, a variety of carbohydrates and polysaccharides build the so-called glycocalyx. Organised in complex glycoproteins and glycolipids, these carbohydrates are involved for instance in recognition and communication interactions of the cell through the binding to other glycoconjugates or lectins.[102,103] Lectins are oligomeric proteins with carbohydrate-specific recognition domains (CRD).[104] The direct interaction between lectins and carbohydrates is often weak, however, strong and specific binding is ensured by nature through the organisation of carbohydrates in high-order polysaccharides and the multivalent arrangement of receptors.[105] Multivalent interactions between lectins and carbhoydrates are involved in a variety of biological recognition processes between, *e.g.*, cells, bacteria, and viruses. During the first step of an infection process by pathogens, multivalent interactions are formed between lectins at the pathogen and the glycocalyx of the host cell. Fig. 2.14(a) shows schematically the multivalent binding of a virus to a cell surface. Through the multivalent binding, a strong adhesion by the pathogen to the host cell is ensured. However, state-of-the-art drugs against viral infection or antibiotics are often monovalent compounds. Thus, in order to compete to the multivalent binding, a high dosis of the drug is needed, as schematically indicated in Fig. 2.14(b).[90,101]

In order to develop efficient binders and inhibitors, the multivalent presentation of ligands on a scaffold is a promising strategy. In specific, multivalent carbohydrate-based inhibitors are promising structures against pathogens, in order to prevent the adhesion of pathogens at cells or to detach pathogens from cells including the inhibition of rebinding.[101,103,106] Not only the ligand-receptor interaction itself, but also scaffolds and linkers of multivalent inhibitors influence the overall bindings affinity. In this context, several scaffold architectures have been synthesised and studied. Fig 2.14 shows schematically the multivalent presentation of ligands on globular multivalent scaffolds (c), dendritic and star-like polymers (d), flexible linear polymers (e), as well as two-dimensional scaffolds (f). Here, the knowledge of the shape and size of the target structure and the organisation and density of receptors are valuable information for the design of efficient inhibitor structures. Furthermore, thermodynamic considerations have to be made, as the degrees of freedom of scaffold and linkers are also affected upon multivalent binding of multiple ligands on the structure. Various excellent reviews were written in the past decade collecting, organising and comparing multivalent

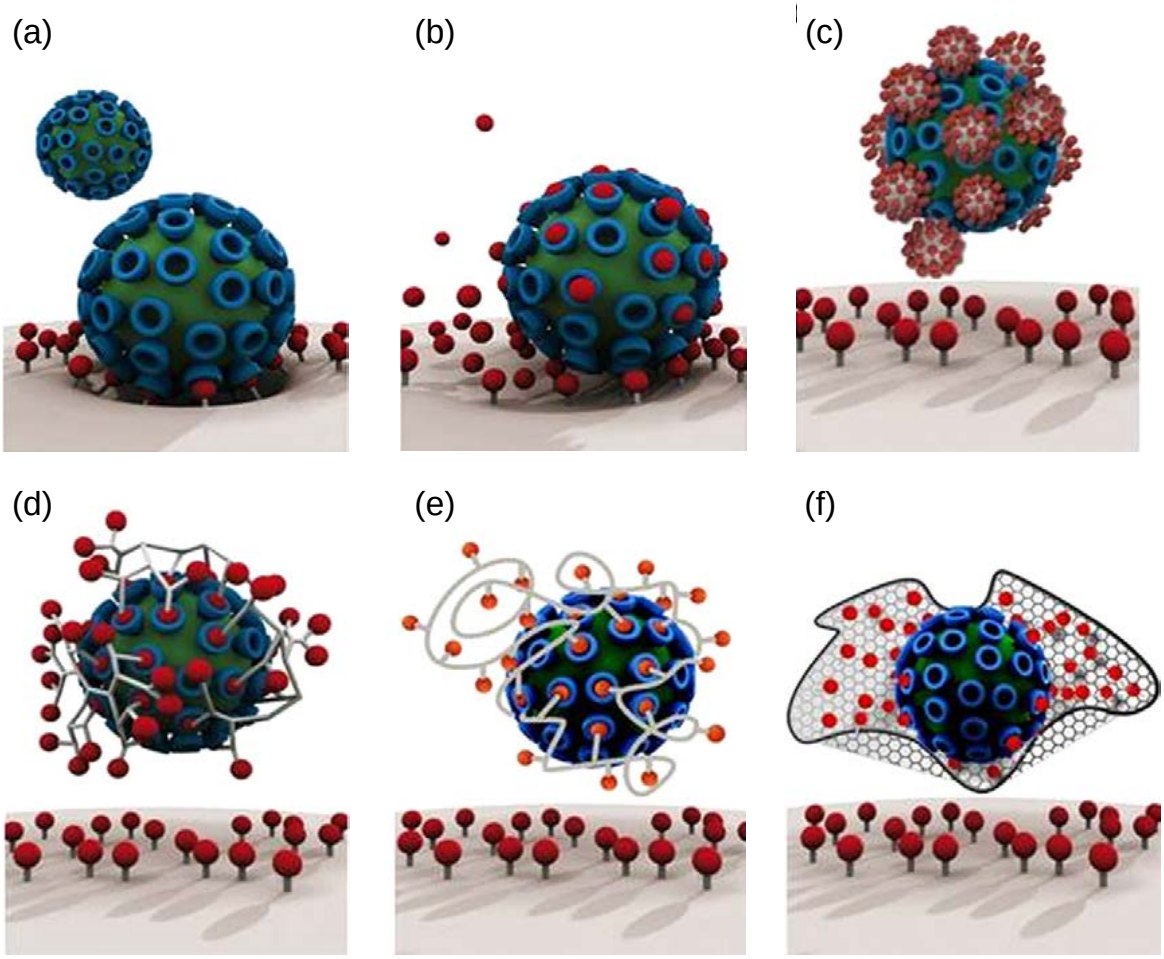

Figure 2.14.: (a) Multivalent binding of a virus to the glycocalyx of a cell. Several inhibiting strategies including (b) monovalent inhibition with a high dosis of a classical small molecule drug; (c) globular multivalent inhibitors, such as functionalised nanoparticles; (d) dendritic and star-like inhibitors; (e) flexible linear inhibitors, such as functionalised polymers; and (f) multivalently functionalised 2D scaffolds with the ability to shield a virus efficiently. Reprinted and adapted with permission from Ref. 101 Copyright 2016 American Chemical Society and Ref. 90 Copyright 2012 John Wiley and Sons.

glycosylated structures for (selected) biological interaction.[101,103,105–109]

2.3.2. Synthetic supramolecular architectures with (multivalent) biological function

Supramolecular assemblies and non-covalent interactions are ubiquitous in nature, as already discussed in previous sections. In contrast, primarily covalent synthetic molecules and polymers have been synthesised and applied in chemical biology. However, these conjugates lack the ability of being adaptive to the environment and to form highly-defined suprastructures at a large size scale, which is characteristic for supramolecular system. Together with an increased knowledge about morphologies and dynamics of water-soluble supramolecular aggregates and polymers over the last decade[3], these systems have gained increased attention for being also applied as functional systems in biology.[43,110–112]

Some prerequisites have to be fulfilled, when considering a supramolecular system for the application in biological systems.[110] First, the supramolecular assembly has to be stable in buffer and under higher salt concentrations. Same is true for the aggregation process together with biologically active ligands, which might change the hydrophilic/lipophilic balance of monomers, compared to unfuctionalised compounds. Here, several functionalisation strategies can be applied, *i.e.*, prefunctionalisation of the monomers or postfunctionalisation of the assembled structure. Moreover, the interaction strength within the supramolecular assembly has to be considered with a view to the targeted interaction *e.g.* with a lectin. As the affinity of multivalent structures also depends on their size and shape, the morphology should not be disturbed upon interaction with biological targets. Hence, the affinity of the supramolecular aggregation should be at least in the same regime as the targeted biological interaction. Thus, a combination of assembly interactions should be considered, as aggregation solely based on the hydrophobic effect might be disturbed by the interaction with other biological systems.

One major advantage of supramolecular structures lies in their dynamic nature and the resulting possibility to adapt and respond to their environment. This is in particular important for the design of efficient multivalent binders that are able to match different target morphologies or clustered receptors, for instance at cell or pathogen surfaces. Over the past years, supramolecular systems based on peptid amphiphiles, host-guest complexes, carbohydrate-functionalised amphiphiles or metal-ligand complexes have been synthesised and applied in drug delivery, sensing, selective imaging, or cell and pathogen interactions.[112,113] In the following paragraphs selected examples based on host-guest complexes and one-dimensional

aggregates are presented.

Recently, Gao *et al.* reported on a self-assembled nanoaggregate based on zwitterionic pillar[5]arene. The weakly positively charged aggregates showed anti-bacterial activity against both, Gram-positive and Gram-negative bacterial strains, and were able to disrupt biofilms of *E. coli* bacteria.[114]

Cyclodextrin-glycoconjugates can be combined with a variety of scaffolds in order to present the carbohydrates multivalently.[106] Depending on the ring size of the cyclodextrins (CD), six, seven, or eight glucopyranoses can be further functionalised with, *e.g.*, carbohydrates in α, β, and γ-CDs, respectively. Cyclodextrins form inclusion complexes with several small organic moieties, such as adamtanyl or benzyl groups with association constants in the micromolar range depending of guest molecule and ring size. Qi *et al.* showed the multivalent functionalisation of a 2D graphene-based sheets. The graphene sheet was functionalised with adamantane, which formed inclusion complexes with mannose-functionalised CDs, yielding a mannose-functionalised 2D sheet, as shown in Fig. 2.15(a). The functionalised sheet was able to sense *E. coli* bacteria and to kill them by IR-irradiation, due to the thermal properties of graphene.[115]

Ravoo and co-workers showed the formation of vesicles by amphiphilic CDs. The CDs at the surface of the vesicles qualify for the inclusion complex formation with a variety of functionalised guest conjugates.[116,117] By the functionalisation with glycoconjugates based for instance on maltose, lactose[118], and mannose[119], binding of the functionalised vesicles to respective lectins was investigated, as schematically shown in Fig. 2.15(b). Furthermore, the ligand density and spacing can be easily varied by the concentration of the guest molecules as indicated in Fig. 2.15(c).

The size and shape of biofunctional materials is of high importance and have been shown to influence binding affinities depending on the biological target.[99,103] Besides well-studied micellar aggregates, also supramolecular one-dimensional architectures, such as fibres, rod-like micelles, helices or tubular assemblies have gained increasing interest for biological applications.[25,31,112,113,120–122] Lee and co-workers synthesised a dendritic mannose-functionalised amphiphile, consisting of the carbohydrate dendron as hydrophilic head group, an aromatic spacer and a hydrophobic alkyl chain.[123] In water, the amphiphile assembled in cyclindrical micelles with a length of around 200 nm. However, upon encapsulation of a small hydrophobic guest molecule, the morphology changed to spherical micelles. Both morphologies were tested regarding their possibility to cluster *E. coli* bacteria in solution. Here, the rod-like micelle reduced the motility of the bacteria significantly better. This effect was explained

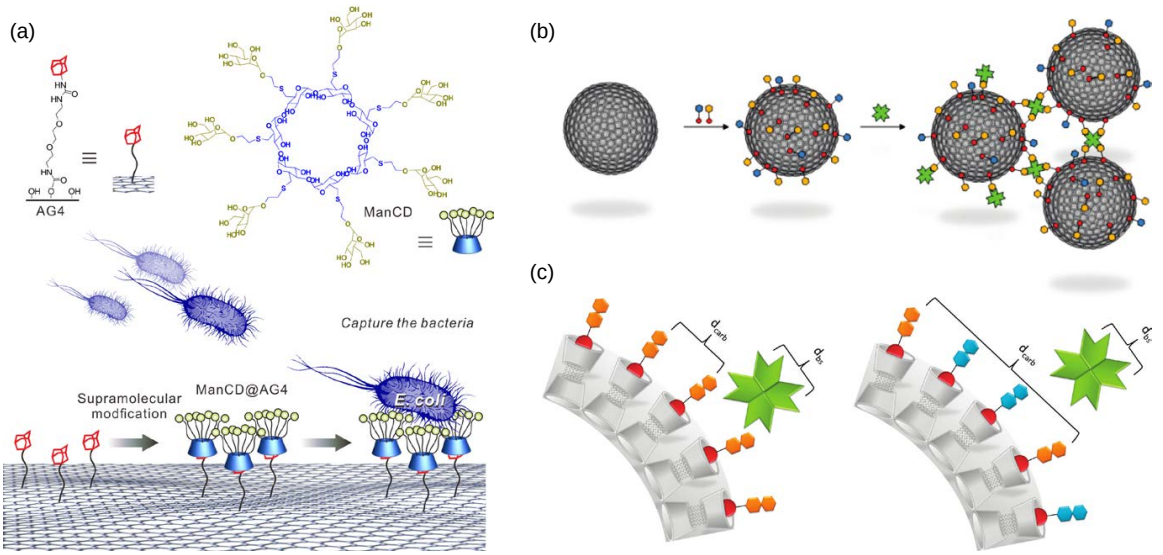

Figure 2.15.: (a) Schematic representation of a supramolecular functionalised graphene sheet by inclusion complex formation of Adamantane and CD-glycoconjugates. (b) CD vesicles functionalised in a supramoelcular system with glycojonjugates and subsequent clustering through lectin binding. (c) By the percentage of glycoconjugates at the vesicle surface, the ligand spacing can be tuned. Reprinted and adapted with permission from Ref. 115 and Ref. 118 Copyright 2015 and 2011 American Chemical Society.

with the higher interference potential of elongated structures with the hairy pili of *E. coli*, where the mannose-receptor lectin FimH is located. In a subsequent study, the influence of the length of fibrous glycosylated structures was investigated.[124] Two dendritic mannosylated amphiphiles were synthesised, which differed in the crystallinity of the aromatic hydrophobic tail. By mixing both amphiphiles in different ratios, the length of the resulting rod-like micelles could be tuned, as shown in Fig. 2.16(b). It was shown by agglutination experiments, that the longer the fibre was, the better bacterial clusters were formed by the aggregation of bacteria dispersed in solution. Furthermore, the proliferation of bacteria was effected to a higher extend by longer fibres.

Besides linear amphiphiles, which assemble into rod- or columnar-like micelles, on the basis of the molecule geometry described by Israelachvili, also discoid amphiphiles assemble primarly in fibrous aggregates. Thus, they are well-suited for the design of glyco-functionalised one-dimensional aggregates.

Brunsveld *et al.* reported on mannose-functionalised supramolecular polymers.[125] C3-symmetrical BTA-based discoid amphiphiles with an extended aromatic core were functionalised with α-D-mannospyranosides. Furthermore, additional glycol side chains ensured sufficient water solubility. The monomers assembled to supramolecular polymers in water, which was

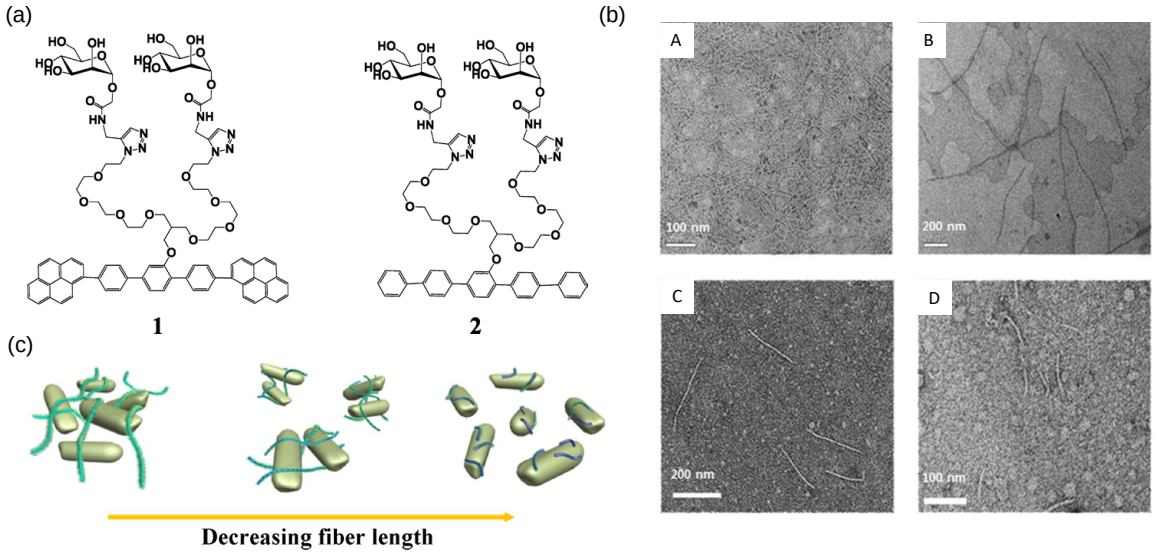

Figure 2.16.: (a) Chemical structures of dendritic mannosylated amphiphiles. (b) Negative-stain TEM images showing rod-like micelles with different length formed by different ratios of amphiphiles 1 and 2; A- 100/0, B- 85/15, C- 50/50, and D- 0/100. (c) Schematic depiction of bacteria cluster formation at different fibre length. Reprinted and adapted with permission from Ref. 115 Copyright 2015 American Chemical Society.

probed by the auto-fluorescence of the aromatic core that occurs upon aggregation. Cultivation with *E. coli* bacteria induced clustering of the polymers together with the bacteria, which was investigated with fluorescence microscopy. The specific binding of mannopyranosides at the polymers to the bacterial lectin FimH was probed by binding studies with FimH active and inactive bacteria strains. By copolymer aggregation of functionalised and non-functionalised monomers, different ligand densities could be obtained, which is a further advantage over covalent architectures. By this, the influence of ligand densities can be investigated without further synthetic effort and subsequent adjustments and optimisations of the architectures can be easily achieved. In the just described approach, only a few percent of functionalised monomers were sufficient to achieve efficient binding to *E. coli* and ConA, indicating the increased binding potency of carbohydrates through organisation into a multivalent polymeric architecture. In a subsequent comparative study with monomers functionalised with mannose only at one side chain or at all side chains, it was found that after valency correction, no difference in the binding affinity of each mannopyranoside was observed by the functionalisation of one monomer with three mannopyranosides.[111]

Besenius *et al.* reported on BTA-based discoid dendritic peptide amphiphiles, functionalised with mannosides for selective binding to murine macrophages and subsequent endocytosis. Here, mannose-functionalisation of the self-assembled nanorods facilitated the uptake into

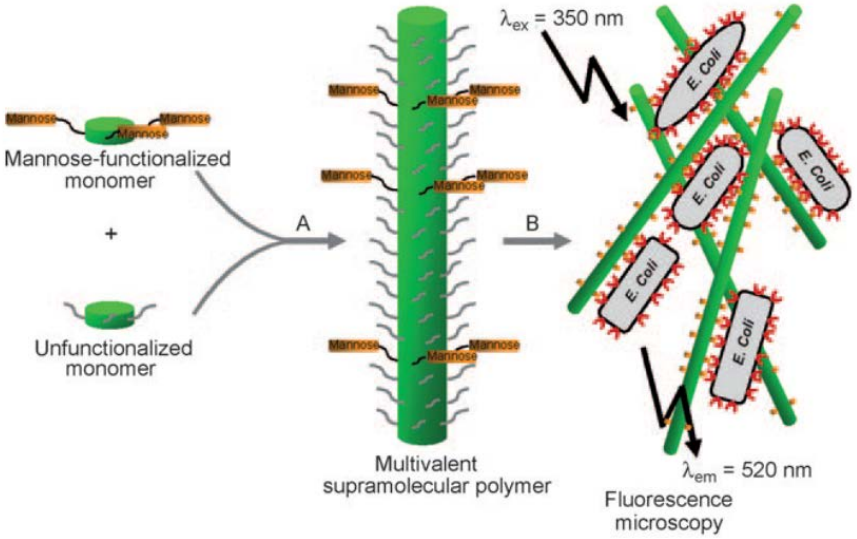

Figure 2.17.: Schematic representation of a mannose functionalised supramolecular polymer inducing *E. coli* clustering by multivalent binding formation between mannosides and FimH receptors at the bacteria. Reprinted with permission from Ref. 101 Copyright 2009 John Wiley and Sons.

the cells without any cytotoxic effects, thus, allowing further functionalisation with various antigens, carbohydrates or immunostimulants for the development of multifunctional anti-tumor vaccines.[126]

Both presented studies utilised extended aromatic or peptide-functionalised cores to stabilise the glyco-functionalised aggregates. In contrast, Leenders and co-workers reported on glycosylated BTA-based amphiphiles with reduced complexity. The central core was functionalised with a hydrophobic alkyl chain and carbohydrates were introduced as polar head group via a triazole linker.[47] A series of molecules comprising β-D-glucose, α-D-glucose, α-D-galactose, and α-D-mannose was synthesised. For the β-D-glucose several lengths of the alkyl chain were investigated, showing the influence of this length on the assembly morphology. Monomers with a C_{12}-spacer assembled in fibrous aggregates, regardless changing carbohydrate functionalisation. By covalent post-modification with a fluorophore, it was shown that the carbohydrates at the surface of the polymer were accessible for binding and furthermore, by this approach, the fibres became visible in fluorescence microscopy. In a subsequent study, it was shown that although glucose-functionalised BTA polymers resembles TEG-functionalised BTA polymers in the morphology, differences regarding the monomer exchange dynamics and the properties of the hydrophobic domain were observed.[127] These results are in particular interesting when considering BTA polymers for multivalent pathogen inhibition or biological recognition processes, as properties such as dynamics and structure might be further tuned

and optimised, *e.g.*, by copolymer formation in order to optimise their desired function.

3 Scientific Aim

The present work aims at the combination of supramolecular and dendritic structures for the enhancement of multivalent ligand-receptor recognition in biological systems. Therefore, the synthesis and investigation of biofunctional multivalent structures, based on supramolecular assemblies and polymers is targeted. In particular, the functionalisation of supramolecular aggregates with dendritic structures as a method to introduce multivalency is aimed.

In the first part of this thesis, the synthesis and analysis of stable one-dimensional water-soluble supramolecular polymers based on 1,3,5-benzenetricarboxamide-based amphiphiles (BTAs) with polyglycerol dendrons is targeted. In this context, the influence of dendron size, as well as alkyl chain length on the aggregation into supramolecular polymers and the resulting dynamics of the polymer will be investigated. In addition, the structure of the supramolecular polymers will be analysed by cryogenic transmission electron microscopy (cryo-TEM) regarding their detailed assembly structure at nanometre resolution. Furthermore, it shall be evaluated, if and how copolymer formation influences the structure and dynamics of the investigated supramolecular polymers.

In the second part of the thesis, glyco-functionalised supramolecular structures shall be investigated regarding their interaction with lectins and bacteria. Here, BTA-based polymers, as well as cyclodextrin (CD)-based vesicles will be used as supramolecular platform. First, the assembly of mannose-functionalised BTA monomers into supramolecular polymers will be investigated, as well as their potential to recognise mannose-binding lectins. Second, spherical CD vesicles shall be functionalised with dendritic glycoconjugates in a supramolecular modular approach. By this approach, an investigation of the influence of ligand concentration in combination with multivalent ligand clustering on lectin and bacteria binding is targeted.

Part II.

Results and discussion

4 Synthesis and characterisation of new BTA-based amphiphiles with polyglycerol-based dendritic head groups

This work has been performed in collaboration with Dr. Xianwen Lou (HDX) and Dr. Lu Su (assembly studies), both Eindhoven University of Technology, The Netherlands.

4.1. Introduction

Supramolecular polymers based on monomers comprising a 1,3,5-benzenetricarboxamide motif (BTA) were studied in detail by Meijer *et al.*, both experimentally as well as theoretically.[46] The molecules are C3-symmetric and discoid. A nonpolar alkyl chain next to the benzene core and a polar terminal head group are the origin of the the amphiphilic character of the molecules. Through one-dimensional stacking, these structure are able to form one-dimensional supramolecular polymers. In order to enable water-solubility, a tetra(ethyleneglycol) (TEG) chain was introduced as head group. In addition, a C_{12}-chain ensured a sufficiently large and stable hydrophobic pocket.[45] Thus, water-soluble one-dimensional supramolecular polymers made from BTAs became accessible with this molecules, i.e. BTA-C_{12}-EG_4 (nBTA). It was shown, that the hydrophobic effect is crucial for initial nucleus formation of few monomers, whereas directional H-bonds between the amid groups stabilise the formation of micrometre-long fibre-like polymers.[48,49]

Water-soluble supramolecular polymers are promising candidates as biologically active materials, *e.g.*, in the field of pathogen inhibition. Here, the concept of multivalency and in particular the multivalent display of biologically active ligands is highly promising.[101] However, poly(ethyleneglycol) (PEG) functionalisation has limitations in this regard. First, only one terminal hydroxyl group does not qualify for direct multivalent functionalisation and secondly, induced hypersensitivity against PEGylated drug conjugates, as well as rapid systemic clearance have been reported.[128,129]

In contrast, polyglycerol-based (PG) compounds exhibit a higher biocompatibility compared to PEG in combination with a very good water-solubility. Polyglycerol can be synthesised as linear polymers (lPG), dendritic or hyperbranched (dPG/ hPG) or as defined dendrons.

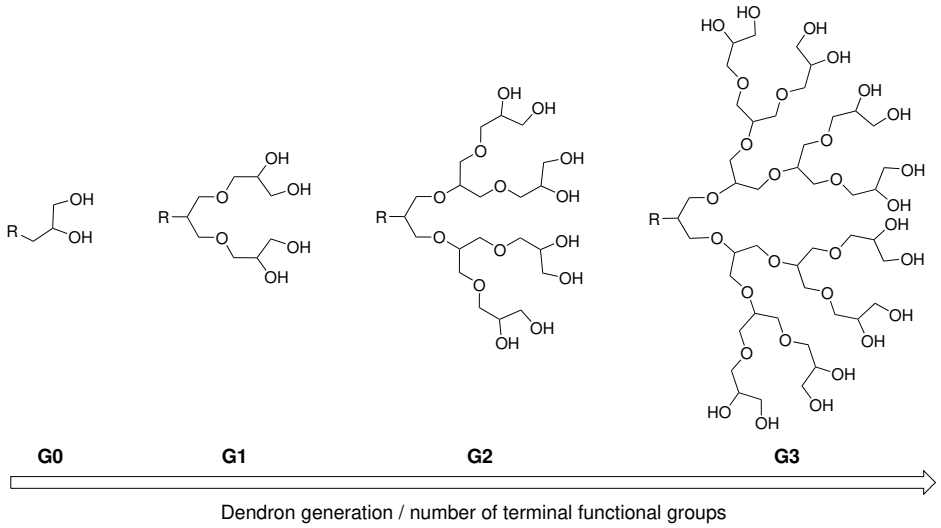

Figure 4.1.: Evolution of polyglycerol-based dendrons with increasing dendron generation and terminal functional groups.

By using different generations of the dendron, the number of terminal hydroxyl groups can be tuned, *i.e.*, two for generation 0 (G0), four for generation 1 (G1), 8 for generation 2 (G2), etc. as shown in Fig. 4.1.[15,128]

Recently, Thota *et al.* introduced a BTA-based amphiphile with a PG-based dendritic head group, *i.e.*, BTA-C_{12}-G1 (dBTA).[28] It was shown that dBTA exhibited a very good water-solubility, but was not able to form one-dimensional supramolecular polymers. Instead, small spherical micelles were formed. This observation was attributed to the increased hydrophilicity of the PG-head group compared to the PEG-chain. Thus, the hydrophilic/lipophilic balance (HLB) was shifted and a one-dimensional supramolecular polymerisation not possible.

It was therefore the aim of this project to synthesise BTA-based amphiphiles with dendritic PG-based head groups and the ability to form one-dimensional supramolecular polymers in water. The structures were varied to increase the hydrophobicity of the BTAs, compared to dBTA. Therefore, the structure of dBTA was modified in two directions, *i.e.*, the elongation of the alkyl chain or the reduction of the size of the dendritic head group. The first approach was to elongate the alkyl chains from C_{12} to C_{16} in order to increase the hydrophobic pocket, resulting in the first target compound BTA-C_{16}-G1. In the second approach, the size of the dendritic head group was reduced from G1 to G0, *i.e.*, one glycerol unit. Here, derivatives with both, C_{12} and C_{16} chains were synthesised, leading to the second and third target molecule of this project, *i.e.*, BTA-C_{12}-G0 and BTA-C_{16}-G0. All target molecules including the structures of nBTA and dBTA are shown in Fig. 4.2.

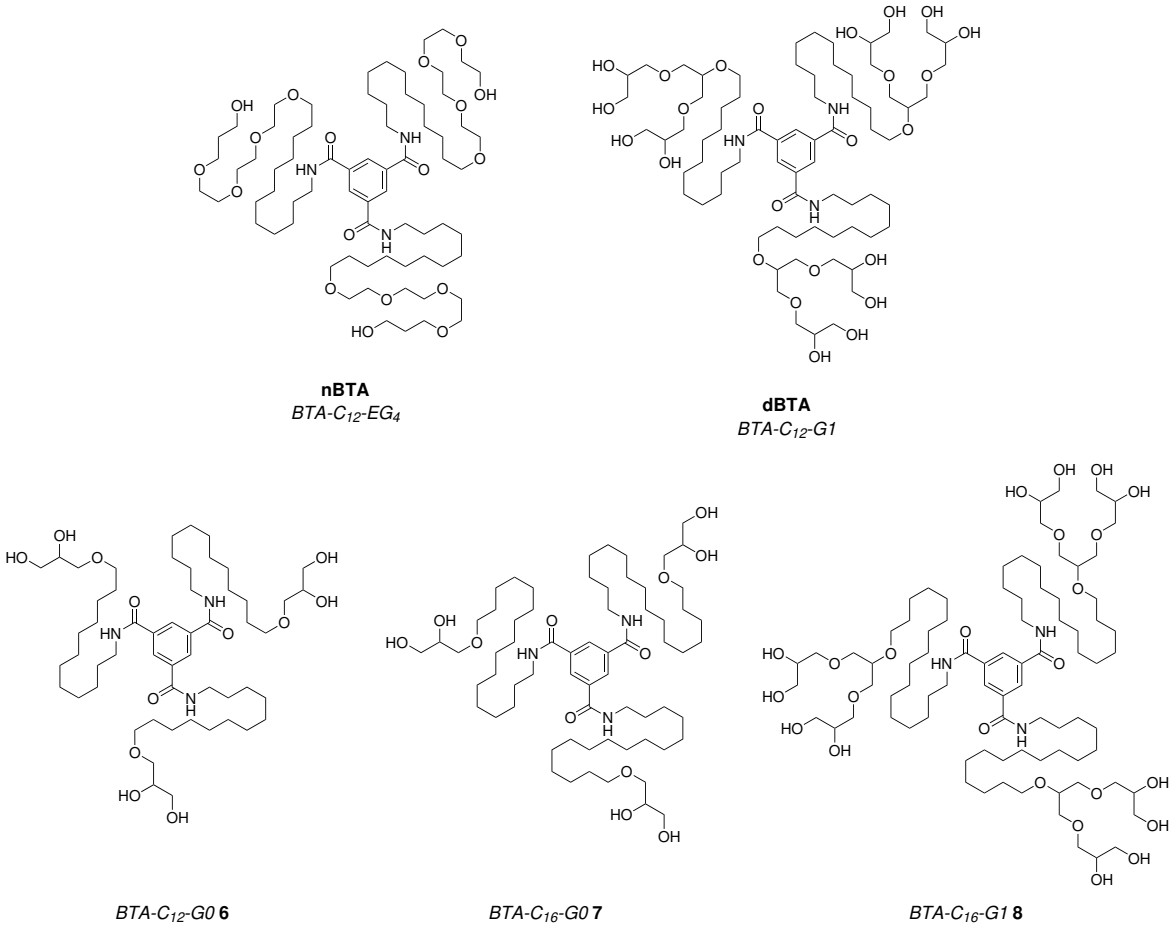

Figure 4.2.: Chemical structures of nBTA, dBTA and the target molecules BTA-C_{12}-G0 **6**, BTA-C_{16}-G0 **7**, and BTA-C_{16}-G1 **8**.

4.2. Results and discussion

4.2.1. Synthesis

Within the framework of this thesis, three new BTAs with dendritic head groups were synthesised, which are shown in Fig. 4.2: BTA-C_{12}-G0 **6**, BTA-C_{16}-G0 **7**, and BTA-C_{16}-G1 **8**. All molecules are C3-symmetric and comprise a Benzene-1,3,5-tricarboxamide core, a hydrocarbon chain, and a polyglycerol dendron as hydrophilic head group. The synthesis was designed in a convergent approach, *i.e.*, the alkyl chains and head groups were synthesised first and in a last step coupled to the benzene core. Where applicable, published procedures were adopted. The synthetic scheme is depicted in detail in Fig. 4.3. The synthesis started for the C_{12}- and C_{16}-derivatives with 1,12-dibromododecane (**1b**), and 1,16-hexadecanediol(**0**), respectively. Both materials are commercially available. After bromination of the latter, the dibromo-derivatives **1a** and **1b** were monofunctionalised with acetal-protected dendrons by substitution reactions. For the G0-functionalisation, isopropylidene glycerol (solketal) was

used. For the G1-functionalisation, hydroxyl terminated and acetal protected G1-dendron (pG1-OH) was used.[18] The reaction yielded **2a-c** in moderate yields, owed to the statistical monofunctionalisation. Subsequently, a primary amine was introduced. Here, different synthesis approaches were tested. First, the substitution of the bromine with an azide group was performed. Afterwards, a reduction with H_2 and Pd/C was attempted. However, dimerisation in combination with the formation of a secondary amine was observed as prominent side reaction.[130] Subsequently, a Staudinger reduction with PPh_3 was carried out. Due to the laborious purification, here, the yield was below expectations. Finally, the Gabriel-synthesis approach was followed. The bromine was substituted in a first step with potassium phthalimide (**3a-c**). Afterwards, the phthalimide was converted to the corresponding primary amine by reduction with hydrazine monohydride, yielding the amines **4a-c** in high purities. The reaction with trimesoyl chloride gave the protected BTAs **5a-c**, which were purified by normal-phase HPLC. In a last step, the acetal groups were cleaved off and the final BTAs **6**, **7**, and **8** were obtained. After HPLC purification and subsequent lyophilisation, the final target molecules were obtained in high purity.

4.2.2. Properties of BTA-C_{16}-G1 in aqueous solution

After completion of the synthesis, the water-solubility and self-assembly of the BTAs in water was investigated. For that purpose a non-covalent synthesis protocol, including heating, vortexing, and slow cooling of the aqueous solution, was applied (*cf.* Methods section for details). Solutions with a target concentration of 500 μM in water of BTAs **6**, **7**, and **8** were prepared. Here, different solubilities of the compounds were observed. BTA-C_{16}-G1 exhibited a very good water solubility, whereas the solution of BTA-C_{12}-G0became cloudy directly after preparation and precipitated minutes after cooling of the solution. BTA-C_{16}-G0 turned out to be almost insoluble in water. Therefore, this compound was not further analysed.

The UV-VIS spectra of BTAs in solution can be used to provide initial insights into the aggregation behaviour of BTAs.[45] The spectroscopic signature of nBTA showed two maxima at around 211 nm and 224 nm, as shown in Fig. 4.4. These bands are attributed to the conformation of the H-bonds between the amide groups in the supramolecular polymer in a columnar stack. In contrast, dBTA, which assembled in spherical micelles[28] exhibited only one maximum at 196 nm. Similarly, the UV-VIS spectrum of BTA-C_{16}-G1 exhibited only one maximum at 195 nm likewise to dBTA. The peak maxima were extracted in all cases from the local slope of the experimental data. BTA-C_{12}-G0, however, showed only minor and nearly constant absorbance over the whole spectral range. This supported the presumption of nearly

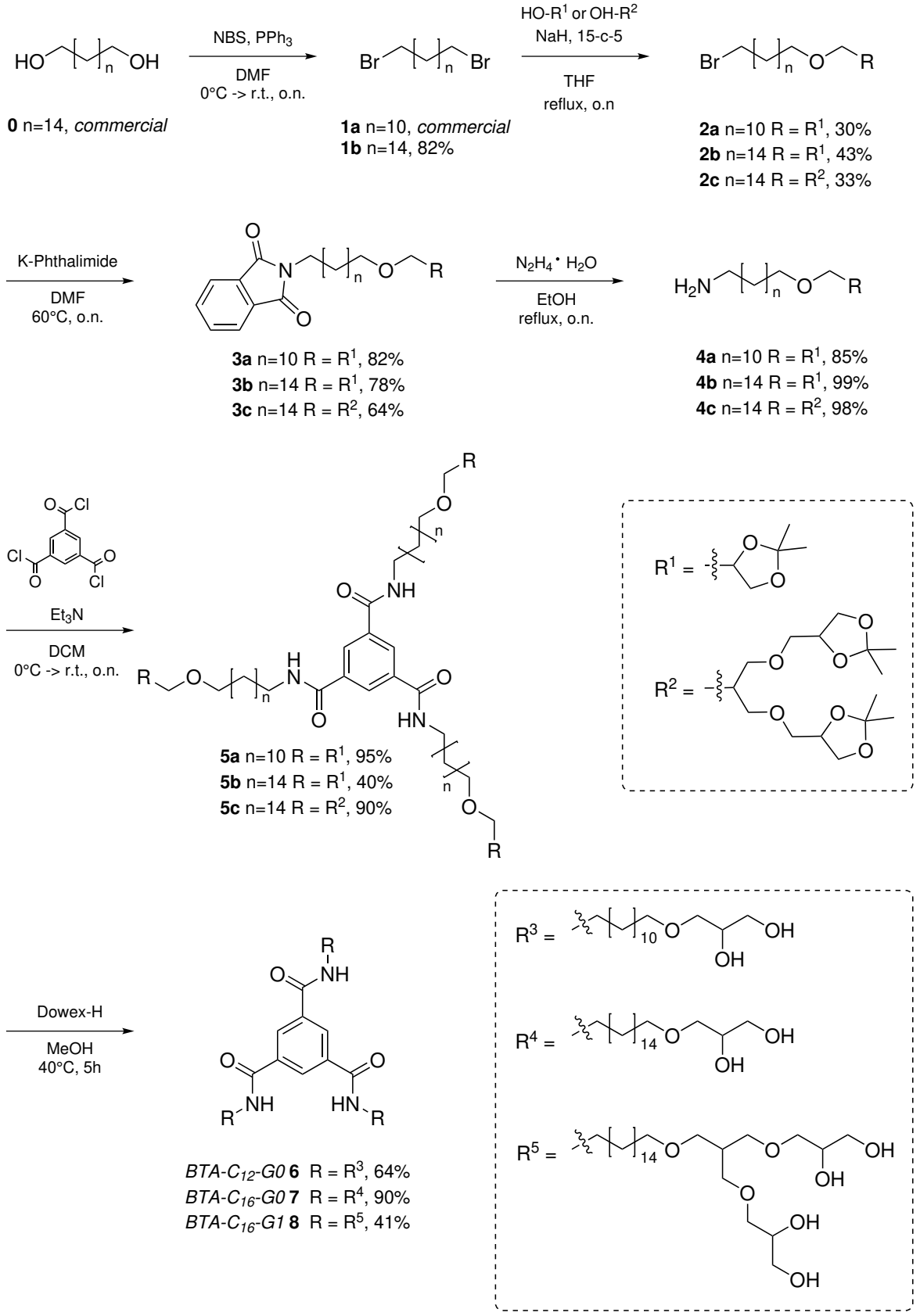

Figure 4.3.: Reaction scheme for the synthesis of BTAs BTA-C_{12}-G0 **6**, BTA-C_{16}-G0 **7**, and BTA-C_{16}-G1 **8**.

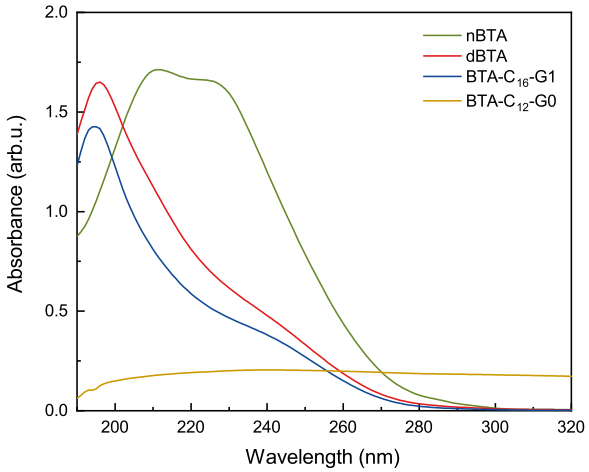

Figure 4.4.: UV-VIS spectra of nBTA, dBTA, BTA-C_{12}-G0 **6**, and BTA-C_{16}-G1 **8** in H_2O (c = 50 μM) at 20 °C .

non-dissolved, dispersed particles in solution. Therefore, only the properties of BTA-C_{16}-G1 in aqueous solution were studied in further detail.

The above discussed spectroscopic signature of BTA-C_{16}-G1 suggested a similar conformation of monomers in the aggregate compared to dBTA, that is, the formation of spherical micelles. Static light scattering (SLS) experiments were therefore conducted to analyse the spatial expansion of the aggregates. Spherical micelles would result in an angle-independent Rayleigh ratio. In contrast, an angular dependence of the scattered light indicates the formation of anisotropic aggregates. As can be seen in Fig. 4.5(a), the Rayleigh ratio of BTA-C_{16}-G1 exhibited an unexpected angular dependence and corresponded to the experimental data obtained for nBTA. The angular dependence of scattering data combined with Rayleigh ratio values obtained in the same range as for nBTA, indicated the formation anisotropic aggregates similar to nBTA.

In order to gain further insights to the formed aggregates, the properties of the hydrophobic pocket were probed by Nile Red encapsulation experiments. Nile Red is insoluble in water but can be encapsulated in hydrophobic pockets of *e.g.* proteins or synthetic supramolecular aggregates.[131] Upon encapsulation, Nile Red exhibits a fluorescence in the red spectral region, which is sensitive to the polarity of the environment of the dye molecule. For both compounds, nBTA and BTA-C_{16}-G1, a fluorescence signal is observed as shown in Fig. 4.5(b), demonstrating the presence of a hydrophobic pocket. When comparing the peak maxima, BTA-C_{16}-G1 exhibited a maximum at higher wavelengths (λ_{max} = 626 nm) in comparison to nBTA (λ_{max} = 612 nm), is attributed to a polar, *i.e.* less hydrophobic, environment of the dye molecule. However, due to the longer alkyl chains in BTA-C_{16}-G1, the reverse effect was

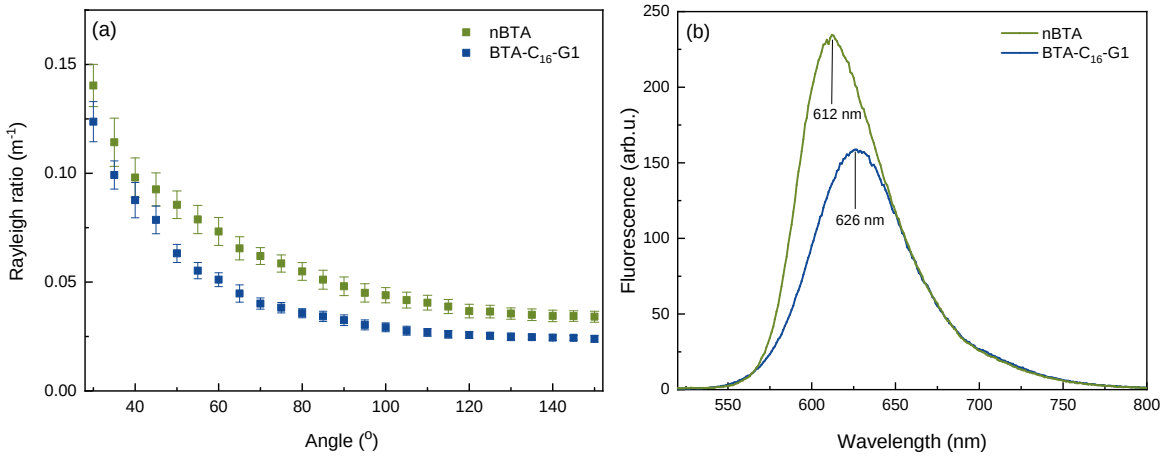

Figure 4.5.: (a) Static light scattering experiments of nBTA and BTA-C_{16}-G1 show the angular dependence of the scattered signals indicating the formation of anisotropic aggregates for both molecules. (b) Nile Red fluorescence data for nBTA and BTA-C_{16}-G1showing the ability of both compounds to encapsulate Nile Red in their aggregates. The red-shifted maxima for BTA-C_{16}-G1 indicates a less hydrophobic environment of the dye.

expected. Here, a large hydration shell, induced by the dendritic head groups or a different structural organisation within the supramolecular aggregate might explain the more polar environment for Nile Red in BTA-C_{16}-G1 aggregates.

The monomer exchange dynamics of supramolecular aggregates can be probed by hydrogen deuterium exchange measurements (HDX).[50] In the experiment, a 500 μM solution of the respective sample in H_2O was 100-times diluted in D_2O. Subsequently, electrospray ionisation mass spectrometry (ESI-MS) experiments are conducted over a period of multiple days.[50] In the recorded spectra, the exchange of hydrogen atoms with deuterium was monitored by quantitative analysis of the respective peaks as a function of time. The schematic process of the HDX-MS experiment is depicted in Fig. 4.6

There are two kinds of exchange-labile hydrogen atoms present in water-soluble BTA-based amphiphiles. First, hydroxyl groups at the polar head groups and, second, the amide groups in the center of the molecule. In the case of molecular solvation all hydrogen atoms are exchanged immediately after dilution with D_2O, as all exchange-labile protons are exposed to the solvent. In supramolecular aggregates, the polar head groups point towards the aqueous surrounding, whereas the hydrophobic pocket is shielded from the solvent. Thus, the exchange-labile protons present in the hydrophobic pocket are shielded from prompt H/D exchange. However, due to the reversible non-covalent interactions within the supramolecular polymer, monomers are constantly exchanged with the bulk water.[61] When monomers

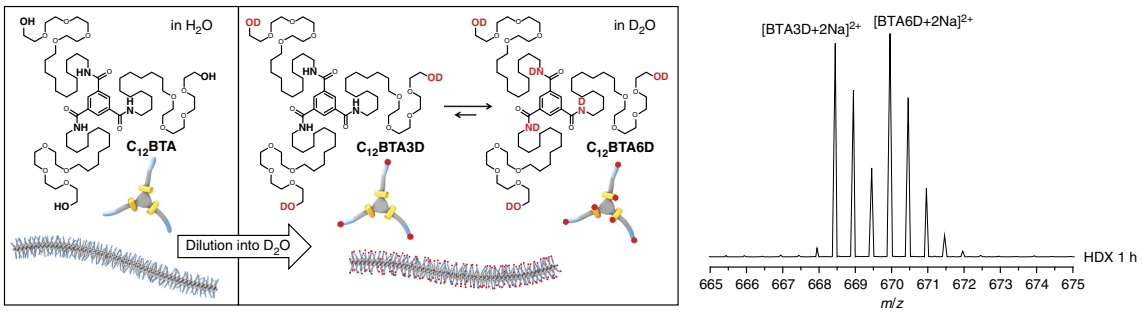

Figure 4.6.: Schematic representation of H/D exchange process upon dilution of a supramolecular polymer (nBTA). (a) Chemical structure of nBTA in water and in D_2O with either only deuterated hydroxyl groups (C_{12}BTA3D) or also deuterated amide groups (C_{12}BTA6D). (b) ESI-MS spectrum 1h after dilution in D_2O showing peaks for both species, C_{12}BTA3D and C_{12}BTA6D. Reprinted with permission from Ref. 50 with permission.

are molecularly dissolved in the bulk water during this process, also the amide protons of the molecule are exchanged with deuterium. The kinetic rate of this process can be used as measure for the dynamics of the supramolecular polymer.[50]

In BTA-C_{16}-G1 15 exchange-labile hydrogen atoms are present, which divide into 12 protons at the hydroxyl groups of the dendritic head groups and three amide protons. As expected, the head group protons were exchanged immediately upon dilution in D_2O, showing the unlimited solvent accessibility of the head groups. In contrast, a different behaviour was observed for the amide protons. The decay of unexchanged amide protons over time ("BTA-3(NH)" in %, BTA12D $\rightarrow$ BTA15D) was analysed and is shown in Fig. 4.7 in comparison to the data obtained from a nBTA solution. After an initial decrease to roughly 70% in the first minutes, the ratio of unexchanged protons remained constant. Furthermore, even after a time period of 100 h, the ratio of unexchanged amide protons remained at 70%. An enlarged view of the initial phase including the first 6 h is depicted in Fig. 4.7(b). Here, a small minimum can be seen in the first two hours, which we, however, attribute to a systematic error and an artefact, as the reverse exchange from deuterium to hydrogen in D_2O is highly unlikely. In sum, BTA-C_{16}-G1 exhibited very low exchange dynamics, which indicates the formation of highly stable aggregates.

In contrast, for nBTA, a different behaviour could be observed. Similarly, a prompt exchange of the outer protons at the hydroxyl groups was observed. However, for the amide protons, the amount of unexchanged amide protons decreased over time after an initial decrease to 45%. In addition, the decay over time could be fitted with a tri-exponential fit, dividing the monomer exchange into three stages, i.e., initial, fast, and slow.[50] For BTA-C_{16}-G1, a similar

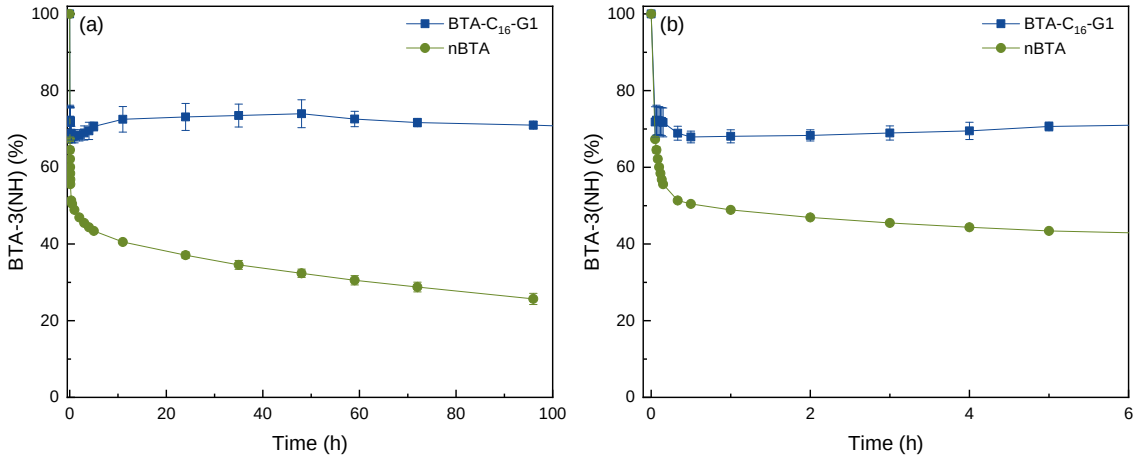

Figure 4.7.: Percentage of unexchanged amide protons (BTA-3(NH)) over time. A 500 μM solution of BTA-C_{16}-G1 and nBTA was diluted 100 times in D_2O and the exchange of hydrogen to deuterium monitored by ESI-MS measurements. (a) Experimental data obtained over 100 h. (b) Depiction of the first 6 h of the measurement.

data analysis and the division into exchange phases could not be applied successfully, owed to almost constant ratio of unexchanged amide protons after an initial exchange in the first minutes. In order to correlate the obtained data from HDX experiments to the structure of the aggregates, including the differences to nBTA, cryo-TEM images of BTA-C_{16}-G1 aggregates were recorded.

Cryo-TEM experiments were carried out to further investigate the supramolecular organisation in water. SLS experiments suggested anisotropic aggregates likewise to nBTA, and indeed, fibrous aggregates were observed as prominent morphology for BTA-C_{16}-G1 as shown in Fig. 4.8. Throughout the recorded images, the fibres appeared both, individually and bundled. Moreover, the bundles were observed twisted around each other as well as aligned parallel [*cf.* Figs. 4.8(a) and (c)]. Additionally, also spherical micelles were observed, as shown in Figs. 4.8(a) and (b).

Strikingly, the appearance of the fibrous aggregates of BTA-C_{16}-G1 differed from those of nBTA. In particular, the contrast of the fibres changed from weak to strong and vice versa. In addition, areas with weaker contrast appeared broader and those with strong contrast more narrow. This effect is shown in Figure 4.8(d) and marked by arrows in the picture. Here, the presence of narrow ribbons in different orientations along the long axis, rather than one-dimensional aggregates with a spherical cross-section, would explain the observed variations in thickness and contrast. Therefore, further investigations of the structural aggregation at nanometre scale (ultrastructure) were carried out and are part of the next section. In ad-

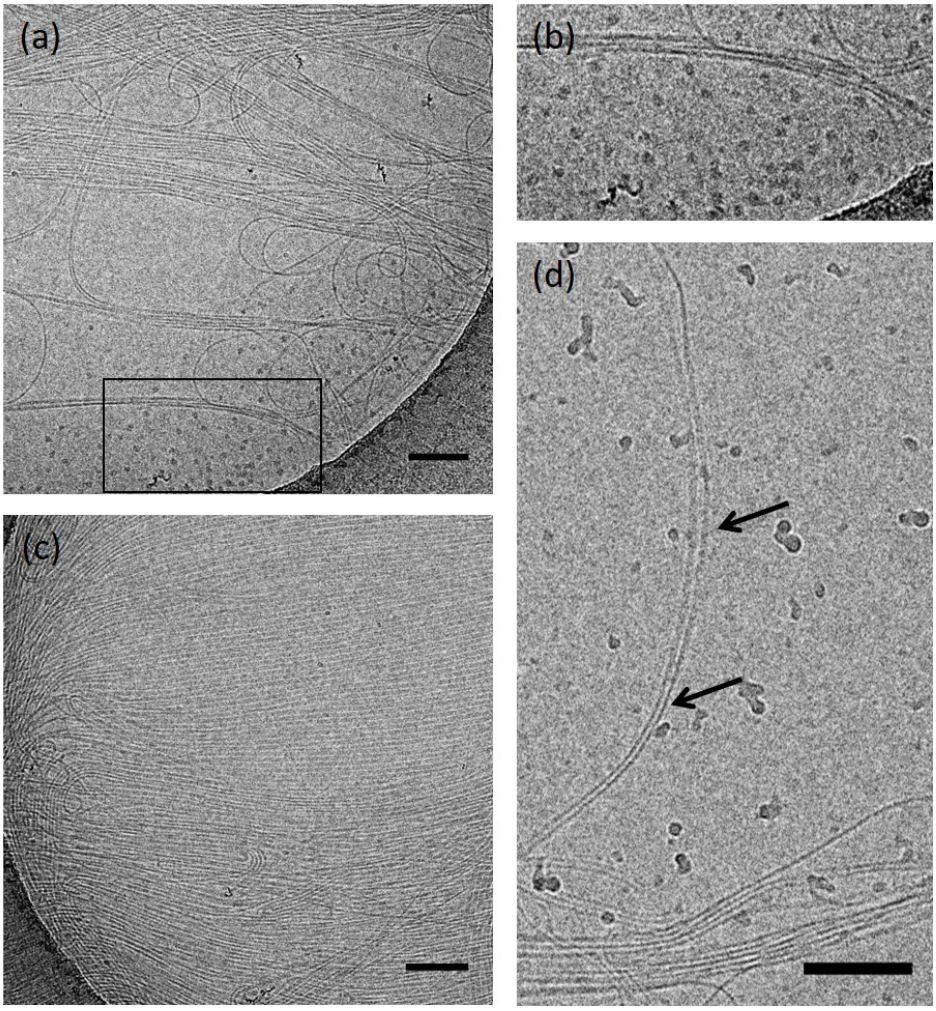

Figure 4.8.: (a) Representative cryo-TEM image of BTA-C_{16}-G1showing the formation of fibre-like aggregates and spherical micelles. (b) Excerpt of black rectangle in (a) for an enlarged depiction of the micelles. (c) Parallel bundles of fibre-like aggregates. (d) By rotation of the aggregates the contrast changes from weak to strong as pointed out by the two arrows in the image. Scale bars represent 100 nm.

dition, the ultrastructure of nBTA was investigated and both structures were compared to each other.

4.2.3. Ultrastructure analysis of nBTA and BTA-C_{16}-G1

Previous work In the previous section, the successful synthesis of a new BTA-based amphiphile with a dendritic head group (BTA-C_{16}-G1) was demonstrated. In addition, the supramolecular aggregation of this amphiphile into micrometre-long fibres was observed by cryo-TEM. However, HDX experiments revealed significant differences between both aggregates in regards of monomer exchange dynamics, *i.e.*, significantly lower monomer exchange

dynamics were observed for BTA-C_{16}-G1 compared to nBTA. These differences might be explainable by subtle differences between both structures that could be identified in cryo-TEM images. For BTA-C_{16}-G1, a narrow, ribbon-like structure of the aggregates was identified. In contrast to that, the fibres of nBTA appeared to have a spherical cross-section in cryo-TEM images. Since structure and function are in general closely related, it was in the following the aim to elucidate the structure of BTA-based supramolecular aggregates at nanometre scale to reveal structural differences that help to understand different functional properties.

Recently, Lafleur and co-workers analysed the ultrastructure of nBTA polymers with cryogenic electron tomography (cryo-ET) and numerical cross-section analysis of the reconstructed volume. In their work, Lafleur *et al.* observed variations in the diameter of the fibrous polymers and compared their findings with high-magnification images using conventional 2D cryo-TEM. Through segmentation of the reconstructed volume after cryo-ET along one polymer fibre, an elliptic contour of the structure perpendicular to the elongated axis of the polymer was determined. In particular, by analysing multiple cross-sections along the fibre, two individual strands of nBTA twisted around each other in a double-helix motif were identified. The repeating unit was determined to be (22.9 ± 1.8) nm.[132]

Double-helix structures are a rather rare morphology, obtained in synthetic supramolecular structures. However, some examples of targeted design of double helices are reported[133], although in most cases covalent polymer strands are held together by different kinds of non-covalent interactions, such as by metal coordination[134], aromatic interactions[135] or H-bonds[136]. Most examples are reported in organic solvents, however, few examples in water are reported as well, such as poly(*m*-phenylenen)s, which assemble by aromatic inter-strand interactions into double helices.[137] Böttcher *et al.* reported on a double-helix in water build from polycationic dendronised polymers.[87] By double-strand formation, the hydrophobic polystyrene backbones were efficiently shielded by the dendritic head groups from water, which was not sufficiently possible in a monomeric structure. In this example, the double-helix structure was revealed by cryo-TEM and subsequent image processing. To this end, individual fibre structures were extracted, aligned and classified, which included a multivariate statistical analysis. By averaging similar classified images, structural informations due to an enhanced signal-to-noise ratio in the resulting images could be obtained.

In this work, we applied the same method in order to elucidate the ultrastructure of nBTA. In the following, we first analysed the ultrastructure with image processing techniques and multivariate statistical analysis (MSA). The obtained results were then compared with the results of Lafleur and co-workers in order to validate the application of MSA for the ultra-

structure analysis of BTA-based one-dimensional aggregates. In a second step, we analysed the, so far unknown, ultrastructure of BTA-C_{16}-G1 at nanometre resolution. A comparison of both structures concludes this analysis.

Ultrastructure analysis of nBTA

In cryo-TEM, different morphologies of nBTA aggregates could be observed for the same sample, showing the versatility and variety of supramolecular aggregation. Some representative cryo-TEM micrographs are shown in Fig. 4.9. Most prominent are micrometre-long, one-dimensional, elongated fibres. These are found as individuals randomly oriented in the sample, as in Fig. 4.9(a), or as bundles, as shown in Fig. 4.9(b). Besides the concentration and age of the sample solution, also the preparation parameters are known to influence the appearance of the sample. During the vitrification, the sample is additionally affected by strong shear forces that might influence fibre orientation or induce bundle formation.[138,139] Besides the fibrous aggregates, at least two other morphologies were observed, *i.e.*, tube-like morphologies, as well as a finger-print pattern. The tube-like morphologies are shown in Fig. 4.9(d). An analysis of this morphology is still pending and will be part of future work. In contrast to the rarely occurring tubes, a third morphology is ubiquitous, that is, a finger-print like pattern, which spanned the whole surface of the sample. An extracted example is shown in Fig. 4.9(c). From the Fast Fourier Transformation (FFT) of the image [inset in (c)], a highly equidistant ordering could be deduced. The clearly defined deflection ring has an inverse radius of 4.5 nm, which fits roughly to the double width of the hydrophobic part in nBTA, *i.e.*, 2 - 2.5 nm. Thus, the surface-covering, finger-print like pattern can be assigned to organised monomers at the surface. Here, an assembly of monomers at the air-water-interface or throughout the volume, likewise to a liquid crystalline phase, are probable explanations.

In order to elucidate details in the ultrastructure of the fibrous aggregates, we applied cryogenic transmission electron microscopy (cryo-TEM) with subsequent image processing using the IMAGIC-5 software package.[79] First, conventional cryo-TEM micrographs were recorded. From these images, individual fibre motifs were extracted. For successful image processing it is important to find a sufficiently large population of straight fibres that lay orthogonal to the electron beam in order to generate a large, processable data set. Furthermore, care was taken that the cut-outs contained no contaminations and crossing fibres. Via rotational and translational image alignment, the structures were brought in vertical orientation and close correlation to each other.

In the next step, we employed a multivariate statistical analysis (MSA) to classify the data

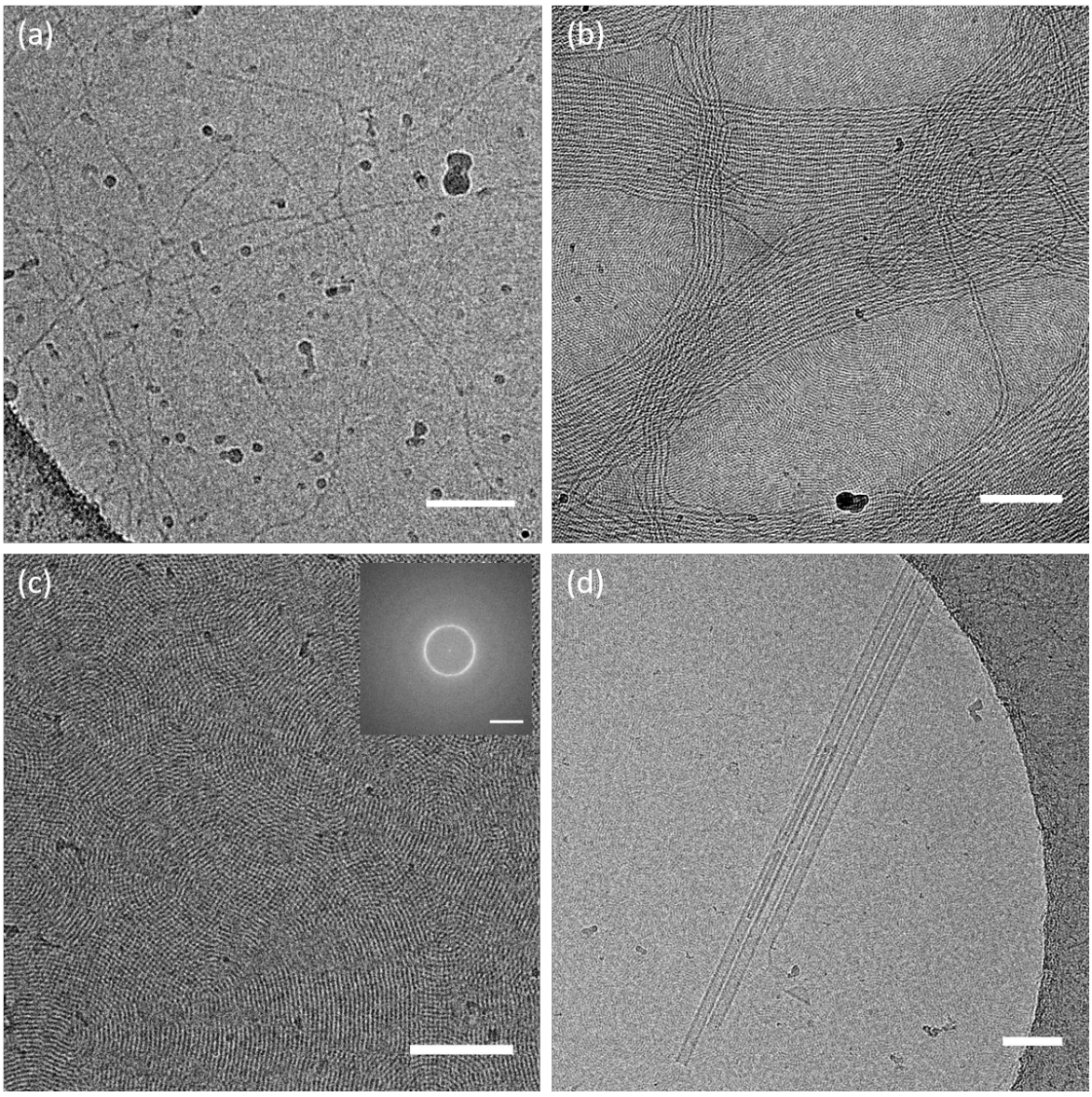

Figure 4.9.: Representative cryo-TEM micrographs of nBTA (500 μM in milliQ) showing examples of (a) individual fibres, (b) fibre bundles, (c) finger-print like surface pattern, and (d) tubular structures. Scale bars represent 100 nm (a, c, d) or 200 nm (b). The inset in (c) shows an FFT image of (c) in which the defined deflection ring shows the equidistant arrangement of features in the finger-print pattern. Scale bar represents 0.3 1/nm

set. A selection of class sum images is shown in Figs. 4.10(a)-(d). As can be seen, the fingerprint pattern is also reflected in some of the class images [Figs. 4.10(b) and (d)], hence, disturbing a clear view of the fibres. However, the presence of two individual strands twisted around each other could be already deduced as dominant motif from these class sum images. As the first cut-outs of (96×96) px only showed a very narrow part of the ultrastructure, we generated a second data set with cut-outs of (200×200) px. After alignment and filtering of the images, an averaged sum image of the data set was generated, which is shown in Fig. 4.10(e). From this, the projection of a double-helix could be clearly identified. Additionally, as the background pattern had no preferred direction in regards to the helix motif, it was levelled out during the sum image creation. Other unspecific density and noise contributions were likewise averaged. As a result, a significant density separation of the motif from the surrounding could be achieved. This effect can be nicely seen in the low density area between the two strands, indicating the separation of the fibres between two knots. The appearance of this feature could be used to differentiate the double-helix structure from a twisted-ribbon structure, where such a density minimum would be absent.

A repeating periodicity, *i.e.*, the distance between two knots and thus half of a helix pitch, could be identified from the data set and was determined with (19.9±0.4) nm. The accuracy of this and further image-based measurements were approximated with roughly one pixel size, corresponding to approx. 0.4 nm.

Subsequent to the 2D analysis, we performed a 3D image-based reconstruction of the double-helix. Therefore, the sum image was symmetrised [Fig. 4.10(f)] in order to equalise unspecific differences. In a next step, the image was scaled up to a length of 360 px. Since the double-helix is rotationally symmetric and the image shows a full period (pitch) of the structure, every pixel row equals the rotation of 1°. From this, 360 images were generated by the shift of one pixel row at each time, thus generating views of the double-helix in 360°. The views of 0°, 45°, and 90° are shown in Fig. 4.11(a). From the projection views in 360 °, a reconstruction was computed subsequently. In Fig. 4.11(b) the resulting cross-section reconstruction image, perpendicular to the long axis of the double-helix, is shown. As expected, two individual strands with a low density area between them could be seen. Unexpectedly, the strands seemed to be slightly oval, which is not intuitive, as the BTA monomers exhibit a C3-symmetry.

The reconstruction was then used to compute a back-projection, in order to judge on the accuracy of the reconstruction. Here, back-projection images were generated, of which the views in 0°, 45°, and 90° are shown in Fig. 4.11(c). By comparison with the input images,

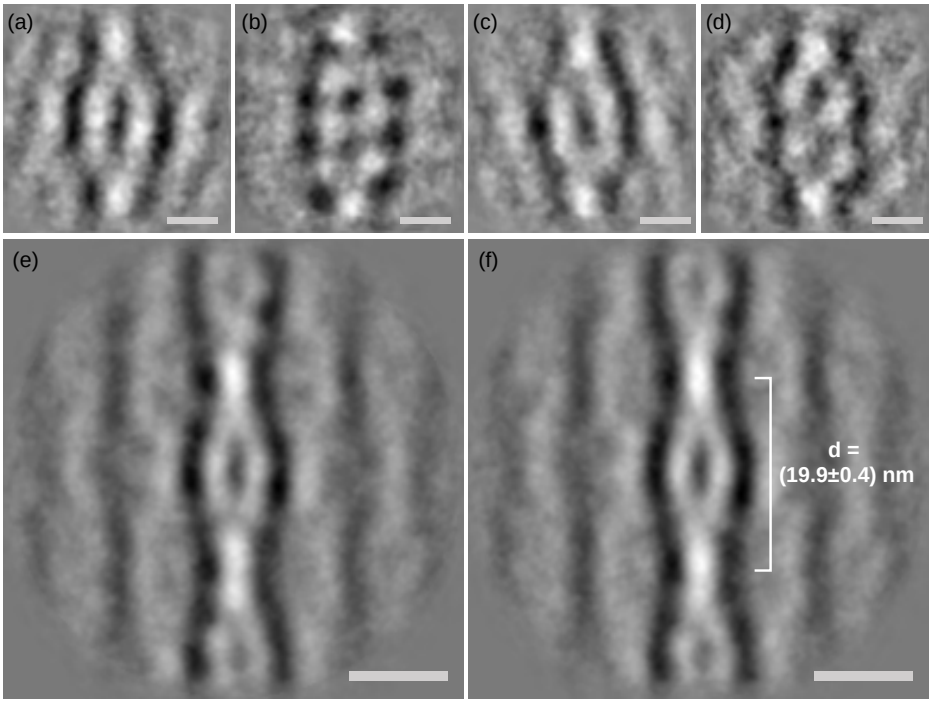

Figure 4.10.: (a)-(d) Class sum images of nBTA after classification of 380 individual fibres showing the presence of two interacting fibre strands. Scale bars represent 5 nm. (b, d) The finger-print pattern superimposes the fibre structure. (e) Sum image of aligned cut-outs (larger than the upper row) showing the projection of a double helix with two repeating units, *i.e.*, one full helix pitch. (f) Sum image after filtering and symmetrisation of (e) in preparation of a 3D reconstruction of the double-helix. Scale bar represent 10 nm.

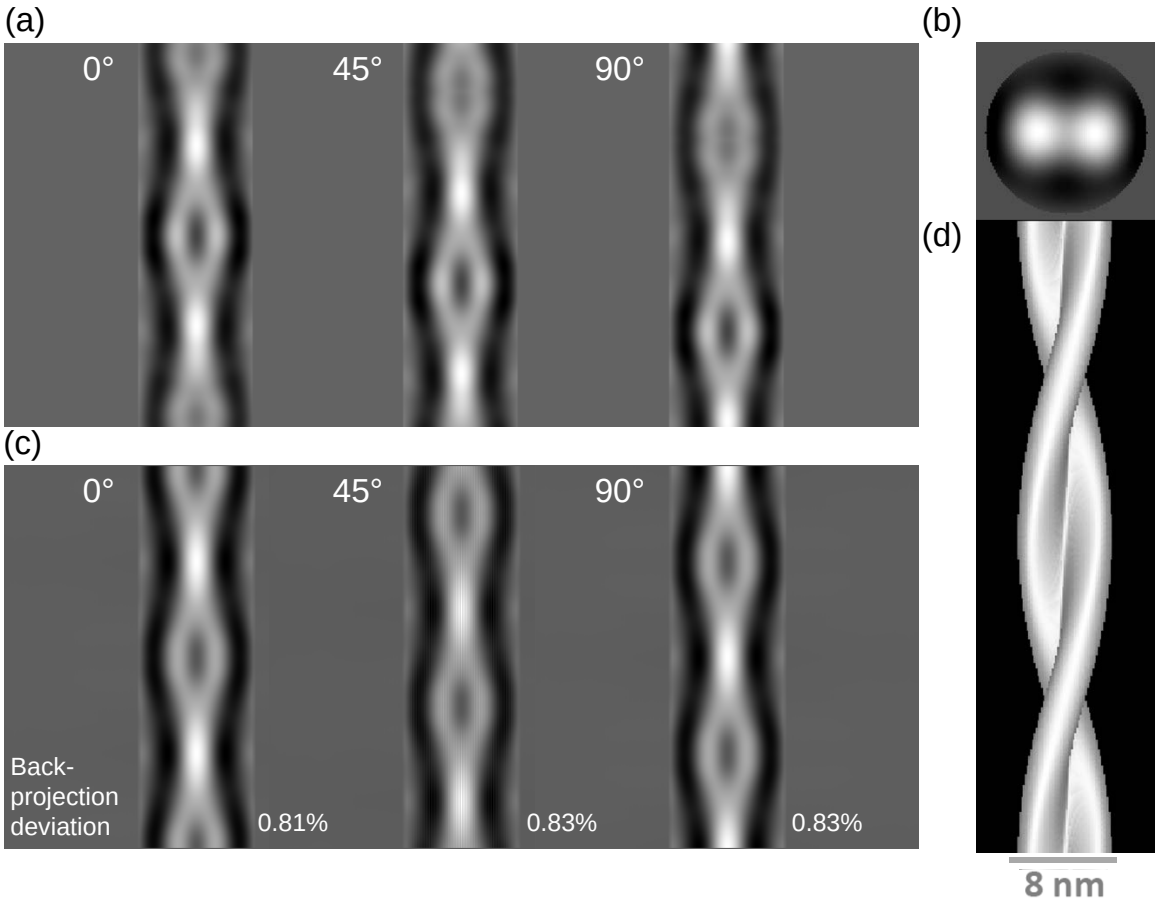

Figure 4.11.: Cryo-TEM image-based 3D reconstruction of the nBTA double-helix (a) Translations of the double-helix along its long axis, representing the rotation around this axis; depiction of projections in 0°, 45°, and 90°. (b) Cross-section of the double-helix after reconstruction showing two individual fibres. (c) Computed back-projection of the reconstruction and calculated deviations to the input data. (d) 3D-depiction of the reconstructed right-handed double-helix. The right-handedness was determined from cryo-ET.

deviations in the order of only 0.8% were obtained, showing the high accuracy of the reconstruction.

In a last step, the reconstruction was depicted in an isosurface representation, as shown in Fig. 4.11(d). Here, points with the same grey value were connected, thus appearing as surface of the reconstructed structure and giving an impression in three dimensions. The threshold of the depicted surface was chosen such that the strands are in contact with each other. Although the projection images give the impression of two completely separated strands, the cross-section of the reconstruction shows a transition area between the strands with low, but significant grey values. Therefore, an interaction between the TEG chains in the periphery of the fibres can be suggested, which is indicated by depicting the strands in contact. In addition, the handedness of the helix had to be determined, as this information can not be revealed from 2D projection images. We therefore performed a tomography (cryo-ET) of nBTA. In the reconstructed volume, a high number of fibres was present. Several fibres were isolated in the volume and analysed by tilting the volume in different directions. By this procedure an impression of the rotation within the double-helix was gained and determined to be right-handed. Although, we could not prove the universality of the right-handedness, our analysis holds true at least for the aggregates in this particular reconstructed volume of the tomography. Thus, a double-helix with a right-handed orientation is shown in Fig. 4.10(d).

In conclusion, by using cryo-TEM, cryo-ET as well as MSA, we could clearly demonstrate that fibrous supramolecular aggregates of nBTA exhibited a double-helix motif in their ultrastructure. Furthermore, the determined length of the repeating unit is in very good accordance to the data obtained by Lafleur *et al.*. Thus, our results support previous results and demonstrate that cryo-TEM in combination with MSA can be used to analyse the ultrastructure of BTA-based aggregates at nanometre scale. Using this knowledge, in the next step the aggregation of BTA-C_{16}-G1 in aqueous solution was analysed.

Analysis of the ultrastructure of BTA-C_{16}-G1

After the successful analysis of the double-helix motif in nBTA, we investigated the ultrastructure of BTA-C_{16}-G1. As described in section 4.2.2, the UV-VIS spectra of both compounds differed significantly. Moreover, the HDX results showed different monomer exchange dynamics of both compounds. We were therefore interested, if also a distinct difference in the ultrastructure of aggregates of both compounds could be found.

From the 2D images, already a ribbon-like structure was supposed, as the width of the struc-

tures changed along the fibre. In addition, the contrast varied from weak for the broader parts to strong when the structures became narrow as can be seen in Fig. 4.12(a). This observation can be assigned to a ribbon-like structure which rotates along the fibre.
Following the above-described procedure, we extracted individual structures and processed them by applying a MSA. Intriguingly, class sum images turned up with two parallel fibres as dominant motif of which one representative image is shown in Fig. 4.12(b). In contrast to nBTA, no double-helix motif could be found in the class sum images. The total width of the structure was determined to be (7.0±0.4) nm. Each single strand exhibited the width of (2.4±0.4) nm. This value fits to the expected dimension of a BTA molecule. Hence, we assigned one strand to represent a one-dimensional stack of BTA-C_{16}-G1 monomers. The macroscopic, ribbon-like structure can be explained by two adjacent fibre strands that appear in pairs as schematically shown in Fig. 4.12(c). Upon rotation along the structure, the overall width of the aggregate changes. Furthermore, the contrast varies in cryo-TEM projection images as the thickness of the aggregate in the beam path changes. Across all cryo-TEM images, these fibre pairs were observed as bundles with other pairs or as individual pairs. However, no single strand was observed so far, as determined by the width of the structures.

4.2.4. Discussion

In sum, the ultrastructures of nBTA and BTA-C_{16}-G1 were analysed at nanometre scale. In both cases, a structure based on two interacting strands was observed. For nBTA, the strands were twisted around each other in a double-helix motif with a recurring repeating unit. For BTA-C_{16}-G1, the strands were found to be parallel next to each other without any regular twist.
In the previous chapter, HDX experiments showed that nBTA polymers exhibited a faster and in total larger H/D exchange of the amide protons than BTA-C_{16}-G1 polymers. This can be interpreted with a more dynamic behaviour in regards of monomer exchange for nBTA. The slow and limited H/D exchange in BTA-C_{16}-G1, however, demonstrated a remarkable high stability of the aggregates. These differences in monomer exchange dynamics might be assigned to structural differences between both molecules. The most pronounced difference in the structure of both monomers is the hydrophilic head group. Whereas nBTA comprises a linear TEG chain, BTA-C_{16}-G1 is equipped with a PG-dendron. In a supramolecular aggregate, the head group shields the hydrophobic pocket from the surrounding water. If the shielding is not sufficient, the interactions, which are stabilising the aggregate, such as H-bonds, may be disturbed and weakened by the solvent.

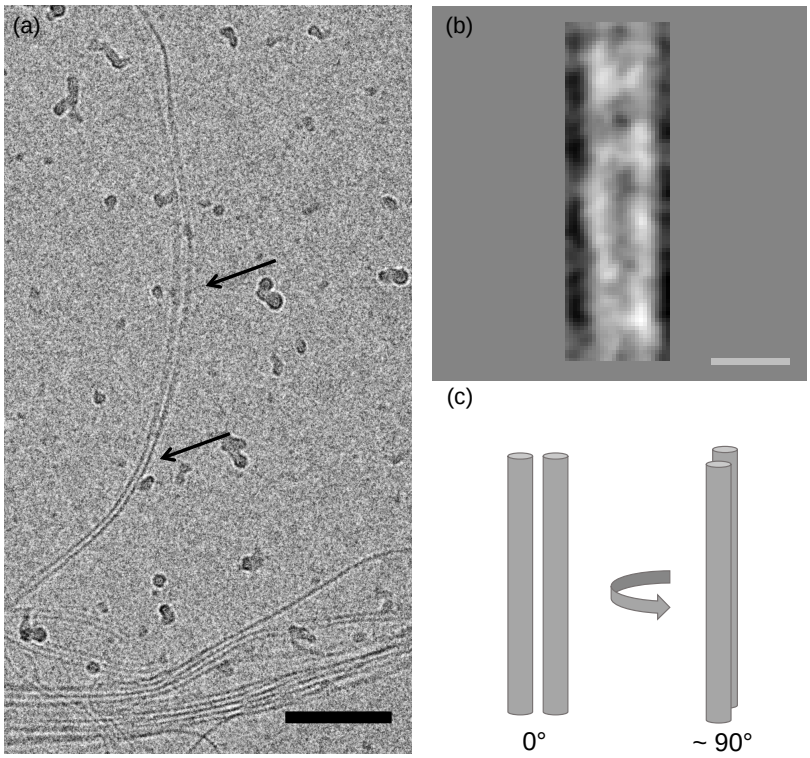

Figure 4.12.: (a) Representative cryo-TEM micrograph of narrow, ribbon-like aggregates of BTA-C_{16}-G1. Arrows point towards modulations of width and contrast of the structure upon turning in the volume. Scale bar represents 100 nm.(b) Representative class sum image after MSA of BTA-C_{16}-G1, indicating two parallel fibre strands. Scale bar represents 10 nm.(c) Schematic depiction of two adjacent fibres in 0° and 90° view to illustrate the origin of the width and contrast modulations.

Possibly, the linear TEG chains in nBTA are too small to stabilise the whole periphery of a cylindrical fibre. In addition, it was recently shown by computational simulations that the stacks of nBTA monomers exhibit so-called hot spots of instability.[51] These defects in the monomer aggregation may lead to hydrophobic patches along the supramolecular fibre. In order to shield these patches, a stabilisation of two fibres through the formation of a double helix is conceivable. In contrast, for BTA-C_{16}-G1, the dendritic head groups are sterically more demanding. Thus, the dendritic head groups might shield the hydrophobic pocket and H-bonds in the supramolecular polymer more effectively. A further shielding through a double helix formation might therefore not be necessary. Recently, it was similarly shown that the addition of a monomer with a dendritic head group increased the stability of nBTA.[28] However, two fibres were still observed as pair and not individually. Here, we presume remaining instabilities and hydrophobic mismatches, which are compensated by pair formation, in order to explain the formation of fibre pairs. However, in both cases, nBTA and BTA-C_{16}-G1, the interactions at molecular level are yet unclear and further investigations and simulations of the systems will be necessary.

4.3. Conclusion and Outlook

In summary, three new BTA-based amphiphiles BTA-C_{12}-G0, BTA-C_{16}-G0, and BTA-C_{16}-G1, comprising dendritic polyglycerol-based head groups, were successfully synthesised. Among them, only BTA-C_{16}-G1 exhibited a good water solubility. It was shown by SLS and cryo-TEM experiments that BTA-C_{16}-G1 formed anisotropic, fibrous supramolecular aggregates in aqueous solution. By HDX experiments, an intriguingly high stability of the aggregates in terms of monomer exchange was observed in comparison to polymers of nBTA. In order to explain the differences, we investigated the ultrastructure of nBTA and BTA-C_{16}-G1 in water at nanometre scale applying cryo-TEM image processing and MSA. Here, we found two remarkably different ultrastructures. For polymers, formed by nBTA monomers, which are functionalised with linear tetra(ethyleneglycol) chains, a double-helix motif was found, supporting previous results obtained by complementary techniques as cryo-ET.[132] In contrast, for BTA-C_{16}-G1, an ultrastructure based on two parallel fibre strands was revealed, forming a narrow ribbon-like structure. The observed differences in the ultrastructure of aggregates of nBTA and BTA-C_{16}-G1 emphasise once more the variety and complexity of supramolecular polymers.

With respect to function of supramolecular polymers, the adjustment of properties is of particular interest. The following chapter will therefore cover the investigation of BTA-based supramolecular copolymers, with a focus on the possibility of tuning certain properties, such as dynamics and structure.

4.4. Experimental section and Supplementary Information

Synthesis All reagents and solvents were obtained from commercial suppliers and used without further purification unless stated otherwise. nBTA and dBTA were kindly provided by the Meijer group (TU Eindhoven, The Netherlands). pG1-OH was synthesised according to published procedures.[140] Reactions requiring dry and oxygen-free conditions were carried out in oven-dried glassware with septa using usual Schlenk techniques. Millipore water (Milli-Q) was obtained from a Merck Millipore Milli-Q Integral System. NMR spectra were recorded on JEOL ECX400, JEOL ECP500, BRUKER AV500 and BRUKER AV700 spectrometers at 400 MHz, 500 MHz and 700 MHz for 1H NMR spectra and 100 MHz, 125 MHz and 175 MHz for 13C NMR spectra, respectively. Chemical shifts are given in parts per million (ppm) in relation to deuterated solvent peak calibration. Flash columns were either performed with Macherey-Nagel silica gel 60 M or at a Combiflash R_f system from Teledyne ISCO.

HPLC purification ***Analytical HPLC*** was performed in isocratic or gradient mode with a Smartline system from Knauer (Berlin, Germany), equipped with dual pumps 1000, degasser, autosampler 3950 and variable wavelength UV detector 2500. The stationary phase was a pre-packed column (250×4 mm) with RP-18 material (RSC-Gel, C18ec, 5μm, 125×4 mm) from RSC (Reinhardshagen, Germany). UV detection was performed at 210 or 225 nm, as indicated. The flow was 1 mL min^{-1}. Eluents were degassed before use.
Preparative HPLC was performed on a high-pressure gradient system (stainless steel), equipped with dual Shimadzu LC-8A pumps, Shimadzu CBM-20A controller, variable wavelength UV detector from Knauer and a Rheodyne injector with 10 mL sample loop. Stationary phase was a pre-packed RP-18 column (RSC-Gel, C18ec, 5μm, 250×32 mm) with precolumn from RSC (Reinhardshagen, Germany). HPLC runs were performed with a total flow rate of 40mL min^{-1}, applying an isocratic elution (45 min, eluent concentration as indicated) with UV detection. The purity of collected fractions was determined by analytical HPLC.

Sample preparation The desired amount of the compound was weighted into a sample vial and the respective volume of water is added. Afterwards a stir bar was added, the mixture was vortexed for 10 s, then heated to 80°C for 15 min under stirring and vortexed subsequently again for 10 s. The samples were left for equilibration over night at room temperature, before further experiments were conducted.
For copolymer solutions, first, stock solutions of homopolymers were prepared according to the above described procedure. After cooling for 5 min, the solutions were mixed in the desired ratio, followed by 10 s of vortexing, heating to 80°C for 15 min and subsequent 10 s of vortexing. The samples were left for equilibration over night at room temperature, before further experiments were conducted.

UV-VIS Ultraviolet-visible (UV-VIS) absorbance spectra were recorded on a Agilent Cary 8454 UV-VIS spectrometer at 20°C with a Julabo 200F temperature controller. The concentration of all samples was 50 μM in milliQ. Suprasil Quartz cuvettes with a pathlength of 1 cm were used.

Static light scattering Experiments were conducted on an ALV/CGS-3 MD-4 compact goniometer system, equipped with a multiple tau digital real time correlator (ALV-7004) and a solid state laser ($\lambda = 532\,\text{nm}$; 40 mW). Scattering intensities were detected over an angular range of 30° to 150° in steps of 5°. Four runs of 10 seconds per angle were averaged. BTA samples were prepared in water at a concentration of 500 μM and were measured in light scattering tubes with an outer diameter of 1 cm. As a reference, samples of only water and only toluene were measured. Water was filtered with 0.2 μm syringe filters (Supor membrane, PALL Corporation) and toluene with a 0.2 μm syringe filter (PTFE membrane, Whatman). The measurements were analysed with AfterALV (1.0d, Dullware) to remove measurements showing obvious scattering from dust. The Rayleigh ratio as a function of the angle was determined, using the following equation

$$R_\theta = \frac{I_{sample} - I_{water}}{I_{toluene}} \times R_{toluene} \times \frac{n^2_{water}}{n^2_{toluene}}$$

, with I_{sample} for the count rate of the sample solution, I_{water} for the count rate of water and $I_{toluene}$ for the count rate of toluene. $R_{toluene}$ is the known Rayleigh ratio of toluene (2.1×10^{-5} m^{-1} at 532 nm), n_{water} is the refractive index of the solvent (1.33) and $n_{toluene}$ is the refractive index of toluene (1.49).

Fluorescence measurements with Nile Red Spectra were recorded on a Varian Cary Eclipse fluorescence spectrometer. A cuvette with an optical path length of 1 cm was used and the temperature was set at 20°C. The sample was excited at $\lambda = 500\,\text{nm}$ and the emission was recorded at 520 - 800 nm with a PMT detector voltage of 800 V. Each measurement was averaged over 5 scans. Samples for fluorescence measurements were prepared at a concentration of 50 μM BTA in water. A Nile Red stock solution with a concentration of 2.5 mM in ACN was diluted 10 times with ACN to a concentration of 0.25 mM. 5 μL of this stock solution was added to 495 μL of the BTA sample to obtain a concentration of 2.5 μM Nile Red in a 50 μM BTA sample. The samples were left to equilibrate at room temperature for 1 hour before the measurements.

HDX A H_2O solution of 500 μM BTA-C_{16}-G1 was diluted 100 times in D_2O (with 0.5 mM of NaAc). HDX-MS measurements were carried out using a XevoTM G2 QTof mass spectrometer (Waters) with a capillary voltage of 2.7 kV and a cone voltage of 80 V. The source temperature was set at 100°C, the desolvation temperature at 400°C, and the desolvation gas flow at 500 L/h. The sample solutions subjected to HDX were introduced into the mass spectrometer using a Harvard syringe pump (11 Plus, Harvard Apparatus) at a flow rate of 50 μL/min.
The obtained data points (y) over time (t) were fitted with a tri-exponential fit, using Origin 2018 and the equation $y = A \times exp(-t \times k_1) + B \times exp(-t \times k_2) + C \times exp(-t \times k_3)$, with A, B, and C giving the fractions and k_1, k_2, and k_3 giving the rate constants of the processes.

Cryogenic transmission electron microscopy (CryoTEM)
Cryo-sample preparation: Droplets (5 μL) of BTA solution with c = 500μM were placed on hydrophilised holey carbon-filmed grids (Quantifoil R1/4) at room temperature. The grids

were surface plasma treated just prior to use (BALTEC MED 020 device at 8.5 mA for 60 s). Vitrified films were prepared in a 'Vitrobot' (PC controlled vitrification robot, Thermo Fisher Scientific) at 22°C and a humidity of 100%. Excess sample solution was removed by blotting using two filter papers for 3-3.5 s. The thin film thus formed was shot into liquid ethane just above its freezing point.

Cryo-TEM: The vitrified samples were transferred under liquid nitrogen into a Talos Arctica 200 kV transmission electron microscope (Thermo Fisher Scientific, USA), using the microscope's autoloader protocol. Micrographs were recorded at a sample temperature of around 100 K using the microscope's low-dose protocol at a primary magnification of 28000× or 45000× and an acceleration voltage of 200 kV. Image recording was done using a Falcon3EC direct electron detector (Thermo Fisher Scientific, USA). The defocus was chosen to be between -3 μm and -6.5 μm to create sufficient phase contrast.

Measurements with phase plate: The objective aperture was replaced by a volta phase plate which was brought into the beam path instead. The phase plate was aligned using the alignment module of the microscope software. After an activation time of several minutes, the phase shift was measured and the astigmatism corrected using "AutoCTF" (Thermo Fisher). As long as the phase shift stayed close to 0.5 π, micrographs were taken with a defocus of around -300 nm. In case of significant higher or lower phase shift the position at the phase plate was shifted.

Cryo-ET: Tomographic tilt series were recorded using the FEI Tomography software (Version 4.5.0, ThermoFisher Scientific Inc., Waltham (MA), USA) in the tilt range of -65°/65° at 2° increments. Total doses of 110-350 e/Å^2 were accumulated on the specimen per tomography at a primary magnification of 28k×. Tilt-images were recorded with the Falcon 3CE direct electron detector at full image size (4096×4096 pixel) and an exposure time of 1.22 s per image. The defocus was chosen to be between - 2-5 μm to create sufficient phase contrast. Alignment and reconstruction was performed in the context of ThermoFisher Inspect 3D software, visualisation with ThermoFisher AMIRA 6.0.

Multivariate statistical analysis (MSA) From cryo-TEM images, individual motifs were extracted using the EMAN tool *boxer*.[141] The dimension, pixel size and total number of the excerpts are summarised in Tab. 4.1. Utilising the software package IMAGIC-5[79], images were aligned with respect to one or multiple reference images, using cross-correlation techniques. The images were furthermore band-pass filtered to exclude low and high spacial frequencies, thus reducing unspecific noise. Subsequently, a mask image was generated, isolating the area of interest in the images. This mask was applied to all images and the MSA was computed. During the process, the number of considered eigenimages and resulting classes was set and refined, if needed. The values are collected in Tab. 4.1.

Table 4.1.: Number and dimensions of extracted images and chosen parameters during MSA.

Sample	cut-out dimension in px	total number of excerpts	considered eigenimages for classification	number of classes
nBTA	96 × 96	360	3	10
	200 × 200	178		
BTA-C_{16}-G1	96 × 96	192	6	10

4.4.1. Synthetic procedures

1,16-Dibromohexadecane - (1)

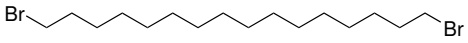

1,16-Hexadecanediol (128 mg, 0.49 mmol) was dissolved in dry DMF under argon atmosphere. The solution was cooled (-10 °C) for 15 min before PPh_3 (520 mg, 2.0 mmol) and N-bromosuccinimide (350 mg, 2.0 mmol) were added. The reaction was stirred vigorously overnight while warming to r.t.. The solvent was then removed under reduced pressure and the residue extracted with EtOAc and water. The combined organic phased were dried with Na_2SO_4 and the solvent was removed by reduced pressure. Purification was achieved by column chromatography (Silica, cHex 100%) yielding the title compound as colourless solid (467 mg, 82%). The reaction was repeated several times to gain enough material for subsequent reactions.

$C_{16}H_{32}Br_2 = 384.240\,g\,mol^{-1}$

^{1}**H-NMR** (400 MHz, $CDCl_3$, δ (ppm)): 3.40 (t, J = 6.9 Hz, 4H, Br-CH_2-), 1.84 (dt, J_1 = 14.5 Hz, J_2 = 6.9 Hz, 4H, Br-CH_2-CH_2-), 1.43-1.25 (m, 24H, CH_2-chain).

^{13}**C-NMR**: (100 MHz, $CDCl_3$, δ (ppm)): 34.20, 32.93, 29.73, 29.70, 29.63, 29.54, 28.87, 28.27.

MS (EI+): calculated ($C_{16}H_{32}Br^+$) = 303.17 g mol^{-1}, observed $\frac{m}{z}$ = 303.17

Br-C16-pG1; 4,4'-(((2-((16-Bromohexadecyl)oxy)propane-1,3-diyl)bis(oxy))bis (methylene))bis(2,2-dimethyl-1,3-dioxolane) - (2c)

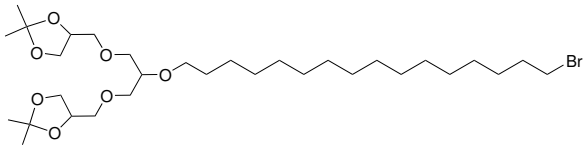

NaH (73.9 mg, 3.25 mmol) was suspended in 220 mL dry THF under argon atmosphere. The solution was cooled to 0 °C, before pG1-OH (1.1 g, 3.43 mmol) was added dropwise. After complete addition, the reaction mixture was heated to 60 °C for 1 h. 1,16-Dibromohexadecane **(1)** (3.45 g, 10.29 mmol) was added and the mixture was kept stirring for further 18 h at 60 °C. THF was evaporated and the residue dissolved in sat. NH_4Cl solution and extracted three

times with DCM. The combined organic layers were dried with Na_2SO_4 and the solvent removed under reduced pressure. Purification was achieved by column chromatography (Silica, Pentane/ EtOAc 3%) yielding the title compound as yellowish oil (611 mg, 33%) $C_{31}H_{59}BrO_7$ = 623.710 g mol^{-1}

^{1}**H-NMR** (400 MHz, Aceton-d_6, δ (ppm)): 4.23-4.17 (m, 2H, dendron -O-CC*H*-CH_2-), 4.02 (dd, J_1 = 8.2 Hz, J_2 = 6.4 Hz, 2H, dendron -O-C*H*$_2$-CH-), 3.70 (dd, J_1 = 8.2 Hz, J_2 = 6.3 Hz, 2H, dendron -O-C*H*$_2$-CH-), 3.58-3.44 (m, 12H, dendron-*H*, Br-C*H*$_2$-, -O-C*H*$_2$-CH_2-), 1.88-1.81 (m, 2H, Br-CH_2-C*H*$_2$-), 1.56-1.49 (m, 2H, -O-CH_2-C*H*$_2$-), 1.46-1.28 (m, 36H, C*H*$_2$-chain, -C*H*$_3$).

Phth-C16-pG1; 2-(16-((1,3-bis((2,2-dimethyl-1,3-dioxolan-4-yl)methoxy)propan-2-yl)oxy)hexadecyl)isoindoline-1,3-dione - (3c)

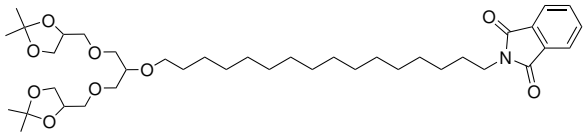

Br-C16-pG1 **(2c)** (610 mg, 0.90 mmol) was dissolved in 20 mL dry DMF under argon atmosphere. After potassium phthalimid (270 mg, 1.47 mmol) was added, the reaction mixture was stirred over night at 60 °C. The solvent was removed under reduced pressure and the residue dissolved in water and extracted three times with EtOAc. The combined organic phases were dried with Na_2SO_4 and the solvent was removed under reduced pressure. Purification was achieved by column chromatography (Silica, Pentane/ EtOAc 3-30%) yielding the title compound as colourless solid (432 mg, 64%) $C_{39}H_{63}NO_9$ = 689.931 g mol^{-1}

^{1}**H-NMR** (400 MHz, Methanol-d_4, δ (ppm)): 7.84-7.77 (m, 4H, Phth-H), 4.26-4.20 (m, 2H, dendron -O-CC*H*-CH_2-), 4.03 (dd, J_1 = 8.2 Hz, J_2 = 6.5 Hz, 2H, dendron -O-C*H*$_2$-CH-), 3.72 (dd, J_1 = 8.0 Hz, J_2 = 6.5 Hz, 2H, dendron -O-C*H*$_2$-CH-), 3.64 (t, J = 7.2 Hz, 2H, Phth-C*H*$_2$-), 3.60-3.47 (m, 11H, dendron-*H*, -O-C*H*$_2$-CH_2-), 1.69-1.62 (m, 2H, Phth-CH_2-C*H*$_2$-), 1.57-1.50 (m, 2H, -O-CH_2-C*H*$_2$-), 1.36-1.21 (m, 36H, C*H*$_2$-chain, -C*H*$_3$).

^{13}**C-NMR**: (100 MHz, Methanol-d_4, δ (ppm)): 168.43, 134.00, 132.06, 122.77, 109.12, 77.88, 74.82, 72.09, 71.12, 71.03, 70.15, 66.32, 37.51, 29.86, 29.47, 29.44, 29.36, 29.29, 28.93, 28.22, 26.60, 25.94, 25.83, 24.42.

Br-C12-pG0; 4-(((12-bromododecyl)oxy)methyl)-2,2-dimethyl-1,3-dioxolane - (2a)

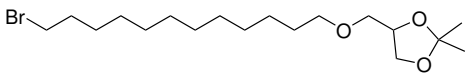

Under argon atmosphere, NaH (60% in mineral oil) (550 mg, 13.70 mmol) was suspended in 150 mL dry THF. Two drops of 15-crown-5 were added and the solution cooled to 0 °C, before Isopropylidene glycerol (1.89 mL, 15.23 mmol) was added dropwise. After complete

addition, the reaction mixture was heated to 70 °C for 2 h. 1,12-Dibromododecane (15.0 g, 45.71 mmol) was added and the mixture was kept stirring for further 20 h at 70 °C. Afterwards, THF was evaporated and the residue dissolved in sat. NH_4Cl solution and extracted three times with DCM. The combined organic layers were dried with Na_2SO_4 and the solvent removed under reduced pressure. Unreacted 1,12-Dibromododecane was recovered by a filter column with Pentane. Purification of the the title compound was achieved by column chromatography (Silica, Pentane/ EtOAc 3-5%) yielding the product as yellowish oil (1.54 g, 30%) $C_{18}H_{35}BrO_3 = 379.379\,g\,mol^{-1}$

^{1}**H-NMR** (500 MHz, Aceton-d_6, δ (ppm)): 4.20-4.16 (m, 1H, dendron -O-C*H*-CH_2-), 4.01 (dd, J_1 = 8.2 Hz, J_2 = 6.4 Hz, 1H, dendron -O-CH_2-CH-), 3.68 (dd, J_1 = 8.2 Hz, J_2 = 6.3 Hz, 1H, dendron -O-CH_2-CH-), 3.50-3.37 (m, 6H, Br-CH_2-, -O-CH_2-CH_2-, -O-CH_2-CH-), 1.88-1.82 (m, 2H, Br-CH_2-CH_2-), 1.56-1.51 (m, 2H, -O-CH_2-CH_2-), 1.45-1.27 (m, 24H, CH_2-chain, CH_3).

^{13}**C-NMR**: (125 MHz, Aceton-d_6, δ (ppm)): 109.46, 75.58, 72.47, 72.01, 67.47, 34.76, 33.58, 28.76, 27.07, 26.81, 25.71.

Phth-C12-pG0; 2-(12-((2,2-dimethyl-1,3-dioxolan-4-yl)methoxy)dodecyl)isoindoline-1,3-dione (3a)

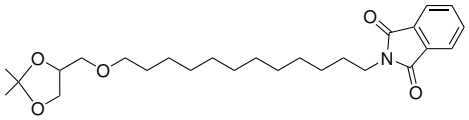

Br-C12-pG0 **(2a)** (1.54 g, 4.05 mmol) was dissolved in 40 mL dry DMF under argon atmosphere. Potassium phthalimid (1.13 g, 6.09 mmol) was added and the reaction mixture was stirred over night at 60 °C. The solvent was removed under reduced pressure and the residue dissolved in water and extracted three times with EtOAc. The combined organic phases were dried with Na_2SO_4 and the solvent was removed under reduced pressure. Purification was achieved by column chromatography (Silica, Pentane/ EtOAc 3-30%) yielding the title compound as colourless solid (1.484 g, 82%) $C_{26}H_{39}NO_5 = 445.600\,g\,mol^{-1}$

^{1}**H-NMR** (400 MHz, Aceton-d_6, δ (ppm)): 7.85-7.84 (m, 4H, Phth-H), 4.21-4.15 (m, 1H, dendron -O-C*H*-CH_2-), 4.01 (dd, J_1 = 8.1 Hz, J_2 = 6.4 Hz, 1H, dendron -O-CH_2-CH-), 3.67 (dd, J_1 = 8.1 Hz, J_2 = 6.3 Hz, 1H, dendron -O-CH_2-CH-), 3.64 (t, J = 7.1 Hz, 2H, Phth-CH_2-), 3.48-3.36 (m, 4H, -O-CH_2-CH_2-), 1.70-1.63 (m, 2H, Phth-CH_2-CH_2-), 1.56-1.49 (m, 2H, -O-CH_2-CH_2-), 1.34-1.27 (m, 22H, CH_2-chain, -CH_3).

^{13}**C-NMR**: (100 MHz, Methanol-d_4, δ (ppm)): 169.72, 135.28, 133.32, 124.04, 110.40, 76.13, 72.75, 72.68, 67.67, 38.79, 30.67, 30.61, 30.56, 30.51, 30.19, 29.47, 27.87, 27.16, 27.06, 25.69.

MS (ESI): calculated ($C_{26}H_{39}NO_5Na^+$) = 468.2720 g mol^{-1}, observed $\frac{m}{z}$ = 468.2716 g mol^{-1}

Br-C16-pG0; 4-(((16-bromohexadecyl)oxy)methyl)-2,2-dimethyl-1,3-dioxolane - (2b)

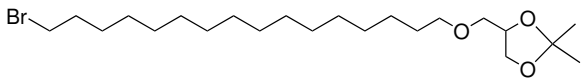

NaH (60% in mineral oil) (230 mg, 0.58 mmol) was suspended in 150 mL dry THF under argon atmosphere. Isopropylidene glycerol (0.76 mL, 6.08 mmol) and two drops of 15-crown-5 were added. The reaction mixture was heated to 60 °C for 1 h. Afterwards, 1,16-dibromohexadecane (7.0 g, 18.23 mmol) was added and the mixture was kept stirring for further 20 h at 60 °C under reflux. Subsequently, THF was evaporated and the residue dissolved in sat. NH_4Cl solution and extracted three times with DCM. The combined organic layers were dried with Na_2SO_4 and the solvent removed under reduced pressure. Purification of the the title compound was achieved by automated column chromatography (Silica, Pentane/ EtOAc 0-20%), while unreacted starting material could be reisolated beforehand with Pentane 100%. The product was obtained as yellowish oil (1.09 g, 43%) with slight impurities of an elimination and double addition side product, which were separated in the subsequent reaction. $C_{22}H_{43}BrO_3 = 435.487\,g\,mol^{-1}$

^{1}**H-NMR** (400 MHz, Aceton-d_6, δ (ppm)): 4.18 (p, 1H, dendron -O-C*H*-CH_2-), 4.01 (dd, J_1 = 8.2 Hz, J_2 = 6.4 Hz, 1H, dendron -O-CH_2-CH-), 3.68 (dd, J_1 = 8.1 Hz, J_2 = 6.3 Hz, 1H, dendron -O-CH_2-CH-), 3.51-3.37 (m, 6H, Br-CH_2-, -O-CH_2-CH_2-, -O-CH_2-CH-), 1.89-1.82 (m, 2H, Br-CH_2-CH_2-), 1.57-1.51 (m, 2H, -O-CH_2-CH_2-), 1.40-1.28 (m, 31H, CH_2-chain, CH_3).

^{13}**C-NMR**: (100 MHz, Aceton-d_6, δ (ppm)): 109.72, 75.87, 72.77, 72.29, 67.77, 35.02, 33.88, 30.71, 30.62, 30.53, 30.46, 30.27, 30.08, 29.89, 29.70, 29.50, 29.05, 27.36, 27.12, 26.00.

Phth-C16-pG0;
2-(16-((2,2-dimethyl-1,3-dioxolan-4-yl)methoxy)hexadecyl)isoindoline-1,3-dione (3b)

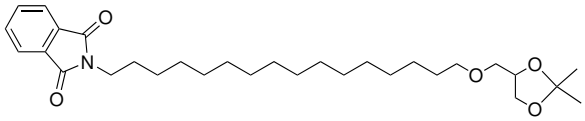

Under argon atmosphere, Br-C16-pG0 **(2b)** (1.00 g, 2.30 mmol) was dissolved in 50 mL dry DMF. Subsequently, potassium phthalimid (0.64 g, 3.45 mmol) was added. The reaction mixture was stirred over night at 60 °C. Afterwards, the solvent was removed under reduced pressure and the residue dissolved in ca. 200 mL water and extracted three times with EtOAc. The combined organic phases were dried with Na_2SO_4 and the solvent was removed under reduced pressure. After purification by column chromatography (Silica, Pentane/ EtOAc 0-30%) the title compound was obtained as colourless solid (0.645 g, ∼79%). $C_{30}H_{47}NO_5 = 501.708\,g\,mol^{-1}$

^{1}**H-NMR** (400 MHz, Aceton-d_6, δ (ppm)): 7.88-7.80 (m, 4H, Phth-H), 4.21-4.15 (m, 1H, dendron -O-C*H*-CH_2-), 4.02-3.99 (m, 1H, dendron -O-CH_2-CH-), 3.69-3.62 (m, 3H, dendron

-O-CH_2-CH-, Phth-CH_2-), 3.48-3.36 (m, 4H, -O-CH_2-CH_2-), 1.70-1.65 (m, 2H, Phth-CH_2-CH_2-), 1.56-1.50 (m, 2H, -O-CH_2-CH_2-), 1.40-1.22 (m, 30H, CH_2-chain, -CH_3).

^{13}**C-NMR**: (100 MHz, Methanol-d_4, δ (ppm)): 206.26, 168.92, 135.07, 133.29, 123.80, 109.62, 75.76, 72.66, 72.18, 67.65, 38.55, 30.51, 30.49, 30.37, 30.18, 29.99, 29.80, 29.60, 27.67, 27.25, 27.01, 25.89.

MS (ESI): calculated ($C_{30}H_{47}NO_5Na^+$) $= 524.3346\,g\,mol^{-1}$
observed $\frac{m}{z}$ $= 524.3361\,g\,mol^{-1}$

The purity of the starting material was estimated with 70% and the yield calculated accordingly.

NH_2-C12-pG0 - (4a)

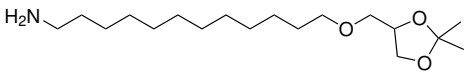

Phth-C12-G0 **(3a)** (1.48 g, 3.33 mmol) was dissolved in 300 mL ethanol. Hyradzine monohydride (4.0 mL, 83.25 mmol) was added and the reaction mixture was kept stirring at 80 °C over night under reflux. Afterwards, the solvent was removed under reduced pressure and the residue dissolved in NaOH (1M). After extraction with DCM, the combined organic phases were dried with Na_2SO_4 and the solvent removed under reduced pressure yielding the title compound (0.90 g, 85%). The product was used without further purification in subsequent reactions. $C_{18}H_{37}NO_3 = 315.498\,g\,mol^{-1}$

^{1}**H-NMR** (400 MHz, Methanol-d_4, δ (ppm)): 4.26-4.20 (m, 1H, dendron -O-CH-CH_2-), 4.04 (dd, J_1 = 8.2 Hz, J_2 = 6.4 Hz, 1H, dendron -O-CH_2-CH-), 3.71 (dd, J_1 = 8.2 Hz, J_2 = 6.4 Hz, 1H, dendron -O-CH_2-CH-), 3.50-3.42 (m, 4H, -O-CH_2-CH_2-), 2.62 (t, J = 7.2 Hz, 2H, H_2N-CH_2-), 1.60-1.53 (m, 2H, H_2N-CH_2-), 1.50-1.43 (m, 2H, -O-CH_2-CH_2-), 1.38-1.31 (m, 21H, CH_2-chain, -CH_3).

^{13}**C-NMR**: (100 MHz, Methanol-d_4, δ (ppm)): 206.26, 168.92, 135.07, 133.29, 123.80, 109.62, 75.76, 72.66, 72.18, 67.65, 38.55, 30.51, 30.49, 30.37, 30.18, 29.99, 29.80, 29.60, 27.67, 27.25, 27.01, 25.89.

MS (ESI): calculated ($C_{18}H_{37}NO_3H^+$) $= 316.2846\,g\,mol^{-1}$, observed $\frac{m}{z} = 316.2895\,g\,mol^{-1}$

NH_2-C16-pG0 - (4b)

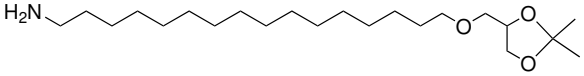

Phth-C16-G0 **(3b)** (0.55 g, 1.10 mmol) was dissolved in 100 mL ethanol. After addition of hyradzine monohydride (1.3 mL, 27.50 mmol), the reaction mixture was heated to 80 °C and kept stirring under reflux over night. The solvent was removed under reduced pressure and the residue dissolved in NaOH (1M) and extracted three times with DCM. The combined organic phases were dried with Na_2SO_4 and the solvent removed under reduced pressure

yielding the title compound (0.42 g, 99%). The product was used without further purification in subsequent reactions. $C_{22}H_{45}NO_3 = 371.606\,g\,mol^{-1}$

^{1}**H-NMR** (500 MHz, Chloroform-*d*, δ (ppm)): 4.28-4.23 (m, 1H, dendron -O-C*H*-CH_2-), 4.05 (dd, J_1 = 8.2 Hz, J_2 = 6.4 Hz, 1H, dendron -O-CH_2-CH-), 3.72 (dd, J_1 = 8.2 Hz, J_2 = 6.4 Hz, 1H, dendron -O-CH_2-CH-), 3.53-3.39 (m, 4H, -O-CH_2-CH_2-), 2.76 (t, J = 7.2 Hz, 2H, H_2N-CH_2-), 1.59-1.50 (m, 4H, H_2N-CH_2-, -O-CH_2-CH_2-), 1.42-1.21 (m, 32H, CH_2-chain, -CH_3).

^{13}**C-NMR**: (125 MHz, Aceton-d_6, δ (ppm)): 206.26, 108.01, 73.99, 70.76, 70.44, 65.72, 49.53, 39.58, 29.06, 28.68, 28.64, 28.47, 26.38, 25.25, 25.13, 23.89.

MS (ESI): calculated ($C_{22}H_{45}NO_3H^+$) = 372.3471 g mol^{-1}, observed $\frac{m}{z}$ = 372.3537 g mol^{-1}

NH_2-C16-pG1 - (4c)

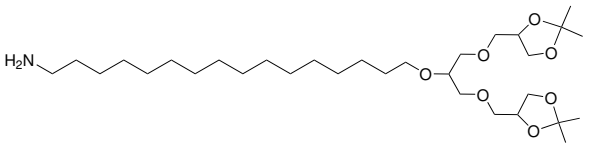

Phth-C16-G1 **(3c)** (0.43 g, 0.62 mmol) was dissolved in 60 mL ethanol. Hyradzine monohydride (0.75 mL, 15.50 mmol) was added and the reaction mixture was heated to 80 °C and kept stirring under reflux over night. Subsequently, the solvent was removed under reduced pressure and the residue redissolved in NaOH (1M) and extracted three times with DCM. The combined organic phases were dried with Na_2SO_4 and the solvent removed under reduced pressure. The title compound (0.34 g, 98%) was obtained and used without further purification in subsequent reactions. $C_{31}H_{61}NO_7 = 559.829\,g\,mol^{-1}$

^{1}**H-NMR** (400 MHz, Methanol-*d4*, δ (ppm)): 4.27-4.21 (m, 2H, dendron -O-CC*H*-CH_2-), 4.06-4.02 (m, 2H, dendron -O-CH_2-CH-), 3.75-3.71 (m, 2H, dendron -O-CH_2-CH-), 3.60-3.48 (m, 11H, dendron-*H*, -O-CH_2-CH_2-), 2.69-2.60 (m, 2H, H_2N-CH_2-), 1.59-1.45 (m, 4H, H_2N-CH_2-, -O-CH_2-CH_2-), 1.41-1.24 (m, 38H, CH_2-chain, -CH_3).

^{13}**C-NMR**: (100 MHz, Methanol-*d4*, δ (ppm)): 110.46, 79.20, 76.16, 73.40, 72.41, 72.34, 71.46, 67.60, 49.00, 42.42, 33.45, 31.15, 30.80, 30.75, 30.63, 30.63, 30.59, 28.03, 27.24, 27.10, 27.06, 25.70, 25.64.

MS (ESI): calculated ($C_{31}H_{61}NO_7H^+$) = 560.4521 g mol^{-1}, observed $\frac{m}{z}$ = 560.4620 g mol^{-1}

BTA-C_{12}-pG0 - (5a)

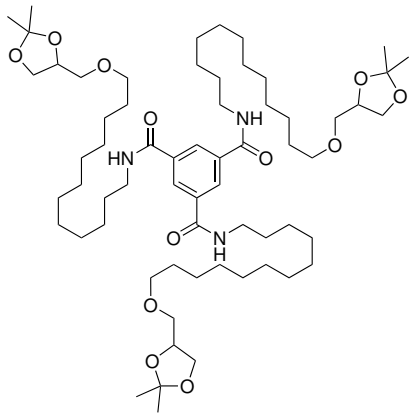

NH_2-C12-pG0 **(4a)** (0.40 g, 1.27 mmol) was dissolved in 40 mL dry DCM under argon atmosphere. Triethylamine (0.35 mL, 2.53 mmol) was added and the solution cooled to 0 °C. 1,3,5-Benzenetricarbonyl trichloride (0.09 g, 0.34 mmol) was dissolved in 0.5 mL dry DCM and added dropwise to the reaction solution. The reaction mixture was stirred over night while warming to r.t.. The solvent was removed under reduced pressure and the product purified through HPLC (DCM/MeOH 1.5%) (0.32 g, 95%). $C_{63}H_{111}N_3O_{12} = 1102.590\,g\,mol^{-1}$

^{1}**H-NMR** (500 MHz, Methanol-*d4*, δ (ppm)): 8.37 (s, 3H, Ar-*H*), 4.25-4.20 (m, 3H, dendron -O-C*H*-CH_2-), 4.04 (dd, J_1 = 8.2 Hz, J_2 = 6.5 Hz, 3H, dendron -O-CH_2-CH-), 3.70 (dd, J_1 = 8.2 Hz, J_2 = 6.4 Hz, 3H, dendron -O-CH_2-CH-), 3.49-3.35 (m, 12H, dendron-*H*, -O-CH_2-CH_2-), 3.38 (t, 6H, HN-CH_2-), 1.66-1.60 (m, 6H, -HN-CH_2-CH_2-), 1.58-1.52 (m, 6H, -O-CH_2-CH_2-), 1.40-1.30 (m, 53H, CH_2-chain, -CH_3).

^{13}**C-NMR**: (125 MHz, Methanol-*d4*, δ (ppm)): 168.52, 136.82, 129.74, 110.43, 76.17, 72.79, 72.71, 67.70, 49.00, 41.23, 30.71, 30.57, 30.49, 28.12, 27.20, 27.09, 25.73.

MS (ESI): calculated ($C_{63}H_{111}N_3O_{12}K^+$) $= 1140.7799\,g\,mol^{-1}$

observed $\frac{m}{z}$ $= 1140.7837\,g\,mol^{-1}$

BTA-C_{16}-pG0 - (5b)

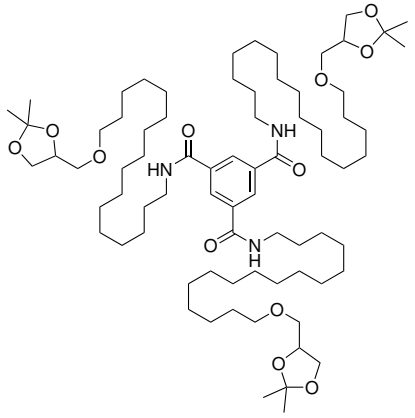

NH_2-C16-pG0 **(4b)** (0.23 g, 0.62 mmol) was dissolved in 20 mL dry DCM under argon atmosphere. Triethylamine (0.17 mL, 1.23 mmol) was added and the solution cooled to 0 °C.

1,3,5-Benzenetricarbonyl trichloride (0.05 g, 0.19 mmol) was dissolved in 0.5 mL dry DCM and added dropwise to the reaction solution. The reaction mixture was kept stirring over night while warming to r.t.. Afterwards, the solvent was removed under reduced pressure. The crude product was purified via HPLC (Hexane/ EtOAc 25%) (94 mg, 40%). $C_{75}H_{135}N_3O_{12}$ = 1270.914 g mol^{-1}

^{1}**H-NMR** (400 MHz, DCM-*d2*, δ (ppm)): 7.51 (s, 3H, Ar-*H*), 4.23-4.17 (m, 3H, dendron -O-C*H*-CH_2-), 4.01 (dd, J_1 = 8.2 Hz, J_2 = 6.4 Hz, 3H, dendron -O-CH_2-CH-), 3.67 (dd, J_1 = 8.2 Hz, J_2 = 6.4 Hz, 3H, dendron -O-CH_2-CH-), 3.58-3.54 (3, 6H, HN-CH_2-), 3.48-3.36 (m, 12H, dendron-*H*, -O-CH_2-CH_2-), 1.81-1.78 (m, 3H, N*H*), 1.60-1.50 (m, 12H, -HN-CH_2-CH_2-, -O-CH_2-CH_2-), 1.38-1.27 (m, 90H, CH_2-chain, -CH_3).

BTA-C_{16}-pG1 - (5c)

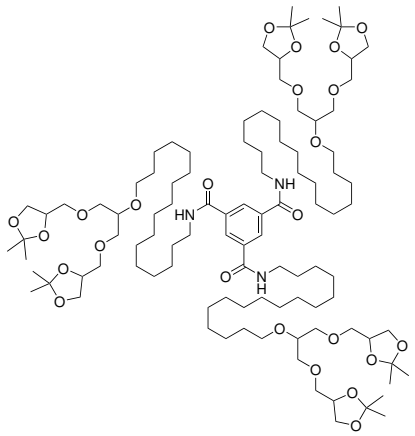

NH_2-C16-pG1 **(4c)** (240 mg, 0.43 mmol) was dissolved in 30 mL dry DCM under argon atmosphere. Triethylamine (0.12 mL, 0.86 mmol) was added and the solution cooled to 0 °C. 1,3,5-Benzenetricarbonyl trichloride (34 mg, 0.13 mmol) was dissolved in 0.5 mL dry DCM and added dropwise to the reaction solution. The reaction mixture was stirred over night while warming to r.t.. The solvent was removed under reduced pressure and the product purified through HPLC (DCM/MeOH 2.5%) (215 mg, 90%). $C_{102}H_{183}N_3O_{24}$ = 1835.583 g mol^{-1}

^{1}**H-NMR** (500 MHz, Methanol-*d4*, δ (ppm)): 8.36 (s, 3H, Ar-*H*), 4.26-4.21 (m, 6H, dendron -O-CC*H*-CH_2-), 4.05-4.02 (m, 6H, dendron -O-CH_2-CH-), 3.74-3.71 (m, 6H, dendron -O-CH_2-CH-), 3.60-3.50 (m, 27H, dendron-*H*, -O-CH_2-CH_2-), 3.41-3.38 (m, 6H, NH-CH_2-), 1.66-1.61 (m, 6H, -HN-CH_2-CH_2-), 1.57-1.52 (m, 6H, -O-CH_2-CH_2-), 1.41-1.26 (m, 114H, CH_2-chain, -CH_3).

^{13}**C-NMR**: (125 MHz, Methanol-*d4*, δ (ppm)): 168.56, 136.86, 129.74, 110.46, 79.22, 76.16, 73.44, 72.45, 72.37, 71.47, 70.62, 67.64, 67.58, 49.85, 49.00, 41.23, 31.17, 30.80, 30.60, 30.49, 28.13, 27.25, 27.14, 27.05, 25.74, 25.64.

MS (ESI): calculated ($C_{102}H_{183}N_3O_{24}Na^+$) = 1857.3084 g mol^{-1}
observed $\frac{m}{z}$ = 1857.3126 g mol^{-1}

BTA-C_{12}-G0 - (6)

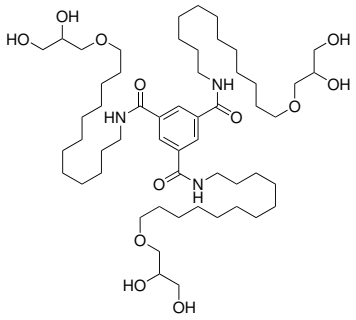

BTA-C12-pG0 **(5a)** (318 mg, 0.29 mmol) was dissolved in 25 mL methanol. Dowex-H (50W-X8, 2eq. by weight) was added and the reaction mixture stirred at 40 °C for 5 h until the reaction was completed based on TLC. Afterwards, the resign was filtered off and the solvent removed under reduced pressure. HPLC purification (RP, 85% MeOH/H_2O) and subsequent lyophilisation yielded the title compound as colourless solid (180 mg, 64%). $C_{54}H_{99}N_3O_{12}$ = 982.395 g mol^{-1}

^{1}**H-NMR** (700 MHz, Chloroform-*d3*, δ (ppm)): 8.13 (s, 3H, Ar-*H*), 3.62-3.59 (m, 3H, dendron -O-C*H*-CH_2-), 3.43 (dd, J_1 = 11.4 Hz, J_2 = 4.3 Hz, 3H, dendron -O-CH_2-CH-), 3.35 (dd, J_1 = 11.4 Hz, J_2 = 6.2 Hz, 3H, dendron -O-CH_2-CH-), 3.29-3.20 (m, 18H, -O-CH_2-CH_2-, HN-CH_2-), 1.45-1.41 (m, 6H, -HN-CH_2-CH_2-), 1.39-1.35 (m, 6H, -O-CH_2-CH_2-), 1.21-1.01 (m, 48H, CH_2-chain).

^{13}**C-NMR**: (176 MHz, Chloroform-*d3*, δ (ppm)): 166.89, 135.03, 128.33, 128.28, 71.88, 71.54, 70.56, 63.60, 29.29, 29.19, 29.11, 26.79, 25.76.

MS (ESI): calculated ($C_{54}H_{99}N_3O_{12}Na^+$) = 1104.7126 g mol^{-1}
observed $\frac{m}{z}$ = 1104.7170 g mol^{-1}

BTA-C_{16}-G0 - (7)

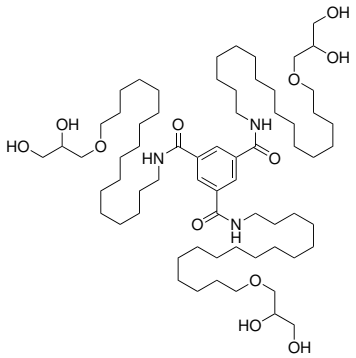

BTA-C16-pG0 **(5b)** (94 mg, 74 μmol) was dissolved in 15 mL methanol. Dowex-H (50W-X8, 2eq. by weight) was added and the reaction mixture stirred at 40 °C for 5 h until the reaction was completed based on TLC. Afterwards, the resign was filtered off and the solvent removed under reduced pressure. HPLC purification (RP, 90% MeOH/H_2O) and subsequent lyophilisation yielded the title compound as colourless solid (77 mg, 90%). $C_{66}H_{123}N_3O_{12}$ = 1150.719 g mol^{-1}

^{1}**H-NMR** (700 MHz, Methanol-*d4* / DCM-*d2* 1:1, δ (ppm)): 8.33 (s, 3H, Ar-*H*), 3.78-3.75 (m, 3H, dendron -O-C*H*-CH_2-), 3.60-3.57 (m, 3H, dendron -O-CH_2-CH-), 3.52-3.49 (m, 3H, dendron -O-CH_2-CH-), 3.47-3.38 (m, 18H, -O-CH_2-CH_2-, HN-CH_2-), 1.65-1.61 (m, 6H, -HN-CH_2-CH_2-), 1.58-1.54 (m, 6H, -O-CH_2-CH_2-), 1.35-1.26 (m, 72H, CH_2-chain).

^{13}**C-NMR**: (176 MHz, Methanol-*d4* / DCM-*d2* 1:1, δ (ppm)): 168.03, 136.23, 129.22, 72.84, 72.38, 71.65, 64.41, 47.53, 41.12, 40.99, 30.36, 30.31, 30.19, 30.09, 27.76, 26.77.

MS (ESI): calculated ($C_{66}H_{123}N_3O_{12}Na^+$) $= 1172.9004\,\mathrm{g\,mol^{-1}}$
observed $\frac{m}{z}$ $= 1172.9010\,\mathrm{g\,mol^{-1}}$

BTA-C_{16}-G1 - (8)

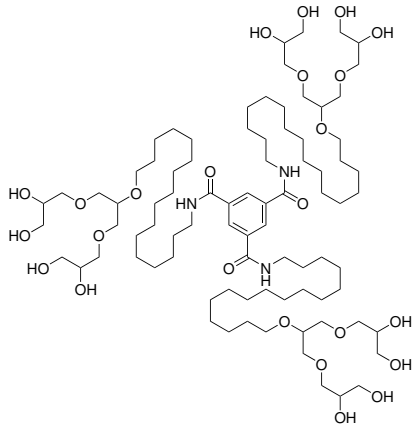

BTA-C16-pG1 **(5c)** (215 mg, 117 μmol) was dissolved in 20 mL methanol. Dowex-H (50W-X8, 2eq. by weight) was added and the reaction mixture stirred at 40 °C for 5 h until the reaction was completed based on TLC. Afterwards, the resign was filtered off and the solvent removed under reduced pressure. HPLC purification (RP, 90% MeOH/H_2O) and subsequent lyophilisation yielded the title compound as colourless solid (77 mg, 41%). $C_{84}H_{159}N_3O_{24}$ = $1595.193\,\mathrm{g\,mol^{-1}}$

^{1}**H-NMR** (500 MHz, Methanol-*d4*, δ (ppm)): 8.37 (s, 3H, Ar-*H*), 3.78-3.73 (m, 6H, dendron -O-CC*H*-CH_2-), 3.63-3.46 (m, 39H, dendron -O-CH_2-CH-, dendron -O-CH_2-CH- dendron-*H*, -O-CH_2-CH_2-), 3.41-3.38 (m, 6H, NH-CH_2-), 1.67-1.61 (m, 6H, -HN-CH_2-CH_2-), 1.59-1.53 (m, 6H, -O-CH_2-CH_2-), 1.40-1.20 (m, 78H, CH_2-chain).

^{13}**C-NMR**: (125 MHz, Methanol-*d4*, δ (ppm)): 167.32, 135.55, 128.44, 77.88, 72.62, 70.89, 70.23, 63.17, 63.01, 39.93, 29.83, 29.49, 29.16, 26.81, 25.90.

MS (ESI): calculated ($C_{84}H_{159}N_3O_{24}Na^+$) $= 1617.1211\,\mathrm{g\,mol^{-1}}$
observed $\frac{m}{z}$ $= 1617.1228\,\mathrm{g\,mol^{-1}}$

5 Structural analysis of BTA-based supramolecular copolymers

This work has been performed in collaboration with Dr. Xianwen Lou (HDX) and Dr. Lu Su (assembly studies), both Eindhoven University of Technology, The Netherlands.

5.1. Introduction

Structure, stability, and function of materials are closely connected to each other. Thus, the knowledge about structural organisation of molecules and about the stability of the formed aggregates plays a key role in the understanding and design of function in supramolecular polymers.

Supramolecular polymers are in particular promising structures for the design of multivalent, biofunctional agents.[3,111] In this context, particular attention is paid to the tuning of structure and stability of supramolecular polymers, in order to optimise the affinity towards pathogens or other biologically relevant targets. However, the synthesis and tailor-made design of monomers that assemble into aggregates with desired properties is very challenging. In order to tackle this problem, the application of supramolecular copolymers with two or more components is a promising approach.[53,101]

Previous work Recently, Thota *et al.* showed the possibility of tuning the stability of a supramolecular copolymer by altering the mixing ratio of two different BTA-based monomers.[28] In this work, the copolymerisation of BTA-C_{12}-EG_4 (nBTA) and BTA-C_{12}-G1 (dBTA) was studied. dBTA was introduced as BTA-derivative with dendritic PG-based head groups, whereas nBTA is functionalised with linear ethyleneglycol chains. Both structures are depicted in Fig. 5.2. nBTA is known to form one-dimensional supramolecular polymers in water, whereas dBTA aggregated in spherical micelles instead. However, it was possible to form one-dimensional supramolecular copolymers of dBTA and nBTA in mixing ratios of 2:1, 1:1, and 1:2, as shown by cryo-TEM experiments.

Hydrogen-deuterium exchange experiments (HDX-MS) were carried out to investigate the monomer exchange dynamics. The experiments revealed different properties of nBTA, dBTA, and their copolymers. The exchange of amide protons against deuterium in nBTA took several days, as can be seen in Fig. 5.1(a).[50] This behaviour reflects the effective shielding of the amide protons in the hydrophobic domain of the supramolecular polymer. In dBTA, however, all amide protons were exchanged immediately, due to the apparently high solvent accessibility of the whole molecule in the micellar aggregates. Interestingly, for the mixtures of nBTA and dBTA, signals for dBTA12D were observed (Fig. 5.1b), which were be assigned to dBTA molecules, in which the dendron protons, but not the amide protons, are exchanged. This observation indicated the presence of shielded amide protons in dBTA and suggested the aggregation of dBTA in a different morphology other than spherical micelles. Furthermore, also the exchange dynamics for nBTA changed in the copolymers, *i.e.*, the exchange rate of NH to ND in nBTA was decreased (Fig. 5.1a). These findings clearly showed that copolymers of nBTA and dBTA had formed, as the properties of both monomers changed.
In order to correlate the differences of the polymer dynamics with structural differences, molecular dynamics (MD) simulations were performed by the authors. The results indicated a higher regularity in the studied 2:1 nBTA/dBTA copolymer, compared to the homopolymer of nBTA. Furthermore, a decreased level of core hydration in the copolymers by 20% was calculated, corroborating the reduced exchange dynamics.

The structures of nBTA and dBTA differ only the structure of their polar head groups. The dendritic head group of dBTA exhibits a higher steric demand, which is apparently advantageous for the stability and regularity of the supramolecular aggregate. However, in cryo-TEM, nanofibres with similar appearance and dimensions were observed for all investigated copolymers. Distinct differences in the morphology that could explain different properties of the supramolecular polymers were yet unsolved. It was therefore the aim of this project to elucidate the ultrastructure of the studied copolymers at nanometre scale.
This chapter will cover the study of two copolymer systems. First, the reported system of nBTA and BTA-C_{12}-G1 (dBTA) was investigated with regards to the ultrastructure of copolymers with different monomer ratios. Second, a new copolymer system of nBTA and BTA-C_{16}-G1 was analysed with regards to aggregation properties, stability of the formed aggregates, and also the ultrastructure of the formed aggregates. A comparison of both systems finalises this chapter.

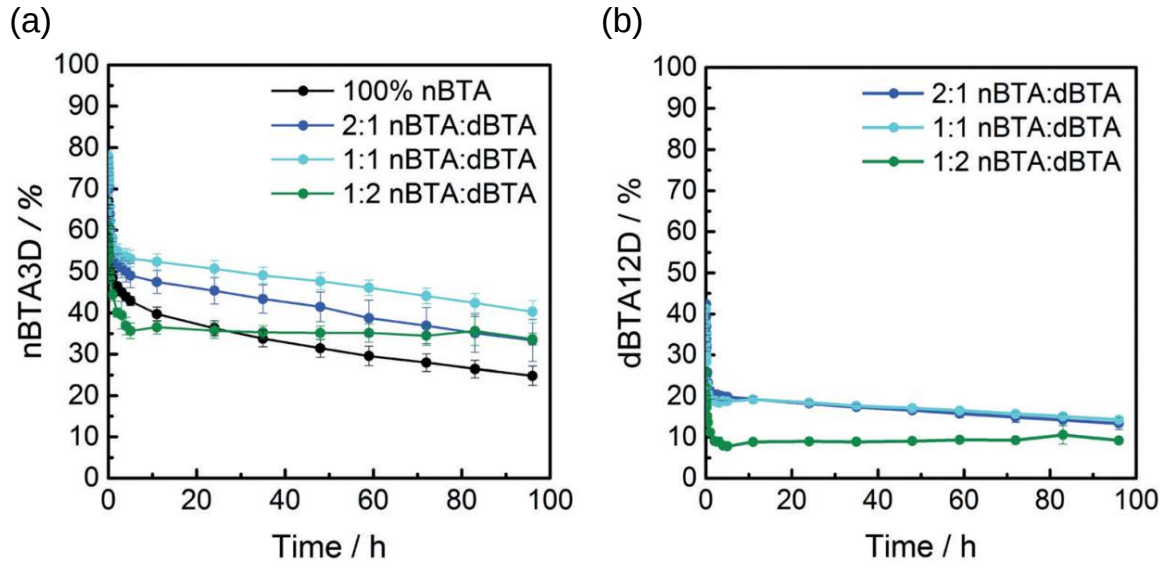

Figure 5.1.: HDX-MS measurements as a function of time, investigating the H/D exchange of exchange-labile protons in the copolymers of nBTA and dBTA after dilution in D_2O. Modified and reprinted from Ref. 28 with permission. Copyright 2018 John Wiley and Sons.

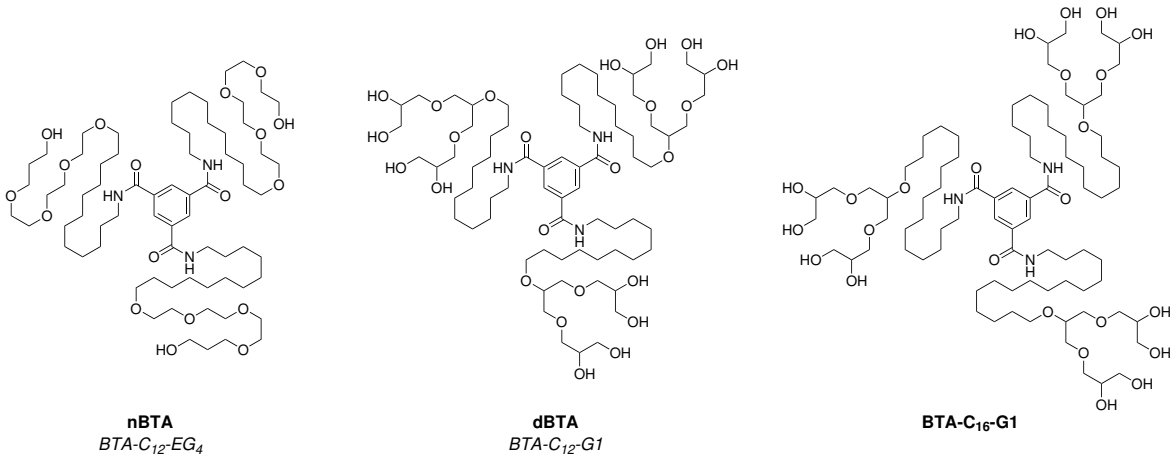

Figure 5.2.: Chemical structures of the investigated BTA monomers: nBTA, dBTA, and BTA-C_{16}-G1.

5.2. Results and Discussion

5.2.1. Ultrastructure investigation of copolymer system nBTA/dBTA

In the course of this study, the ultrastructure of copolymers with monomer mixing ratios of 1:2, 1:1, and 2:1 (nBTA:dBTA) were investigated. The samples were prepared by mixing stock solutions of both compounds followed by a non-covalent synthesis protocol including heating, vortexing and slow cooling (*cf.* methods and materials section for more details). In Fig. 5.4(a), UV-VIS spectra of all copolymer samples are shown. The comparison of UV-VIS spectra of both, homo- and copolymers, showed a high similarity between the spectra of nBTA and those of the 2:1 and 1:1 mixtures. This observation indicated a high similarity of the conformations of BTA molecules in the copolymers, compared to the homopolymer of nBTA and hence a strong dominating influence of nBTA on the properties of the copolymers.[28] The 1:2 mixture exhibited a decreased absorbance in the spectral range of 210-240 nm. In addition, a slight shoulder at 195 nm was observed, corresponding to the absorbance maximum of dBTA. Thus, a different organisation of H-bonds in the aggregates was supposed, resulting from a decreased influence of nBTA on the properties of the copolymer.

For the investigation of the ultrastructure of nBTA/dBTA copolymers, cryo-TEM micrographs of the respective copolymer samples were recorded and analysed, by multivariate statistical analysis (MSA) and classification techniques. Cryo-TEM micrographs were recorded using a Volta phase plate for an enhanced contrast in the images. In Fig. 5.3 two representative micrographs of nBTA/dBTA copolymers (1:1) are shown, illustrating the differences between both imaging conditions. The drastic gain in contrast can be clearly seen by comparing both images. This enhanced contrast is advantageous during the manual picking of cut-outs of individual fibre structures and the subsequent alignment of the images prior to the MSA. In addition, the images can be recorded closer to the focus and thus with less defocus, which leads to a clear reduction of defocus-induced artefacts, as introduced in section 2.2.1.

Cryo-TEM images of the copolymers are shown in Figs. 5.4(b)-(d). In all images, several micrometre-long fibres were observed as predominant morphology. Interestingly, in the images of 2:1 and 1:1 mixtures, also twisted, loop-forming fibres were observed and are marked by a dashed rectangle in Fig. 5.4(b). In the case of the 1:2 copolymer, this was observed to a lesser extend. Here, small micellar aggregates were observed in addition to the nanofibres, as pointed out in Fig. 5.4(d).

In order to analyse the ultrastructure of the copolymers, we took several hundred cut-outs

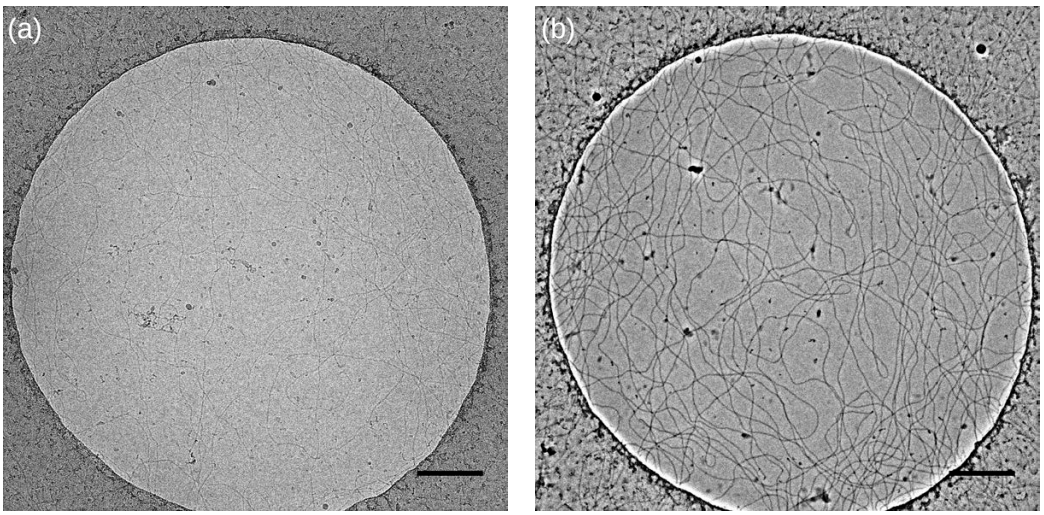

Figure 5.3.: Representative cryo-TEM micrographs of nBTA/dBTA copolymers (1:1) illustrating the contrast enhancement effect of a phase plate. (a) Conventional defocus contrast conditions with objective aperture and a defocus of -5 μm. (b) Micrograph taken with a volta phase plate and a defocus of -400 nm. Scale bars represent 200 nm.

with individual fibres manually from the recorded images. After rotational and translational alignment, a MSA was conducted. In Fig. 5.5 representative class sum images of the copolymers are shown next to the sum image of nBTA.

For nBTA, a double-helix ultrastructure was revealed by image processing, as presented in the last chapter. It was therefore the question, if this motif was also present in the ultrastructures of copolymers of nBTA and dBTA. As can be clearly seen in Figs. 5.5(b) and (c), the ultrastructures of 2:1 and 1:1 copolymer exhibited similar double-helical structures. Both class sum images are representative, which means that most of the obtained class sum images showed a double-helix motifs with only slight variations. The length of the repeating unit from knot to knot was determined to be (17.9±0.4) nm for the 2:1 copolymer and (17.5±0.4) nm for the 1:1 copolymer. Thus, the repeating unit was shorter as for the homopolymer of nBTA [(19.9±0.4) nm].

As already implied from UV-VIS spectra, 1:2 copolymers exhibited different properties. In the fibres of the copolymer, a slightly different ultrastructure was observed, as shown in Fig. 5.5(d). The double-helix motif almost vanished and the impression of a single fibre was given. However, an undulation in the density along the fibre with a repeating unit of (14.9±0.4) nm could be observed, which was even shorter as for 2:1 and 1:1 copolymers. Although no distinct separation between two individual fibres could be deduced from the images, the thickness of around 6 nm of the structure indicated the interaction of more than one fibre, according to

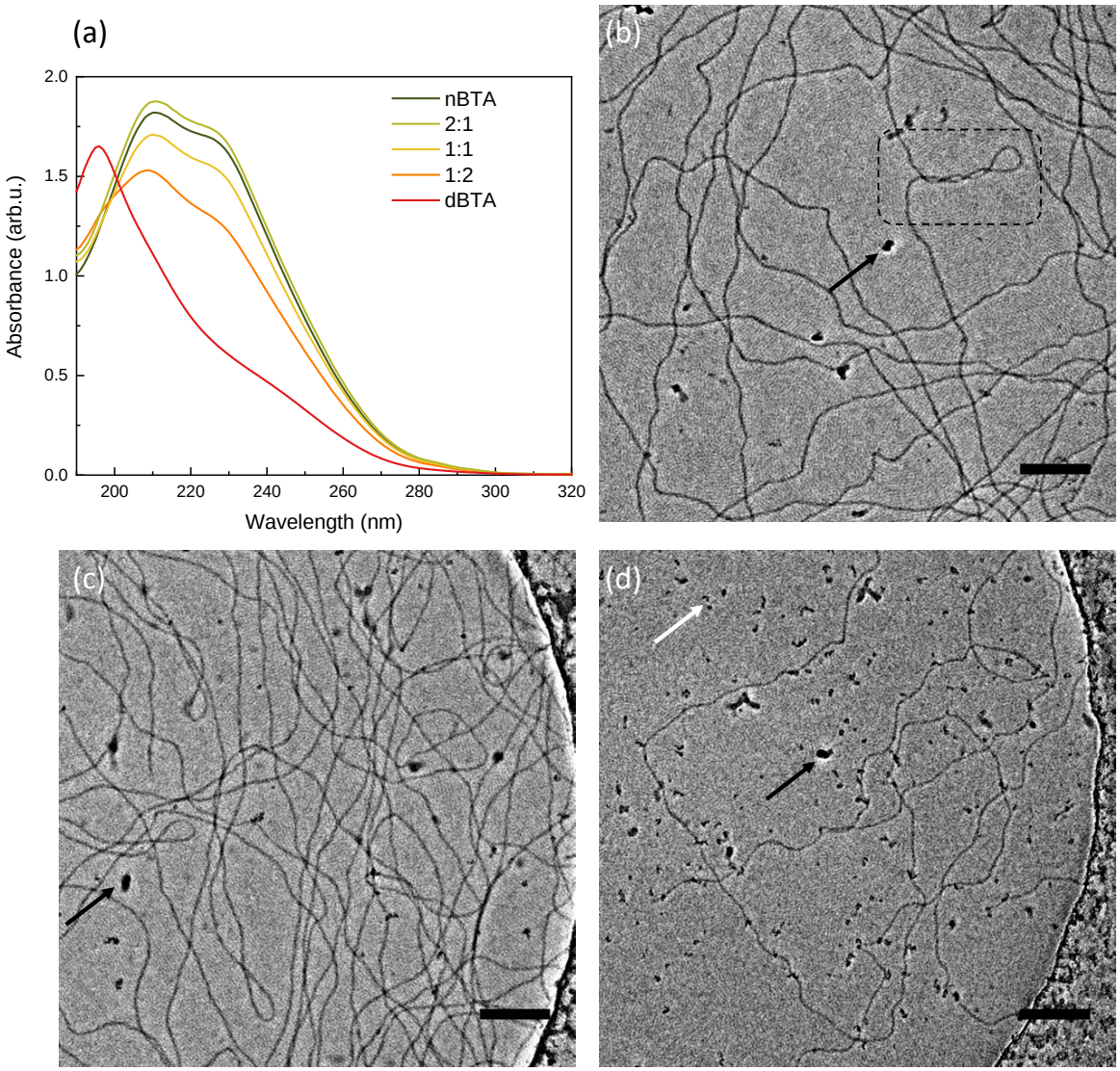

Figure 5.4.: (a) UV-VIS spectra of nBTA, dBTA and 2:1, 1:1, and 1:2 mixtures thereof in water (c = 50 μM, 1 cm pathlength). Representative cryo-TEM micrographs of nBTA/dBTA copolymers recorded with phase plate: (b) 2:1, (c) 1:1, and (d) 1:2 (c = 500 μM, scale bars represent 100 nm). In all cases, micrometre-long nanofibres were observed as most prominent morphology. Twisted, loop-forming fibres were observed for 2:1 and 1:1 mixtures of which one in marked by a rectangle in (b). Larger dark spots are ice crystals or surface contaminations (black arrows). Smaller particles are embetted in ice and originate from spherical micelles (white arrow). Both, spectra and images, represent the sample state two days after sample preparation.

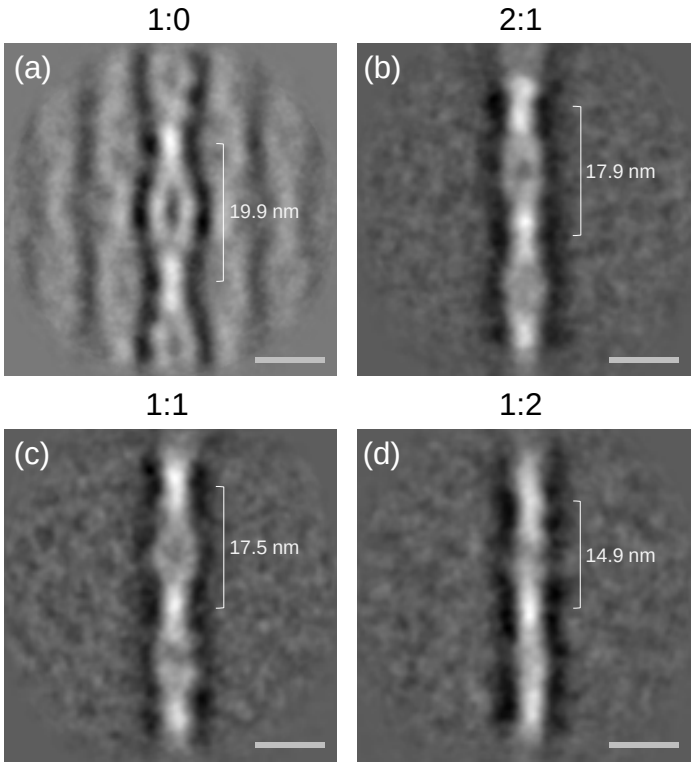

Figure 5.5.: (a) Sum image of aligned images of nBTA showing the double-helix ultrastructure of the nanofibres. (b)-(c) Class sum images after MSA of nBTA/dBTA copolymers in mixtures of: 2:1 (b), 1:1 (c), and 1:2 (d). Numbers represent the length of the repeating unit of the double-helix (accuracy = 0.4 nm), showing the decreasing helix pitch with increasing amount of dBTA in the copolymer. Scale bars represent 10 nm.

the dimensions of the double-helix strands of around 2-3 nm. Here, a dense twist of two fibres into the resulting structure might provide a probable explanation.
In sum, the double-helix motif was also observed in the ultrastructure of nBTA/dBTA copolymers. Here, the more dBTA was present in the mixture, the shorter the repeating unit of the helix became. The decreasing length of the repeating unit with increasing mixing ratios of dBTA might be explained by an increase of the axial curvature of both helices upon copolymer formation. Thus, the twist of the double-helix increase, resulting in a shorter helix pitch. Moreover, the increased curvature and, thus, increased strain in the aggregate may provide an explanation for the loop formation of the double-helix as observed in Figs. 5.4(b) and (c). The shortage of the helix pitch culminated in a structure, where both strains were no longer separated.
In the next section, the investigation of a new supramolecular copolymer system between nBTA and BTA-C_{16}-G1 is presented. Similar to the just discussed supramolecular copolymer, the properties in solution, as well as the ultrastructure of the formed aggregates, were examined.

5.2.2. Investigation of the supramolecular copolymerisation of BTA and BTA-C_{16}-G1

In chapter 4, the synthesis and characterisation of a new water-soluble BTA-based amphiphile (BTA-C_{16}-G1) was reported. In comparison to the well-studied BTA-C_{12}-EG_4 (nBTA), remarkable low dynamics in the aggregates were observed. Furthermore, significant differences were elucidated between the ultrastructure of the fibrous, elongated supramolecular aggregates of both. By image processing techniques and multivariate statistical analysis (MSA) it was shown that the nanofibres formed by nBTA exhibited a double-helix ultrastructure. For BTA-C_{16}-G1 however, two parallel fibrous strands, forming a narrow ribbon, were observed. Copolymer solutions were prepared according to a non-covalent synthesis protocol including heating, cooling, and vortexing (see methods and materials section). In the course of this study, we studied mixing ratios of 2:1, 1:1, and 1:2, with the numbers referring to the nBTA:BTA-C_{16}-G1 ratio.
UV-VIS spectra in aqueous solution were recorded after one and eight days of equilibration at room temperature. Both spectra are shown in Figs. 5.6(a) and (b). In general, following the mixtures from an excess of nBTA (2:1) towards an increasing amount of BTA-C_{16}-G1 (1:2), the two characteristic maxima for nBTA at 210 nm and 228 nm decreased, whereas a maximum at 196 nm increased. An additional peak was not observed in any investigated

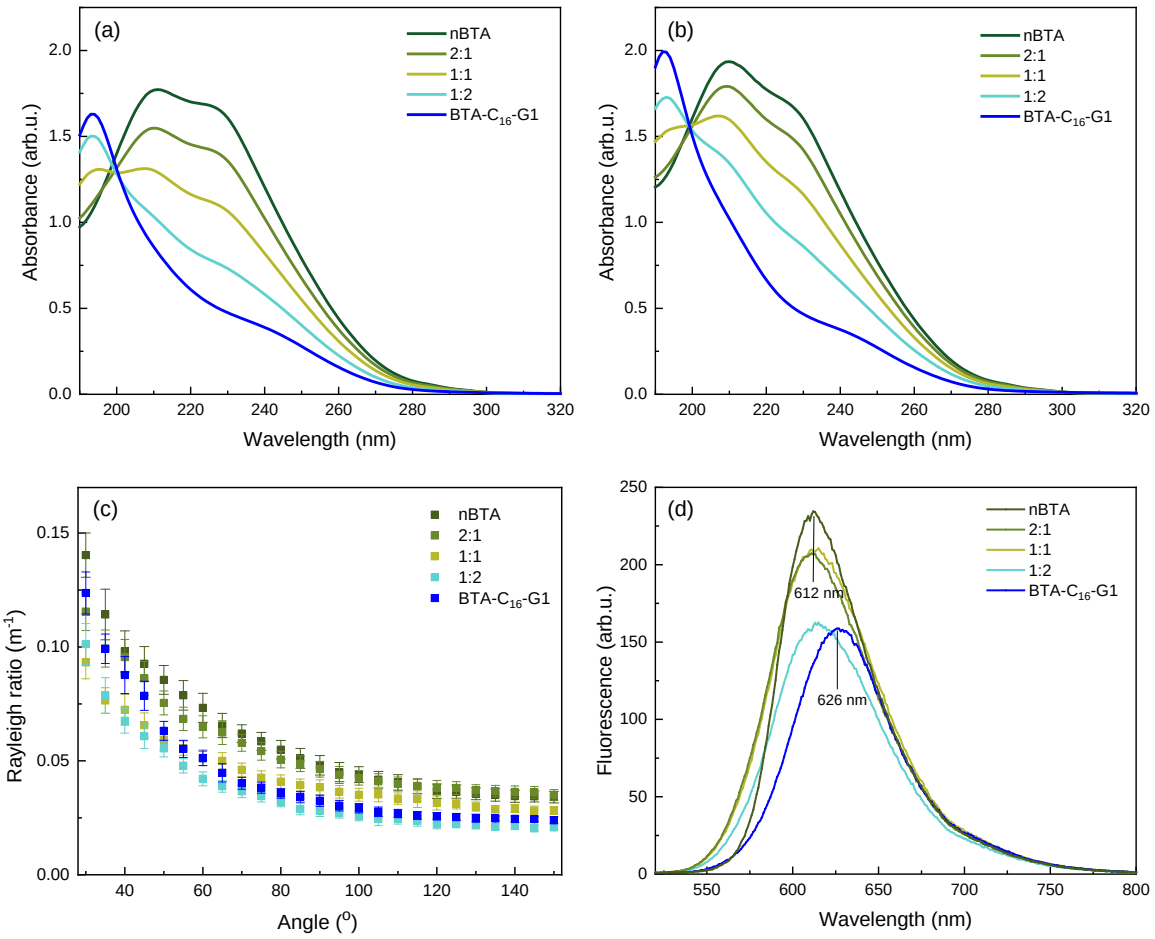

Figure 5.6.: Aggregation experiments of nBTA, BTA-C_{16}-G1, and mixtures thereof in water. UV-VIS spectra at different time points after sample preparation: (a) 1 day, (b) 8 days (c = 50 μM, 1 cm pathlength). (c) Static light scattering experiments show the angular dependence of the scattered signals indicating that all measured mixtures form anisotropic aggregates. Error bars indicate standard deviation (d) Nile Red fluorescence experiments probing the hydrophobic pocket of formed polymers.

Table 5.1.: Rate constants obtained from tri-exponential fits of HDX experiments for the initial, fast, and slow exchanging parts, as well as the contributions to the process in %.

Compound	$k_{initial}$ (h^{-1})	k_{fast} (h^{-1})	k_{slow} (h^{-1})	Initial (%)	Fast (%)	Slow (%)
nBTA (100%)	$2.08 \cdot 10^{1}$	0.42	$5.56 \cdot 10^{-3}$	45.8	11.0	42.7
nBTA (50%)	$3.20 \cdot 10^{1}$	0.80	$1.03 \cdot 10^{-3}$	43.1	9.7	47.2
BTA-C_{16}-G1 (50%)	$2.90 \cdot 10^{1}$	0.17	$2.64 \cdot 10^{-3}$	22.9	21.0	57.0
BTA-C_{16}-G1 (100%)	-	-	-	-	-	-

case. We therefore supposed similar one-dimensional aggregates, as observed for nBTA and BTA-C_{16}-G1 in solution. This presumption was corroborated by Nile Red encapsulation experiments. Nile Red serves as a probe for hydrophobic environment, as the fluorescence of the dye depends on the polarity of its environment.[131] In all cases, the samples showed similar fluorescence spectra in terms of intensity and maximum as shown in Fig. 5.6(d), thus, indicating the presence of a hydrophobic pocket with a similar polarity. Moreover, in static light scattering (SLS) experiments, an angular dependence of the Rayleigh ratio could be observed in all cases, as can be seen in Fig. 5.6(c). This effect indicated the formation of anisotropic, non-spherical aggregates.

When comparing the spectra of one and eight days of equilibration, an increase of the signals became apparent, whereby signals in the wavelength range of 190-230 nm seemed to increase stronger than the absorption signals for longer wavelength. As the UV-VIS absorption is influenced by the H-bond configuration within the aggregates, structural changes over time, referred to as ageing effects, could be supposed. We therefore recorded cryo-TEM images of the samples after one and 14 days. Here, in fact, one-dimensional aggregates were found for all samples, which will be further discussed in the next section. However, no remarkable differences were observed over time, indicating a high stability of the formed aggregates with only minor ageing effects, at least over several days.

HDX measurements were performed for 1:1 and 1:2 copolymers. As observed before, the solvent-accessible protons of the head groups were exchanged by deuterium immediately. Therefore, only the exchange of amide protons is followed as a function of time. Here, remarkable differences in comparison to the homopolymers were observed, as can be seen in Fig. 5.7. The H/D exchange rate of nBTA amide protons was significantly reduced in both copolymers, irrespective of the mixing ratio. In contrast, the dynamics for BTA-C_{16}-G1 were increased with increasing amount of nBTA in the copolymer, which resulted in a higher ex-

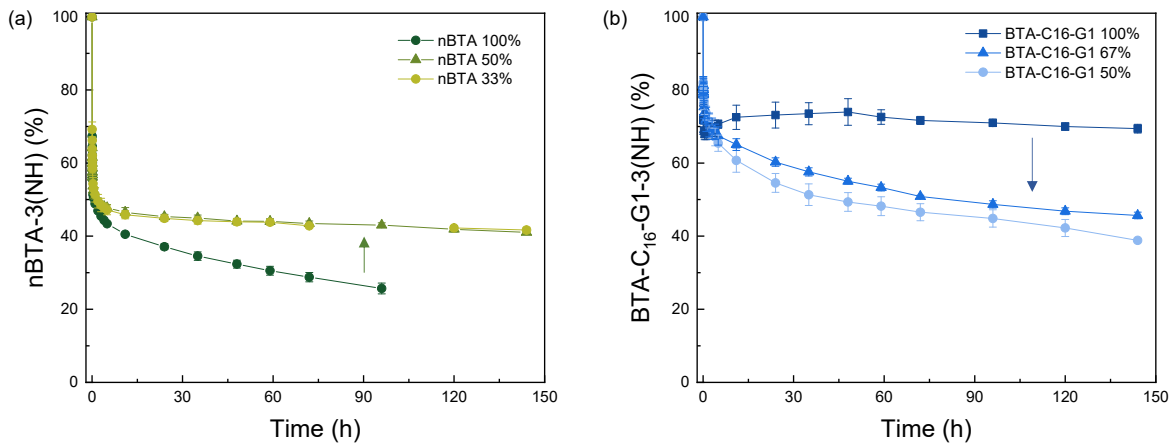

Figure 5.7.: HDX-MS experiments as a function of time, investigating the H/D exchange of exchange-labile protons in homopolymers of nBTA, BTA-C_{16}-G1 and their copolymers after dilution in D_2O. (a) Decay of unexchanged amide protons in nBTA in a pure solution (100%), a 1:1 copolymer (50%), and a 1:2 copolymer (33%), shows a stabilisation effect through copolymer formation, irrespective of the ratio. (b) Decay of unexchanged amide protons in BTA-C_{16}-G1 in a pure solution (100%), a 1:2 copolymer (67%), and a 1:1 copolymer (50%), shows a destabilisation effect through copolymer formation with increasing ratio of nBTA in the copolymer. As both compounds show altered H/D-exchange dynamics upon copolymerisation, a successful copolymer formation can be inferred.

change rate as compared to its homopolymer.

By fitting the obtained data with a tri-exponential fit, three stages of H/D exchange in BTA based polymers can be distinguished, *i.e.*, initial, fast, and slow. For all stages, a rate constant k and the fraction of the process in % can be determined.[50] This fit was applied to the HDX data of the 1:1 copolymer and the obtained parameters are summarised in Table 5.1. For nBTA, the fraction of the slow exchange increased at the expense of the initial exchange, leading to a slower and in total reduced H/D exchange of the amide protons. For BTA-C_{16}-G1, the opposite behaviour was observed. The aggregates of BTA-C_{16}-G1 homopolymers were found to be highly stable, such that a tri-exponential fit, dividing the H/D exchange into different stages, could not be applied. However, in a 1:1 mixture with nBTA, the dynamics were increased significantly and a tri-exponential fit could be applied successfully. Although the fraction of initial exchange was still low, the rate of the slow exchange increased drastically such that it was more than double the rate for nBTA in the copolymer. As a result, after five days, the amount of exchanged amide protons of nBTA and BTA-C_{16}-G1 became equal. In sum, the exchange dynamics of nBTA were decreased upon copolymer formation with BTA-C_{16}-G1. Contrarily, the exchange dynamics of BTA-C_{16}-G1, which are very low in

homopolymers, were increased upon copolymer formation with nBTA. Taken together, the properties of both, nBTA and BTA-C_{16}-G1 were altered. This effect showed the successful formation of copolymers, as both species were affected.

Analysis of the Ultrastructure

Cryo-TEM images were recorded for copolymer samples in mixing ratios of 2:1, 1:1, and 1:2. In a first step, we compared the observed aggregate morphologies qualitatively. In all cases, micrometer-long nanofibres were found as dominant morphology, as can be seen in Figs. 5.8-5.10. In addition, a fingerprint-like pattern across the whole ice layer was observed in all samples. This pattern was already observed in pure nBTA samples and might be caused by monomer aggregation at the air-water interface or a kind of liquid crystalline phase across the whole volume. Furthermore, tube-like aggregates were found [Figs. 5.8(b), 5.9(b), and 5.10(b)], as already observed for nBTA homopolymers. However, due to the rare occurrence, this morphology was not further studied as part of this project. Here, future work may provide further insights.

Despite the similarities in the cryo-TEM data at first view, also subtle differences were observed in the images. In case of the 2:1 copolymer, two kinds of nanofibres were observed upon detailed analysis. First, nanofibres with a twisted appearance, similar to those of nBTA homopolymers were observed, as can be seen in Fig. 5.8(c) marked with a white arrow. On the other hand, also fibres with thickness and contrast modulations, as observed for BTA-C_{16}-G1 homopolymers were observed (black arrow in Fig. 5.8(c)).

For the 1:1 mixtures, twisted and ribbon-like fibres were found too, as can be seen in Fig. 5.9(a). In addition, very thin fibres were observed, as shown in Fig. 5.9(b). Some of these thin fibres appeared to be oriented along the fingerprint pattern. The thickness was determined to be around 2 nm, which would fit to the dimensions of a single strand of stacked nBTA or BTA-C_{16}-G1 molecules. The fingerprint-pattern is supposed to origin from assembled monomers at the water-air interface, thus, these single strands might be embedded and stabilised in this organised layer.

In Fig. 5.10 representative cryo-TEM images observed for the 1:2 mixture are shown. Here, bundled, as well as individual fibrous structures were observed predominantly [5.10(a)], but also tube-like structures [5.10(b)], micelles [5.10(c)], and very thin fibres [5.10(d)]. For the micelles, a separate analysis was conducted by MSA, to see if any persistent three-dimensional structure was present. However, the micelles were structurally too diverse in size and shape,

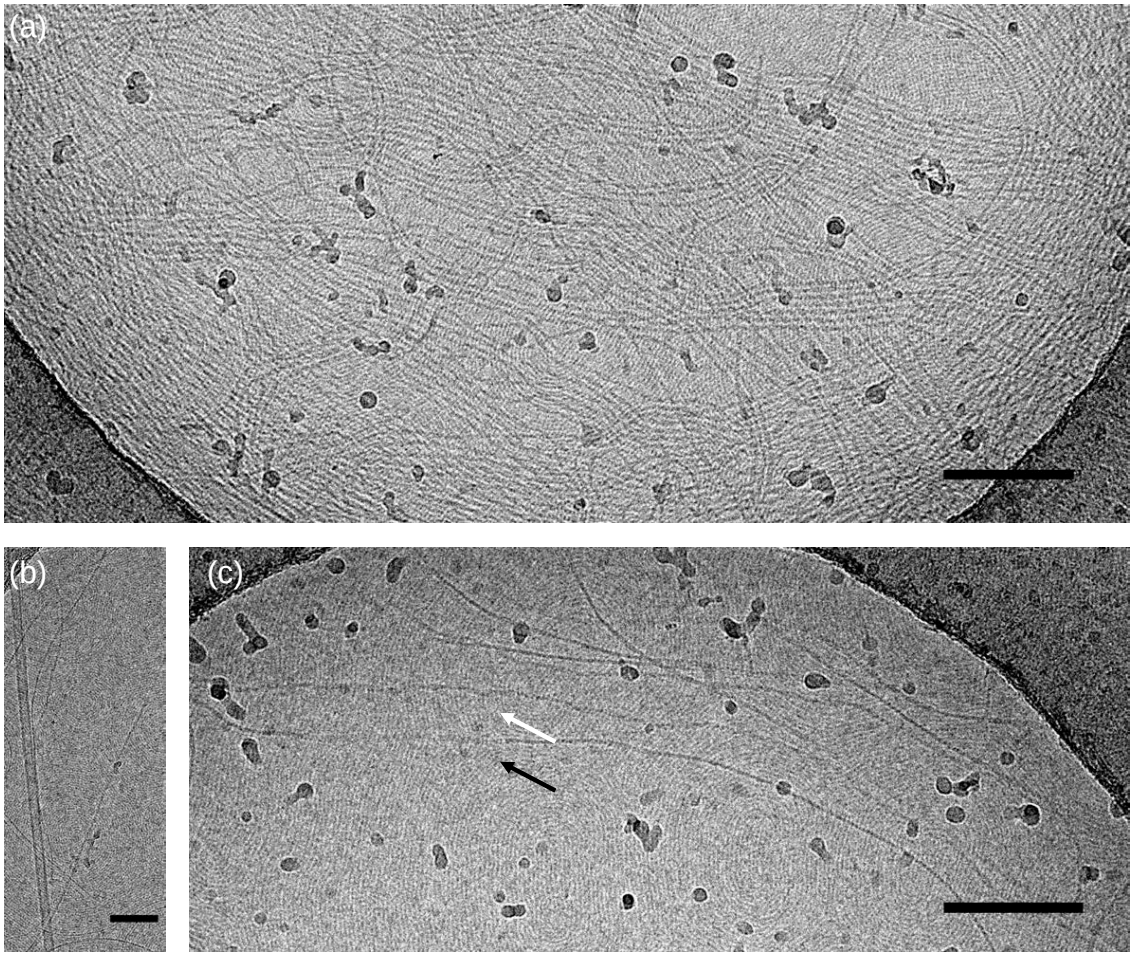

Figure 5.8.: Representative cryo-TEM images of a 2:1 mixture of nBTA and BTA-C_{16}-G1 (c = 500 μM in milliQ). (a) Micrometre-long fibres were observed as predominant aggregate type, but also tube-like aggregates (b) were present. (c) Within the nanofibres, narrow ribbon-like structures (black arrow), as well as twisted fibres (white arrow) were observed. Scale bars represent 150 nm in subfigures (a) and (c) and 100 nm in subfigure (b).

which is why no further insights in the structure of the micelles could be obtained.

The variety of observed aggregates shows the flexibility and adaptivity of supramolecular copolymers. Subtle variation in the parameters of the preparation process, as well as age of the sample, mixing ratio or concentration influences the resulting morphologies and induces multiple aggregation types even within one sample.

After qualitatively evaluating similarities and differences in the images, the focus was set on the nanofibres in the following analysis. Here, an ultrastructure analysis by MSA and subsequent classification of the cryo-TEM data were carried out. If different fibre types were present, focus was set on the twisted structures. The resulting class sum images for all copolymers are shown in Fig. 5.11. For the 2:1 mixture, shown in Fig. 5.11(a), a double-helix

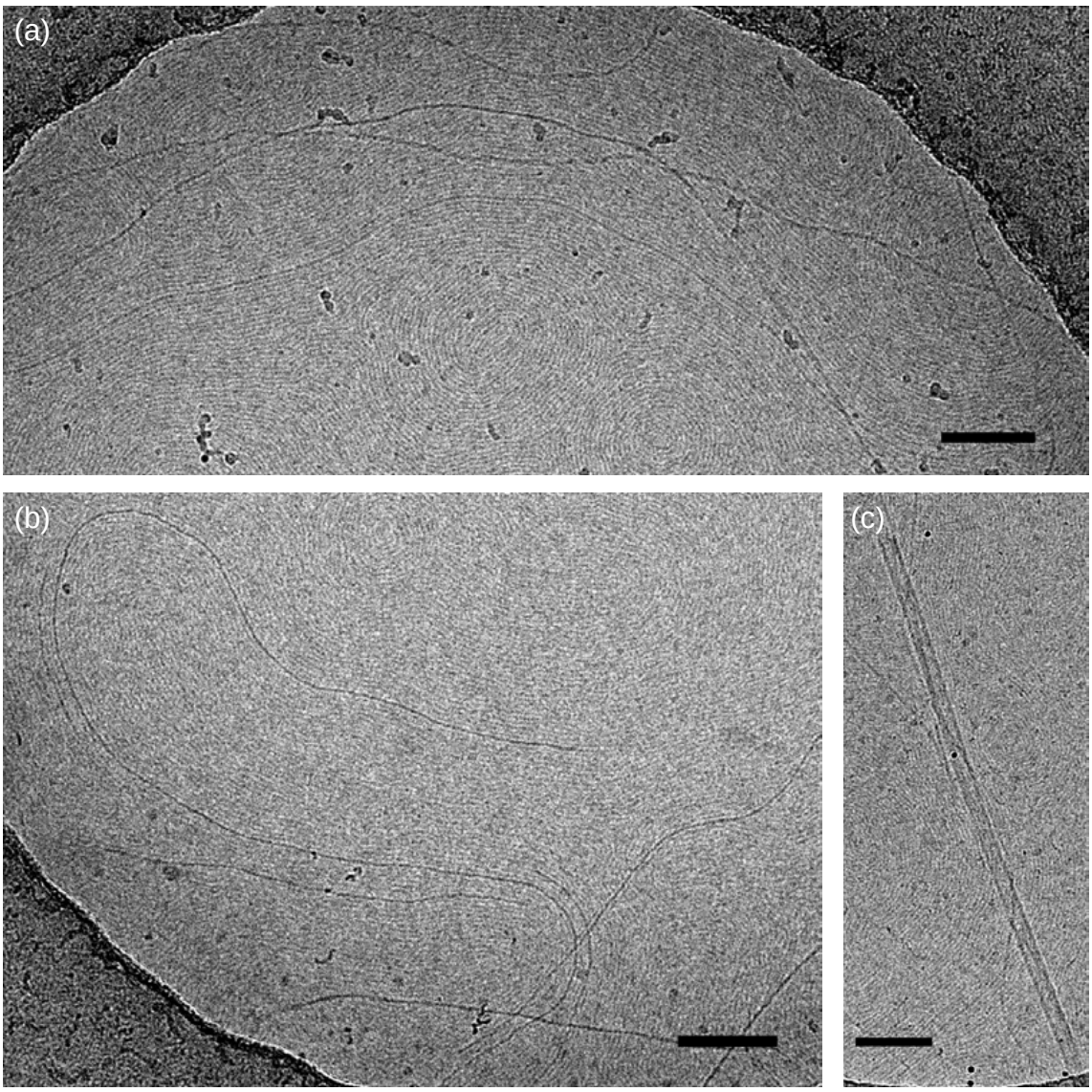

Figure 5.9.: Representative cryo-TEM images of a 1:1 mixture of nBTA and BTA-C_{16}-G1 (c = 500 μM in milliQ). (a) Micrometre-long fibres were found predominantly, partly individual or as bundles. Furthermore, additional morphologies, such as tubes (b), micelles (c) and thin fibres (d) were observed. Scale bars represent 100 nm.

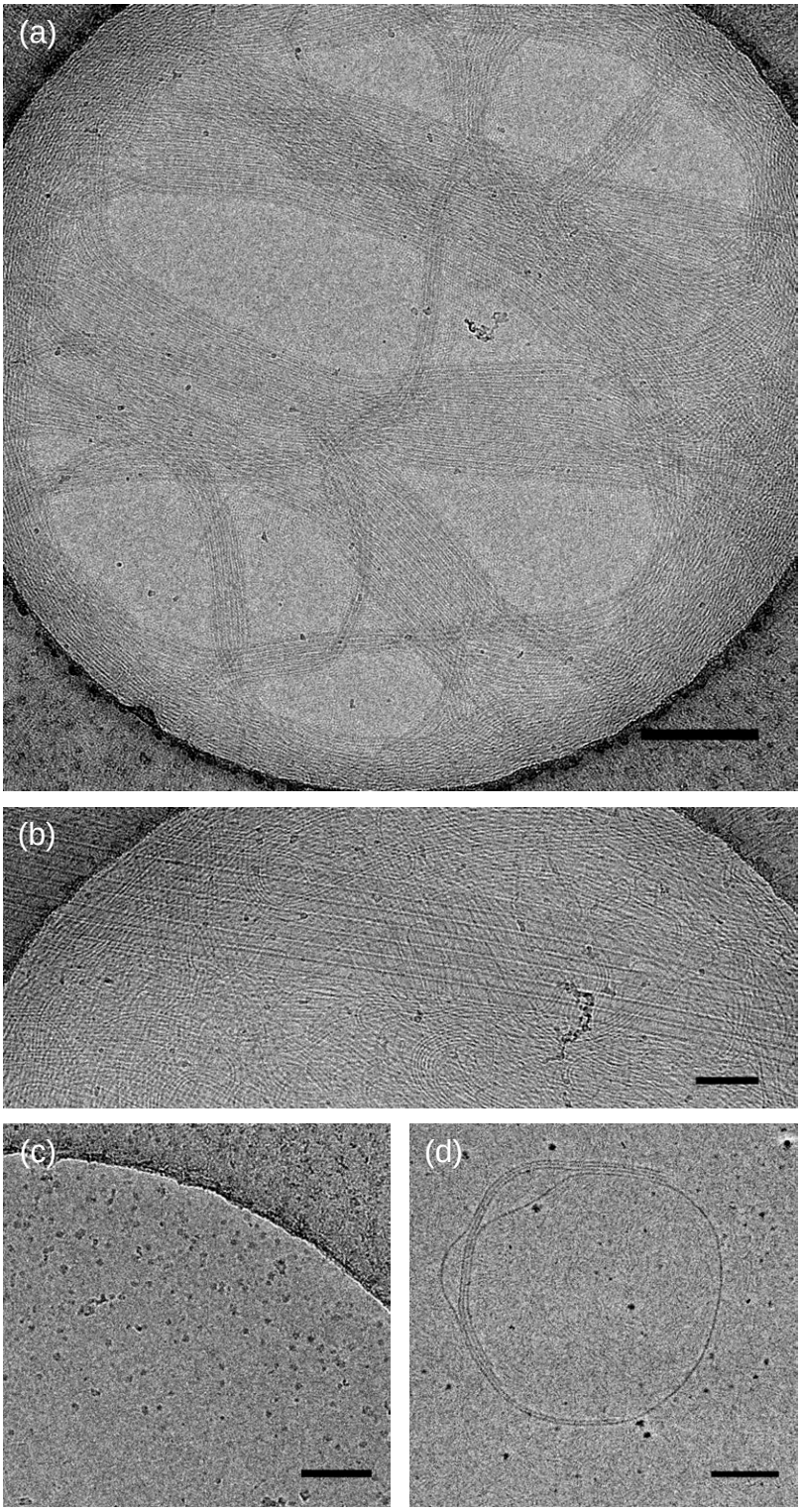

Figure 5.10.: Representative cryo-TEM images of a 1:2 mixture of nBTA and BTA-C_{16}-G1 (c = 500 μM in milliQ). Micrometre-long fibres were observed (a), as well as very thin fibres (b) and tube-like structures (c). Scale bars represent 200 nm in subfigure (a) and 100 nm in subfigures (b), (c), and (d).

ultrastructure in the fibres could be clearly elucidated with a repeating unit of (21.6±0.4) nm. Thus, the length of the repeating unit is slightly larger as observed for nBTA homopolymers (≈20 nm). For the 1:1 copolymer sample, two representative class sum images are depicted, showing two different ultrastructures. In the first case, shown in Fig. 5.11(b), a double-helix motif was obtained with a repeating unit of (32.0±0.4) nm. However, in the second class, shown in Fig. 5.11(c), a fibre with a diameter of around (3.8±0.4) nm was observed. No further density variations along the fibre were observed, thus, a single fibre could be suggested. However, the monomer dimensions were approximated with 2.5 - 3.0 nm. Furthermore, additional thin fibres were observed in the cryo-TEM images with diameters of around 2.0 nm. Therefore, an interaction of more than one strand is presumed. However, spatial resolution and method limitations were reached at that point. Additional techniques such as cryogenic electron tomography (cryo-ET) and subsequent three-dimensional reconstructions might help to elucidate more details of the ultrastructure in the future.

After having revealed double-helix motifs in the ultrastructure of 2:1 and 1:1 copolymers of nBTA/BTA-C_{16}-G1, we however observed a significantly different ultrastructure for the 1:2 copolymer sample. Two parallel fibre strands with diameters of (2.2±0.4) nm each were observed in the class sum images as shown in Fig. 5.11(d). The overall width of the structure was determined with (6.7±0.4) nm. According to the measured diameters, two strands of one-dimensionally stacked aggregates are likely to explain the observations. As already observed for BTA-C_{16}-G1 homopolymers, these ribbon-like structures differ significantly in their appearance compared to the double-helices, as their contrast and thickness varies while they rotate in the volume. By twisting a double-stranded fibre by 90°, a motif with the diameter of a single fibres would be observable. And indeed, in the second class sum image, a single-strand motif with a diameter of (2.9±0.4) nm was obtained. Thus, we assign the second obtained class sum image, shown in Fig. 5.11(e), to the side view orientation.

In sum, different ultrastructures were obtained for mixtures of nBTA and BTA-C_{16}-G1. The nanofibres obtained from a 2:1 mixture exhibited a double-helix motif in its ultrastructure with a slightly increased repeating unit, compared to the homopolymer of nBTA. This tendency was continued for the 1:1 copolymer, *i.e.*, a even further increased repeating unit of the double-helix was observed. Moreover, two parallel strands were observed for the 1:2 copolymer (as also for BTA-C_{16}-G1 homopolymers). The two parallel strands can be thought as a double-helix with an infinitely long repeating unit. Thus we propose, that the copolymerisation of nBTA with an increasing amount of BTA-C_{16}-G1 leads to the unwinding of the supramolecular double-helix.

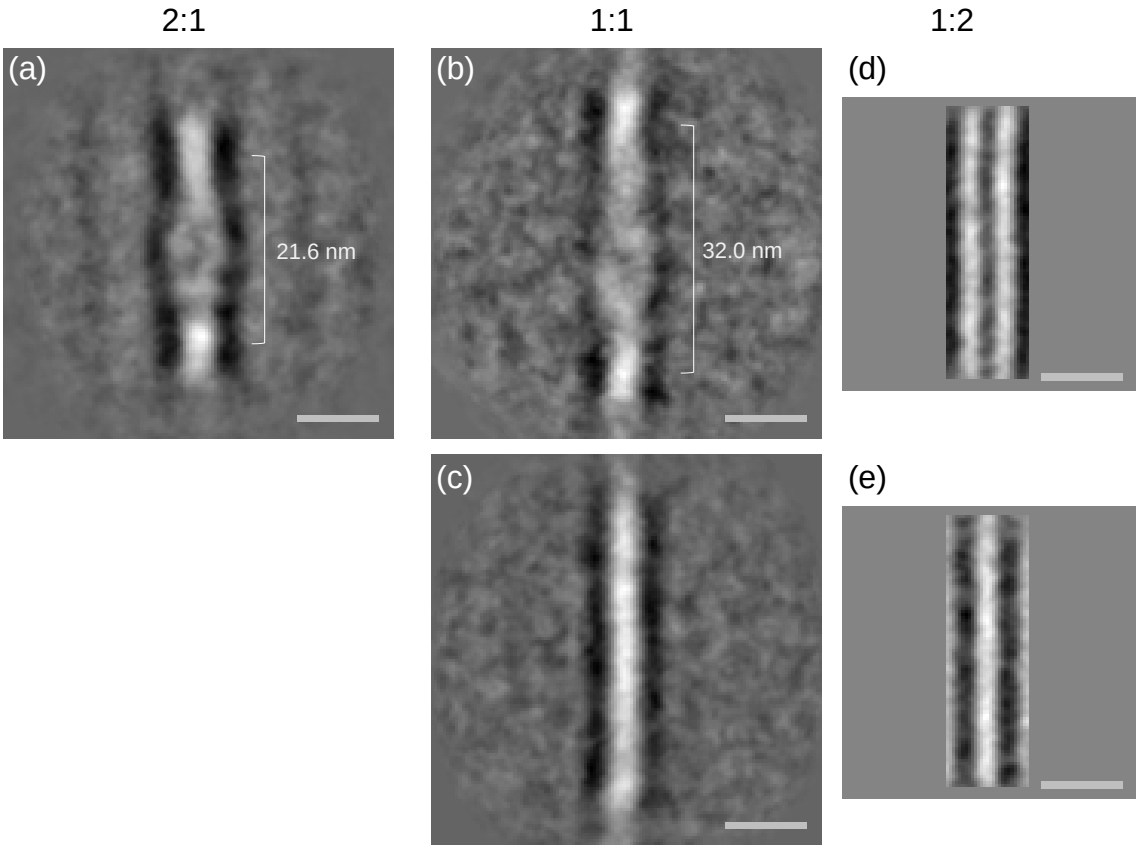

Figure 5.11.: Class sum images after image processing and MSA of cryo-TEM images of nBTA/ BTA-C_{16}-G1 copolymers with different monomer ratios: 2:1 (a), 1:1 (b)(c), and 1:2 (d)(e). Numbers represent the length of the repeating unit of the double-helix (accuracy = 0.4 nm), showing the increasing helix pitch with increasing amount of BTA-C_{16}-G1 in the copolymer. Images are depicted using the same scaling, scale bars represent 10 nm.

Table 5.2.: Summary of obtained repeating unit lengths of supramolecular double-helices, noted in nanometre. The length decreases in copolymers of nBTA and dBTA with decreasing nBTA ratio, whereas it increases in copolymers of nBTA and BTA-C_{16}-G1 analogously.

nBTA/dBTA			nBTA	nBTA/BTA-C_{16}-G1		
1:2	1:1	2:1	100%	2:1	1:1	1:2
14.9	17.5	17.9	19.9	21.6	32.0	-

5.2.3. Comparison of both copolymer systems and discussion

In the previous sections we investigated the structure of supramolecular copolymers at nanometre scale. Two systems were analysed, that are, nBTA/dBTA and nBTA/BTA-C_{16}-G1. Between both systems, we found opposite variations in the ultrastructure. Taking the double-helix structure of nBTA as starting point, the helix pitch was shortened with an increasing amount of dBTA in the mixture. In contrast, the helix pitch was elongated upon addition of BTA-C_{16}-G1, resulting in a complete unwinding of the double helix and the presence of two parallel fibre strands above 50mol% of BTA-C_{16}-G1. The values of all investigated copolymers are collected in Tab. 5.2.

BTA-C_{16}-G1 and dBTA exhibit a very similar chemical structure. Both amphiphiles are functionalised with PG-based G1-dendrons as polar head groups. However, the hydrophobic alkyl chains differ in their lengths, i.e., C_{12} for dBTA and C_{16} for BTA-C_{16}-G1. The length of the hydrophobic alkyl chain was shown to have an large impact on the stability and properties of BTA-based supramolecular polymers.[45] The stabilisation of intermolecular H-bonds highly depends on the size and strength of the hydrophobic pocket in the resulting aggregate. Pure dBTA is not able to form one-dimensional polymers, whereas BTA-C_{16}-G1 does assemble into stable, fibrous aggregates with two parallel fibre strands. This effect can be attributed to the increased chain length in BTA-C_{16}-G1.

Here, we propose that the structure changes in the mixtures of BTAs can be understood as transition between the ultrastructures of both homopolymers. Along the transition from nBTA and BTA-C_{16}-G1 the helix pitch in increased, which can be understood as straightening of the fibre strands. In the maximum, the strands are completely de-twisted. For dBTA, such a straightforward transition is not possible, as dBTA assembles in small micelles. However, the increased curvature of helix strands in copolymers with increasing amounts of dBTA can be thought similarly as transition from fibres towards micellar aggregates.

A still remaining question concerned the possible link between modulations in the ultrastructure and the altered dynamics of the supramolecular co-/polymers. It was shown in experiments and by simulations that homopolymers of nBTA exhibit defects with increased dynamic behaviour.[48,61] These dynamic hotspots can be compared to grain boundaries or defects in crystals, respectively. However, all-atom molecular dynamics (MD) simulations revealed that copolymers of nBTA and dBTA exhibit an increased regularity. It was therefore supposed that dBTA replaces the hotspots in the supramolecular polymer, thus, decreasing the monomer exchange dynamics in these areas.[28] Also for mixtures with BTA-C_{16}-G1, decreased exchange dynamics of nBTA were observed. Here we suppose that also the addition of BTA-C_{16}-G1 reduces the formation of hot spots/ defects in the polymer.

When comparing 1:1 mixtures with nBTA, the H/D exchange dynamics of BTA-C_{16}-G1 monomers was increased. In contrast those of dBTA were decreased compared to their homopolymers (*cf.* Fig 5.7). This apparent contrast can be explained by the completely different behaviours in pure solutions. Whereas BTA-C_{16}-G1 forms one-dimensional aggregates with very low exchange dynamics, dBTA is not able to form stacked polymers, but assembles in small aggregates instead. In these aggregates the amid protons are not shielded against deuterium exchange. Thus, the opposite variation in the dynamics upon mixing with nBTA results from starting points at two opposite extrema.

Although the precise molecular interactions are subject of assumptions at this stage, some indications and probable explanations can be given. First, through copolymer formation with nBTA, both BTAs with dendritic head group were able to decrease exchange dynamics by exchanging dynamic hotspots in the supramolecular polymers. Second, the ultrastructure variations in copolymers can be a understood as transitions between the structures of both homopolymers. However, further computational simulations of the systems are needed to gain detailed insights into the interplay of monomers in these supramolecular copolymers.

5.3. Conclusion

In conclusion, we studied structure and properties of supramolecular BTA-based copolymers in solution. We demonstrated that image processing and statistical analysis of 2D cryo-TEM images are powerful techniques to analyse differences in supramolecular polymers at nanometre scale. In particular two copolymer systems were investigated: nBTA/dBTA and nBTA/BTA-C_{16}-G1. In the studied mixing ratios of 2:1, 1:1, 1:2, micrometre-long

one-dimensional fibres were observed as predominant morphology. We could show that at ≥50mol% of nBTA in the mixtures, the fibres exhibited at double-helix motif of two fibre strands. With increasing amount of dBTA in the mixture, the helix pitch decreased. However, a decreasing pitch length was observed with increasing amount of BTA-C_{16}-G1. Both observations can be understood as structural transition in the copolymers between the morphologies of the respective homopolymers.

By investigating and comparing dynamics of the copolymers with HDX-MS, we found that compared to pure nBTA, copolymerisation with dBTA as well as with BTA-C_{16}-G1 reduced the monomer exchange dynamics of the nBTA monomers in the supramolecular polymer. Here, the dendritic polyglycerol-based head groups in dBTA and BTA-C_{16}-G1 seem to stabilise the supramolecular polymer. The investigation of structural variations near molecular resolution in combination with investigations on dynamics and stability of supramolecular polymers addresses important questions in the field of non-covalent synthesis. The obtained findings may help in the future to tune and adjust properties of non-covalently synthesised polymers and pave the way towards future applications with different functions.

5.4. Methods and Materials

Synthesis BTA-C_{12}-EG_4 (nBTA) and BTA-C_{12}-G1 (dBTA) were synthesised according to published procedures[28] and provided by the Meijer group (Eindhoven University of Technology, The Netherlands). BTA-C_{16}-G1 was synthesised according to procedures described in chapter 4.

Sample preparation For copolymer solutions, pure stock solutions of both compounds were prepared following a standard non-covalent synthesis protocol. The desired amount of the compound was weighted into a sample vial and the respective volume of water is added. Afterwards a stir bar was added, the mixture was vortexed for 10 s, then heated to 80°C for 15 min under stirring and vortexed subsequently again for 10 s. After cooling for 5 min, the solutions were mixed in the desired ratio, followed by 10 s of vortexing, heating to 80°C for 15 min and subsequent 10 s of vortexing. The samples were left for equilibration over night at room temperature, before further experiments were conducted.

UV-VIS Ultraviolet-visible (UV-VIS) absorbance spectra were recorded on a Agilent Cary 8454 UV-VIS spectrometer at 20°C with a Julabo 200F temperature controller. The concentration of all samples was 50 μM in milliQ. Suprasil Quartz cuvettes with a pathlength of 1 cm were used.

HDX A 1:1 mixture of nBTA and BTA-C_{16}-G1 in H_2O with a concentration of 500 μM was diluted 100 times in D_2O (with 0.5 mM of NaAc). HDX-MS measurements were carried out using a XevoTM G2 QTof mass spectrometer (Waters) with a capillary voltage of 2.7 kV and a cone voltage of 80 V. The source temperature was set at 100°C, the desolvation temperature at 400°C, and the desolvation gas flow at 500 L/h. The sample solutions subjected to HDX were introduced into the mass spectrometer using a Harvard syringe pump (11 Plus, Harvard Apparatus) at a flow rate of 50 μL/min.
The obtained data points (y) over time (t) were fitted with a tri-exponential fit, using Origin 2018 and the equation $y = A \times exp(-t \times k_1) + B \times exp(-t \times k_2) + C \times exp(-t \times k_3)$, with A, B, and C giving the fractions and k_1, k_2, and k_3 giving the rate constants of the processes.

Cryogenic transmission electron microscopy (Cryo-TEM)
Cryo-sample preparation: Droplets (5 μL) of BTA solution with c = 500 μM were placed on hydrophilised holey carbon-filmed grids (Quantifoil R1/4) at room temperature. The grids were surface plasma treated just prior to use (BALTEC MED 020 device at 8.5 mA for 60 s). Vitrified films were prepared in a 'Vitrobot' (PC controlled vitrification robot, Thermo Fisher Scientific) at 22°C and a humidity of 100%. Excess sample solution was removed by blotting using two filter papers for 3-3.5 s. The thin film thus formed was shot into liquid ethane just above its freezing point.
Cryo-TEM: The vitrified samples were transferred under liquid nitrogen into a Talos Arctica 200 kV transmission electron microscope (Thermo Fisher Scientific, USA), using the microscope's autoloader protocol. Micrographs were recorded at a sample temperature of around 100 K using the microscope's low-dose protocol at a primary magnification of 28000× and an acceleration voltage of 200 kV. Image recording was done using a Falcon3EC direct electron

detector (Thermo Fisher Scientific, USA). The defocus was chosen to be between -3 μm and -6.5 μm to create sufficient phase contrast.
Measurements with phase plate: The objective aperture was replaced by a volta phase plate which was brought into the beam path instead. The phase plate was aligned using the alignment module of the microscope software. After an activation time of several minutes, the phase shift was measured and the astigmatism corrected using "AutoCTF" (Thermo Fisher). As long as the phase shift stayed close to 0.5 π, micrographs were taken with a defocus of around -300 nm. In case of significant higher or lower phase shift the position at the phase plate was changed.

Multivariate statistical analysis (MSA) From cryo-TEM images, individual motifs were extracted using the EMAN tool *boxer*.[141] The dimension, pixel size and total number of the excerpts are summarised in Tab. 5.3. Utilizing the software package IMAGIC-5[79], images were aligned with respect to one or multiple reference images, using cross-correlation techniques. The images were furthermore band-pass filtered to exclude low and high spacial frequencies, thus reducing unspecific noise. Subsequently, a mask image was generated, isolating the area of interest in the images. This mask was applied to all images and the MSA was computed. During the process, the number of considered eigenimages and resulting classes was set and refined, if needed. The values are collected in Tab. 5.3.

Table 5.3.: Number and dimensions of extracted images and chosen parameters during MSA of copolymer samples of nBTA/dBTA and nBTA/BTA-C_{16}-G1.

Copolymer mixing ratio	cut-out dimension in px	total number of excerpts	considered eigenimages for classification	number of classes
nBTA/dBTA				
2:1	128 × 128	1252	6	30
1:1	128 × 128	446	9	10
1:2	128 × 128	757	9	10
nBTA/BTA-C_{16}-G1				
2:1	128 × 128	127	3	10
1:1	128 × 128	1264	20	30
1:2	96 × 96	799	26	50

6 BTA-based amphiphiles for multivalent pathogen inhibition

This work has been performed in collaboration with Dr. Lu Su (synthesis, assembly studies; UV-VIS, CD and SLS) (Eindhoven University of Technology, The Netherlands) and Kim Silberreis (MBL complement assay) (Charité Universitätsmedizin Berlin, Germany). Dr. René Lafleur (Eindhoven University of Technology, The Netherlands) is thanked for providing cryo-TEM images of BTA-mannose.

6.1. Introduction

Multivalent carbohydrate-recognition processes are omnipresent in nature, *e.g.* during an infection process between carbohydrates at the glycocalyx of cells and lectins with specific carbohydrate-recognition domains at pathogens.[104] Furthermore, due to the supramolecular organisation of glycoconjugates at the cell surface, structural optimisation of the ligands can take place, in order to adapt to receptor geometries. Inspired by these biological processes, glyco-functionalised supramolecular architectures are promising functional materials for the interaction and inhibition of multivalent biological receptors, due to their adaptivity based on reversible interactions.[60,101] Despite the adaptivity of the inhibitor structure, also the morphology has shown to have an impact on efficient pathogen inhibition. Recently, Bhatia *et al.* showed that linear flexible polyglycerol, functionalised with sialic acid for influenza virus inhibition, had a higher inhibitory potential compared to analogously functionalised dendritic polyglycerol.[142] Therefore, the combination of both, linear and flexible, as well as a supramolecularly assembled, is believed to be highly beneficial for the design of efficient inhibitors.

BTA-based one-dimensional supramolecular polymers have been reported as suitable scaffold for biological functionalisation in different approaches, including the functionalisation with DNA, peptides, and carbohydrates.[44,47,127,143,144] Functionalisations of such supramolecular polymers with mannose were reported among others by the Brunsveld group and Besenius group. Besenius and coworkers studied functionalised supramolecular polymers for macrophage uptake, a process relevant for the development of anti-tumor vaccines. The

binding to the cells and subsequent uptake could be significantly increased through the mannose funtionalisation.[126] Brunsveld an co-workers investigated mannose-functionalised supramolecular polymers with regard to lectin and *E. coli* binding. In their studies, binding of mannosides present at the supramolecular polymer to FimH receptors at *E. coli* bacteria induced clustering and cross-linking of the bacteria. Ligand-density studies showed, that only a small percentage of functional mannoside ligands at the supramolecular polymer was enough to inhibit the binding sites at the lectin Concanavalin A (ConA) with K_D values in the micromolar range, due to the cluster glycoside effect and multivalent binding effects.[113,125] However, both systems included monomers with extended aromatic or peptide-based hydrophobic cores in order to sufficiently stabilise the supramolecular polymer. This includes high synthetic effort and the resulting polymers are comparably stiff structures.

Only recently, the synthesis of of BTAs, functionalised with alkyl chains and different monosaccharides via triazole coupling, including β-D-glucose, α-D-glucose, α-D-galactose, and α-D-mannose was reported. Here it was shown that depending on the alkyl chain length the molecules were able to assemble into one-dimensional aggregates.[47]

In this study, we investigated novel BTA-based supramolecular polymers, with alkyl chains forming the hydrophobic pocket and α-D-mannose coupled via ether linkage to the molecular. We investigated the supramolecular aggregation in one-dimensional polymers and studied the influence of a tetra(ethyleneglycol) linker next to the mannoside, as well as copolymer formation with non-glycofunctionalised BTAs. Furthermore, multivalent lectin binding to two mannose-binding lectins was investigated and a perspective is given towards multivalent pathogen inhibition.

6.2. Self-assembly of BTA-mannose and BTA-EG_4-mannose

Two mannosylated BTA molecules were investigated regarding their assembly properties in water, including their co-assembly with nBTA. Fig. 6.1 shows the structures of nBTA, BTA-mannose, and BTA-EG_4-mannose, respectively. Both mannosylated structures were synthesised and provided by Dr. Lu Su; the synthesis of both compounds will be published elsewhere.

Assembly studies of BTA-mannose and co-assembly studies with nBTA In order to study its self-assembly, BTA-mannose was tried to dissolve in water. However, the compound was not completely soluble in water, supposedly due to the relatively high hydrophobicity of the

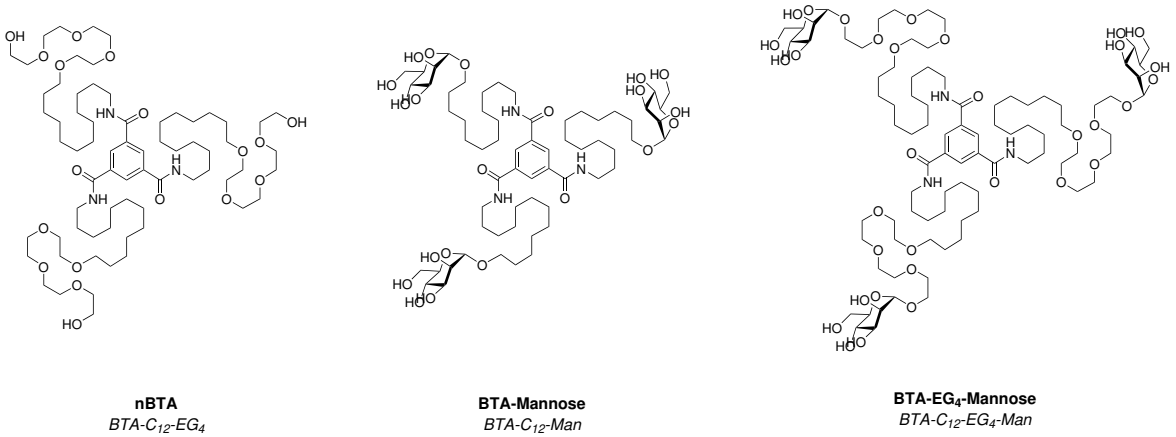

Figure 6.1.: Chemical structures of nBTA and mannosylated BTA structures BTA-mannose and BTA-EG$_4$-mannose.

compound and strong interactions between the carbohydrate moieties. It was therefore necessary to follow a non-covalent synthesis protocol, including injection and dialysis. In brief, BTA-mannose was initially dissolved in methanol. An aliquot of this solution was injected into a stirred water solution and the resulting solution was dialysed against water to remove methanol. Further details are given in the methods section of this chapter. The mixtures of BTA-mannose and nBTA were prepared by co-solvating both solid compounds in the desired ratio together with water. Subsequently, a non-covalent synthesis protocol including heating, vortexing and slow cooling was followed. By this method mixtures of BTA-mannose with 33 mol%, 50 mol%, and 67 mol% of nBTA were prepared. In the following, these mixtures are referred to as 2:1, 1:1, and 1:2 mixtures, respectively. The detailed co-assembly procedure is also part of the methods section of this chapter.

The UV-VIS spectra of nBTA shows two characteristic maxima at 211 and 225 nm. These absorbance maxima are associated with the intermolecular H-bonds of one-dimensional nBTA polymers and their conformation. The spectra of BTA-mannose and of the mixtures with nBTA also showed these two absorbance maxima as can be seen in Fig. 6.2(a), indicating a similar assembly into one-dimensional polymers and similar electronic and geometric properties of the aggregate. Static light scattering experiments (SLS) supported this assumption, as the Rayleigh ratio of BTA-mannose showed an angular dependency, similar to nBTA, as can be seen in Fig. 6.2(b). This effect is observed for anisotropic structures, such as fibre-like aggregates. In such cases, the count rate of the scattered light varies with the angle of the incoming light. However, pure BTA-mannose showed significantly higher Rayleigh ratio values, indicating the presence of larger aggregates, such as bundled fibres or structures with larger diameters.

In addition, circular dichroism (CD) experiments were conducted. Here, a positive CD effect with two maxima at 212 nm and 250 nm was observed for BTA-mannose as shown in Fig. 6.2(d), indicating that a preferred helicity is present in the formed aggregates, which might be induced by the stereocenter in α-D-mannose. Temperature-dependent UV-VIS and CD spectra were recorded for BTA-mannose [Figs. 6.2(c) and (d)] in order to analyse the temperature stability of the formed aggregates. Upon a temperature increase, UV-VIS and CD spectra remained without changes up to 70°C. Above this temperature, the intensity of the maximum at 225 nm in the UV-VIS spectrum decreased significantly and the maximum at 211 nm exhibited a blue-shift. In the CD spectra, the positive CD effect almost vanished. The observations indicated that the aggregated structures dissolved molecularly above of 70 °C.
By cryo-TEM, the aggregation into one-dimensional supramolecular polymers, in particular, micrometre-long fibres with diameters of few nanometres, could be confirmed. For pure BTA-mannose, bundled fibres were observed, as shown in Fig. 6.3(a), which corroborated the assumptions made, as high Rayleigh ratios were obtained in SLS experiments for this sample. Fig. 6.3(b) shows a micrograph, recorded from a 1:1 mixture of BTA-mannose and nBTA. Here, only single fibres and no bundles were observed.

Assembly studies of BTA-EG_4-mannose and co-assembly studies with nBTA In the next step, the assembly of BTA-EG_4-mannose in water was investigated. BTA-EG_4-mannose exhibited a better water solubility compared to BTA-mannose. Therefore, BTA-EG_4-mannose could be directly dissolved in water followed by heating, vortexing and cooling according to the assembling protocol described in the method section of this chapter. Mixtures of BTA-EG_4-mannose and nBTA were prepared by mixing aliquots of stock solutions of both compounds, following the previously described assembling protocol. The structures of nBTA and BTA-EG_4-mannose differ only in the functionalisation with α-D-mannose. However, the UV-VIS spectrum of BTA-EG_4-mannose differed significantly from the one obtained for nBTA. As can be seen in Fig. 6.4(a), only one distinct maximum could be observed at 195 nm. Thus, a different kind of aggregation compared to nBTA was supposed. The change in optical absorption is likely to result from a change in the electronic structure of BTA-EG_4-mannose assemblies compared to nBTA assemblies. This change is supposed to stem from a different assembly morphology, including conformational changes of the H-bonds.
SLS experiments corroborated the suggestion of a different aggregation behaviour of pure BTA-EG_4-mannose in water compared to nBTA. Here, no angular dependence of the scattered signal was obtained, as can be seen in Fig. 6.4(b). This effect indicated molecular

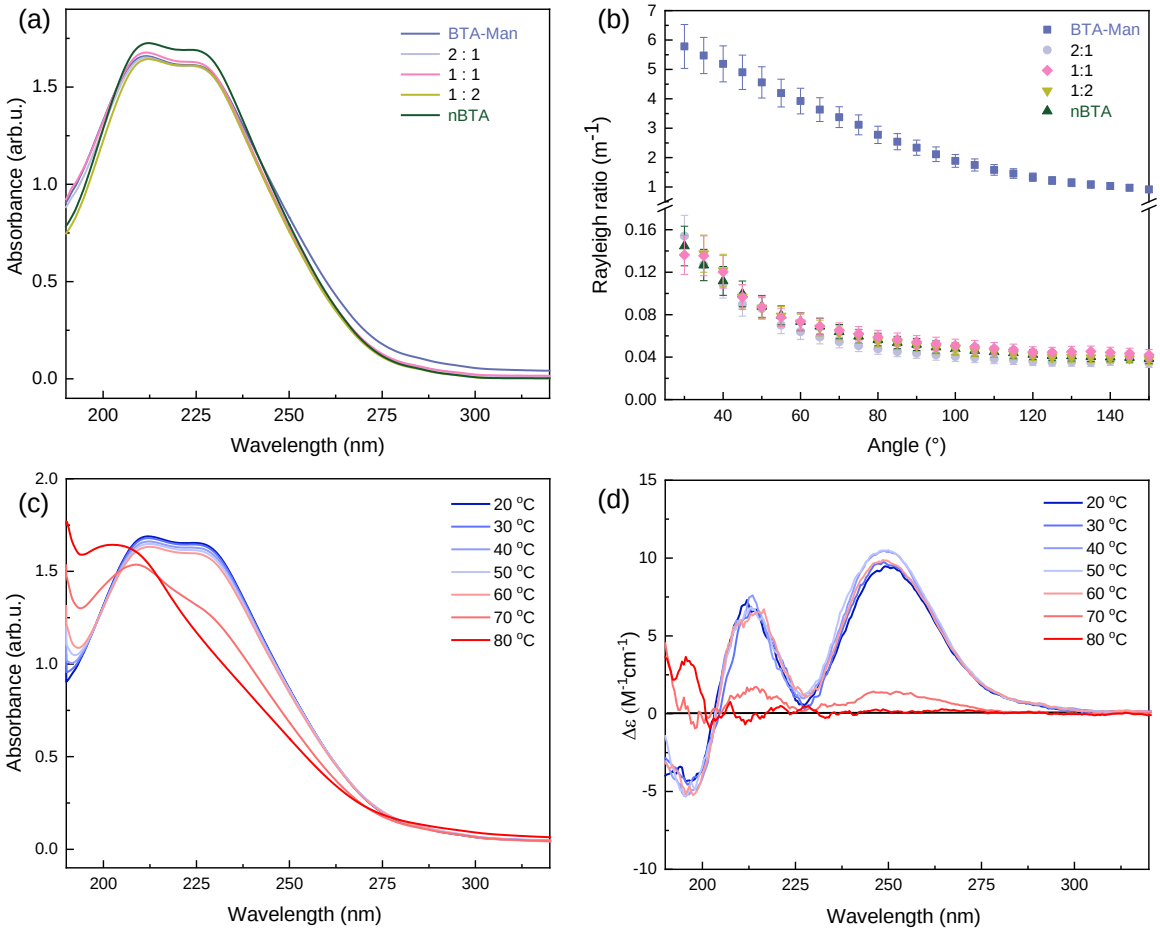

Figure 6.2.: UV-VIS (a) and SLS (b) spectra of BTA-mannose, nBTA and mixtures thereof in aqueous solution at 20 °C (c = 50 μM for UV-VIS measurements and 500 μM for SLS experiments). Two maxima at 211 and 225 nm in the UV-VIS spectra and angular dependency of the SLS data indicate fibre formation. The high Rayleigh ratio for BTA-mannose indicates aggregation in larger aggregates. Bottom row: Temperature dependent UV-VIS (c) and CD spectra (d) of BTA-Mannose in aqueous solution at 20 °C and c = 50 μM. From both cases, aggregate stability up to 70° could be inferred.

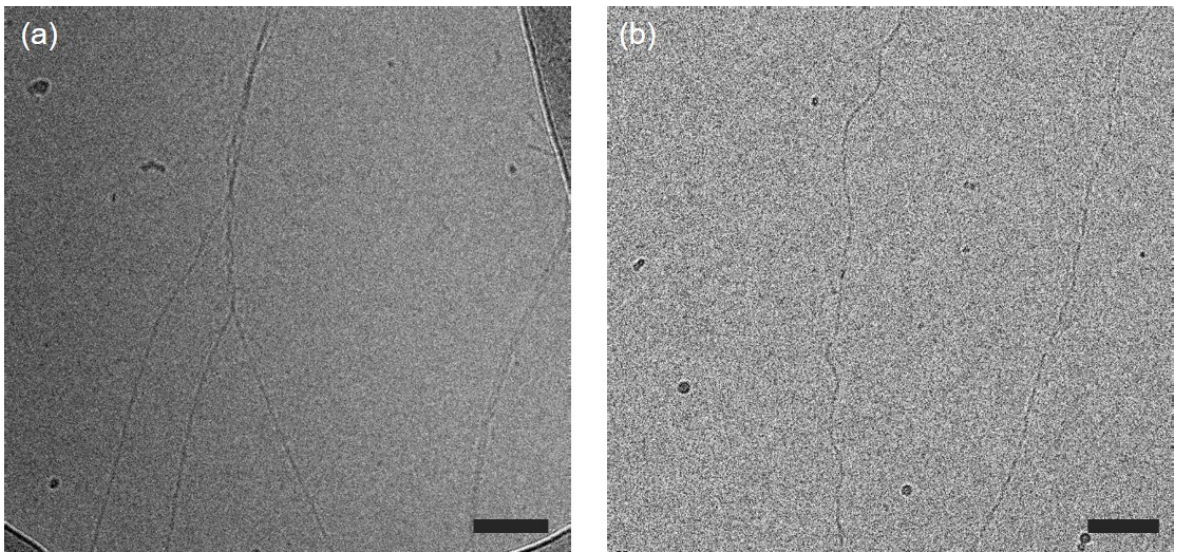

Figure 6.3.: Cryo-TEM images show bundled fibres for BTA-mannose (a) and individual fibres for a 1:1 mixture of BTA-mannose and nBTA in water (b) (c = 500 μM). Scale bars represent 100 nm.

solvation or the presence of spherical particles. For mixtures of BTA-EG_4-mannose and nBTA, UV-VIS spectra with two characteristic maxima, similar to nBTA, were observed. In addition, an angular dependence of the SLS data was observed, pointing towards anisotropic assemblies, *e.g.*, fibres.

As BTA-EG_4-mannose is a promising candidate for biological applications and was synthesised in this regard, self-assembly in buffer solutions, *i.e.*, in PBS and HEPES buffer, was also investigated. The resulting spectra in PBS are shown in Fig. 6.5(a) and those obtained from solutions in HEPES buffer in Fig. 6.5(b). The spectra of nBTA and those of mixtures of BTA-EG_4-mannose/nBTA in PBS showed a similar spectroscopic signature, although the absorbance intensity for nBTA was slightly lower. In contrast, the spectra of pure BTA-EG_4-mannose showed only one maximum. Thus, the UV absorbance characteristics resembled those obtained in milliQ, which indicated a similar aggregation behaviour.
In HEPES buffer, a variety of mixing ratios were investigated from 9 mol% to 91 mol% of BTA-EG_4-mannose. The spectroscopic signature was varied compared to spectra obtained of solutions in water, however, absorbance in the same spectral region was observed. Mixtures up to 50 mol% BTA-EG_4-mannose showed the same curve as pure nBTA, indicating a similar type of aggregation. With higher ratios of BTA-EG_4-mannose, the intensity decreased and one peak at 217 nm became more distinct, suggesting a change in the aggregation behaviour. Taken together, the measurements indicated that BTA-EG_4-mannose, nBTA and mixtures

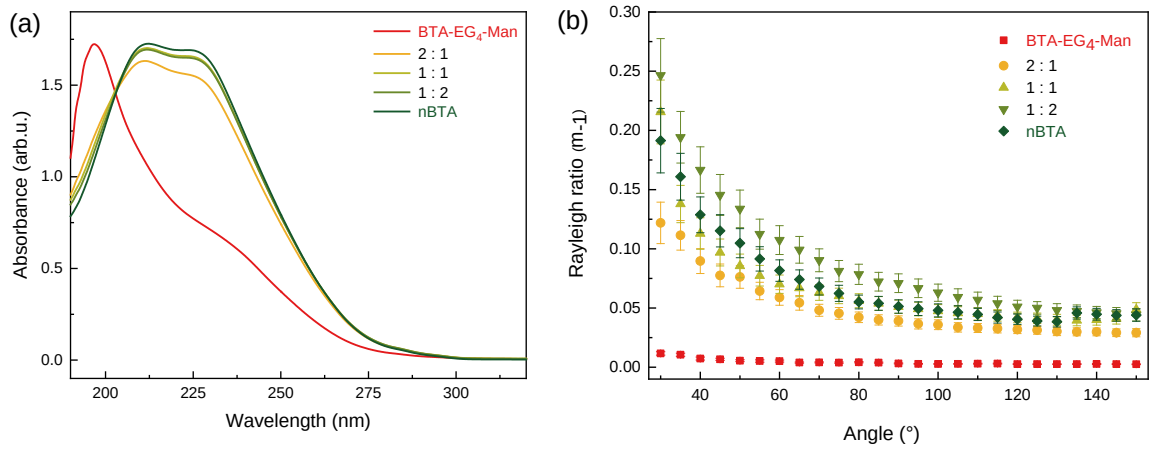

Figure 6.4.: UV-VIS (a) and SLS (b) spectra of BTA-EG$_4$-mannose, nBTA and mixtures thereof in aqueous solution at 20°C (c = 50 μM for UV-VIS measurements and 500 μM for SLS experiments). Scattering data of co-assemblies with nBTA indicate the presence of anisotropic aggregates. Scattering data for pure BTA-EG$_4$-mannose point towards molecular solvation or the presence of small spherical aggregates.

of both also aggregated in buffer solutions into one-dimensional polymers. Therefore, we applied the solutions in biological assays (*vide infra*).

Cryo-TEM of solutions in water confirmed the presumptions about the morphologies of the assemblies. For BTA-EG$_4$-mannose spherical micelles with diameters of around 10 nm were observed, as can be seen in Fig. 6.6(a). In contrast, in mixtures of BTA-EG$_4$-mannose and nBTA in ratios of 5:1, 2:1, and 1:1, micrometre long fibres with diameters of around 6-8 nm were observed as predominant morphology. Representative images are shown in Figs. 6.6(b), (c), and (d). At first sight, the observed fibres look similar. However, for copolymer solutions with 83 mol%, 67 mol% and 50 mol%, which are equal to mixing ratios of 5:1, 2:1, and 1:1, respectively, we analysed the obtained images in detail. Therefore, excerpts with individual fibres were generated. By image alignment and multivariate statistical analysis, we analysed if one or more characteristic structural motifs in the fibres were present. Such a structural motif at nanometre scale is referred to as ultrastructure in the following.

In chapter 4, we were able to show that in nBTA two fibre strands assemble in a double-helix motif with a repeating unit of (19.9±0.4) nm. The repeating unit is determined from the knot-to-knot distance in averaged projection images, hence, it reflects the half of one helix pitch. In a 1:1 mixture of BTA-EG$_4$-mannose and nBTA such a double-helix motif was also obtained as characteristic ultrastructure, as shown in Fig. 6.7(c). However, the according knot-to-knot distance was found to be slightly shorter, *i.e.*, (18.3±0.4) nm. The diameter at the widest part was (6.3±0.4) nm. As the helix pitch was varied compared to nBTA as-

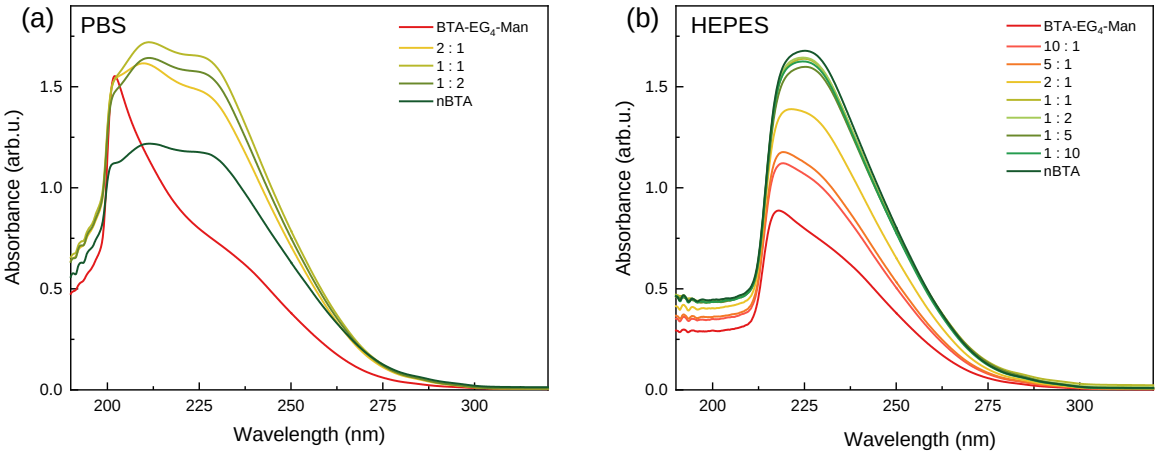

Figure 6.5.: UV-VIS spectra of BTA-EG_4-mannose and mixtures with nBTA in buffer solutions at 20°C and c = 50 μM: (a) PBS (b) HEPES buffer. Spectra in both buffer solutions resemble those obtained from solutions in water, indicating the assembly in similar structures.

semblies, we assume that both compounds successfully co-assembled into a supramolecular copolymer and that mannose is present in the fibre structure.

For the 5:1 mixtures, only one fibre strand with a diameter of around (6.3±0.4) nm could be observed in the processed image, after image alignment and averaging [Fig. 6.7(a)]. Interestingly, a density and thickness undulation with a recurring length of (8.3±0.4) nm was observed. Thus, the structure is neither a plain single fibre nor a double-helix. The same effect was observed for the 2:1 mixture, as shown in a class sum image in Fig. 6.7(b). However, the origin of thickness undulations could not be further investigated at that point by the methods applied.

In sum, we could show that BTA-EG_4-mannose forms small, spherical micelles in aqueous solution, but co-assembles with nBTA in nanofibres in all investigated mixing ratios. Interesting differences were found in the ultrastructure of the fibres. The 1:1 mixture assembled in a double-helix motif, which is also characteristic for pure nBTA. In contrast, for mixtures with 83 mol% and 67 mol% BTA-EG_4-mannose (5:1, 2:1), single strands with a repeating thickness undulation were observed. However, the origin of these undulations are not yet revealed. As structure and function are generally closely connected, these findings are valuable information when it comes to the investigation of the biological function of supramolecular assemblies.

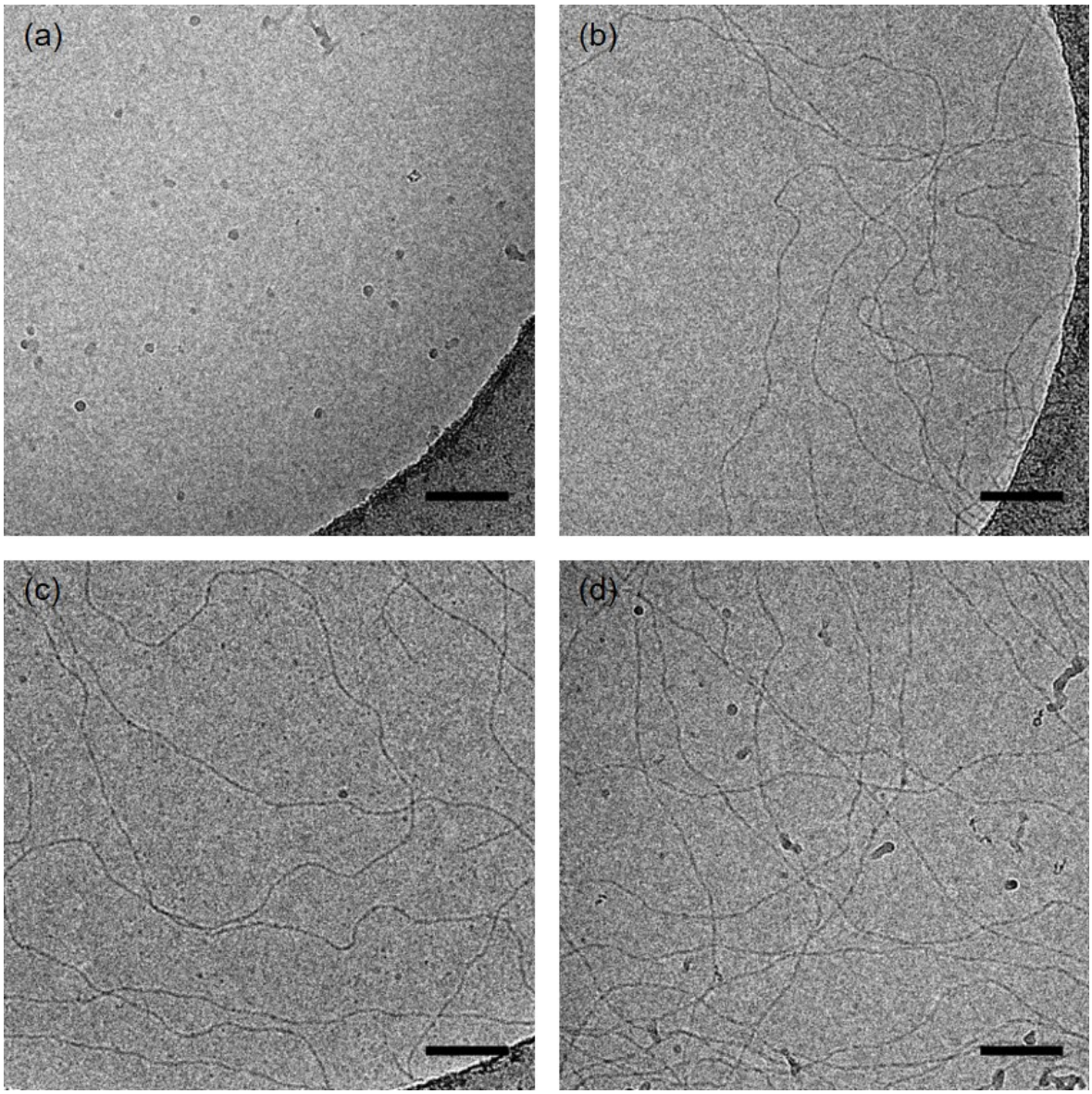

Figure 6.6.: Cryo-TEM images for BTA-EG_4-mannose and mixtures with nBTA in water (c = 500 μM). For pure BTA-EG_4-mannose (a), spherical micelles with diameters around 10 nm were observed. In contrast, fibres were observed for BTA-EG_4-mannose/nBTA mixtures in ratios of (b) 2:1, (c) 1:1, and (d) 1:2. Scale bars represent 100 nm.

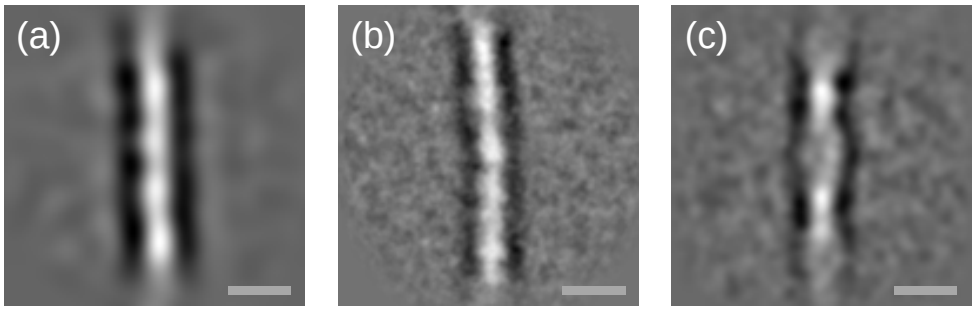

Figure 6.7.: (a) Sum image of aligned images of BTA-EG_4-mannose and nBTA copolymers in a ratio of 5:1, showing a single fibre strand with density undulation. (b)-(c) Class sum image after MSA of BTA-EG_4-mannose/nBTA copolymers in mixtures of 2:1 (b) and 1:1 (c), showing the transition from a straight fibre strand to a double-helix motif in the ultrastructure of the aggregates.

6.3. Biological function

In the last section, aggregation studies for two new mannose-functionalised BTA molecules were reported. In this section, their biological function in terms of lectin binding will be covered. Furthermore, an outlook towards bacteria interaction will be given.

6.3.1. Ligand binding

MBL Complement Assay In a first assay, the binding capability of mannosides in BTA-mannose and BTA-EG_4-mannose polymers was compared. Therefore, a complement pathway assay with mannose-binding lectin (MBL) was used. The activation of complement is one of the first actions in the innate immune defense.[145] In the lectin pathway, MBL (among other lectins) binds to carbohydrates on pathogens or damaged cells. By this action, a cascade reaction is started. If mannosylated synthetic compounds bind to MBL, the lectin is no longer able to activate the complement cascade, thus, a decreased activity signal is obtained in the resulting data, compared to the negative controls. We tested BTA-mannose and BTA-EG_4-mannose, both in co-assemblies with nBTA in mixing ratios of 1:2 and 2:1. Pure nBTA served as negative control, and Methyl-α-D-mannose (Me-Man) was included in the assay as monomeric comparison.

As expected, pure nBTA showed no significant effect in the assay, proofing that nBTA monomers, which are also present in the copolymers, do not influence the binding. Moreover, also Me-Man did not show any significant inhibition of the complement cascade in the investi-

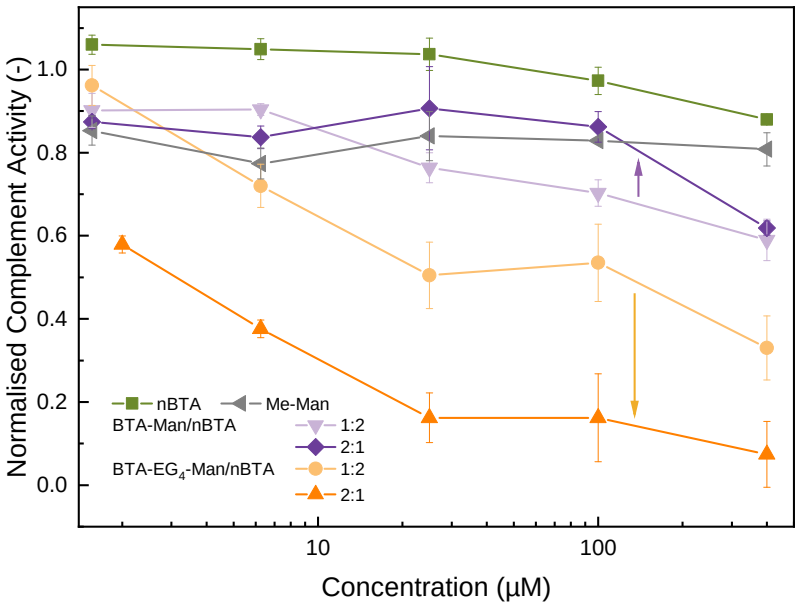

Figure 6.8.: Complement activity of MBL as a function of inhibitor concentration. Two mannosylated BTA-copolymers with different linker lengths were investigated, *i.e.*, BTA-mannose and BTA-EG_4-mannose, in two mixing ratios with nBTA. Pure nBTA and Methyl-α-D-mannose (Me-Man) were included as comparing controls. Solid lines are guide to the eye.

gated concentration range up to 400 μM. Also BTA-mannose/nBTA copolymers showed only a slight inhibitory effect, whereas unexpectedly, copolymers with 33 mol% BTA-mannose showed an higher inhibition than those with 66 mol% above a concentration of 10 μM, although less mannosides were present in the mixture.

Intriguingly, a remarkable difference between BTA-mannose and BTA-EG_4-mannose in terms of their binding to MBL was observed. Copolymers of BTA-EG_4-mannose/nBTA showed a significantly higher inhibition of the complement activity, than copolymers of BTA-mannose/nBTA, in both mixing ratios. Both mannosylated compounds differ in the presence of a tetra(ethyleneglycol) (TEG) linker, inducing a larger cross section of the monomer (*cf.* Fig. 6.1). In copolymers of nBTA and BTA-EG_4-mannose, the mannosides of BTA-EG_4-mannose were therefore thought to be present at the surface of the copolymer due to larger cross-section of the monomer. Thus, the mannosides were accessible for MBL and maintained their function. For BTA-mannose, however, the mannosides might be hidden between the TEG chains of nBTA and, hence, were not able to bind to MBL. As a result, we focused on the further investigation of BTA-EG_4-mannose and its function in the following studies.

In the next step, IC_{50} values for different mixing ratios of BTA-EG_4-mannose and nBTA were determined and are listed in Table 6.1. IC_{50} values mark the concentration at which an

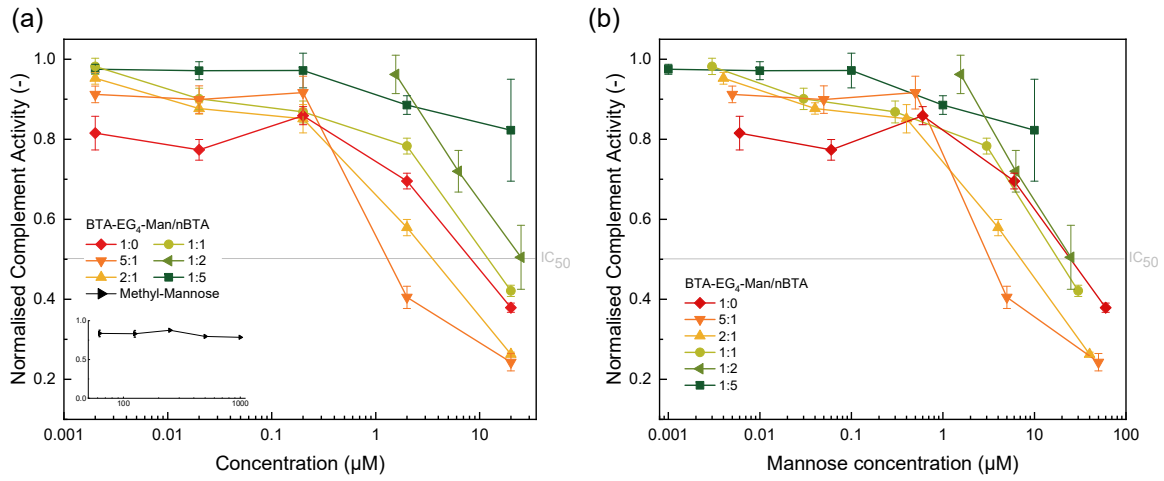

Figure 6.9.: Complement activity of MBL as a function of inhibitor concentration, *i.e.*, mannosylated BTA assemblies in different mixing ratios. Data were normalised with regard to an untreated solution. (a) Data depicted as function of the overall inhibitor concentration, (b) as function of the mannose concentration in the solutions. Crossings of the grey line indicate the IC_{50} value of each compound, showing inhibition in the low micromolar concentration range. Inset in (a) shows data for Methyl-Mannose in an extended concentration range. Connecting lines are guide to the eye.

inhibition of 50% compared to negative controls is achieved. As expected, decreasing IC_{50} values were obtained with increasing BTA-mannose concentration in the copolymers from 1:2 to 5:1. Here, IC_{50} values in the low micromolar range between 25 and 1.7 μM were determined. For the mixing ratio of 1:5 with only 17 mol% BTA-EG_4-mannose an IC_{50} value $\geq$ 20 μM has to be assumed, as an inhibition of more than 50% was not reached in the measured concentration range.

Strikingly, pure BTA-EG_4-mannose (spherical micelles) exhibited an IC_{50} value of 13 μM, which lies between the values of 1:1 (16 μM) and 2:1 (7 μM) copolymers (fibres). This result indicated that the assembly in one-dimensional fibrous structures is advantageous for lectin binding. MBL is a tetrameric lectin in its active form, which means that four binding sites are present for one lectin complex. In order to inhibit all binding sites, a linear, flexible architecture is considered to be beneficial, as one fibre would be able to bind to several binding sites. In case of a globular structure, four inhibitors would be needed to achieve the same effect. Although the overall concentration of mannosides in copolymers with nBTA is less compared to pure BTA-EG_4-mannose, more mannosides might be exposed to the surrounding, thus, being able to bind. This effect became even more pronounced, when the data were specifically analysed with regards to the mannose concentration in the mixture, instead of

Table 6.1.: IC_{50} values obtained from a MBL complement assay for copolymers of BTA-EG_4-mannose and nBTA.

ratio BTA-EG_4-mannose/nBTA	1:2	1:1	2:1	5:1	1:0
BTA-EG_4-mannose (mol%)	33	55	67	89	100
IC_{50} (μM) (overall concentration)	25	16	7	2	13
IC_{50} (μM) (mannose concentration)	25	14	13	4	39

the overall compound concentration. Here, the IC_{50} value of pure BTA-EG_4-mannose is by a factor of 10 worse than the most effective copolymer with 83 mol% BTA-EG_4-mannose. Moreover, copolymers with only 33 mol% BTA-EG_4-mannose are still by a factor of 1.5 more effective in terms of MBL inhibition.

Summarised, we could show that the linker design in functional supramolecular copolymers is an important factor in order to ensure the availability of functional groups as binding partners to receptor units. Furthermore, the assembly of mannosylated BTAs in fibres, instead of spherical micelles, increased the inhibition efficiency, *i.e.*, a lower mannose concentration was needed to achieve the same inhibition effect in this assay. In this line, also subtle differences in the ultrastructure might have an impact on the binding efficiency. As discussed above, the ultrastructure of the copolymers changed from structured single-fibres to double-helices between mixing ratios of 1:1 and 2:1. Here, further investigations combined with simulations will be needed in the future to elucidate the resulting effects on flexibility and ligand accessibility of aggregates.

Interaction with ConA In a next assay, turbidity measurements with ConA were carried out. ConA is a plant-lectin, obtained from jack bean, tetrametric at pH 7.4, and exhibits one specific binding site for α-D-mannose per unit.[104] Structures that bear a large number of mannosides, such as multivalently functionalised polymers, cross-link through the binding to ConA in solution. In turbidimetric measurements, the absorbance at one wavelength is monitored over time as measure for agglutination and induced turbidity, which occur upon binding and cross-linking of lectin and substrates.

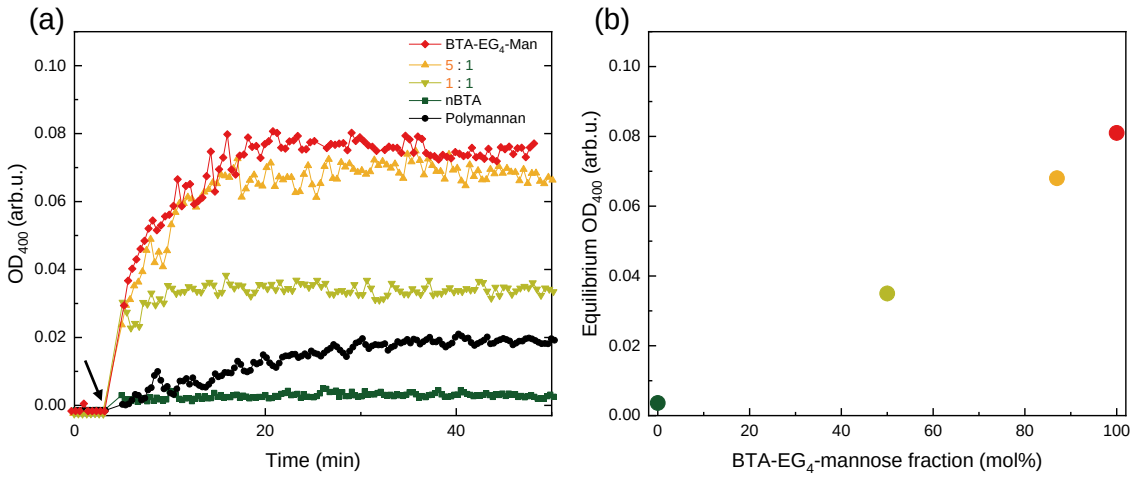

Figure 6.10.: (a) Absorbance at λ= 400 nm (OD_{400}) measured as a function of time. Agglutination of ConA with copolymers of BTA-EG_4-mannose and nBTA in different mixing ratios. $c_{BTA} = 4\,\mu$M, $c_{ConA} = 0.1$ mg/mL. The black arrow marks the time point of ConA addition. (b) Equilibrium absorbance as a function of molar ratio of BTA-EG_4-mannose, determined by linear fitting of the respective data between t = 20 min and 50 min.

In this assay, BTA-EG_4-mannose and BTA-EG_4-mannose/nBTA copolymers with ratios of 5:1 and 1:1 were studied. nBTA was added as negative control without biologically active functional groups and, as expected, no turbidity was induced after 45 min. In contrast, for all mannosylated BTA polymers, an increased turbidity upon addition of ConA to the respective solutions was observed, as shown in Fig. 6.10(a). Polymannan, a highly mannosylated natural polysaccharid, was added as further comparison in the same weight-based concentration as pure BTA-EG_4-mannose. However, only a slow and faint increase of absorbance was observed compared to BTA-EG_4-mannose. For BTA-EG_4-mannose, a significantly higher absorbance was observed, indicating a higher (weight-based) binding affinity towards ConA. In the previous MBL assay, pure BTA-EG_4-mannose showed inferior lectin binding compared to copolymers with nBTA. This effect was attributed to the different assembly geometries. In this assay, however, an almost linear dependency between turbidity and BTA-EG_4-mannose concentration in homo- and copolymers was obtained as depicted in Fig. 6.10(b). These results are seemingly contradictory, however, they can be explained by the different assay set-ups. In the MBL assay, a flexible, linear morphology was apparently advantageous, as a multivalently functionalised polymer can bind multivalently to the same lectin complex in order to shield all binding sites of MBL. In contrast, turbidity in the ConA assay is induced by intermolecular cross-linking. Thus, also globular inhibitors with a high number of binding sites might be as effective as linear inhibitors. An additional effect by possible network

formation of fibres was not observed in this case. As an outlook, experiments with different concentrations of ConA might provide further insights into differences between inhibitor geometries and ligand concentration.

Both assays showed that mannosylated BTA structures can be applied as efficient lectin inhibitors. This was shown by experiments with MBL and ConA. In both cases, mannosylated BTA polymers exhibited a more efficient binding than monomeric mannosides or the polysaccharide Polymannan. Furthermore, the MBL assay indicated that an assembly in fibrous structures is advantageous for the binding efficiency. However, these effects highly depend on the assay set-up, as OD400 measurements showed.

6.3.2. Perspective - Towards multivalent pathogen binding with BTA polymers

A major goal of this project is the inhibition of interactions between mannosylated BTA polymers and *E. coli* bacteria. *E. coli* bacteria bind via filamentous protein assemblies, *i.e.*, type 1 pili, to endothelial cells. In particular, the outermost protein FimH has a carbohydrate recognition domain (CRD) specific for α-D-mannose, which is present at the glycocalyx of endothelial cells.[146] Between mannosides at the cell surface and FimH, sheer-force dependent catch-bonds are formed.[147] Via this mechanism, *e.g.*, uropathogenic *E. coli* bacteria bind to bladder epithelial cells, causing bladder infections after subsequent invasion into the epithelial cell.[148]

By interaction of FimH with mannosylated synthetic compounds, an inhibition of the CRDs can be achieved, thus, preventing the bacteria from binding to cells. Moreover, detaching bacteria from cells, after binding has already occurred, is possible. In this anti-adhesive approach, the binding affinity of mannose-functionalised compounds has to be higher than the affinity to the glycocalyx of endothelial cells. Multivalently functionalised compounds and aggregates have been shown to be potent inhibitors in this regard. We hypothesise that highly flexible, dynamic and one-dimensionally assembled BTA-based supramolecular polymers are particularly suitable. In these assemblies, both, the geometry and position of functional groups along the structure are adjustable and adaptive towards different target structures, especially compared to covalently bound or stiff structures.

In a first experiment, we incubated BTA-EG_4-mannose (as 5:1 copolymer with nBTA) with *E. coli* in solution and investigated the mixture via cryo-TEM. With this experiment, we aimed for the visualisation of co-localisation between bacteria and BTA polymers. We experienced that the differentiation between pili and BTA fibres is not trivial as both structures exhibit diameters in the same size range of around 8 nm. However, pili are rather stiff structures and

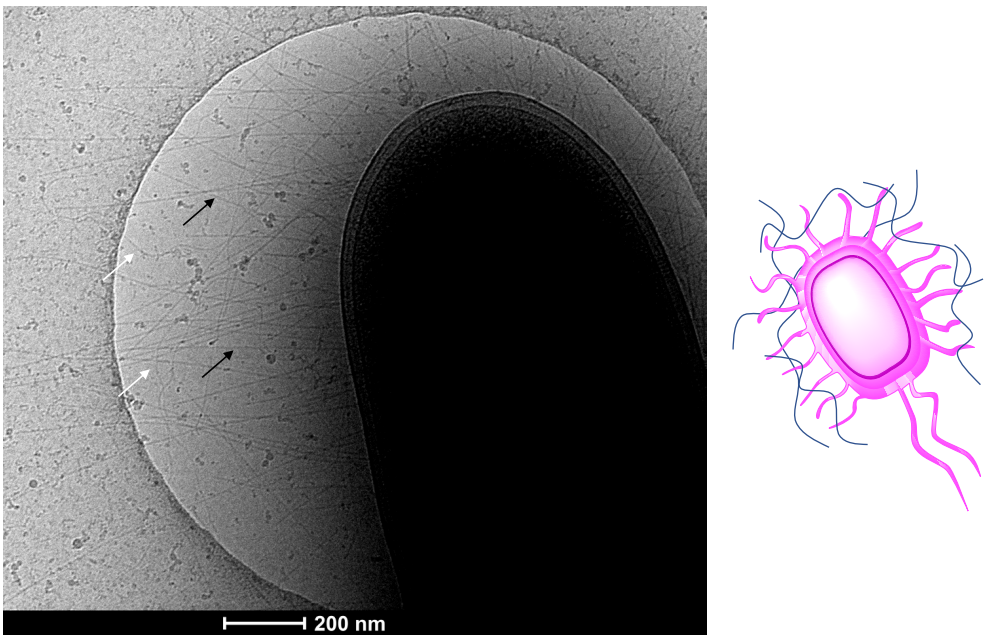

Figure 6.11.: Left: Cryo-TEM of *E. coli* (ORN178) and BTA-EG_4-mannose/nBTA 5:1 copolymers in HEPES buffer. Black arrows point at pili of the bacterium. White arrows point at BTA nanofibres. Both structures were found closely located to each other indicating interactions between ligands and receptors. Right: Schematic depiction of interaction between *E. coli* (pink) and polymer fibres (blue).

are perpendicularly oriented to the bacterium membrane, whereas BTA polymers are highly flexible, which helped us to discriminate both structures. As can be seen in Fig. 6.11, BTA fibres and pili were found in close proximity to each other. Although being just preliminary and qualitative, these results indicate that mannosylated BTA polymers interact with *E. coli* and should be further investigated in terms of bacteria interaction and inhibition. We are confident that future *in vitro* experiments will provide further insights in this regard.

The effect of local concentration of ligands plays a key role in the concept of multivalency. Thus, we aim for the optimisation of mannosylated BTA molecules such that more than one functional mannoside group is present per BTA arm. In Fig. 6.12 target structures with two and four mannosides per BTA arm are depicted. The respective unfunctionalised molecules with terminal hydroxyl groups were synthesised in the framework of the present work, as described in chapter 4. These structures will serve as precursors for the target molecules presented here. In particular, BTA-C_{12}-GO and BTA-C_{16}-G0 are promising candidates, as they exhibited only little water solubility, which will be drastically increased by the functionalisation with six mannosides per molecule. First test reactions showed promising results in

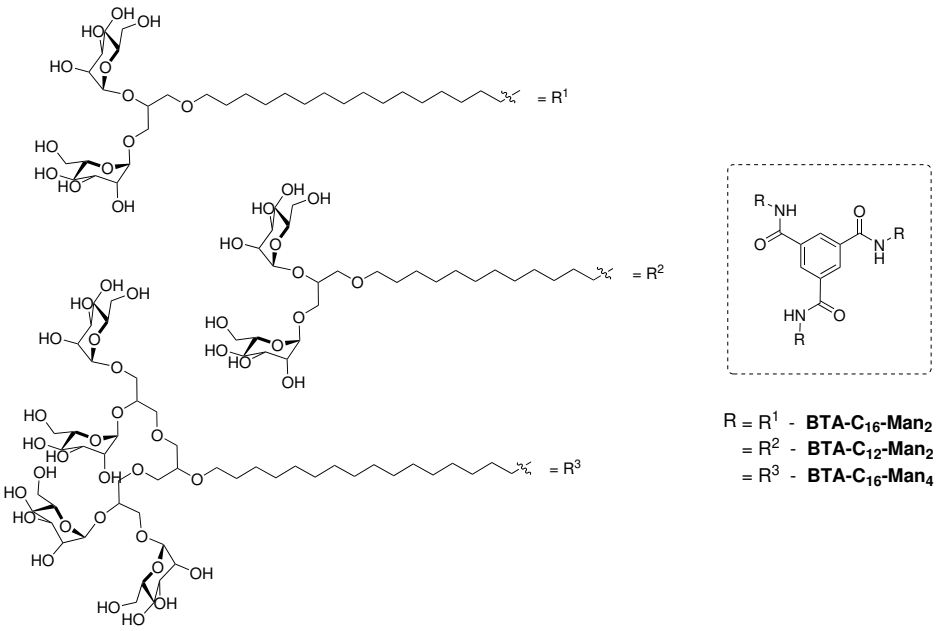

Figure 6.12.: Chemical structures of multivalently functionalised BTA molecules as target compounds for future projects.

terms of functionalisation and the synthesis will be completed in the near future in order to start with assembly studies and assays on their functionality.

6.4. Conclusions

In conclusion, the successful supramolecular polymerisation of mannose-functionalised BTA structures, including their applicability for mannose-specific lectin binding, was shown. We investigated two slightly different mannosylated BTAs, *i.e.*, BTA-mannose and BTA-EG_4-mannose, which differed in the presence of a tetra(ethyleneglycol) linker (EG_4) between hydrophobic alkyl chain and mannose. Self-assembly studies in water using UV-VIS, SLS, and cryo-TEM showed that BTA-EG_4-mannose forms small spherical micelles, whereas BTA-mannose assembles into one-dimensional fibrous aggregates. Due to the strong inter-carbohydrate interactions, a nanoprecipitation assembly protocol had to be followed in order to dissolve BTA-mannose in water. By co-assembling the structures with nBTA, we were able to obtain one-dimensional copolymers in all cases. A MBL complement assay revealed that the mannosides in BTA-mannose/nBTA copolymers were not able to bind to mannose-specific receptors and were therefore assumed to be trapped between the EG_4-chains of nBTA. In contrast, copolymers of BTA-EG_4-mannose and nBTA showed successful binding to MBL and were able to inhibit the complement activity with IC_{50} values in the low micromolecular

range. In addition, we showed successful binding to ConA by turbidity measurements. The influence of aggregate morphologies was shown by the comparison of both lectin assays, as the binding to ConA was only dependent on the overall mannose concentration, whereas in the complement assay, one-dimensional structures showed superior binding properties in comparison to spherical micelles. This effect underlined the importance of structural optimisations in view of desired functions. In this regard, we revealed by cryo-TEM image analysis structural differences in the copolymers at nanometre scale. Double-helix ultrastructures, as observed for pure nBTA, were found for BTA-EG_4-mannose/nBTA copolymers. However, from 67 mol% of BTA-EG_4-mannose in the copolymer, single fibre strands with a further density and thickness undulation were revealed. These interesting findings will help towards the design of sophisticated carbohydrate-functionalised supramolecular polymers for various applications. Moreover, an outlook towards pathogen inhibition and further multivalent functionalisation was given, which will be realised and investigated in the near future.

6.5. Methods and Materials

Synthesis BTA-C_{12}-EG_4 (nBTA) was synthesised according to published procedures[45] and provided by the Meijer group (Eindhoven University of Technology, The Netherlands). BTA-mannose and BTA-EG_4-mannose were synthesised by Dr. Lu Su (Eindhoven University of Technology, The Netherlands). The synthesis will be published elsewhere.

Sample preparation

Non-covalent synthesis protocol 1: Heating/Cooling

The desired amount of the compound was weighted into a sample vial and the respective volume of water was added. Afterwards a stir bar was added, the mixture was vortexed for 10 s, then heated to 80°C for 15 min under stirring and vortexed subsequently again for 10 s. The samples were left for equilibration over night at room temperature, before further experiments were conducted.

For copolymer solutions, pure stock solutions of both compounds were prepared according to the protocol described above. After cooling for 5 min, the stock solutions were mixed in the desired ratio, followed by 10 s of vortexing, heating to 80°C for 15 min and subsequent 10 s of vortexing. The samples were left for equilibration over night at room temperature, before further experiments were conducted.

For samples in buffer solution, stock solutions in milliQ were prepared, which were subsequently diluted in buffer until the desired concentration.

Non-covalent synthesis protocol 2: Nanoprecipitation/Dialysis A stock solution of BTA-Man was prepared in methanol (c = 10 mM). An aliquot of this solution was injected into a stirred milliQ solution with a known volume. The solution was stirred for additional 30 min, before being left equilibrating at r.t. over night. The solution was then dialysed for 2 days against water (MWCO = 1 kDa) in order to remove methanol. The resulting concentration was determined according to the total volume of the solution after dialysis.

UV-VIS UV-VIS data were recorded on a Jasco V-650 UV-VIS spectrometer with a Jasco ETCT-762 temperature controller. The concentration of all samples was 50 μM in milliQ, PBS, or HEPES buffer. Suprasil Quartz cuvettes with an optical path length of 1 cm were used.

Static light scattering Experiments were conducted on an ALV/CGS-3 MD-4 compact goniometer system, equipped with a multiple tau digital real time correlator (ALV-7004) and a solid state laser (λ = 532 nm; 40 mW). Scattering intensities were detected over an angular range of 30° to 150° in steps of 5°. Four runs of 10 seconds per angle were averaged. BTA samples were prepared in water at a concentration of 500 μM and were measured in light scattering tubes with an outer diameter of 1 cm. As a reference, samples of only water and only toluene were measured. Water was filtered with 0.2 μm syringe filters (Supor membrane, PALL Corporation) and toluene with a 0.2 μm syringe filter (PTFE membrane, Whatman). The measurements were analysed with AfterALV (1.0d, Dullware) to remove measurements showing obvious scattering from dust. The Rayleigh ratio as a function of the angle was determined, using the following equation

$$R_\theta = \frac{I_{sample} - I_{water}}{I_{toluene}} \times R_{toluene} \times \frac{n^2_{water}}{n^2_{toluene}},$$

With I_{sample}, I_{water}, and $I_{toluene}$ for the count rate of the sample solution, of water, and for toluene, respectively. $R_{toluene}$ is the known Rayleigh ratio of toluene (2.1×10^{-5} m^{-1} at

532 nm), n_{water} is the refractive index of the solvent (1.33) and $n_{toluene}$ is the refractive index of toluene (1.49).

Cryogenic transmission electron microscopy (Cryo-TEM)
Cryo-sample preparation: Droplets (5 μL) of BTA solution with c = 500μM were placed on hydrophilised holey carbon-filmed grids (Quantifoil R1/4) at room temperature. The grids were surface plasma treated just prior to use (BALTEC MED 020 device at 8.5 mA for 60 s). Vitrified films were prepared in a 'Vitrobot' (PC controlled vitrification robot, Thermo Fisher Scientific) at 22°C and a humidity of 100%. Excess sample solution was removed by blotting using two filter papers for 3-3.5 s. The thin film thus formed was shot into liquid ethane just above its freezing point.
Cryo-TEM: The vitrified samples were transferred under liquid nitrogen into a Talos Arctica 200 kV transmission electron microscope (Thermo Fisher Scientific, USA), using the microscope's autoloader protocol. Micrographs were recorded at a sample temperature of around 100 K using the microscope's low-dose protocol at a primary magnification of 28000× and an acceleration voltage of 200 kV. Image recording was done using a Falcon3EC direct electron detector (Thermo Fisher Scientific, USA). The defocus was chosen to be between -3 μm and -6.5 μm to create sufficient phase contrast.
Cryo-TEM with E. coli E. coli bacteria (ORN178) were grown in medium until $OD_{600} = 1$ of the solution was reached. A 500 μM stock solution of the respective BTA mixture in water was prepared. 10 μL bacteria solution, 50 μL BTA solution and 40 μL HEPES buffer (pH 7.4, 20 mM HEPES, 1 mM $CaCl_2$, 1 mM $MnCl_2$, 150 mM NaCl) were mixed. Subsequently, cryo-TEM grids were prepared according to the protocol described above.
Measurements with phase plate: The objective aperture was replaced by a volta phase plate which was brought into the beam path instead. The phase plate was aligned using the alignment module of the microscope software. After an activation time of several minutes, the phase shift was measured and the astigmatism corrected using "AutoCTF" (Thermo Fisher). As long as the phase shift stayed close to 0.5 π, micrographs were taken with a defocus of around -300 nm. In case of significant higher or lower phase shift the position at the phase plate was changed.
Cryo-TEM of BTA-Man and BTA-Man/nBTA: Cryogenic transmission electron microscopy (cryo-TEM) was performed on samples with a concentration of 250 μM (BTA-Man) or 500 μM (BTA-Man/nBTA 1:1). Vitrified films were prepared in a 'Vitrobot' instrument (Mark III, PC controlled vitrification robot, Thermo Fisher Scientific) at 22°C and at a relative humidity of 100%. In the preparation chamber of the 'Vitrobot' a 3 μL sample was applied on a Lacey film (LC200-CU, Electron Microscopy Sciences). These films were surface plasma treated just prior to use (Cressington 208 carbon coater operating at 5 mA for 40 s). Excess sample was removed by blotting using filter paper for 3 seconds and the thin film thus formed was shot (acceleration about 3 g) into liquid ethane just above its freezing point. Vitrified films were transferred into the vacuum of a CryoTITAN equipped with a field emission gun that was operated at 300 kV, a post-column Gatan energy filter, and a 2048 x 2048 Gatan CCD camera. Microscopy images were taken at low dose conditions, at 24000× magnification and at focus values of 10 μm or 15 μm.

Multivariate statistical analysis (MSA) From cryo-TEM images, individual motifs were extracted using the EMAN tool *boxer*.[141] The dimension, pixel size and total number of the excerpts are summarised in Tab. 6.2. Utilising the software package IMAGIC-5[79], images were aligned with respect to one or multiple reference images, using cross-correlation techniques. The images were furthermore band-pass filtered to exclude low and high spacial frequencies, thus reducing unspecific noise. Subsequently, a mask image was generated, isolat-

ing the area of interest in the images. This mask was applied to all images and the MSA was computed. During the process, the number of considered eigenimages and resulting classes was set and refined, if needed. The values are collected in Tab.6.2.

Table 6.2.: Number and dimensions of extracted images and chosen parameters during MSA of copolymer samples of BTA-EG_4-mannose/nBTA.

BTA-EG_4-mannose/ nBTA ratio	cut-out dimension in px	total number of excerpts	considered eigenimages for classification	number of classes
5:1	128 × 128	950	-	-
2:1	128 × 128	1014	7	20
1:1	128 × 128	596	2	20

MBL Complement assay The complement activity was tested by using the WIESLAB complement system MBL pathway kit (Euro Diagnostica) according to published procedures.[145] Briefly, human serum was diluted 1:101 with diluent CP and treated, if applicable, with different final concentrations of BTA (co-)polymers, mannan (Sigma-Aldrich), and Methyl-α-D-mannose (Me-Man) (Sigma-Aldrich). After a 5 min preincubation step at room temperature, the samples were distributed into the respective manufacturer's well plate and were again incubated (1 h, 37°C). Subsequently, the wells were washed three times with the washing buffer and refilled with 100 μL of antibody-enzyme conjugate solution. Another incubation step (30 min, 20-25°C) was followed by a second washing step as described before. Finally, 100 μL of the substrate solution was added and incubated for 30 min at room temperature before the well absorbance at 405 nm was measured on a microplate reader (Tecan). The untreated serum was set to 100% activity, and the potency of the inhibitor concentrations was calculated. The concentration, where the complement activity was reduced by 50%, was identified as the IC_{50} value.

OD400 Measurements The aggregation of BTA polymers and ConA (Sigma-Aldrich) were analysed by optical density measurements at $\lambda = 400$ nm (OD_{400}) using a Cary 50 Bio Photospectrometer (Varian), equipped with a Xenon lamp. Samples were measured in disposable PMMA cuvettes with an optical path length of 1 cm. 1 mL of a 4 μM BTA solution in HEPES buffer (pH 7.4, 20 mM HEPES, 1 mM $CaCl_2$, 1 mM $MnCl_2$, 150 mM NaCl) was put in a cuvette. The measurement was started and the absorbance was measured every 1-5 s. After an equilibration period of around 5 min, 10 μL of ConA (10 mg/mL from stock solution) were added and the measurement continued for at least 45 min. Blank values (plain solvent) were subtracted from the data and the resulting values plotted and analysed using the software Origin2018b (OriginLab Corporation, Northampton/USA).

7 Multivalently functionalised vesicles for ligand-receptor recognition

This section is based on the paper *"A Toolbox Approach for Multivalent Presentation of Ligand-Receptor Recognition on a Supramolecular Scaffold"*, which has been partially modified. Citation: S. Ehrmann‡, C.-W. Chu‡, S. Kumari‡, K. Silberreis, C. Böttcher, J. Dernedde, B. J. Ravoo, R. Haag, *J. Mater. Chem. B.* **2018**, *6*, 4216-4222. (‡equal contribution) Reproduced with permission from the Royal Society of Chemistry.

Author contributions This project was carried out as a cooperation project between the Freie Universität Berlin (SE, SK, CB, RH), the Westfälische Wilhelms-Universität Münster (CWC, BJR), and the Charité Berlin (KS, JD). Synthesis of the compounds was done by me, Chih-Wei Chi and Shalini Kumari (*cf.* Synthetic procedures). ITC measurements were done by Chih-Wei Chu, SPR measurements by Kim Silberreis, Chih-Wei Chu and me, OD_{400} measurements by Chih-Wei Chu, MST measurements by Shalini Kumari, the *in vitro* assay by Kim Silberreis, and the cryo-TEM experiments by me. The data were analysed and interpreted by me, Chih-Wei Chu, and Shalini Kumari with contributions from all authors. We wrote the manuscript together, with main contributions from me and Chih-Wei Chu.

7.1. Introduction

In biological systems, cell-linked carbohydrates generate the glycocalyx, which is involved in diverse fundamental processes, such as cell-cell recognition and downstream signalling in living organisms.[104,149] The interactions, *e.g.*, carbohydrate-lectin binding, are usually weak and non-covalent. A multivalent display of ligands and receptors on complementary surfaces, however, is a well-known concept in nature to realise higher specificity and stronger relative binding affinities.[91] For instance, the adhesion of bacteria to cell surfaces requires multivalent protein-carbohydrate interactions.[150,151] In particular, the adhesion of uropathogenic *E. coli* (UPEC) to uroepithelial cells in the urinary tract is mediated by the binding of α-D-mannosides, presented on cell surface proteins, to the bacterial lectin FimH of type I pili of UPECs.[152] In this specific case, urinary tract infections (UTI) are mostly caused by antibiotic

resistant *E. coli* strains[153–155] and therefore alternative treatment options are badly needed. To achieve an effective inhibition of bacterial colonisation of tissues, synthetic multivalent scaffolds as binding competitors are a promising option. Different variables including valency, topology, density and cluster effects of carbohydrates at synthetic scaffolds are currently under investigation.[96,103,156–158] Biomimetic materials have obtained increasing interest in this regard in recent years. Glycoconjugates and supramolecular self-assembled glycoclusters have been used to generate multivalent systems[106], including liposomes[159], glycopeptides[160] and dendrimersomes[161], and fluorescent glycoprobes[162]. The development of a toolbox system, mimicking the glycocalyx and being easily variable by adapting different suitable ligands is therefore of high interest.

Bilayer vesicles are dynamic supramolecular structures that can be used as mimic for the glycocalyx by functionalisation of the surface of the vesicles with carbohydrates.[118] Cyclodextrins are cyclic oligosaccharides, containing D-glucopyranose as repeating units. The special orientation of glucopyranose units in cyclodextrins shapes a conical structure with a hydrophobic cavity. In addition, the hydroxyl groups on both sides at the open ring allows for further functionalisation.[163] By amphiphilic functionalisation with alkyl chains and oligo(ethylene glycol) chains, the formation of bilayer vesicles was reported.[116] Depending on the number of glucopyranose units (6 for α-, 7 for β- and 8 for γ-cyclodextrins), the size of the hydrophobic cavity ranges from 5.7 to 9.5 Å, thus enabling the formation of inclusion complexes with different hydrophobic guest molecules in water.[164] For β-CD, adamantane is known to be a well-fitting inclusion guest ($K_a \sim 10^4$ M^{-1}). By choosing different guest conjugates, the self-assembled cyclodextrin vesicles (CDV) are versatile scaffolds for various applications.[117,165,166] A similar host-guest system based on amphiphilic cucurbit[6]uril and spermidine derivatives was reported for Concanavalin A (ConA) recognition[167] and photoresponsive capture and release of lectins could be achieved by introducing azobenzene motifs[168] into the ligand structure.

The enhanced development of a toolbox scaffold system that enables diverse variation of its ligands and the investigation of subsequent ligand recognition were the aims of this work. The versatility concept was demonstrated by a few examples. Therefore, CDVs were non-covalently functionalised with two different kinds of lectin-recognising ligands. Mannose-presenting ligands were applied for the binding to ConA and FimH expressing *E. coli*, whereas sulphate-presenting ligands were used to show L-selectin binding. ConA is a plant lectin, homotetrameric at neutral pH and has four carbohydrate recognition domains for mannosides. L-selectin is an adhesion protein that supports the attachment of leukocytes to endothelial

cells during the inflammation process.[169–172] PSGL-1 is one of the physiological ligands for L-selectin, bearing an anionic sulphotyrosine residue, which binds to the positively charged region of L-selectin.[173,174] Due to this electrostatic interaction, sulphated ligands with a high local anionic charge density have been reported previously for the effective binding to L-selectin[175] including derivatives of heparin[176] and dendritic polyglycerol sulphates[177] (dPGS), which were blocking the interaction between leukocytes and endothelial cells.

To enhance the binding affinity of ligands towards the CDV surface, also divalent adamantane anchoring moieties were considered.[178,179] In addition, we synthesised ligands with different amounts of mannosides and sulphate groups, respectively, to investigate the influence of ligand density on CDVs in terms of target recognition. Therefore, interactions with the desired lectins were investigated by surface plasmon resonance (SPR) and microscale thermophoresis experiments (MST) as well as turbidimetric analysis of rising aggregates (OD_{400}). Furthermore, all host-guest complexes were analysed regarding their physicochemical properties by ITC measurements. In a second step, binding of mannose-decorated CDVs to FimH expressing *E. coli* was investigated by cryo-TEM experiments and studied in a competitive binding assays to the uroepithelial cell line RT4.

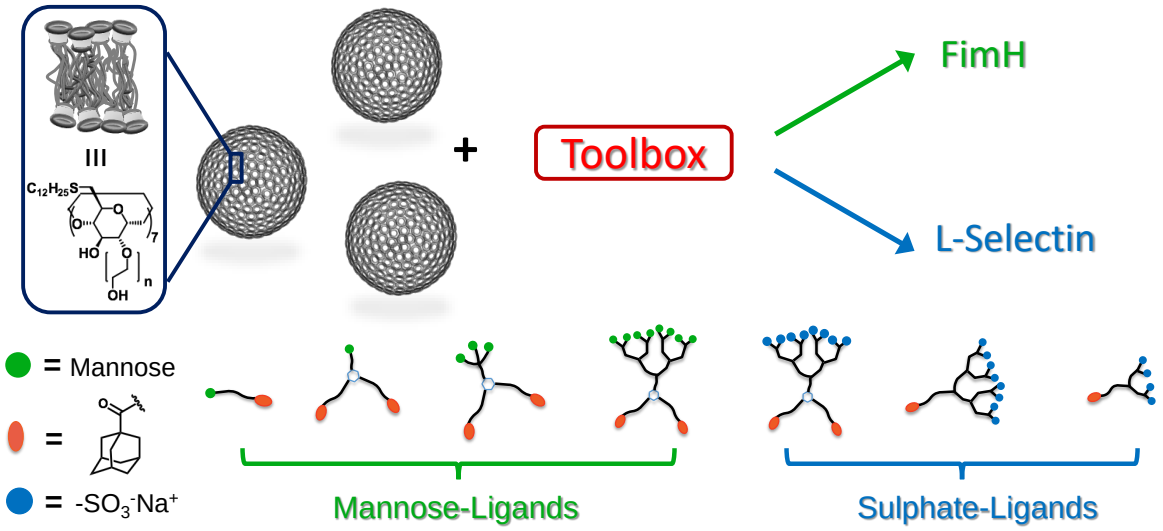

Figure 7.1.: Schematic depiction of the investigated supramolecular toolbox approach for multivalent ligand-receptor recognition.

7.2. Results and Discussion

7.2.1. Synthesis

In order to explore the multivalent supramolecular binding of cyclodextrin vesicles (CDVs), seven different ligands were synthesised, four of them bearing mannosides and three with sulphate group functionalisation. The valency of the ligands included mono-, tri- and octavalent mannosides as well as tetra- and octavalent sulphation in order to study the effect of multivalent ligand-receptor binding. The ligands were designed so that on one side of the structure a motif of one or two adamantyl residues allowed for the complexation to β-cyclodextrins (β-CD) at the surface of CDVs. Adamantyl groups are known to form inclusion complexes with β-CD with an affinity constant of around $K_a \sim 10^4\ M^{-1}$ for monovalent 1:1 binding. Divalent binding with two adamantane residues per ligand, however, can lead to an apparent affinity constant of up to $K_a \sim 10^7\ M^{-1}$ plus additional kinetic stabilization of the complex.[180] On the opposite side of the ligands, either mannose or sulphate groups were introduced. The synthetic ligands are shown in 7.2 and their detailed synthesis procedures are described in section 7.4.2. The octavalent mannoside ligand $\mathbf{Ad_2Man_8}$ was synthesised as shown schematically in Fig. 7.15. A polyglycerol-based dendron was synthesised according to published procedures[18] and coupled to a two-adamantane precursor by amide bond formation. Afterwards, the acetal-protection groups of the dendron were cleaved off using Dowex® resin. The free hydroxyl groups were then converted into terminal alkyne groups by the addition of 4-pentynoic acid *via* esterification. Subsequently, azido-mannosides were clicked onto the dendron's terminal alkyne groups *via* copper-catalysed azide-alkyne cycloaddition (CuAAC) under optimised conditions. The reaction was stirred for four days at elevated temperature (50 °C). The addition of a piece of copper wire[181] along with $CuSO_4$ and sodium ascorbate turned out to facilitate the reaction drastically and led to full octavalent functionalisation. Sulphate-adamantyl conjugates were synthesised in a similar procedure. Here, the terminal hydroxyl groups were sulphated using a sulphur trioxide pyridine complex. Amphiphilic β-cyclodextrins functionalised with alkyl and polyethylene glycol chains were synthesised according to previous reports.[117] β-Cyclodextrin vesicles (CDV) were obtained by extrusion, yielding vesicles with diameters between 100 and 200 nm.

7.2.2. Physicochemical characterisation

In order to investigate the vesicle's size and morphology, dynamic light scattering (DLS) and cryogenic transmission electron microscopy (cryo-TEM) experiments were carried out.

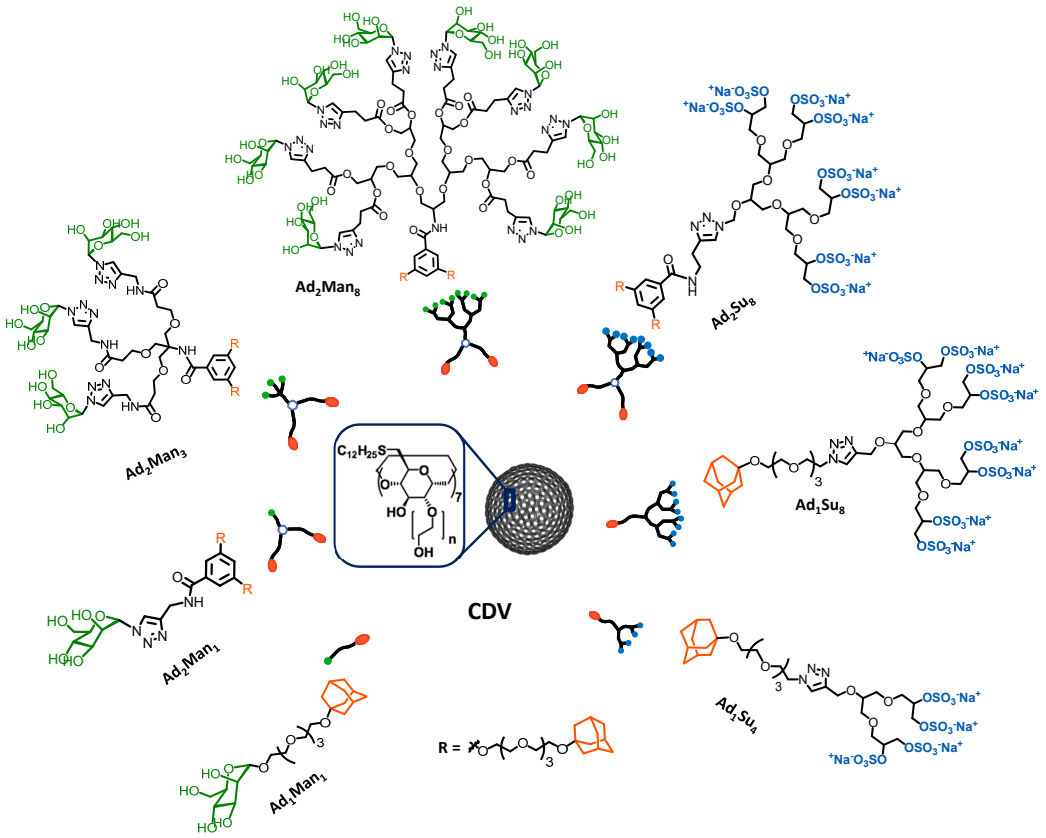

Figure 7.2.: Schematic representation of the synthesised adamantyl ligands with mannose and sulphate motifs and amphiphilic cyclodextrin vesicles.

Cryo-TEM images show mono- and multilayered vesicles with diameters of (177 ± 40) nm (Fig. 7.3A). These values closely correlate with the range of 140 to 180 nm obtained by DLS measurements (Fig. 7.3D), regardless of the solvent used (Milli-Q, HEPES, PBS+/+). Even after addition of mannoside ligands, the shape and size of the vesicles remained similar as can be seen in Fig. 7.3B and C.

The host-guest interaction was investigated between adamantane mannoside ligands (**Ad$_1$Man$_1$**, **Ad$_2$Man$_1$**, **Ad$_2$Man$_3$**, and **Ad$_2$Man$_8$**) and β-CD as non-aggregated β-CD allows unhindered inclusion complex formation with adamantane. Measurements were carried out by isothermal titration calorimetry (ITC) using 1:1 complexes of adamantane and β-CD (Table 7.1). Each titration was performed with a 10-fold higher host concentration in relation to the guest molecule. All ligands showed association constants in the range of 10^4 M^{-1}, which are in the typical range of adamantane to β-CD binding and are in line with previous results.[166] The thermodynamic parameters of **Ad$_1$Man$_1$**, **Ad$_2$Man$_1$**, and **Ad$_2$Man$_3$** are consistent (negative ΔH and positive ΔS), while for **Ad$_2$Man$_8$** the change in entropy (ΔS) is slightly negative and the change in enthalpy (ΔH) is slightly increased. We attribute this behaviour

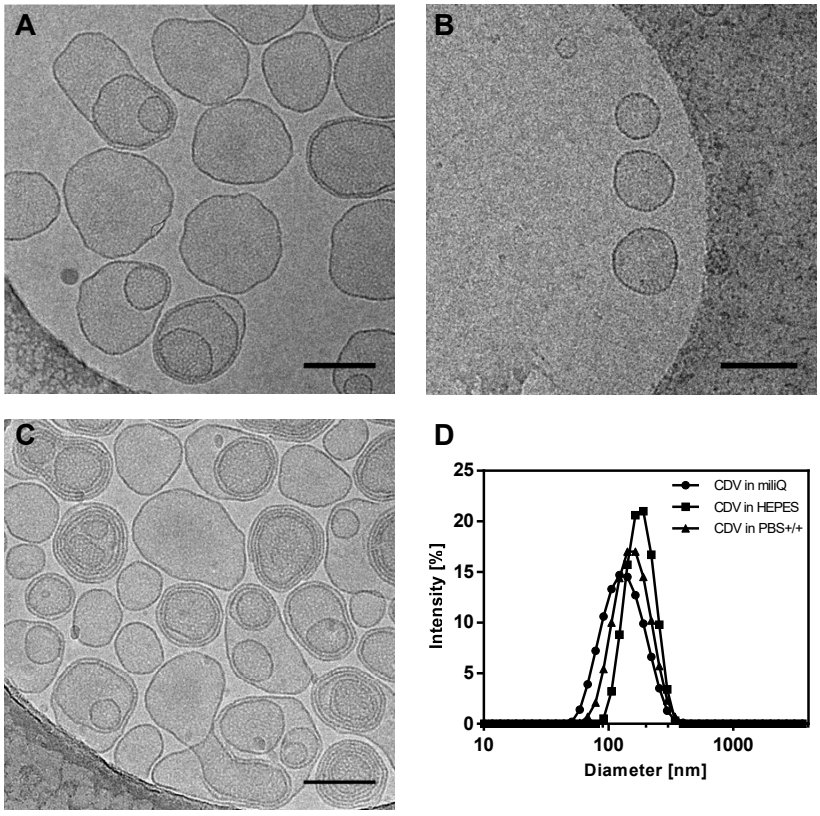

Figure 7.3.: Cryogenic transmission electron microscopy of CDVs in water: (A) 1 mM CDV; (B) 100 μM CDV + 25 μM **Ad$_2$Man$_1$** ; (C) 100 μM CDV + 25 μM **Ad$_2$Man$_8$**. Scale bars represent 150 nm in all figures. The displayed cryo-TEM images are representative and show uni- and multilamellar vesicles as well as their structural stability even after the addition of mannoside ligands. (D) Size distribution of CDVs in different aqueous media measured by dynamic light scattering.

to the bulky and strongly hydrated octavalent mannose dendron, which will significantly reduce the entropic bonus of releasing hydration water from the adamantane. Instead, it will be first solvated by the dendron and then included by the β-CD, so that the net gain in entropy due to the desolvation is minimal or even negative. In addition, ΔH is higher presumably because of multiple weak but favourable hydrogen bonds between the dendron and the β-CD. However, the resulting association constant K_a lies within the same range of the other ligands, which results in a stable inclusion complex formation for all ligands. Furthermore, due to the divalent binding of the ligands **Ad$_2$Man$_1$**, **Ad$_2$Man$_3$**, and **Ad$_2$Man$_8$** to the membrane of CDVs, increased binding affinities ($K_a \sim 10^7$ M^{-1}) and additional stabilisation effects for the complexes can be assumed as shown by Huskens *et al.*[179] The corresponding titration plots including fitting curves are given in Figs. 7.4, 7.5, and 7.6.

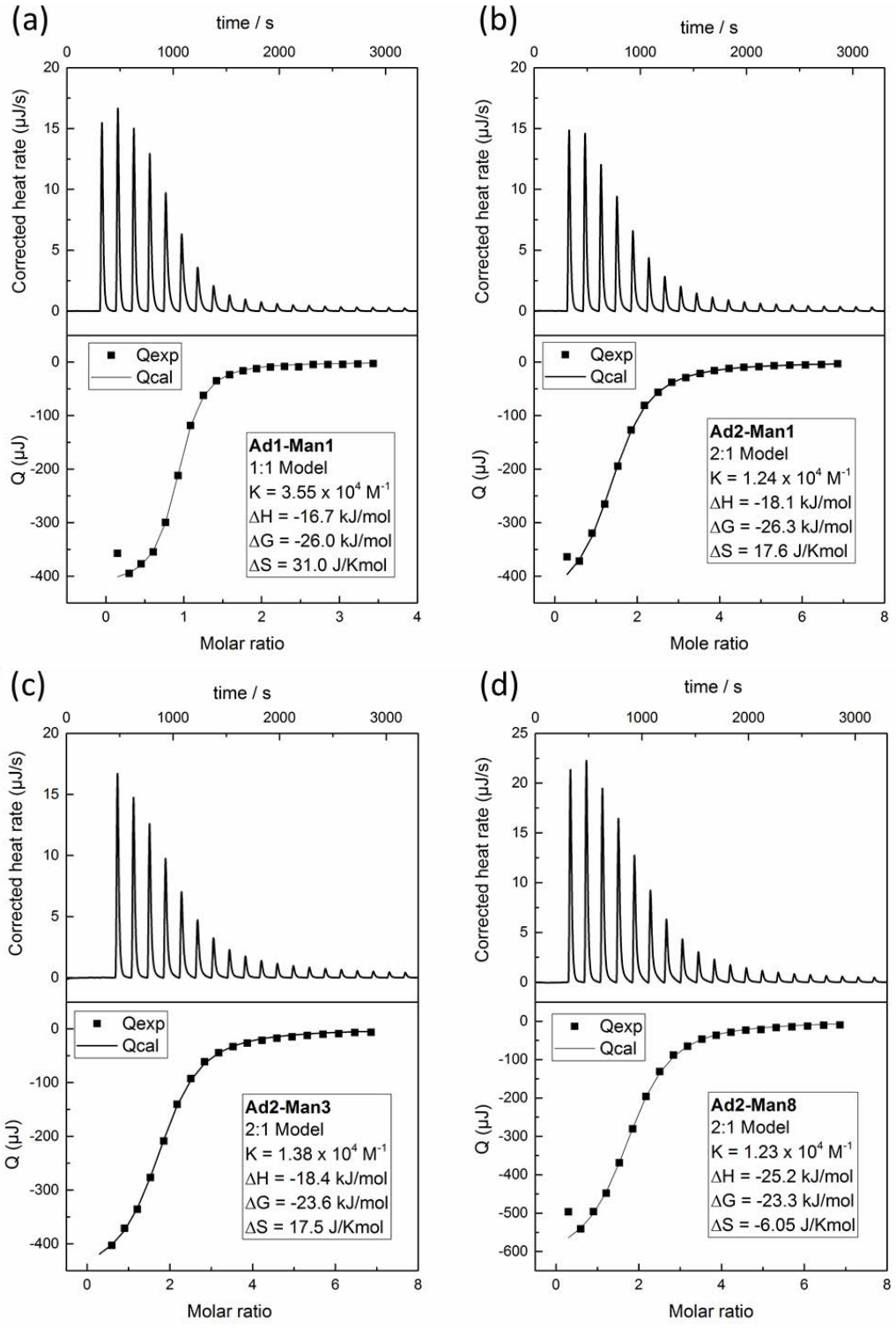

Figure 7.4.: Physicochemical properties of adamantane-mannose ligands determined by ITC (a) $\mathbf{Ad_1Man_1}$, (b) $\mathbf{Ad_2Man_1}$, (c) $\mathbf{Ad_2Man_3}$ and (d) $\mathbf{Ad_2Man_8}$.

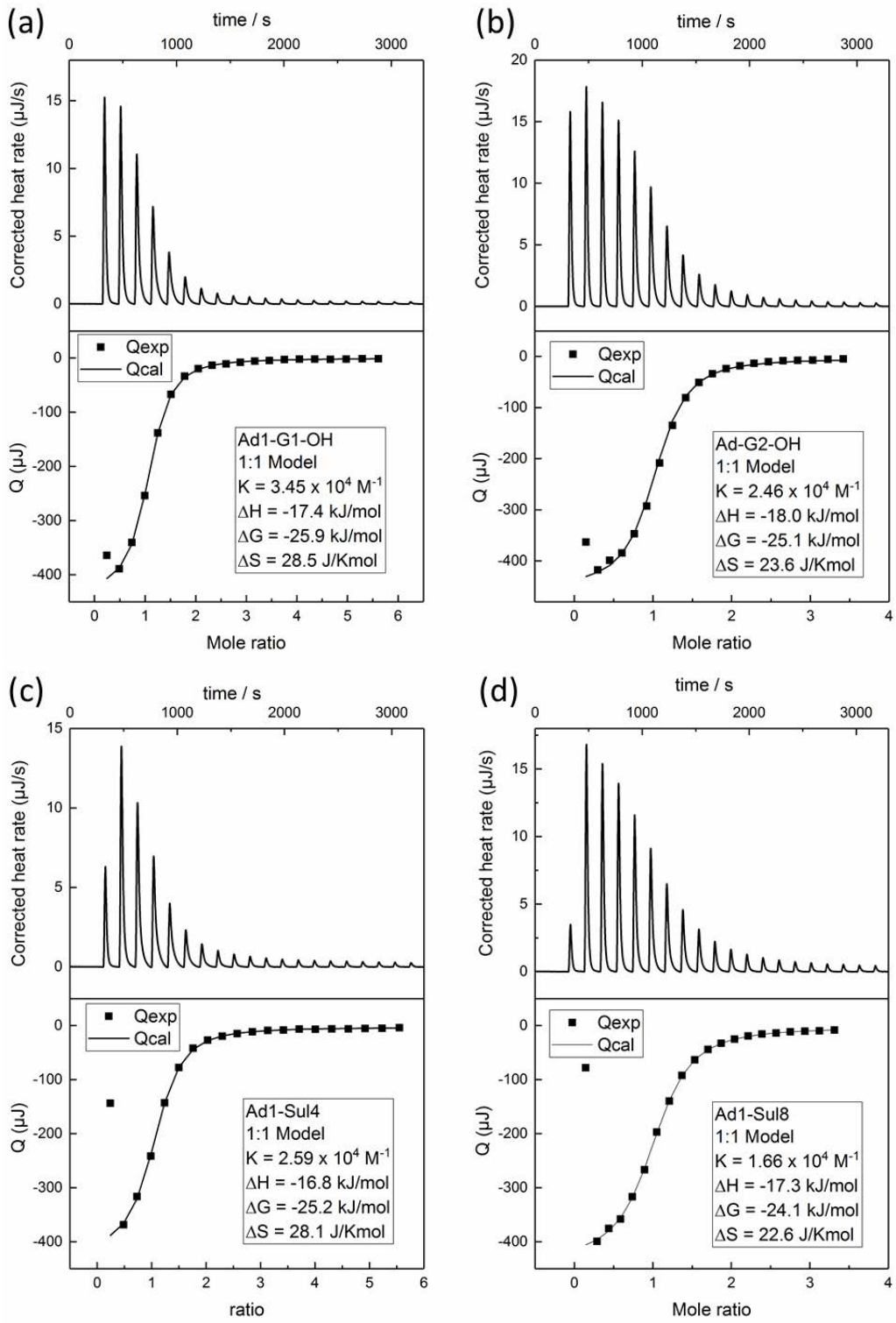

Figure 7.5.: Physicochemical properties of adamantane-dendron and adamantane-sulphates ligands determined by ITC (a) $\mathbf{Ad_1OH_4}$, (b) $\mathbf{Ad_1OH_8}$, (c) $\mathbf{Ad_1Su_8}$ and (d) $\mathbf{Ad_1Su_8}$.

Table 7.1.: Summary of physicochemical properties for adamantane-mannose ligand complexes determined by ITC.

Ligand at CDV	ΔH (kJ mol^{-1})	ΔG (kJ mol^{-1})	ΔS (J K^{-1} mol^{-1})	K$_a$ (M^{-1})
$\mathbf{Ad_1Man_1}$	-16.7	-26.0	31.0	$3.55 \cdot 10^4$
$\mathbf{Ad_2Man_1}$	-18.1	-26.3	17.6	$1.24 \cdot 10^4$
$\mathbf{Ad_2Man_3}$	-18.4	-23.6	17.5	$1.38 \cdot 10^4$
$\mathbf{Ad_2Man_8}$	-25.2	-23.3	-6.1	$1.23 \cdot 10^4$

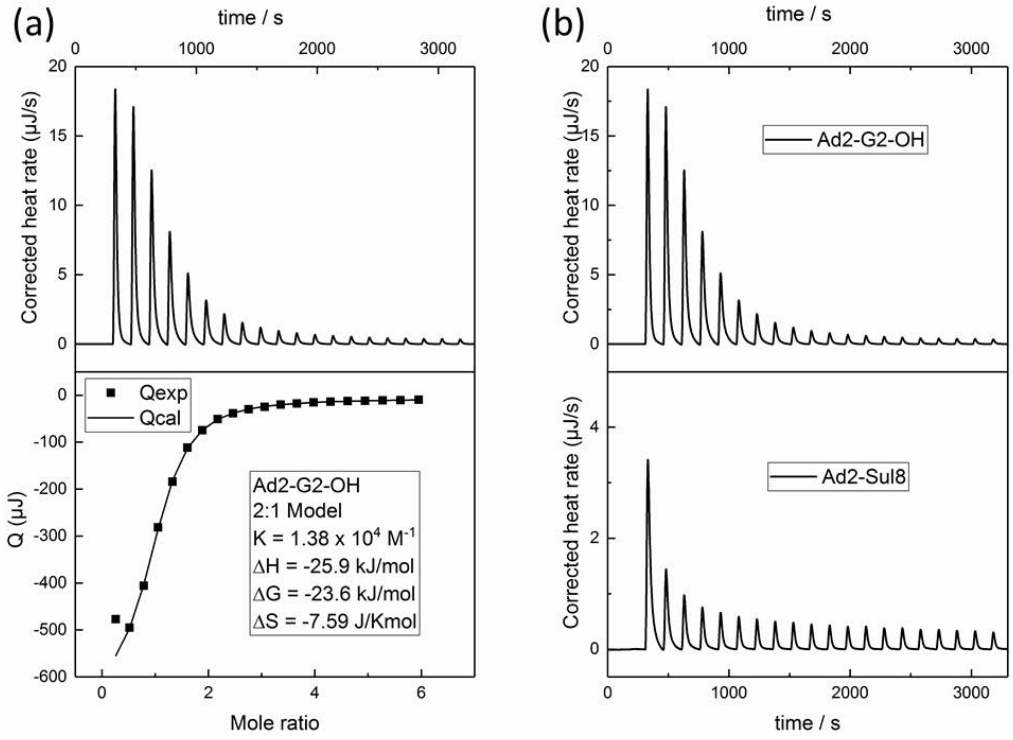

Figure 7.6.: (a) ITC of $\mathbf{Ad_2OH_8}$ (Ad2-G2-OH) and (b) comparison of ITC plots of $\mathbf{Ad_2OH_8}$ and $\mathbf{Ad_2Su_8}$.

Table 7.2.: Summary of physicochemical properties for adamantane-dendron and sulphate complexes determined by ITC and zeta-potential (ζ).

Ligand at CDV	ΔH (kJ mol^{-1})	ΔG (kJ mol^{-1})	ΔS (J K^{-1} mol^{-1})	K$_a$ (M^{-1})	ζ (mV)
β-CDV	-	-	-	-	-10.0 ± 1.7
Ad$_1$OH$_4$	-17.4	-25.9	28.5	$3.45 \cdot 10^4$	-9.5 ± 0.4
Ad$_1$Su$_4$	-16.8	-25.2	28.1	$2.59 \cdot 10^4$	-14.6 ± 1.1
Ad$_1$OH$_8$	-18.0	-25.1	23.6	$2.46 \cdot 10^4$	-8.5 ± 0.9
Ad$_1$Su$_8$	-17.3	-24.1	22.6	$1.66 \cdot 10^4$	-16.3 ± 2.4
Ad$_2$OH$_8$	-25.9	-23.6	-7.6	$1.38 \cdot 10^4$	-5.3 ± 0.2

In a second set of experiments, the non-covalent interactions between β-CD and the sulphated adamantyl ligands were investigated by ITC. Additionally, the non-sulphated analogues (OH-group terminated) were included in this assay to examine the effect of sulphation on the thermodynamic parameters. Again, reasonable binding affinities (K$_a \sim 10^4$ M^{-1}) for adamantane to β-CD were observed for all ligands (Tab. 7.2). In the case of **Ad$_2$OH$_8$**, a binding affinity comparable to the mannose-functionalised ligands (*cf.* Tab. 7.1) was obtained. A similar effect as before could be observed, i.e., a negative change in entropy and an increased change in enthalpy, which we again attribute to the strongly hydrated and bulky octavalent dendron in combination with two adamantane moieties. By comparing the titrations of **Ad$_2$OH$_8$** and **Ad$_2$Su$_8$**, an unexpected behaviour was observed, *i.e.*, the sulphated ligand showed not only a lower heat rate change by a factor of five than **Ad$_2$OH$_8$**, but also reached the thermal equilibrium already after three titrations (Fig. 7.6). This observation suggests that a self-assembled structure of **Ad$_2$Su$_8$** was present as the amphiphilicity of **Ad$_2$Su$_8$** increased due to the sulphation of the highly branched head group in comparison to the uncharged **Ad$_2$OH$_8$**. Thus, the adamantane groups were hindered from binding to β-CD. For all other ligands, this behaviour was not observed. Zeta-potential measurements were carried out to investigate the charge of CDVs after the complexation with neutral and sulphated ligands at the CDV surface (Table 7.2). For the dendritic neutral ligands, **Ad$_2$OH$_4$** and **Ad$_1$OH$_8$**, the zeta-potential remained unchanged after addition of the ligands in comparison to the bare CDVs (ζ = -8-10 mV), which also contain ethylene glycol side chains at the vesicle surface. In contrast, the decoration of CDVs with the sulphated ligands **Ad$_1$Su$_4$** and **Ad$_1$Su$_8$** led to an increased negative zeta potential (ζ = -14-16 mV), as the negatively charged ligands changed the surface environment after their complexation to CDVs. In the following, supramolecular complexes, consisting of CDVs and mannose-functionalised or sulphated adamantyl ligands,

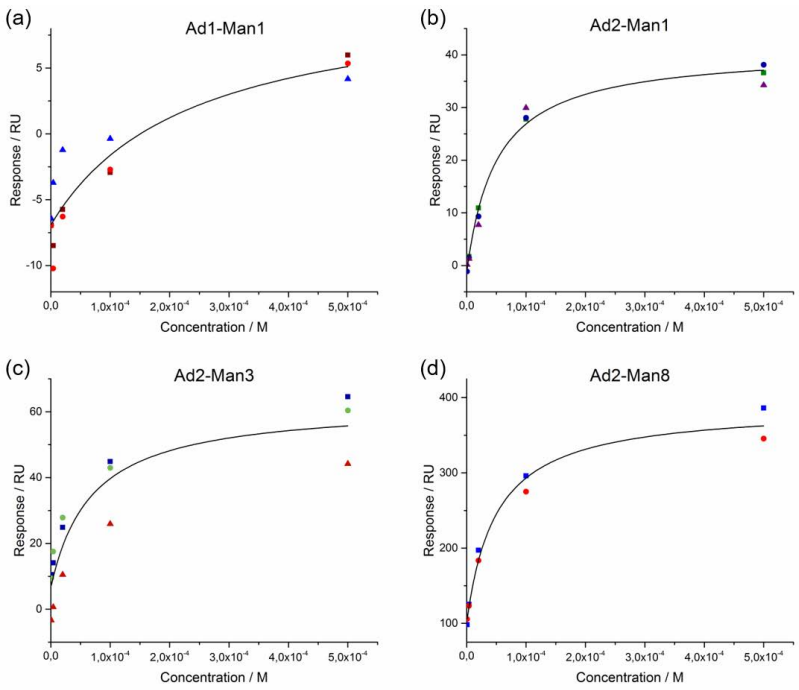

Figure 7.7.: Resulting binding isotherms derived from single-cycle kinetic measurements of (a) $\mathbf{Ad_1Man_1}$, (b) $\mathbf{Ad_2Man_1}$, (c) $\mathbf{Ad_2Man_3}$ and (d) $\mathbf{Ad_2Man_8}$.

respectively, were investigated regarding their binding affinities towards lectins.

7.2.3. Lectin binding

Surface plasmon resonance (SPR) SPR were performed to analyse the binding affinities of mannose-functionalised CDVs to the lectin Concanavalin A (ConA). ConA originates from the jack bean *Canavalia ensiformis* and forms homotetramers above pH 7 and in the presence of Ca^{2+} as well as Mn^{2+} ions.[104] The carbohydrate recognition site is specific for mannose and glucose, which has turned ConA into a well-studied model system for mannose-binding. In this assay, the aim was to compare binding affinities between the synthetic mannose-functionalised ligands as well as the respective ligand-functionalised vesicles to ConA. Therefore, ConA-biotin was immobilised on a streptavidin-functionalised SPR sensor chip, whereas mannose ligands and ligand-functionalised vesicles, dissolved in HEPES buffer, were run in a continuous flow over the sensor chip (Fig. 7.10A). In a kinetic titration series, binding measurements were conducted with increasing concentrations of the respective sample. Subsequently, K_D values for each sample were determined by single cycle kinetics and the resulting binding isotherms (Figs. 7.10B, C and Figs. 7.7, 7.8). The results are summarised in Table 7.3.

Due to non-specific binding of dissociated adamantane to the dextrane layer on the SPR

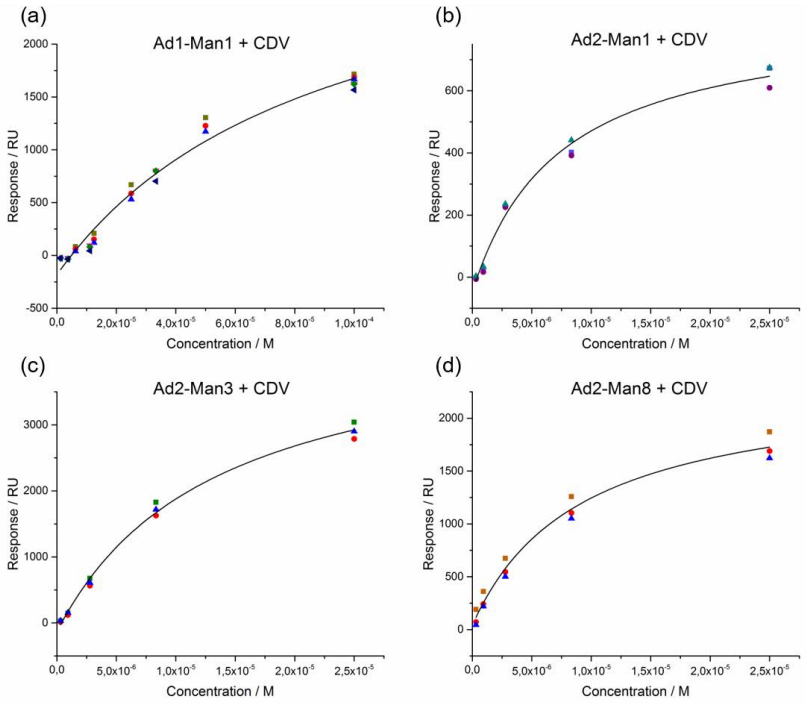

Figure 7.8.: Resulting binding isotherms derived from single-cycle kinetic measurements of guest-functionalised CDVs (a) $\mathbf{Ad_1Man_1}$, (b) $\mathbf{Ad_2Man_1}$, (c) $\mathbf{Ad_2Man_3}$ and (d) $\mathbf{Ad_2Man_8}$.

chip, additional cyclodextrin was added to the SPR running buffer. In order to efficiently shield the adamantyl moiety, β-CD and γ-CD were added as surfactants to the buffer during the measurements with mannoside ligands and ligand-decorated vesicles, respectively. γ-CD was able to prevent binding of adamantyl moieties to the dextrane layer, however, reversible binding to the CDVs was still favoured due to the much higher binding affinity of adamantane to β-CD. According to reported literature, the affinity between adamantane and γ-CD ($K_a = \sim 10^2$ M^{-1}) was two orders lower than for β-CD ($K_a = \sim 10^4$ M^{-1}).[182] In order to prove that the addition of γ-CD did not affect our supramolecular system, control experiments were performed. Shape and size consistency of the vesicles after the addition of γ-CD was confirmed by DLS and Cryo-TEM experiments. Determined hydrodynamic diameters were found to remain unchanged, which indicates morphological stability upon addition of γ-CD (Fig. 7.9a). The corresponding micrographs obtained from cryo-TEM experiments showed likewise mono- and multilayer vesicles with intact membranes. Secondly, the influence of addition γ-CD on agglutination of ligand-decorated CDV in the presence of ConA was studied by OD_{400} measurements (Fig. 7.9b). $\mathbf{Ad_2Man_3}$ and $\mathbf{Ad_2Man_8}$ were applied as test ligands. It can be seen that the effect of additional γ-CD is of minor influence since all of the measurements show a similar absorbance and aggregation rate. These experiments supported our

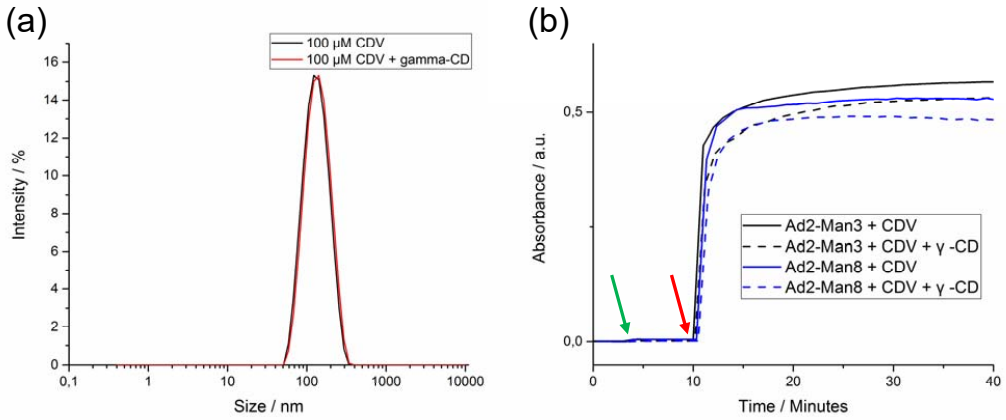

Figure 7.9.: (a) Size of CDV and in presence of 10 mM γ-CD determined by DLS. (b) Agglutination of ligand-decorated CDV in presence and absence of 10 mM γ-CD with 0.1 mg/mL lectin ConA (OD_{400}). Arrows indicate the addition of ligands (green) and ConA (red).

claims that our SPR setup gave us reliable results.

At first, binding affinities of mannose-functionalised conjugates (**Ad$_1$Man$_1$**, **Ad$_2$Man$_1$**, **Ad$_2$Man$_3$**, and **Ad$_2$Man$_8$**) to ConA were measured. The determined K_D values ranged from 50-234 mM (Table 7.3).

Subsequently, CDVs were decorated with the ligands through the formation of adamantane-β-CD inclusion complexes. The concentrations of ligands were chosen such that full decoration of the vesicles by complexation of every cyclodextrin was theoretically enabled (referred to as 100% surface coverage). Here, determined K_D values ranged from 7-89 mM. By comparison with the corresponding values for the conjugates itself, the binding was strengthened by a factor of approx. three to seven through the multivalent display of ligands at CDVs, highlighting the effectivity of multivalent organisation of ligands. However, differences in the binding affinities resulting from different carbohydrate valencies (one to eight) could not be discriminated at that point.

The obtained values are comparable to recent studies also using SPR.[183–186] However, in contrast to the present approach, these works used covalently synthesised glycoclusters and glycopolymers. By using a supramolecular multivalent approach, a facile adaptation to different targets in terms of *e.g.* valency and type of ligand is enabled.

OD_{400} agglutination assay for surface coverage dependent measurements Additional aggregation experiments with turbidimetric measurements (OD_{400}) investigated the optimisation of the surface coverage of vesicles with mannoside ligands by altering the ratio of

Table 7.3.: Binding affinities obtained from SPR of mannose-conjugates and mannose-functionalised CDVs.

Ligand	K_D (μM)	
	Bare ligand	Ligand displayed on CDVs
$\mathbf{Ad_1Man_1}$	234	89
$\mathbf{Ad_2Man_1}$	50	7
$\mathbf{Ad_2Man_3}$	69	13
$\mathbf{Ad_2Man_8}$	50	9

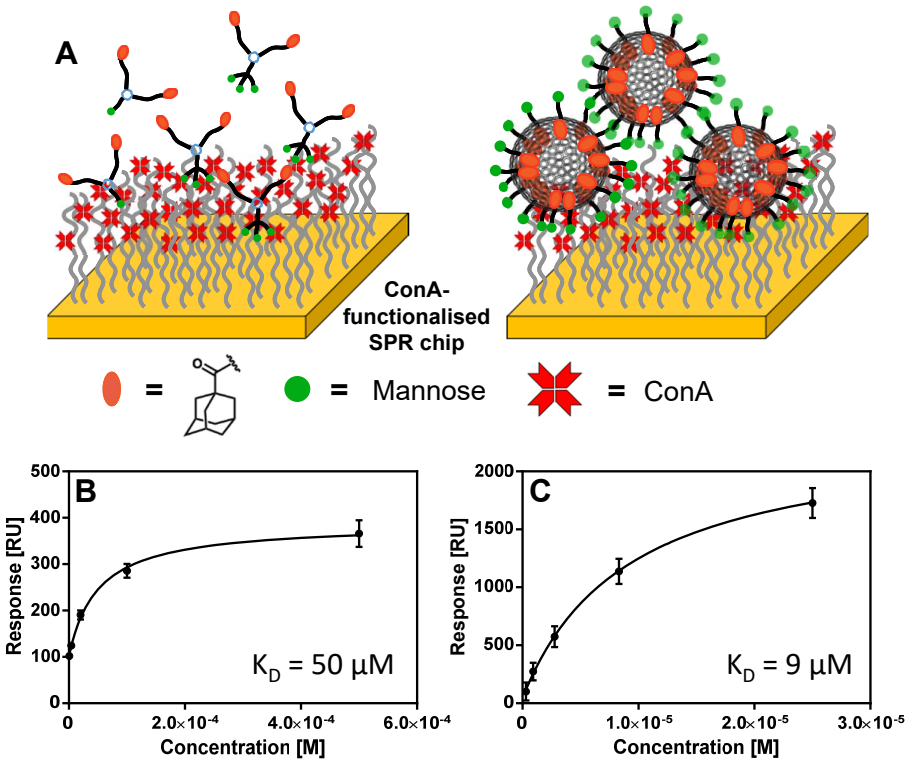

Figure 7.10.: (A) Schematic depiction of SPR experiment setup. (B) Determination of binding affinities for mannoside functionalised ligands (left) as well as ligand functionalised vesicles (right) to ConA. (C) Corresponding binding isotherms are shown exemplary for $\mathbf{Ad_2Man_8}$.

ligand to host moiety. The agglutination of vesicles, which was mediated by binding to ConA, was observed by optical density measurements at a fixed wavelength of $\lambda = 400\,\mathrm{nm}$ (OD_{400}). Concentrations of vesicles and mannoside ligands were chosen so that, in general, every cyclodextrin formed an inclusion complex with an adamantyl residue. This concentration relation is referred to as 100% surface coverage.

In a first experiment, the agglutination of the vesicles with different ligands was tested (Fig. 7.11b). Here, all vesicles exhibited a surface coverage of 100%. All tested ligand-vesicles complexes showed high capabilities to provoke agglutination, as can be seen by the increasing optical absorption with time. Additionally, $\mathbf{Ad_2Man_1}$ not only showed agglutination but also an additional cross-linking of CDVs even in absence of ConA (area between green and red arrow in Fig. 7.11c). This behaviour was observed and described before by Kauscher *et al.*[166] and can be understood from the ability of the two adamantyl residues to bind to two different vesicles, hence, inducing intervesicular crosslinking. For larger mannoside complexes ($\mathbf{Ad_2Man_3}$ and $\mathbf{Ad_2Man_8}$), the self-aggregation from CDVs was no longer observed due to the highly branched and sterically demanding mannoside structures. In order to investigate the dependence between the CDV surface coverage and their aggregation behaviour, a second set of experiments with changing carbohydrate concentrations on the CDVs was performed. A lower concentration of ligands on the vesicle's surface was achieved by replacing the mannosides with inactive adamantyl tetraethyleneglycol (**Ad-TEG-OH**). The ratio between active and inactive ligands was varied between 10% and 100%, in order to receive the desired surface coverage. Ligand-concentration dependent aggregation was observed in all cases (Fig. 7.12). Fig. 7.11c compares the measured absorbance at a fixed time ($t = 40\,\mathrm{min}$) for different surface coverage and different ligands. A bisected behaviour with two distinct regions was observed, which are indicated by grey lines as guide to the eye in Fig. 7.11c. For surface coverage below 20%, the gain in absorbance is rather steep for all ligands. With further surface coverage, the curve flattens drastically and no substantial increase of aggregation is observed. Hence, a threshold of around 20% surface coverage for effective aggregation can be deduced from the measured data. Furthermore, no significant difference was observed for the three ligands tested. This behaviour can be explained by considering the assay setup, *i.e.*, to initiate aggregation, two functionalised CDVs need to bind through their ligands to one of the four binding sites of the same ConA. Here, the valency of the ligand plays an inferior role, as a simple monovalent binding in both cases already leads to aggregation. By considering the dimensions of the CDVs compared to ConA, it appears to be obvious that an increased ligand concentration after a certain threshold does not affect the aggregation substantially due to

steric reasons. At the utmost, the strength and stability of the aggregate might be increased due to additional crosslinking. The selectivity of our supramolecular scaffold was confirmed by additional OD_{400} experiments. A similar setup as before was applied, while the lectin PNA instead of Con A was added to the guest functionalised CDV solutions. Peanut agglutinin (PNA) is a plant lectin protein and binds to galactose. As can be seen in Fig. 7.11d, the addition of PNA induced only a slightly increased optical density, which can be attributed to light scattering by PNA at 400 nm. The optical density remained constant without further increase, showing that our system does not show unspecific binding, but bound specifically to mannose receptors at ConA.

L-Selectin binding analysis using label-free microscale thermophoresis (MST) In order to demonstrate the versatility of our toolbox system, the sulphated ligands and respective CDV sulphate complexes were applied in a L-selectin binding assay. Here, the dissociation constant was determined by microscale thermophoresis experiments (MST). MST is a powerful technique to study the interaction between proteins and small molecules in solution with low sample consumption.[187] The technique makes use of molecular migration due to an applied temperature gradient.[188] Binding affinities are evaluated from the changes in the thermophoretic behaviour resulting from binding of the ligand to the protein.[189]
The sulphated ligands $\mathbf{Ad_1Su_4}$ and $\mathbf{Ad_1Su_8}$ without CDVs showed randomly fluctuating values for the MST response throughout the ligand titration range. However, likewise to the mannose-functionalised ligands, an optimised binding behaviour due to multivalent display of the ligands on CDVs was observed. In the presence of vesicles, characteristic s-shaped and mirrored-s-shaped sigmoidal binding curves could be obtained (Fig. 7.13). The different appearances of the binding curves can be attributed to different thermophoretic movements of the respective ligands.[189] From these experimental data, K_D values of 34 mM for $\mathbf{Ad_1Su_4}$ and 25 mM for $\mathbf{Ad_1Su_8}$ were determined. These values are in the same range of those observed from mannoside-ConA binding experiments (*cf.* SPR experiments) and underline the broad and easy applicability of non-covalently functionalised CDVs in biological binding approaches by simply changing the functionalised ligands.

***In vitro* assay - bacteria binding** Mannose-functionalised CDVs were further studied in a competitive in vitro assay. Here, the ability to remove bound *E. coli* bacteria (ORN178, FimH+) from the human uroepithelial cell line RT-4 was investigated. The adhesion of UPECs to uroepithelial cells, subsequent biofilm formation in the urinary system, and further

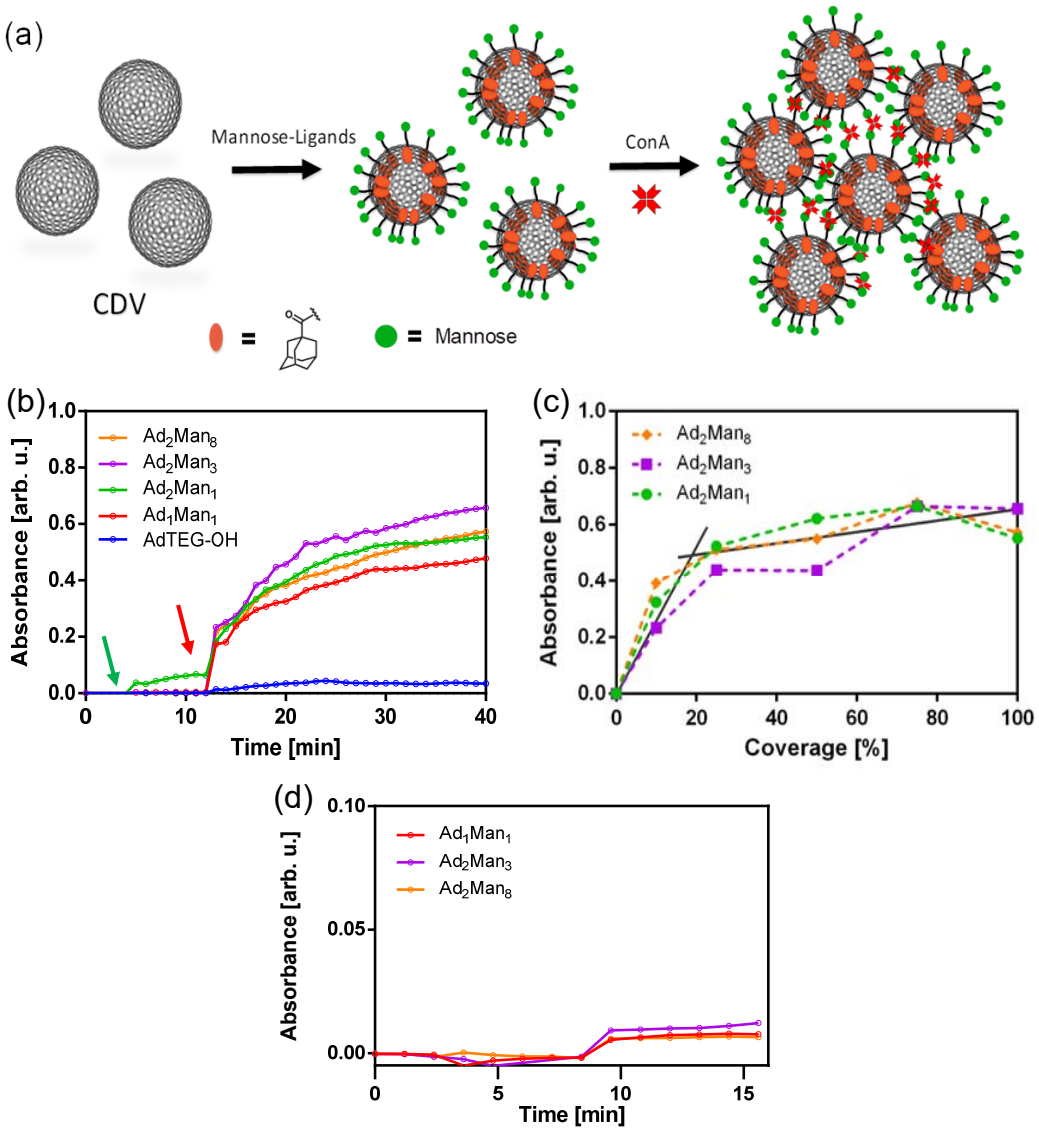

Figure 7.11.: Optical density measurements at $\lambda = 400\,\text{nm}$. (a) Schematic presentation of the aggregation experiment. (b) Agglutination of vesicles with 100% surface coverage of different ligands in the presence of 0.1 mg/mL ConA over time. Arrows represent the addition of ligands (green) and ConA (red). (c) Agglutination at t = 40 min of CDV + mannoside ligands in relation to the ligand surface coverage. Connection lines and grey lines are guides to the eye. (d) Agglutination experiment with functionalised vesicles and PNA. Arrows represent the addition of ligands (green) and PNA (red) - Note the expanded y-scale. All measurements were carried out in HEPES buffer (pH 7.4, 20 mM HEPES, 1 mM $CaCl_2$, 1 mM $MnCl_2$).

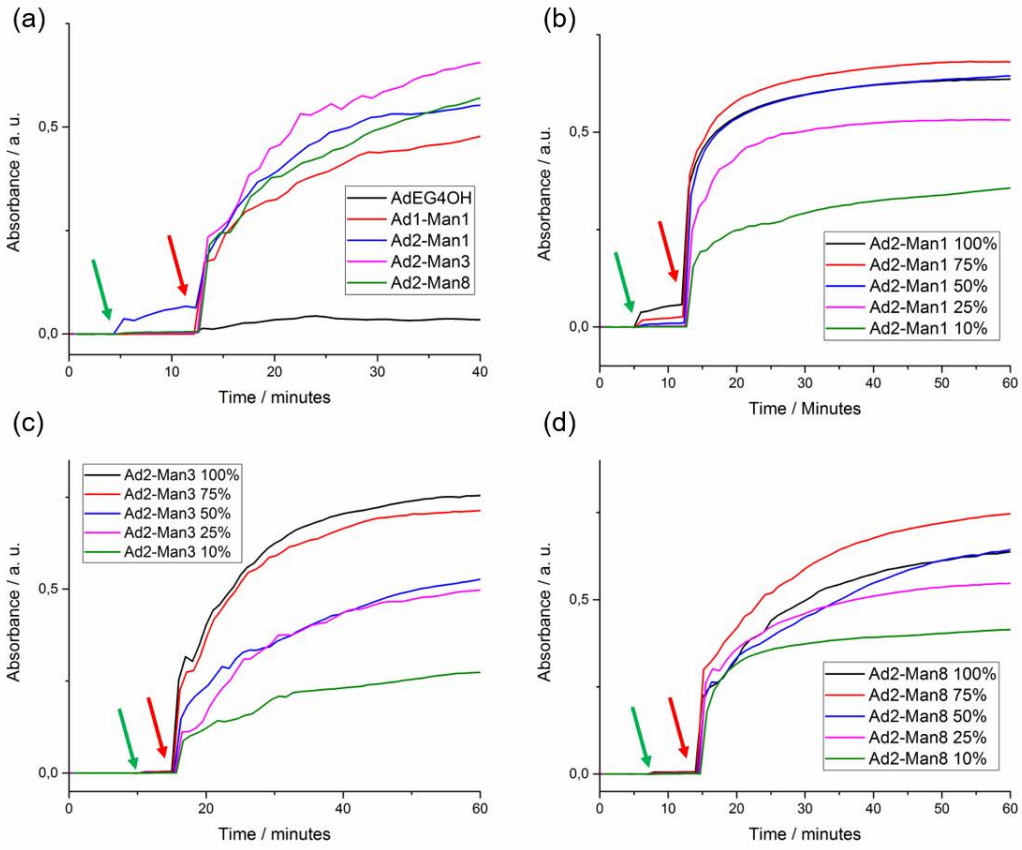

Figure 7.12.: (a) Agglutination of 100% coverage of different ligands on vesicles. Reduced agglutination with respect to decreased surface coverage of (b) $\mathbf{Ad_2Man_1}$, (c) $\mathbf{Ad_2Man_3}$, and (d) $\mathbf{Ad_2Man_8}$ functionalised vesicles. Percentage values were obtained by mixtures with guest **Ad-TEG-OH**. All measurements were carried out in the presence of 0.1 mg/mL ConA.

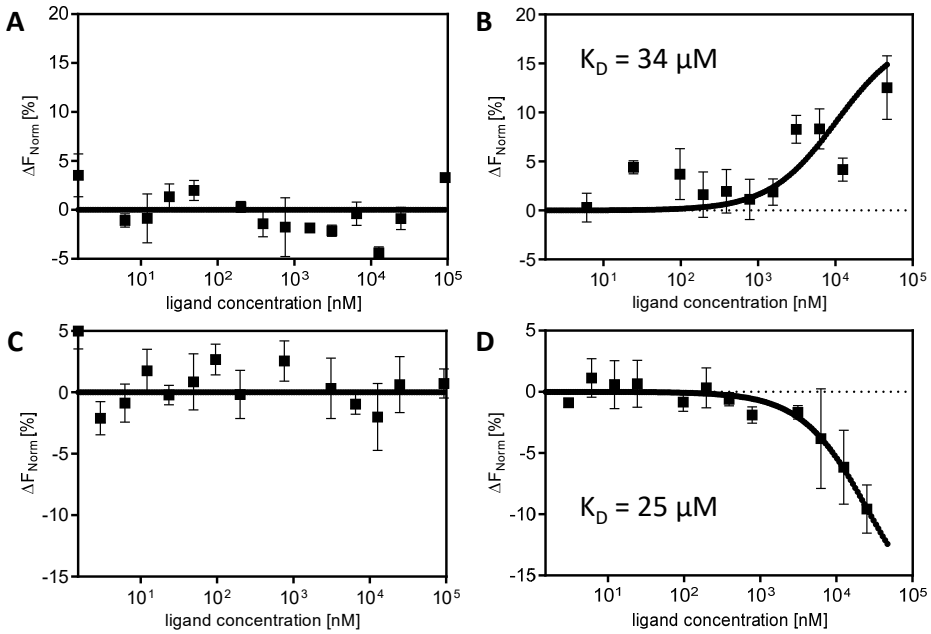

Figure 7.13.: MST dose-response curves of sulphated ligands $\mathbf{Ad_1Su_4}$ (A) without vesicles and (B) with vesicles and $\mathbf{Ad_1Su_8}$ (C) without vesicles and (D) with vesicles. All systems are titrated against L-selectin (100 mM). Sulphated ligands without vesicles show no interaction with L-selectin, whereas in the presence of vesicles significant binding was observed. Each graph displays data merged from three independent experiments.

bacterial invasion can lead to a severe inflammation.[190,191] Strategies to prevent or disrupt the initial adhesion process are of increasing importance especially due to an increasing number of antibiotic resistant strains.[192] The adhesion is mediated by the recognition and binding of the lectin FimH at the Type 1 pili of UPECs to carbohydrates at the glycocalyx of epithelial cells. FimH bears a carbohydrate recognition domain, which is specific for α-D-mannose. In this context, mannose-functionalised synthetic structures with high binding affinities towards FimH are highly promising anti-adhesive drug candidates.

The potential of our system to detach UPECs from uroepithelial cells was investigated using an *in vitro* assay. Uroepithelial RT-4 cells were incubated with *E. coli* strain ORN178 for 1 h. Afterwards, mannose-functionalised vesicles were added and incubated for 15 min together with cells and bacteria. In case of successful competitive binding, the vesicles would detach the bacteria from cell surfaces. The assay principle is depicted in Fig. 7.14A. Subsequently, the supernatant with detached bacteria was harvested and plated in serial dilutions on agar plates. Colonies were counted after overnight incubation at 37 °C and the detaching ability was calculated as relative activity in relation to PBS buffer solution as negative control. All bi-adamantane ligands, carrying one, three and eight mannose residues were

tested (**Ad$_2$Man$_1$**, **Ad$_2$Man$_3$**, **Ad$_2$Man$_8$**). Furthermore, ligand concentrations were chosen such that both half and full coverage of the vesicles was achieved. For comparison, also the monovalent methyl-α-D-mannopyranoside (Me-Man) was included. The non-carbohydrate ligand **Ad-TEG-OH** served as a control to exclude unspecific binding. As can be seen in Fig. 7.14B, tri- and octavalent mannoside ligands were able to release significantly more bacteria from RT-4 cell layers than the monovalent and control ligands. Furthermore, Me-Man and **Ad$_2$Man$_1$** did show the same or even less detaching activity compared to the inactive control ligand **Ad-TEG-OH**.

In the following, different coverage densities of the vesicles with ligands were tested. As can be seen in Fig. 7.14B, the coverage density, *i.e.*, half and full coverage with ligands on the CDV's surface, had no influence on the detaching efficiency. These findings seem to be non-intuitive at the first glance, *i.e.*, one would expect a direct dependence between the detaching efficiency and ligand density. However, the above-described results can be interpreted by considering the effect of local density of binding sites. The pili of the UPECs exhibit only a single mannose-binding site, which is located at the outermost protein, *i.e.*, FimH. At the beginning of our cell experiments, this binding site was bound to the mannosides at the uroepithelial RT4 cell membrane. By adding the functionalised vesicles, alternative mannosides were offered for binding. Since binding is a dynamic process, binding and debinding occurs occasionally. If an alternative binding site other than the natural mannosides at the cell membrane were present during debinding, FimH may bind to these alternatives. Binding to these alternatives becomes even more favourable, if they are arranged in multivalent clusters. If this is the case, they exhibit a high local concentration of binding sites. An increase of the high local concentration of binding sites leads to a decreased dissociation rate[193,194] and statistically favoured rebinding. Hence, FimH stayed bound to the dendritic mannoside clusters. These mannoside clusters are present in the tri- and octavalent mannose ligands, explaining the increased detaching efficiency compared to the monovalent mannosides and the inactive ligand. Thus, multivalency is an important aspect for enhancing binding efficiencies in biological systems.

In addition, cryo-TEM images of UPECs and CDVs were taken (Fig. 7.14C-E). Here, CDVs were functionalised with either the inactive ligand **Ad-TEG-OH** or the octavalent mannoside ligand **Ad$_2$Man$_8$**. For UPECs incubated with CDVs plus the inactive Ad-TEG-OH ligand, no binding of vesicles to the pili of the bacteria could be observed (Figs. 7.14C and D). However, vesicles, functionalised with **Ad$_2$Man$_8$** ligands, show clear co-localisation to the bacteria and their pili (Fig. 7.14E), supporting the above results from the *in vitro* assays.

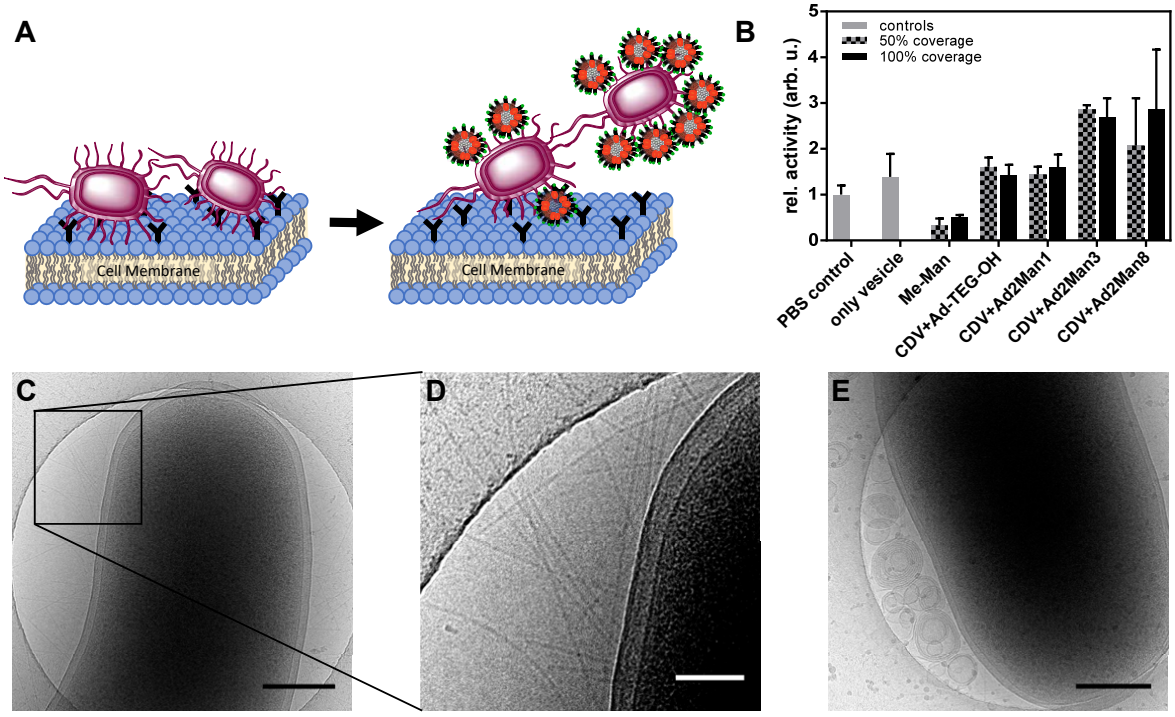

Figure 7.14.: (A) Schematic presentation of the bacteria-detaching assay. Left, FimH pili of *E. coli* bind to the mannosylated surface proteins of RT-4 cells; right, mannose-functionalised CDVs are added and competitive binding liberates *E. coli*. (B) Detaching ability of different functionalised vesicles to disturb cell-bacteria interaction. Representative cryo-TEM micrographs show mannose-dependant CDV binding to *E. coli* cells. (C) Control: *E. coli* + CDV + **Ad-TEG-OH**; (D) control: close-up picture of cell membrane and pili. (E) *E. coli* + CDV + $\mathbf{Ad_2Man_8}$. Scale bars are 300 nm for (C and E) and 100 nm for (D).

Furthermore, the cryo-TEM images prove that binding occurs to the functionalised vesicles and not to free and non-complexed ligands in solution.

7.3. Conclusion

In conclusion, we performed a thorough study on multivalently functionalised CDVs for lectin binding. Functionalisation of the vesicles was realised by novel carbohydrate and sulphate ligands, namely mono-, tri- and octavalent mannosides as well as tetra- and octavalent sulphates. These different ligands were used in a toolbox approach to demonstrate enhanced lectin binding through multivalent display of the ligands at the vesicle's surface. Our toolbox approach easily allowed addressing different biologically relevant receptors by modifying the supramolecular system with corresponding ligands, *i.e.*, mannosides for ConA binding as well as sulphated ligands for L-selectin binding. Finally, we demonstrated in an *in vitro* assay that our mannose-functionalised vesicles are an efficient system for detaching *E. coli* from

uroepithelial cells. FimH antagonists as anti-adhesive compounds reduce the bacterial load and therefore could be further developed for wash out strategies as a treatment option with respect to antibiotic resistant UPEC strains. In the future, new strategies to target different pathogens using the toolbox approach presented in this work will be anticipated.

7.4. Supplementary Information

7.4.1. Methods and Materials

Synthesis All reagents and solvents were obtained from commercial suppliers and used without further purification unless stated otherwise. Reactions requiring dry and oxygen-free conditions were carried out in oven-dried glassware with septa using usual Schlenk techniques. Millipore water (Milli-Q) was obtained from a Merck Millipore Milli-Q Integral System. NMR spectra were recorded on JEOL ECX400, JEOL ECP500, BRUKER AV500 and BRUKER AV700 spectrometers at 400 MHz, 500 MHz and 700 MHz for 1H NMR spectra and 100 MHz, 125 MHz and 175 MHz for 13C NMR spectra, respectively. Chemical shifts are given in parts per million (ppm) in relation to deuterated solvent peak calibration. Flash columns were either performed with Macherey-Nagel silica gel 60 M or at a Combiflash R_f system from Teledyne ISCO. HPLC purification was conducted using a Puriflash PF-50C18HP RP-cartridge (20 g) from Interchim (France) and UV detection (254 nm). Ultrafiltration was carried out under 5 bar N_2, using cellulose membranes (MWCO = 1000 Da).

Surface Plasmon Resonance (SPR) Experiments were performed on a Biacore X100 instrument (GE Healthcare Europe, Freiburg, Germany) at 25°C, using HBS-Ca-Mn buffer (10 mM HEPES, pH 7.4, 150 mM NaCl, 0.1 mM $CaCl_2$ and 0.01 mM $MnCl_2$) in all cases. Biotinylated ConA (Vector Labs, Biozol, Eching, Germany) was immobilised on a streptavidin sensor chip (GE Healthcare, final response 2600 RU), whereas the reference lane was left unfunctionalised. Each cycle consisted of a 120 s period of sample contact time (association phase) followed by a 600 s dissociation phase. The regeneration was achieved in two steps (regeneration buffer 1) 800 mM methyl-α-D-mannopyranoside (60 s), buffer 2 10 mM MES (pH 6.1 + 1 mM $CaCl_2$ + 1 mM $MnCl_2$). β-CD (10 mM) was added to the running buffer during the measurements of mannose-adamantyl conjugates to ConA to shield the adamantyl moiety efficiently from unspecific binding to the dextran layer of the sensor chip. For the measurements of the ligand-decorated vesicles, γ-CD (10 mM) was added as a surfactant. All sample measurements were analysed with single cycle kinetics. Therefore, a concentration series of each sample was measured in triplicates. The determination of K_D values was performed with response unit (RU) data points taken at 15 s before injection stop using built-in software of the Biacore X100. Corresponding binding isotherms were plotted.

L-selectin binding measurements using label-free microscale thermophoresis (MST) Label-free microscale thermophoresis was used to measure the binding interactions between L-selectin and adamantane-coupled sulphated dendrons in the presence and absence of cyclodextrin vesicles according to the following protocol. For each measurement, a dilution series with constant L-selectin concentration but varying ligand concentrations was prepared in PBS. No significant ligand-derived autofluorescence was detected at 280 nm wavelength. The final L-selectin concentration was 100 μM. Approximately 1.5 μL of each sample was loaded in a premium capillary. All measurements were performed at 22°C. The thermophoretic movement of fluorescent L-selectin was monitored with a laser on for 30 s and off for 5 s keeping the MST power at 40% and LED power at 20%. Fluorescence was measured before laser

heating ($F_{Initial}$) and after 30 s of laser irradiation (F_{Hot}). The K_D values were then calculated from three independent thermophoresis measurements using the NanoTemper software (NanoTemper Technologies, Munich, Germany).

Cryogenic transmission electron microscopy (Cryo-TEM)
Cryo-sample preparation: Droplets (5 μL) of sample solution were placed on hydrophilised holey carbon-filmed grids (Quantifoil R1/4) at room temperature. The grids were surface plasma treated just prior to use (BALTEC MED 020 device at 8.5 mA for 60 s). Vitrified films were prepared in a 'Vitrobot' (PC controlled vitrification robot, FEI) at 22°C and a humidity of 100%. Excess sample was removed by blotting using two filter papers for 3.5 s and the thin film thus formed was shot (acceleration about 3 g) into liquid ethane just above its freezing point.
Cryo-TEM: The vitrified samples were transferred under liquid nitrogen into a Talos Arctica transmission electron microscope (FEI, Thermo Fisher), using the microscope's autoloader protocol. Micrographs were recorded at a sample temperature of around 100 K using the microscope's low-dose protocol at a primary magnification of 28000x and an acceleration voltage of 200 kV. Image recording was done using a falcon direct electron detector (FEI Company, Oregon, USA). The defocus was chosen to be 6.5 μm in all cases to create enough phase contrast.

Dynamic Light Scattering (DLS) DLS measurements were performed on a Malvern Zetasizer Nano in quartz suprasil or disposable UV micro cuvettes (Brand). Samples were prepared in Milli-Q, PBS or HEPES buffer and filtered through a 0.45 μm membrane prior to the measurement.

Optical density (OD_{400}) The aggregation of the guest decorated CDV and ConA were analysed by optical density measurements at $\lambda = 400$ nm (OD_{400}) using a V-650 double-beam spectrophotometer with a PAC-743 automatic 6-position cell block. Samples were prepared in disposable PMMA cuvettes with a path length of 1 cm and sample volume of 1 mL. The spectra were plotted and analysed using the software spectra analysis. Typically, 1 mL of a 20 μM CDV solution in HEPES buffer (pH 7.4, 20 mM HEPES, 1 mM $CaCl_2$, 1 mM $MnCl_2$) was put in a cuvette. After an equilibration period of 5 min, 10 μL of the ligand solution (stock solutions of 1 mM for Ad_1-systems and 0.5 mM for Ad_2-systems) were added and gently mixed. The artificial glycocalyx was then formed within another 5 min. After the addition of 10 μL of ConA (10 mg/mL from stock solution) the agglutination occurred immediately and the solution turned turbid.

Isothermal titration calorimetry (ITC) ITC was carried out from a TA Instruments Nano ITC Low Volume with a cell volume of 170 μL using ITCRun version 2.1.7.0 Firmware version 1.31. All titrations were performed by using a 50 μL syringe and 20 injections of 2.5 μL at a temperature of 25°C. A stirring rate of 350 rpm was applied while titrating the CD to the ligands solution. All samples were dissolved in distilled deionised water (ddH_2O). All data were corrected by subtraction of a blank titration of CD into pure water before analysis.

Cell experiments - bacteria detaching assay The potential of detaching uropathogenic bacteria of human urinary bladder epithelial cells using functionalised synthetic structures was analysed in a bacterium detaching assay. Therefore, functionalised cyclodextrin vesicles (CDV) with different two-adamantane ligands, including mono-, tri- and octavalent mannose were investigated. As a control the inactive ligand Ad-TEG-OH was used. To reach a half and a full coverage of the CDV, the adamantane ligands were set in a 100 fold higher concentration

than the CDV in ratios between 1:2 for one-adamantane systems and 1:4 in two-adamantane systems. The human uroepithelial RT-4 cells (DSMZ-German collection of microorganisms and cell cultures, Braunschweig, Germany) were seeded in a 24-well plate (TPP) at a cell density of 70,000 cells/cm^2 in RPMI 1640 (Gibco, Darmstadt, Germany), 10% FCS (Biochrom, Berlin, Germany) and 1% penicillin/streptavidin (Biochrom, Berlin, Germany). An incubation overnight (37°C, 5% CO_2) allowed the cells to adhere. The uropathogenic *Escherichia coli (E. coli)* strain 178 was grown in LB-medium with 10 μg/mL tetracycline until the culture reached an optical density at a wavelength of 600 nm (OD_{600}) of 1, measured by using a spectrophotometer (Ultrospec 300 by Pharmacia Biotec, Munich, Germany). Bacteria were centrifuged at 4000 rpm, 21°C, 10 min (Megafuge 2.0R, Heraeus Instruments, Hanau, Germany). Afterwards they were washed two times by using TBS-Ca-Mn-Buffer containing 50 mM Tris, 150 mM NaCl, 1 mM $CaCl_2$ and 1 mM $MnCl_2$ (all Carl Roth GmbH & Co. KG, Karlsruhe, Germany). The bacteria suspension was diluted to a final OD_{600} of 0.001.
RT-4 cells were washed two times with the same TBS-Ca-Mn-buffer before they were incubated with 100 μL of the bacteria suspension (OD_{600} = 0.001) for 1 h, 37°C on a plate rocker. Again, the cells were washed two times with the TBS-Ca-Mn-buffer to get rid of the unbound bacteria. Subsequently, 100 μL of prepared functionalised CDV loaded with adamantane-mannose ligands were applied to detach bound bacteria from cell surfaces during a 15 min incubation at 37°C. For quantification, the supernatant was collected and dilutions spread on selective LB-agar plates. After an overnight incubation (37°C), the grown colonies were counted.

7.4.2. Synthetic procedures

The synthesis of $\mathbf{Ad_1Man_1}$, $\mathbf{Ad_2Man_1}$, and $\mathbf{Ad_1Man_3}$ was carried out by Chih-Wei Chu, the synthesis of $\mathbf{Ad_1Su_4}$, $\mathbf{Ad_1Su_8}$, and $\mathbf{Ad_1Su_8}$ by Shalini Kumari. The corresponding synthetic procedures are published or cited in the Supporting Information of S. Ehrmann, C.-W. Chu, S. Kumari *et al.*, *J. Mater. Chem. B.* **2018**, *6*, 4216-4222.

G2-Amin[19] and α-D-mannopyranosyl monoazide[195] were synthesised according to published procedures by me and Diadamantane-carboxylic acid was kindly provided by Chih-Wei Chu.

7.4.3. Synthesis of $\mathbf{Ad_2Man_8}$

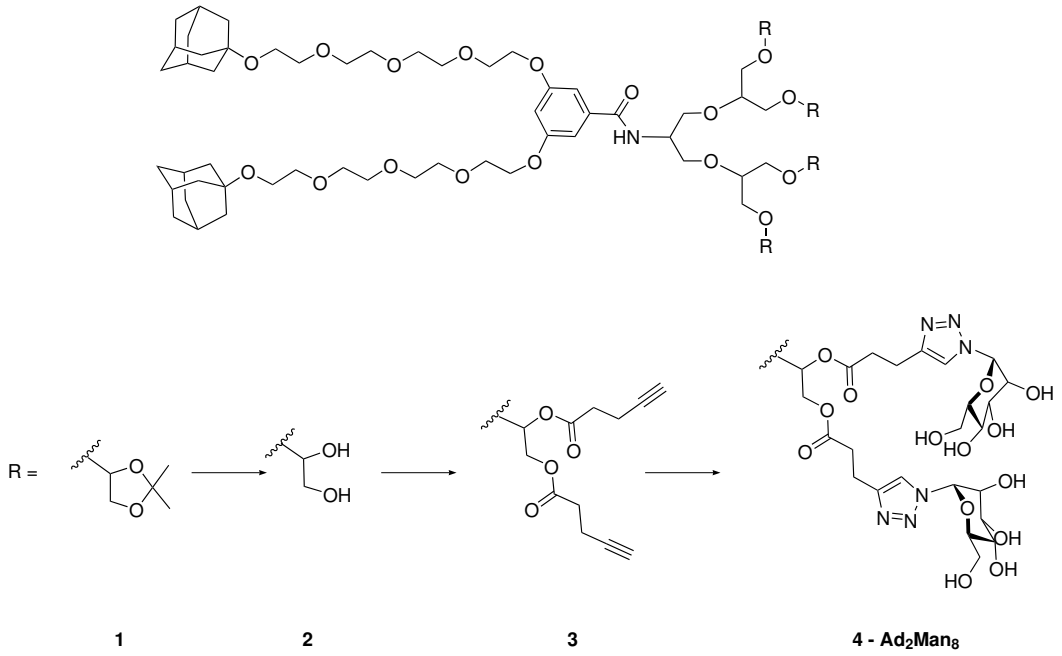

Figure 7.15.: Synthesis route of octa-mannoside ligand $\mathbf{Ad_2Man_8}$.

$\mathbf{Ad_2}$-pG2 - (1)

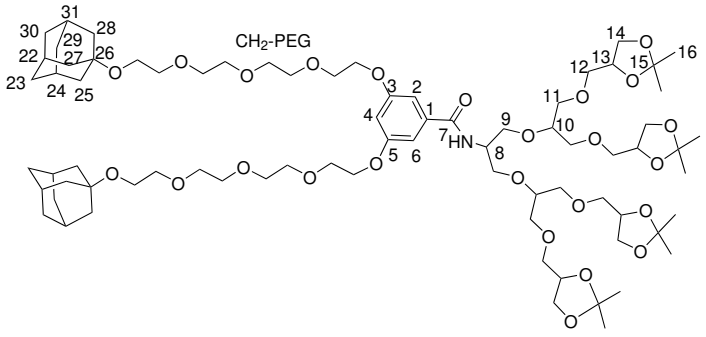

Diadamantane-carboxylic acid (400 mg, 0.52 mmol) and G2-Amine[19] (539 mg, 0.77 mmol) were dissolved in dry THF (10 mL) under argon atmosphere. After cooling to 0°C, EDC·HCl (148 mg, 0.77 mmol) and catalytic amounts of DMAP were added to the reaction mixture,

which was kept stirring overnight while warming to room temperature. Afterwards, the solvent was removed under reduced pressure. The residue was dissolved in DCM and washed with $NaHCO_3$ solution, brine and water. The organic layer was dried over Na_2SO_4 before being concentrated in vacuo. The crude product was purified by column chromatography (Silica, DCM/MeOH (0-4%)), which yielded the desired product as yellow oil (523 mg, 69%).
$C_{76}H_{125}NO_{25} = 1452.818\,g\,mol^{-1}$

^{1}**H-NMR** (400 MHz, Methanol-d_4, δ (ppm)): 1.28-1.32 (m, 12H, H-16), 1.34-1.38 (m, 12H, H-16), 1.64 (q, J = 12.6 Hz, 12H, H-23,-29,-30), 1.75 (d, J = 2.7 Hz, 12H, H-25,-27,-28), 2.11 (s, 6H, H-22,-24,-31), 3.45-3.71 (m, 50H, CH_2-PEG/H-8-12,-14), 3.84-3.85 (m, 4H, CH_2-PEG), 3.97-4.04 (m, 4H, H-14), 4.15-4.17 (m, 4H, CH_2-PEG), 4.18-4.23 (m, 4H, H-13), 6.70-6.71 (m, 1H, H-4), 7.01-7.03 (m, 2H, H-2,-6).

^{13}**C-NMR**: (100 MHz, Methanol-d_4, δ (ppm)): 24.43, 25.87, 30.66, 36.21, 41.26, 48.56, 59.15, 66.29, 66.41, 67.70, 69.47, 70.29, 70.33, 70.51, 70.93, 71.22, 72.19, 72.29, 74.82, 74.95, 78.58, 106.06, 109.17, 136.49, 160.22, 168.18.

MS (ESI-TOF) ($\frac{m}{z}$) : calculated ($C_{76}H_{125}NO_{25}H^+$) = 1452.8613, found 1452.8633; calculated ($C_{76}H_{125}NO_{25}Na^+$) = 1474.8433, found 1474.8448.

Ad_2-G2 - (2)

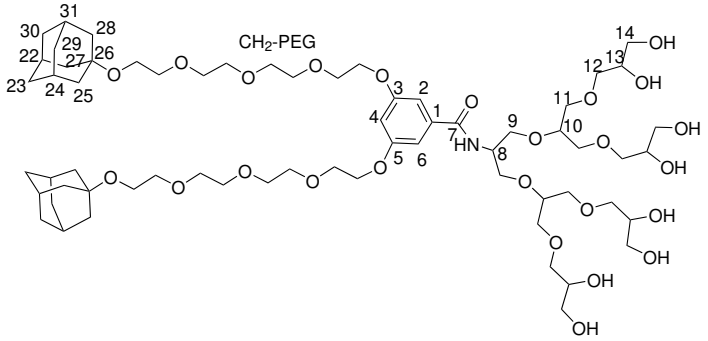

Acetal-protected diadamantane-G2 **1** (490 mg, 0.34 mmol) was dissolved in 10 mL methanol. After addition of Dowex-H (2 eq, by weight), the reaction mixture was kept stirring until complete conversion was reached. The reaction was monitored by TLC and NMR. After completion, Dowex-H was filtered off and washed with methanol. The filtrate was concentrated in vacuo yielding the title compound as slight yellow oil (415 mg, 95%).
$C_{64}H_{109}NO_{25} = 1292.558\,g\,mol^{-1}$

^{1}**H-NMR** (400 MHz, Methanol-d_4, δ (ppm)): 1.64 (q, J = 12.4 Hz, 12H, H-23,-29,-30), 1.75 (d, J = 2.7 Hz, 12H, H-25,-27,-28), 2.11 (s, 6H, H-22,-24,-31), 3.44-3.76 (m, 50H, CH_2-PEG/H-8-14), 3.84-3.86 (m, 4H, CH_2-PEG), 4.15-4.17 (m, 4H, CH_2-PEG), 6.70-6.71 (m, 1H, H-4), 7.01-7.02 (m, 2H, H-2,-6).

^{13}**C-NMR**: (100 MHz, Methanol-d_4, δ (ppm)): 30.66, 36.19, 41.23, 59.13, 63.14, 67.66, 69.46, 70.30, 70.46, 70.89, 71.09, 71.64, 72.33, 72.67, 78.55, 105.98, 136.44, 160.18, 168.41.

MS (ESI-TOF) ($\frac{m}{z}$) : calculated ($C_{64}H_{109}NO_{25}Na^+$) = 1314.7181, found 1314.7256.

Ad_2-G2-Propargyl - (3)

2 (50 mg, 0.039 mmol) was dissolved in dry THF under argon atmosphere. After cooling to 0°C, 4-pentynoic acid (61 mg, 0.62 mmol), EDC·HCl (119 mg, 0.62 mmol) and catalytic

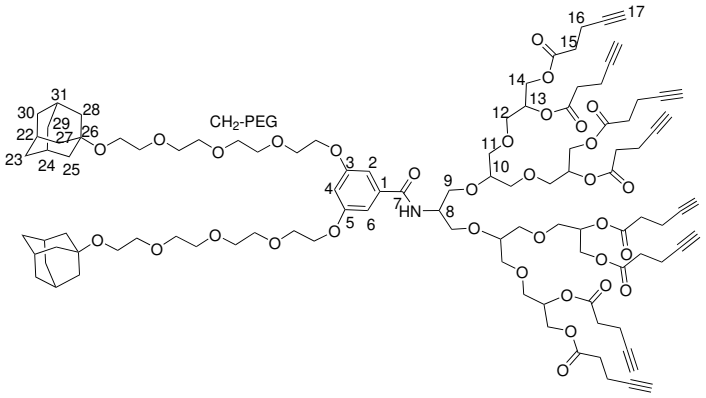

amounts of DMAP were added. The reaction solution was kept stirring for 16 h while warming to room temperature. Afterwards, the solvent was removed under reduced pressure. The residue was dissolved in DCM and washed with $NaHCO_3$ solution and water. The organic layer was dried over Na_2SO_4 before being concentrated in vacuo. The crude product was purified by column chromatography (Silica, ethyl acetate). The pure product was obtained as slight yellow oil (72 mg, 93%).

$C_{104}H_{141}NO_{33} = 1933.246\,g\,mol^{-1}$

^{1}**H-NMR** (700 MHz, Methanol-d_4/Aceton-d_6, δ (ppm)): 1.65 (q, J = 12.2 Hz, 12H, H-23,-29,-30), 1.76 (s, 12H, H-25,-27,-28), 2.13 (s, 6H, H-22,-24,-31), 2.33 (s, 8H, H-17), 2.44-2.50 (m, 16H, H-16), 2.53-2.59 (m, 16H, H-15), 3.59-3.87 (m, 50H, CH_2-PEG/H-8-14), 4.19-4.42 (m, 13H, CH_2-PEG/H-8-14), 5.18-5.21 (m, 4H, H-13), 6.72 (s, 1H, H-4), 7.03 (s, 2H, H-2,-6).

^{13}**C-NMR**: (176 MHz, Methanol-d_4/Aceton-d_6, δ (ppm)): 13.72, 30.58, 32.92, 33.07, 33.09, 36.16, 41.21, 59.10, 62.65, 67.66, 68.76, 68.98, 69.23, 69.39, 70.30, 70.42, 70.56, 70.88, 71.11, 71.30, 72.14, 78.74, 82.24, 104.28, 106.00, 136.45, 160.14, 167.81, 171.29, 171.56.

MS (ESI-TOF) ($\frac{m}{z}$) : calculated ($C_{104}H_{141}NO_{33}Na^+$) = 1954.9278, found 1954.9352; calculated ($C_{104}H_{141}NO_{33}{Na_2}^{2+}$) = 988.9585, found 988.9656.

Ad_2-Man_8 - (4)

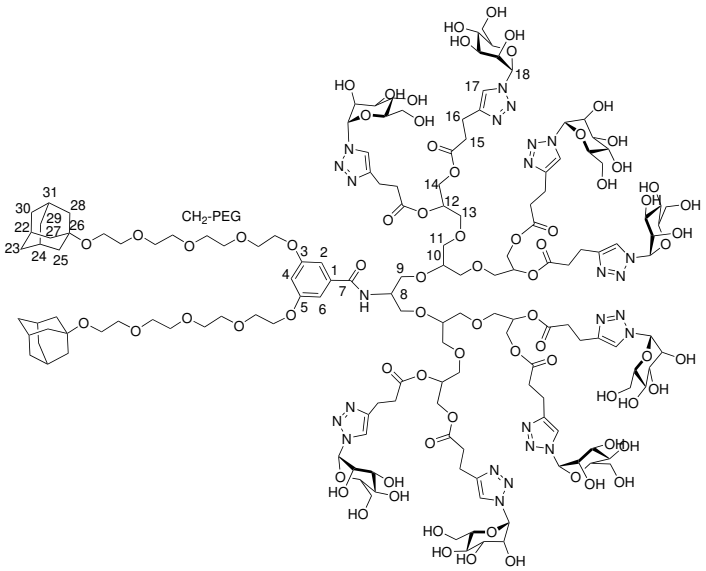

α-D-mannopyranosyl monoazide[195] (51 mg, 0.248 mmol) and **3** (30 mg, 0.015 μmol) were dis-

solved in 2 mL of dry DMF. A small piece of copper wire was added to the solution. Copper(II)sulphate pentahydrate (4 mg, 0.015 μmol) and sodium ascorbate (12 mg, 0.060 mmol) were dissolved in 0.5 mL water each and mixed before being added to the reaction solution, which was stirred at 50°C for 4 d. Afterwards, the solvent was evaporated and the residue was re-dissolved in water. Remaining salts were removed by ultrafiltration (MWCO = 1 kDa) in water. Purification of the crude product by HPLC (H_2O/MeOH 20-80%) and subsequent lyophilisation yielded the desired product as a white solid (23 mg, 43%).

$C_{152}H_{229}N_{25}O_{73}$ = 3574.606 g mol^{-1}

^{1}**H-NMR** (700 MHz, D_2O, δ (ppm)): 1.54-1.62 (m, 12H, H-23,-29,-30), 1.71 (s, 12H, H-25,-27,-28), 2.09 (s, 6H, H-22,-24,-31), 2.82 (s, 16H, H-15), 3.06 (s, 16H, H-16), 3.37-4.80 (m, 112H, H-PEG, -Dendron, -Mannose), 5.24 (s, 4H, H-12), 6.14 (s, 8H, H-18), 6.82 (s, 1H, H-4), 7.11 (s, 2H, H-2/-6), 8.04 (s, 8H, H-17).

^{13}**C-NMR**: (176 MHz, Methanol-d_4, δ (ppm)): 20.23, 20.30, 30.51, 32.76, 32.96, 35.99, 41.00, 58.98, 60.88, 62.81, 66.32, 66.99, 67.60, 68.66, 69.26, 69.34, 69.95, 70.04, 70.19, 70.63, 70.76, 71.05, 72.87, 73.40, 76.82, 79.82, 86.73, 106.08, 112.37, 136.16, 146.41, 159.96, 172.58, 172.91.

MS (ESI-TOF) ($\frac{m}{z}$) : calculated ($C_{152}H_{229}N_{25}O_{73}Na_2{}^{2+}$) = 1809.2380, found 1809.2501; calculated ($C_{152}H_{229}N_{25}O_{73}Na_3{}^{3+}$) = 1213.8217, found 1213.8320.

8 Abstract

In this work, we present the combination of supramolecular structures and dendritic functionalisation with a view to multivalent ligand-receptor recognition. To this end, we studied two supramolecular systems, *i.e.*, 1,3,5-benzenetricarboxamide (BTA)-based one-dimensional polymers and spherical β-cyclodextrin-based vesicles.

We could show that dendronised BTA-C_{16}-G1 molecules, functionalised with dendritic polyglycerol head groups, assemble in water in stable one-dimensional polymers with a high aspect ratio. HDX experiments showed remarkable low exchange dynamics of the monomers within the polymer. By cryo-TEM and subsequent image processing, an intriguing ultrastructure, consisting of two adjacent fibre strands, was revealed for the fibrous aggregates. Moreover, a double-helix ultrastructure was elucidated for ethylene-glycol functionalised nBTA polymers, comprising linear side chains.

Intriguingly, the length of the double-helix pitch could be varied by copolymer formation as a function of the monomer ratio. Starting from nBTA polymers, the pitch length was increased with an increasing amount of BTA-C_{16}-G1, which can be interpreted as unwinding of the double-helix towards the presence of two parallel strains. At the same time, the monomer exchange dynamics of nBTA were lowered upon copolymer formation with BTA-C_{16}-G1. Contrarily, the helix pitch of nBTA polymers was decreased upon copolymer formation with BTA-C_{12}-G1, leading to a higher axial curvature of the polymer strands. BTA-C_{12}-G1 itself assembles in spherical micelles, hence, a morphology with a high spatial curvature. However, also here, the monomer exchange dynamics of nBTA were lowered in copolymers with BTA-C_{12}-G1, underlining a stabilisation effect induced by the dendritic head groups. These results contribute to the understanding of the interplay between structure and dynamics of supramolecular polymers, which is of fundamental interest when designing functional materials.

Multivalent carbohydrate-recognition processes are omnipresent in nature, for instance, between the cell surface and pathogens during infection processes. Glyco-functionalised supramolecular architectures are promising functional materials for the interaction and inhibition of multivalent biological receptors due to their adaptivity based on reversible interactions and variable copolymer formation. Aiming for one-dimensional functional architectures, we

studied two mannose-functionalised BTAs with and without an ethyleneglycol (EG) spacer, regarding their assembly into supramolecular polymers and their ability to efficiently bind to mannose-binding lectins. BTA-mannose was shown to assemble into a fibre structure, whereas the BTA-EG_4-mannose formed spherical micelles instead. However, copolymer formation with non-glycosylated nBTA resulted in the assembly of fibres and made it possible to adjust the carbohydrate concentration within the polymer. We could show that multivalent copolymers of BTA-EG_4-mannose and nBTA were able to bind to mannose-binding lectin (complement assay) and concanavalin A (ConA) (turbidity assay) with K_D values up to the low micromolar range for the latter case. Our results obtained from lectin binding studies with two different mannose-binding proteins underline that for the design of efficient binders, structural knowledge of both the binder and the receptor structure is crucial. As a perspective, the combination of dendronised BTAs with carbohydrate functionalisation is believed to result in potent multivalent biofunctional materials.

Based on β-cyclodextrin vesicles (CDVs), a supramolecular toolbox approach for multivalent ligand-receptor recognition was established. A series of bifunctional ligands for CDVs was synthesised. These ligands comprise on one side adamantane, enabling the functionalisation of CDVs with these ligands, and either mannose or sulphate group moieties on the other side for biological receptor recognition. The physicochemical properties of the host-guest complexes formed by β-cyclodextrin and adamantane were determined by isothermal titration calorimetry (ITC). Ligand-lectin interactions were investigated by surface plasmon resonance experiments (SPR) for the mannose ligands and ConA. Microscale thermophoresis (MST) measurements were applied for sulphate-dependent binding to L-selectin. In both cases, a multivalent affinity enhancement became apparent when the ligands were presented on the CDV scaffold. Furthermore, not only the clustering between our supramolecular mannosylated complex and Escherichia coli (*E. coli*) expressing the lectin FimH was visualised by cryo-TEM, but also the competitive character to detach bound E. coli from a cell line representing the uroepithelial cell surface was demonstrated. Thus, a facile and effective supramolecular toolbox was established for various ligand-receptor recognition applications.

9 Zusammenfassung

Die Kombination von supramolekularen Strukturen und der dendritischen Funktionalisierung dieser Strukturen ist vielversprechend im Hinblick auf die Optimierung von multivalenten Wechselwirkungen zwischen Ligangen und biologischen Rezeptoren. In diesem Zusammenhang haben wir in der vorliegenden Arbeit zwei supramolekulare Systeme untersucht. Diese sind 1,3,5-Benzenetricarboxamid (BTA)-basierte eindimensionale Polymere und sphärische β-Cyclodextrin-basierte Vesikel.

Wir konnten nach erfolgreicher Synthese zeigen, dass BTA-C_{16}-G1, welches mit dendritischen Polyglycerin-Kopfgruppen funktionalisiert ist, stabile eindimensionale supramoelkulare Polymere in Wasser ausbildet. HDX-Experimente zeigten die bemerkenswert geringe Austauschdynamik der Monomere innerhalb des Polymers mit dem umgebenden Wasser. Durch Kryo-TEM und anschließende Bildverarbeitung wurde eine Ultrastruktur aus zwei nebeneinander angeordenten Fasersträngen für die supramolekularen Polymere identifiziert. Darüber hinaus wurde für Ethylenglykol-funktionalisierte nBTA-Polymere, die mit linearen Seitenketten funktionalisiert sind, eine Doppelhelix-Ultrastruktur aufgelöst.

Interessanterweise konnte die Länge des Doppelhelix-Pitches (Ganghöhe) durch Copolymerbildung in Abhängigkeit vom Monomeranteil variiert werden. Ausgehend von nBTA-Polymeren wurde die Pitchlänge mit zunehmendem Anteil von BTA-C_{16}-G1 vergrößert, was als Entwinden der Doppelhelix zu zwei parallelen Strängen interpretiert werden kann. Gleichzeitig wurde die Monomeraustauschdynamik von nBTA bei der Copolymerbildung mit BTA-C_{16}-G1 gesenkt. Im Gegensatz dazu wurde die Pitchlänge der Doppelhelix bei der Copolymerbildung mit BTA-C_{12}-G1 verringert, was zu einer höheren axialen Krümmung der Polymerstränge führte. BTA-C_{12}-G1 selbst aggregiert in Kugelmizellen, einer Morphologie mit hoher räumlicher Krümmung. Aber auch hier wurde die Monomeraustauschdynamik von nBTA in Copolymeren mit BTA-C_{12}-G1 gesenkt, was einen generellen Stabilisierungseffekt durch die dendritischen Kopfgruppen unterstreicht. Diese Ergebnisse tragen zum Verständnis des Zusammenspiels zwischen der Struktur und Dynamik supramolekularer Polymere bei, welches bei der Entwicklung funktionaler Materialien von grundlegendem Interesse ist.

Multivalente Wechselwirkungen zwischen Zuckerliganden und Proteinrezeptoren sind in der Natur allgegenwärtig, z.B. zwischen der Zelloberfläche und Pathogenen während des Infek-

tionsprozesses. Glyko-funktionalisierte supramolekulare Architekturen sind vielversprechende Materialien für die Interaktion mit multivalenten biologischer Rezeptoren und der Inhibierung dieser. Dieses resultiert aus der Adaptivität der supramolekularen Strukturen, basierend auf den ihnen zugrunde liegenden reversiblen Wechselwirkungen und der Möglichkeit zu vielfältiger und variabler Copolymerbildung. In dieser Arbeit haben wir zwei mannose-funktionalisierte BTAs, mit und ohne Ethylenglykol (EG)-Ketten zwischen Mannose und dem restlichen Molekül, hinsichtlich ihrer Aggregation zu eindimensionalen supramolekularen Polymeren untersucht. Zusätzlich haben wir die Bindungsaffinitäten zu zwei Lektinen mit Mannoserezeptoren untersucht. Es zeigte sich, dass BTA-Mannose in Wasser zu Fasern aggregierte, während BTA-EG_4-mannose stattdessen kugelförmige Mizellen ausbildete. Die Copolymerbildung mit nicht-glykosyliertem nBTA führte jedoch in beiden Fällen zur Bildung von supramolekularen Fasern und ermöglichte es, die Kohlenhydratkonzentration im Polymer einzustellen. Wir konnten zeigen, dass Copolymere aus BTA-EG_4-mannose und nBTA in der Lage waren, Mannose-bindendes Lektin (Komplementassay) und Concanavalin A (ConA) (Trübungsassay) mit K_D-Werten im unteren mikromolaren Bereich zu binden. Unsere Ergebnisse aus Lektinbindungsstudien mit zwei verschiedenen mannosebindenden Proteinen unterstreichen, dass für das Design effizienter Inhibitoren strukturelle Kenntnisse sowohl über den Binder, als auch über den Rezeptor entscheidend sind. Für die Zukunft ist es vielversprechend, dendritisch funkitonalisierte BTAs mit Kohlenhydraten zu funktionalisieren, um möglichst effektive multivalente biofunktionale Architekturen zu erhalten.

Basierend auf β-Cyclodextrinvesikeln (CDVs) wurde ein supramolekularer Toolbox-Ansatz zur multivalenten Ligand-Rezeptor Wechselwirkung entwickelt und untersucht. Eine Reihe von bifunktionalen Liganden für CDVs wurde dazu synthetisiert. Diese Liganden sind auf der einen Seite mit Adamantan, das die Funktionalisierung von CDVs mit diesen Liganden ermöglicht und auf der anderen Seite entweder mit Mannose- oder Sulfatgruppeneinheiten zur Wechselwirkung mit biologischen Rezeptoren funktionalisiert. Die physikalisch-chemischen Eigenschaften der, aus β-Cyclodextrin und Adamantan gebildeten, Wirt-Gast-Komplexe wurden durch isotherme Titrationskalorimetrie (ITC) bestimmt. Die Wechselwirkungen zwischen Liganden und Lektinen wurden durch Oberflächenplasmonenresonanzspektroskopie (SPR) für die Mannoseliganden und ConA untersucht. Mikroscale Thermophorese-messungen (MST) wurden für Untersuchung der Bindung von sulfatierten Liganden an L-selectin verwendet. In beiden Fällen zeigte sich eine Affinitätssteigerung durch die multivalente Präsentation der Liganden auf dem CDV-Gerüst. Darüber hinaus wurde durch Kryo-TEM Experimente die Bindung zwischen den supramolekularen mannosylierten Vesikeln und Escherichia coli (*E.*

coli) Bakterien, visualisiert werden, welche über das mannosebindene Lektin FimH an den Bakterien ausgebildet wird. Ebenso konnte gezeigt werden, dass die mannosylierten Vesikel kompetitiv *E. coli* Bakterien von mannose-expimierenden Uroepithelzellen ablösen können. Zusammengefasst wurde eine einfache und effektive supramolekulare Toolbox für verschiedene Anwendungen von Ligand- und Rezeptorwechselwirkungen entwickelt.

Part III.

Appendix

A. Acknowledgement/Danksagung

Ich möchte allen danken, die in den letzten vier Jahren direkt oder indirekt zum Erfolg dieser Arbeit beigetragen haben.

Ich danke Prof. Rainer Haag für das mir entgegengebrachte Vertrauen, mich vor vier Jahren als Doktorandin in seine Gruppe aufzunehmen. Ich möchte mich für die kontinuierliche wissenschaftliche und finanzielle Förderung meiner Forschungsprojekte bedanken sowie für die zahlreichen Möglichkeiten der Weiterentwicklung. Ebenso möchte ich mich für fortwährende wissenschaftliche, also auch persönliche Unterstützung mit Rat und Tat bedanken.

My sincere thanks go to Prof. Bert Meijer for his support in the BTA collaboration project, both scientifically, as well as on a personal level. I would like to thank for letting me be part of the Meijer group during my visit in Eindhoven, and for being the second reviewer of my thesis.

Ich möchte mich ganz herzlich bei PD Dr. Christoph Böttcher für die Einführung in die Welt der Elektronenmikroskopie bedanken und für die Unterstützung als Zweitbetreuer im Rahmen der SFB Graduiertenschule. Die unzähligen Stunden vor dem Mikroskop, die geduldige Hilfe bei meinen ersten cryo-TEM und Tomographieversuchen oder wenn mal wieder etwas nicht am Mikroskop klappte, die großartige Unterstützung bei der Analyse der BTA Strukturen und die stets offene Tür für meine Fragen zur Mikroskopie oder meinen Amphiphilen habe ich nie als selbstverständlich erachtet. Ebenso danke ich herzlich für die Anregungen und Korrekturen während des Schreibprozesses dieser Arbeit, sowie für die Möglichkeit auch in Zukunft die Welt der supramolekularen Chemie durch das Elektronenmikroskop erforschen zu können.

I would like to thank all my cooperation partners in Eindhoven, Münster and Berlin, without whom my projects would never have been successful. I would like to thank Dr. Bala Thota for guiding my first steps in the world of supramolecular chemistry and the initiation of the combination of dendrons and BTAs both in Berlin and in Eindhoven. My thanks go to Dr. Lu Su, Dr. René Lafleur, Dr. Xianwen Lou, and Dr. Simone Hendrikse-Lafleur for the great cooperation and fruitful discussions about supramolecular polymers. Furthermore, my thanks go to the whole Meijer group for the nice (although short) stay in Eindhoven and Carla Bouwman for the administrative support in Eindhoven. I would like to thank Dr. Chih-Wei Chu and Prof. Bart Jan Ravoo for the very good cooperation on the cyclodextrin vesicles, which I initially thought would be a small side project and eventually turned out to be a

major project of my doctoral thesis.
Ich danke meinen "biologischen" Kooperationsspartnern Kim Silberreis und Dr. Jens Dernedde für die sehr gute Zusammenarbeit, insbesondere für die Diskussionen zu unseren Projekten und Kim für ihre Geduld mit den E.colis und Zellen. Ich danke meinen Studenten Jahaziel Jahzerah und Klaus Omoregbee für ihre Unterstützung bei der BTA Synthese im Rahmen ihrer Forschungsprojekte.
Ein besonderer Dank geht an alle derzeitigen und ehemaligen Kollegen im Labor 34.02 und Büro 34.04. Es war mir eine große Freude und ein großer Spaß mit euch zusammen zu arbeiten, mit euch die Abzüge zu teilen, die Spülmaschine auszuräumen und den Müll wegzubringen und sich vor allem gegenseitig bei Erfolg und Misserfolg der Forschung zu unterstützen! Ebenso danke ich der 11:15 Lunch-group und dem Kuchenkolloquium für unzählige Mittags- und Kaffeepausen mit tollen Gesprächen und viel Spaß in der Uni, als auch bei gemeinsamen Unternehmungen oder Cocktailabenden. Ich danke Loryn Theune für ihre Freundschaft seit unserem gemeinsamen Bachelorstudium an der FU, für gute Gespräche bei einem Kaffee und wertvolle Unterstützung vom Beginn des Studiums bis zur Abgabe der Doktorarbeit.
Ich möchte mich bei Dr. Wiebke Fischer, Eike Ziegler, Jutta Hass, Katharina Tebel und Lydia Alnajjar für die reibungslose Unterstützung bei allen administrativen Angelegenheiten bedanken, bei Vertragsverlängerungen, Dienstreiseabrechnungen, Zwischenberichten, Publikationseinreichungen, etc.. Dr. Carlo Fasting und Marleen Selent danke ich für wertvolle Unterstützung bei HPLC Aufreiningungen, Katharina Goltsche für unermüdlichen Dendronnachschub und "gute Abzugsnachbarschaft", sowie der ganzen AG Haag für die Unterstützung, die gute Atmosphäre in der Gruppe und lustige Gruppenfahrten.
Ich danke den Kollegen der TEM Abteilung Dr. Boris Schade, Dr. Kai Ludwig, Andrea Schulz und Dr. Tarek Hilal für ihre Unterstützung bei meinen Projekten, insbesondere Kai und Boris für Hilfe an den Mikroskopen, bei Auswertungen, beim Präparieren und zahlreichen spontanen Problemlösungen, wenn das Mikroskop mal wieder nicht das machte, was es sollte.
Ich danke dem SFB765, der Graduiertenschule und der Dahlem Research School für finanzielle Unterstützung und die Möglichkeiten der persönlichen Weiterentwicklung auch ausserhalb des Labors. Mein Dank gilt ebenso der Core Facility BioSupraMol für unzählige NMR und MS Messungen, wie auch der Materialverwaltung für den unermüdlichen Nachschub an Methanol und DCM.
Ich bin meiner gesamten Familie und meinen Freunden dankbar für all die Unterstützung, die ich erfahren durfte, fürs Zuhören und den Ausgleich und die Zerstreuung, wenn es mal

wieder stressig im Labor wurde. Ich danke insbesondere meinen Eltern und meiner Schwester für ihre großartige und liebevolle Unterstützung, bei allem was ich tue.
Zu guter Letzt, last but not least, bin ich meinem Partner Felix unendlich dankbar für seine Liebe und Unterstützung in den vergangenen Jahren, für das unermüdliche Korrekturlesen dieser Arbeit, für das Interesse, das Verständnis und die Unterstützung bei allem was ich tue, für die Motivation in schwierigen Phasen und die unzähligen schönen Momente, die wir gemeinsam erlebt haben und noch erleben werden.

B. Curriculum Vitae

The curriculum vitae is not included in the online version for reasons of data protection.

C. List of Publications

L. Gao, F. Zabihi, **S. Ehrmann**, S. Hedtrich, and R. Haag; Supramolecular nanogels fabricated via host-guest molecular recognition as penetration enhancer for dermal drug delivery, *J. Control. Release*, **2019**, *300*, 64-72.

L. Gao‡, M. Li‡, **S. Ehrmann**, Z. Tu, and R. Haag; Positively Charged Nanoaggregates Based on Zwitterionic Pillar[5]arene that Combat Planktonic Bacteria and Disrupt Biofilms, *Angew. Chem. Int. Ed.*, **2019**, *58*, 3645-3649.

P. Dey‡, T. Bergmann‡, J. L. Cuellar-Camacho, **S. Ehrmann**, M. S. Chowdhury, M. Zhang, I. Dahmani, R. Haag, and W. Azab; Multivalent Flexible Nanogels Exhibit Broad-Spectrum Antiviral Activity by Blocking Virus Entry, *ACS Nano*, **2018**, *12*, 6429-6442.

S. Ehrmann‡, C.-W. Chu‡, S. Kumari‡, K. Silberreis, C. Böttcher, J. Dernedde, B. J. Ravoo and R. Haag; A toolbox approach for multivalent presentation of ligand-receptor recognition on a supramolecular scaffold, *J. Mater. Chem. B*, **2018**, *6*, 4216-4222.

B. N. S. Thota, X. Lou, D. Bochicchio, T. F. E. Paffen, R. P. M. Lafleur, J. L. J. van Dongen, **S. Ehrmann**, R. Haag, G. M. Pavan, A. R. A. Palmans, E. W. Meijer; Supramolecular Copolymerization as a Strategy to Control the Stability of Self-Assembled Nanofibers, *Angew. Chem. Int. Ed.* **2018**, *57*, 6843-6847.

M. Dimde‡, F. Neumann‡, F. Reisbeck, **S. Ehrmann**, J. L. Cuellar-Camacho, D. Steinhilber, N. Ma, R. Haag; Defined pH-sensitive nanogels as gene delivery platform for siRNA mediated in vitro gene silencing, *Biomater. Sci.*, **2017**, *5*, 2328-2336.

S. T. R. Müller, T. Hokamp, **S. Ehrmann**, P. Hellier, T. Wirth; Ethyl Lithiodiazoacetate: Extremely Unstable Intermediate Handled Efficiently in Flow, *Chem. Eur. J.* **2016**, *22*, 11940-11942.

‡ - equal contribution

D. NMR spectra

In this appendix, the NMR spectra of the compounds synthesised in chapter 4 are shown.

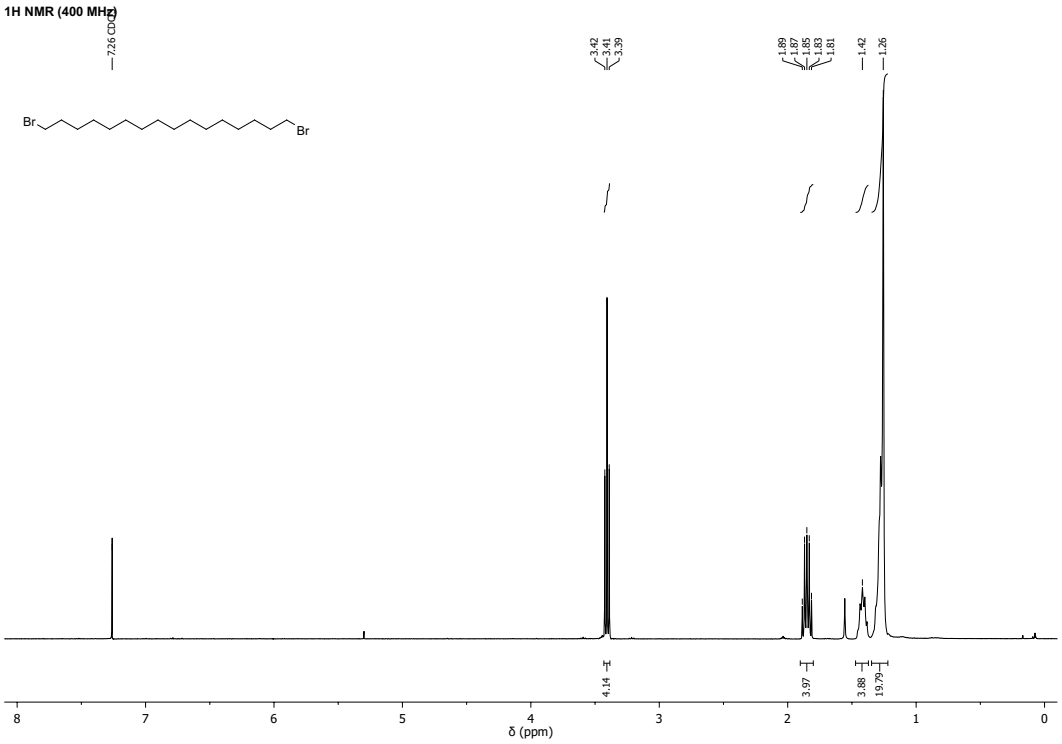

Figure D.1.: ^{1}H-NMR (400 MHz, $CDCl_3$) of 1,16-Dibromohexadecane.

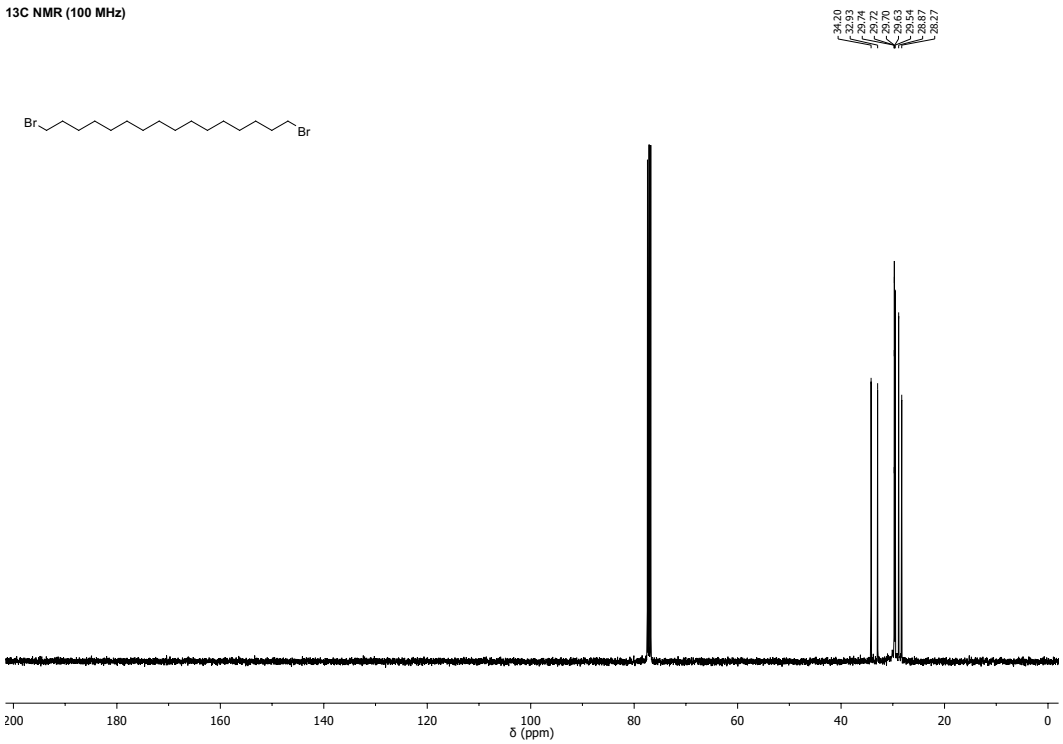

Figure D.2.: ^{13}C-NMR (100 MHz, $CDCl_3$) of 1,16-Dibromohexadecane **1**.

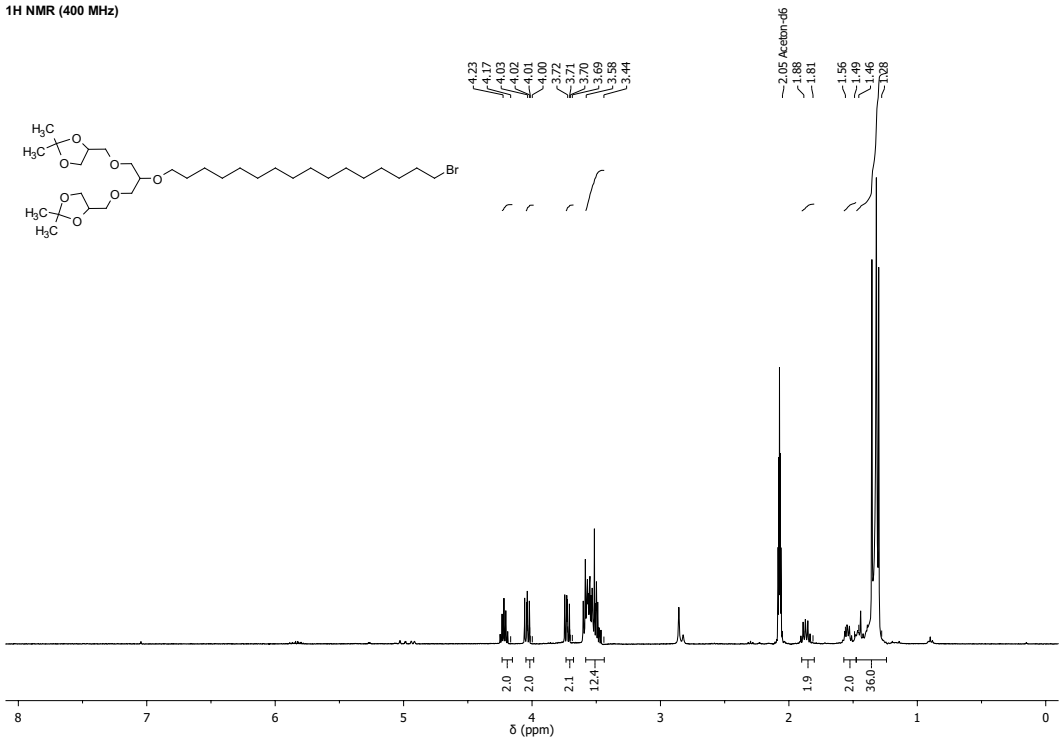

Figure D.3.: ^{1}H-NMR (400 MHz, Aceton-d_6) of Br-C16-pG1 **2c**.

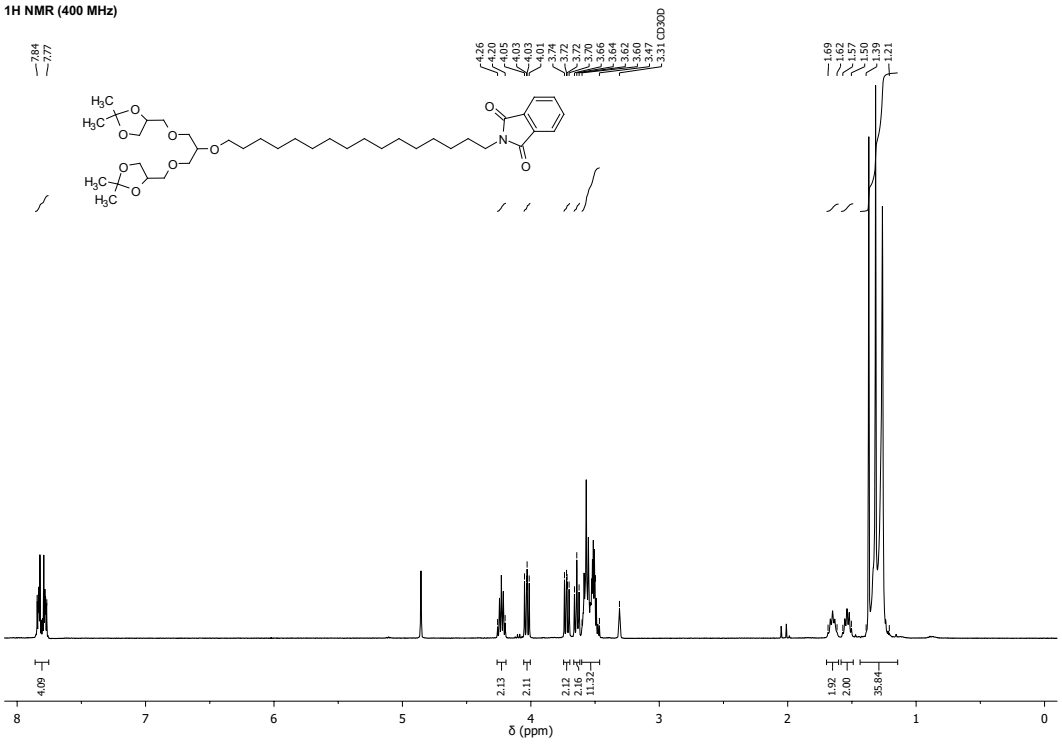

Figure D.4.: ^{1}H-NMR (400 MHz, Methanol-d_4) of Phth-C16-pG1 **3c**.

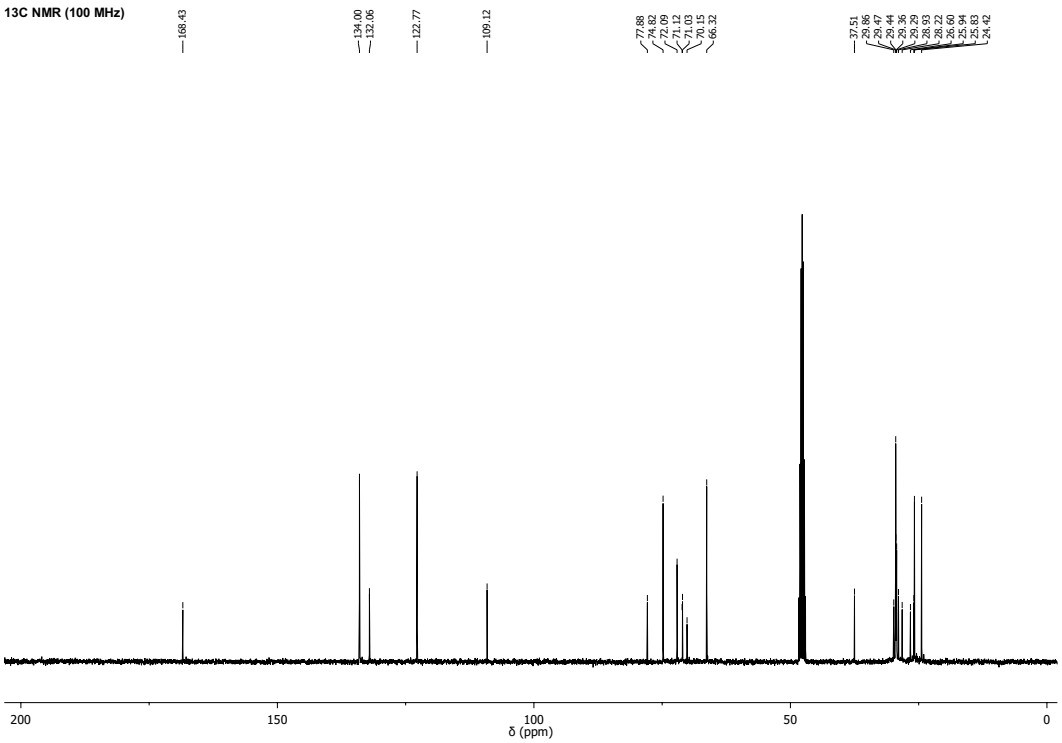

Figure D.5.: ^{13}C-NMR (100 MHz, Methanol-d_4) of Phth-C16-pG1 **3c**.

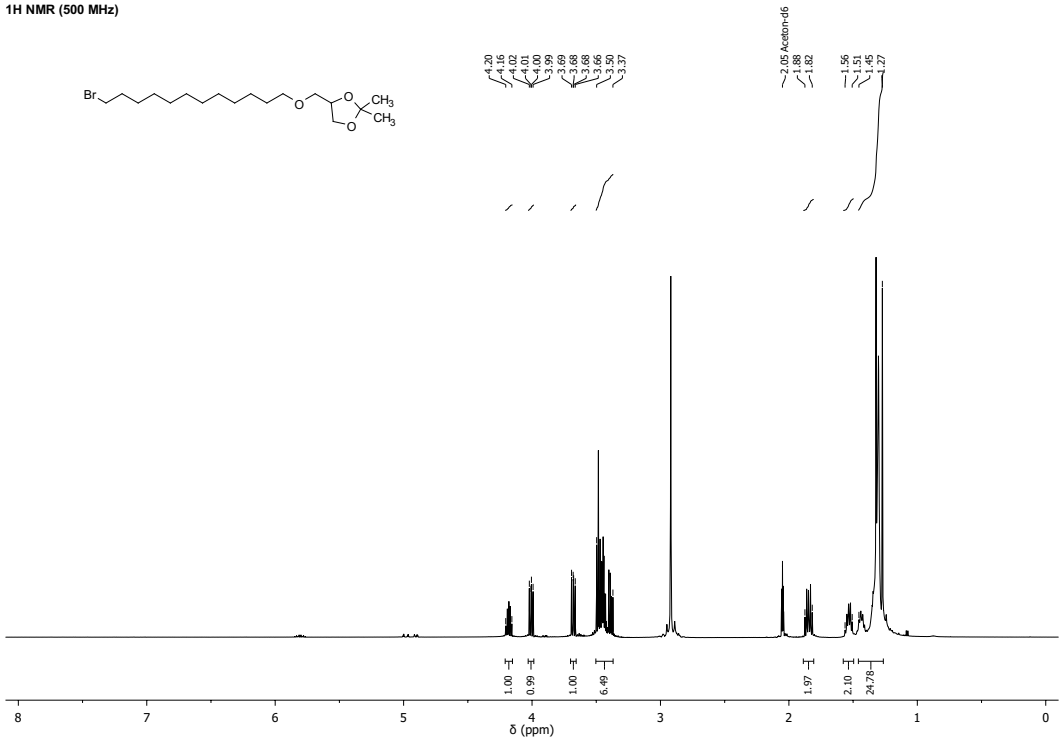

Figure D.6.: ^{1}H-NMR (500 MHz, Aceton-d_6) of pG0-C12-Br **2a**.

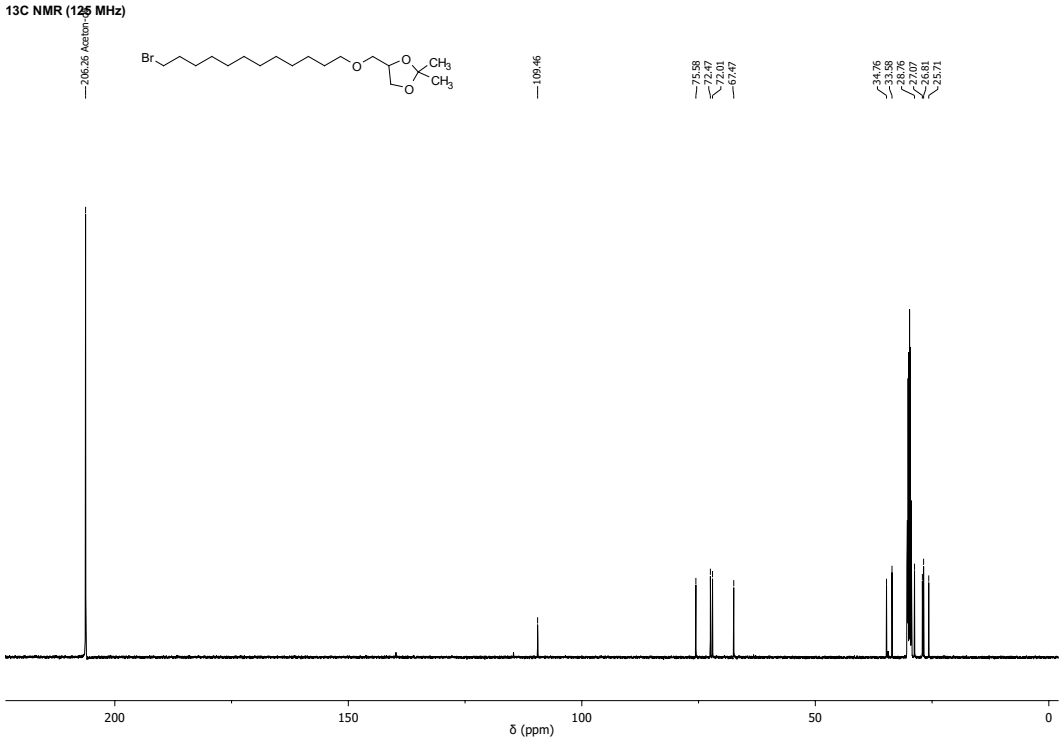

Figure D.7.: ^{13}C-NMR (125 MHz, Aceton-d_6) of pG0-C12-Br **2a**.

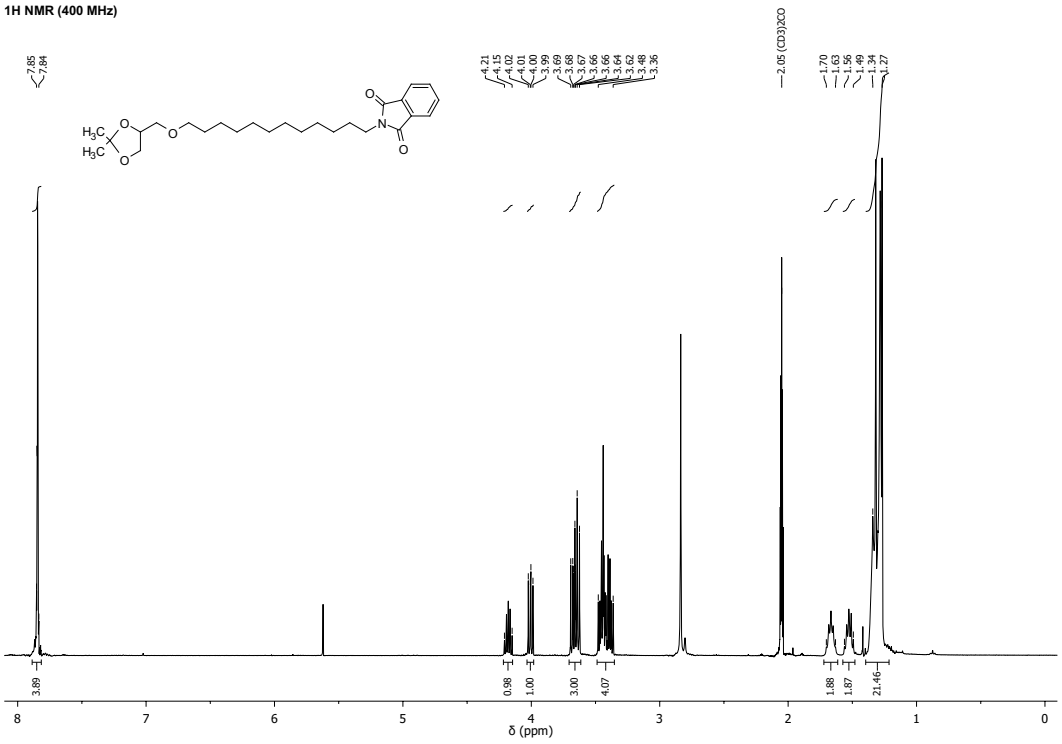

Figure D.8.: ^{1}H-NMR (400 MHz, Aceton-d_6) of Phth-C12-pG0 **3a**.

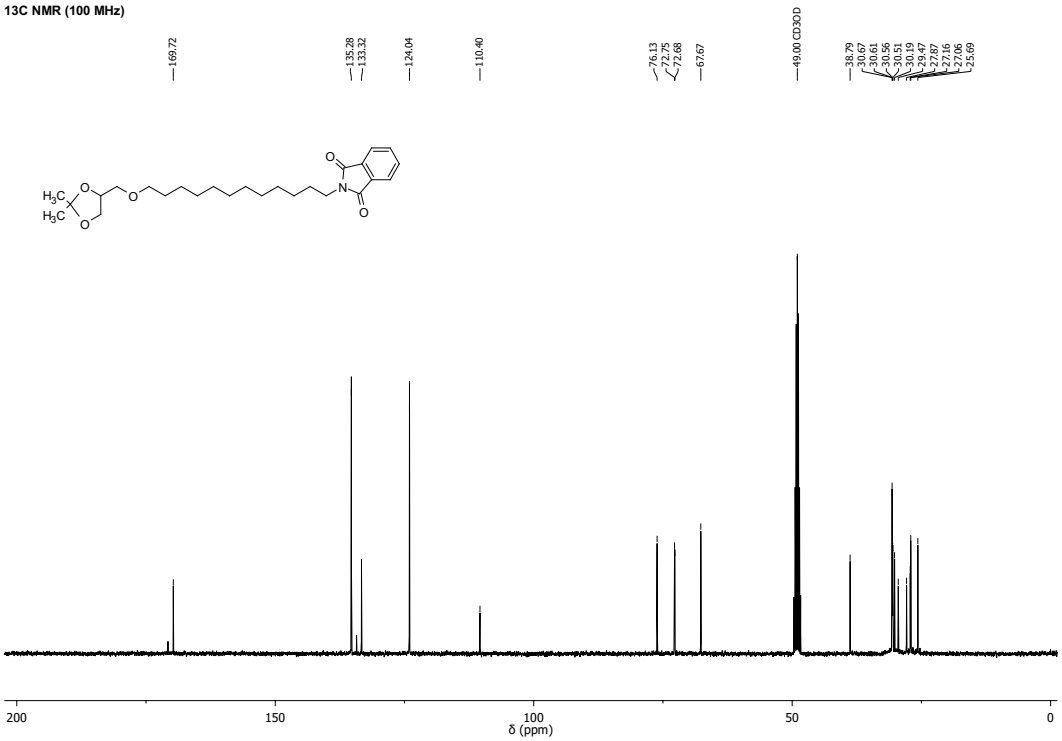

Figure D.9.: ^{13}C-NMR (100 MHz, Methanol-d_4) of Phth-C12-pG0 **3a**.

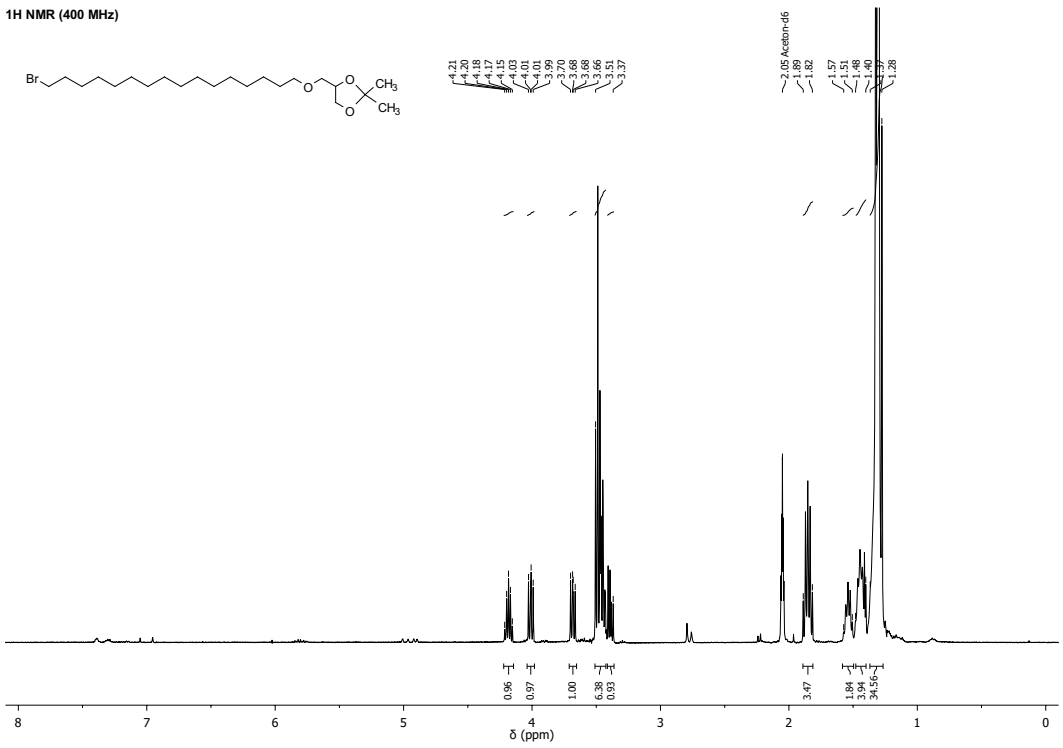

Figure D.10.: ^{1}H-NMR (400 MHz, Aceton-d_6) of Br-C16-pG0 **2b**.

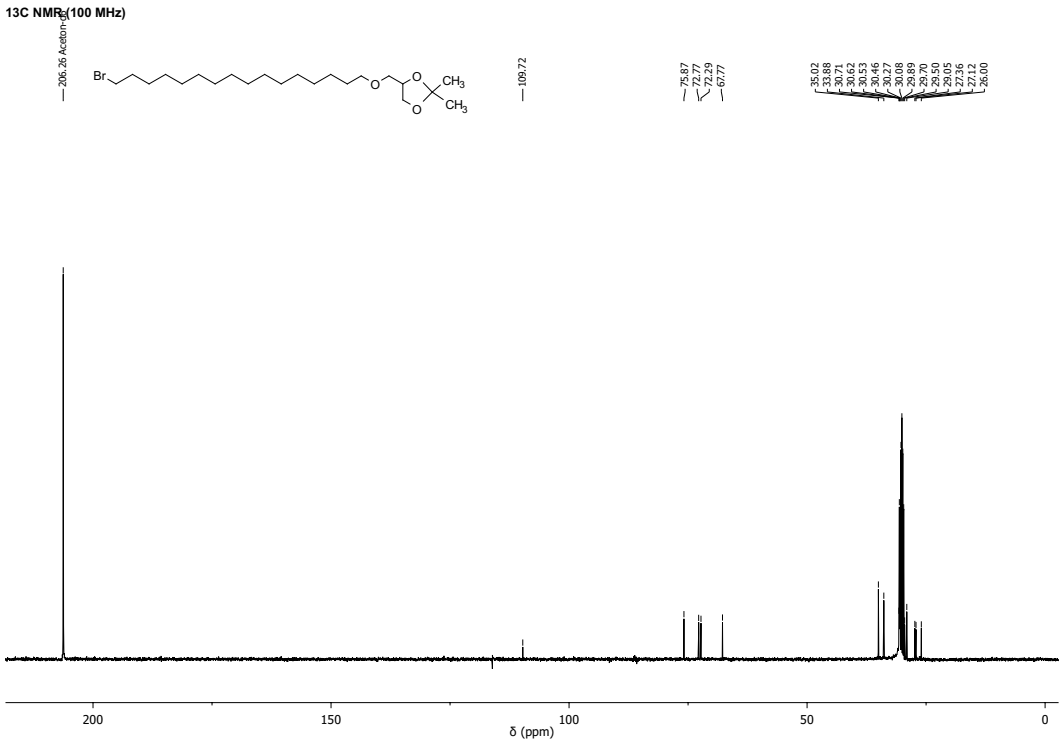

Figure D.11.: ^{13}C-NMR (100 MHz, Aceton-d_6) of Br-C16-pG0 **2b**.

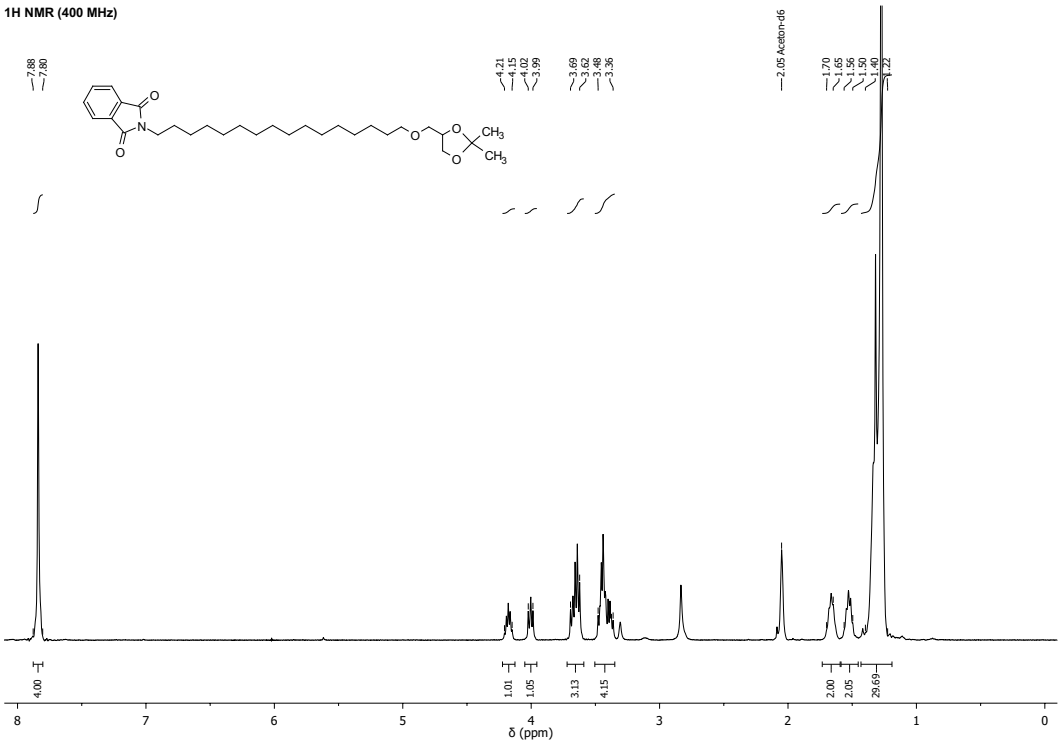

Figure D.12.: ^{1}H-NMR (400 MHz, Aceton-d_6) of Phth-C16-pG0 **3b**.

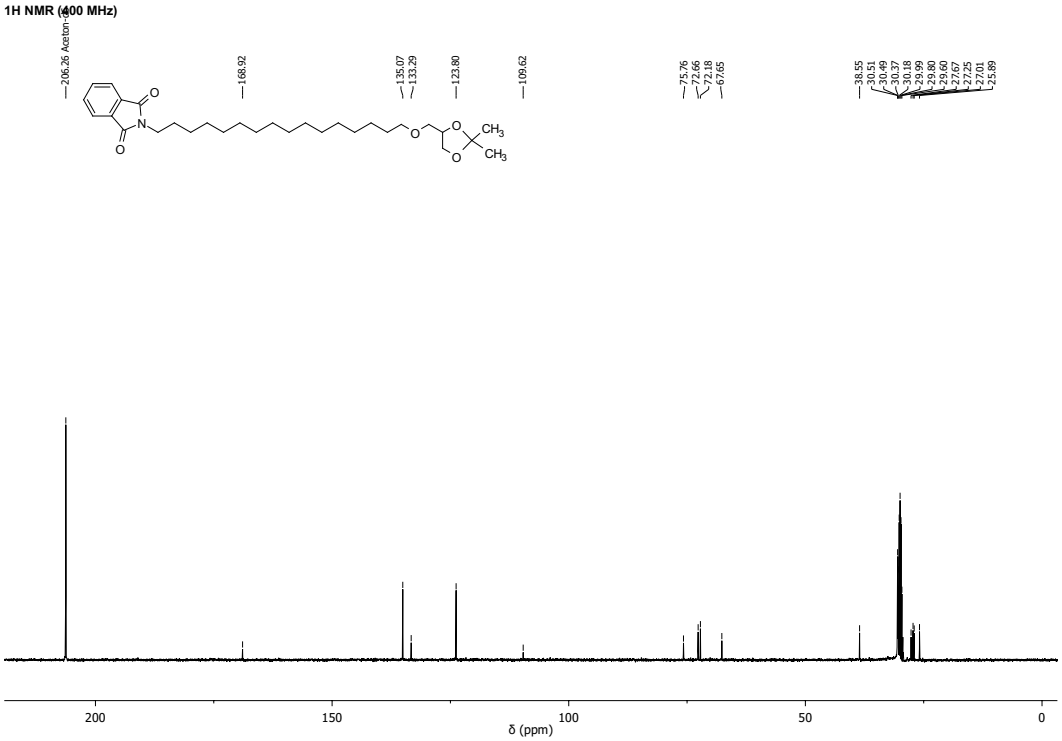

Figure D.13.: ^{13}C-NMR (100 MHz, Methanol-d_4) of Phth-C16-pG0 **3b**.

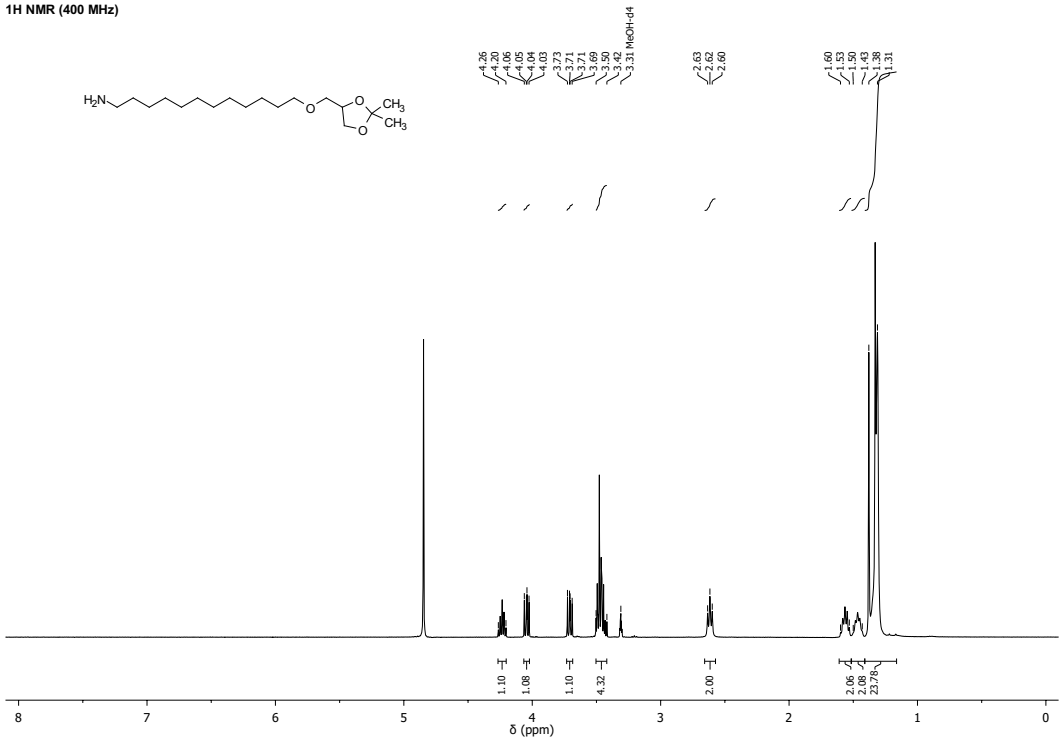

Figure D.14.: ^{1}H-NMR (400 MHz, Methanol-d_4) of NH_2-C12-pG0 **4a**.

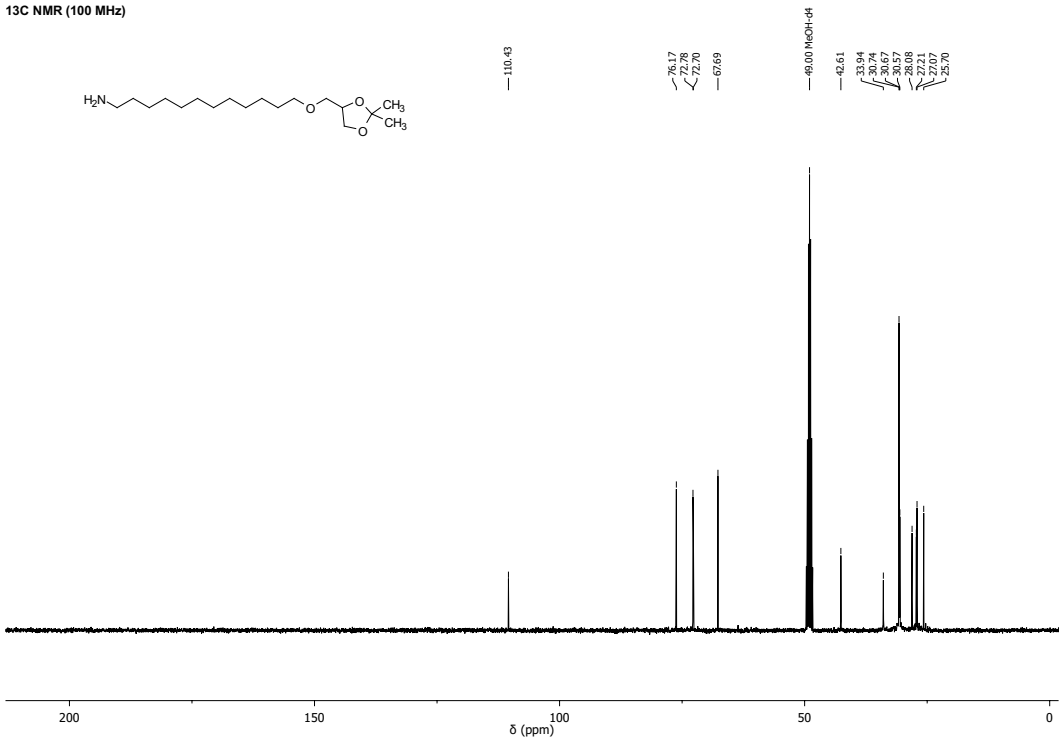

Figure D.15.: ^{13}C-NMR (100 MHz, Methanol-d_4) of NH_2-C12-pG0 **4a**.

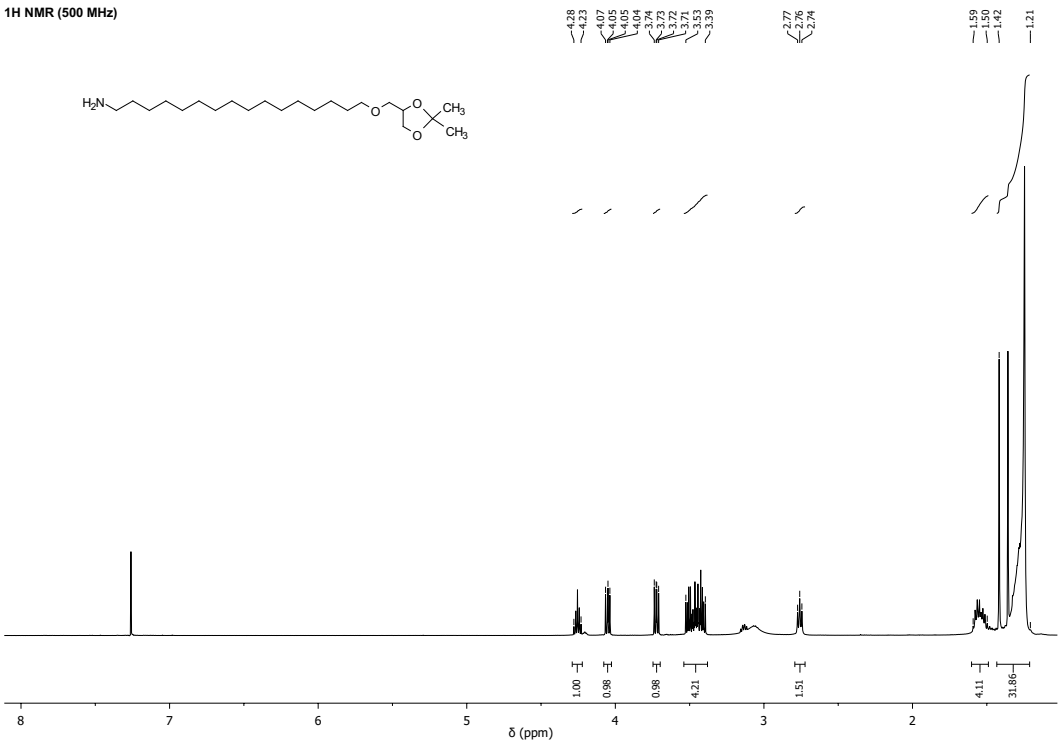

Figure D.16.: ^{1}H-NMR (500 MHz, Chloroform-d) of NH_2-C16-pG0 **4b**.

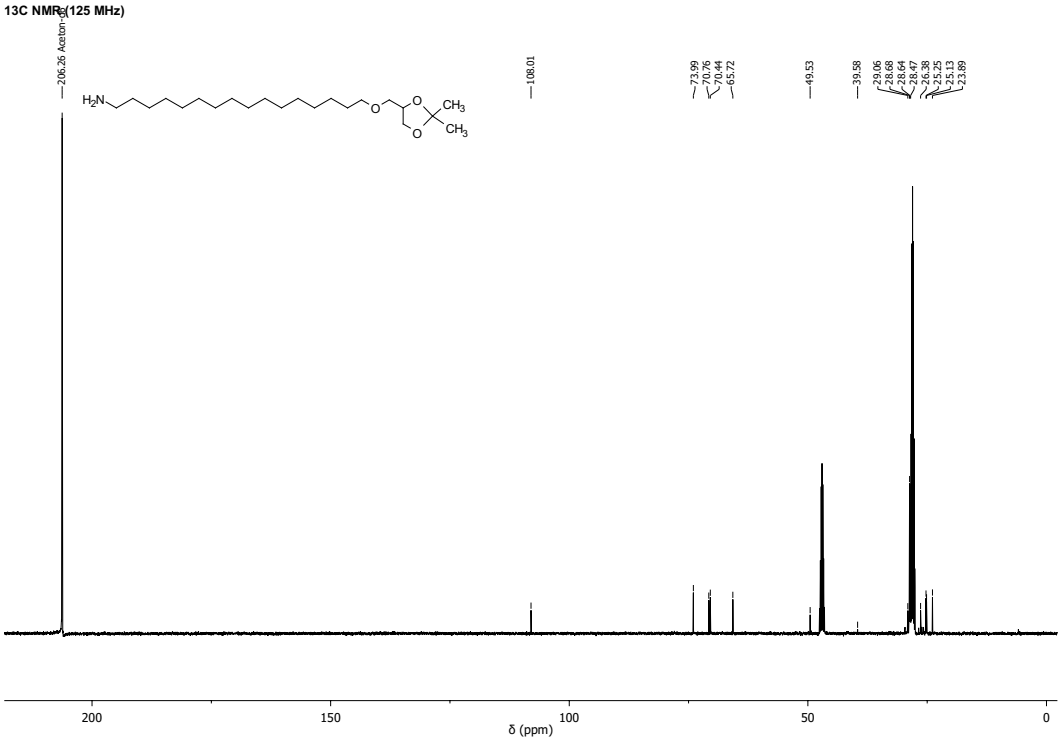

Figure D.17.: ^{13}C-NMR (125 MHz, Aceton-d_6) of NH_2-C16-pG0 **4b**.

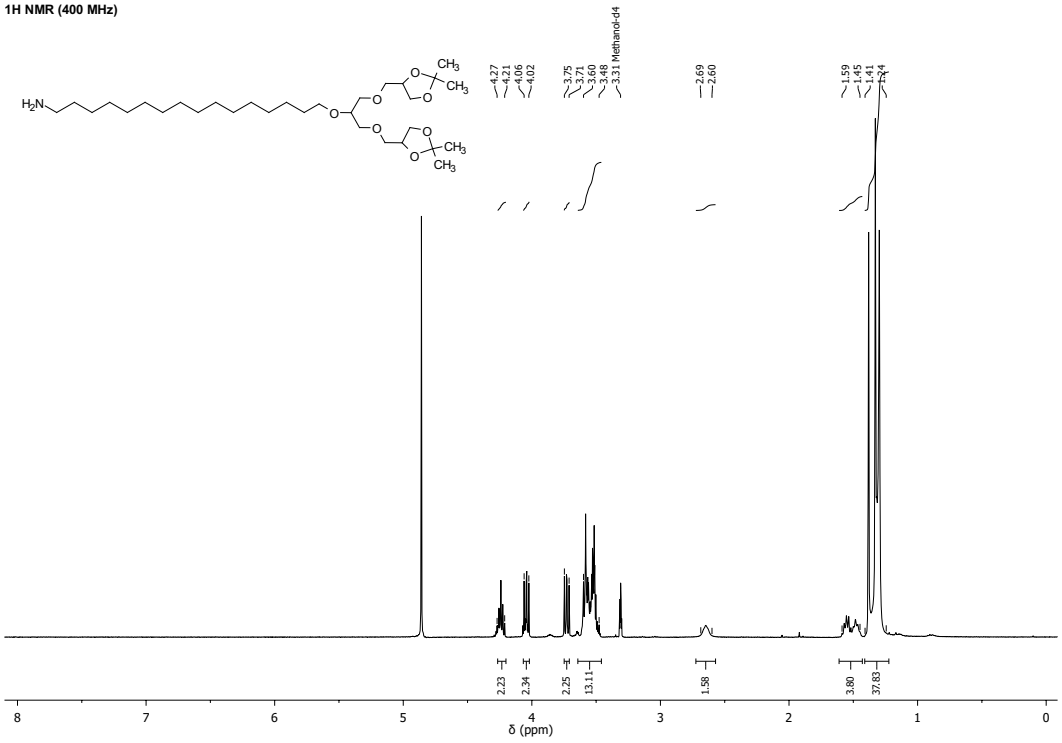

Figure D.18.: ^{1}H-NMR (400 MHz, Methanol-*d4*) of NH_2-C16-pG1 **4c**.

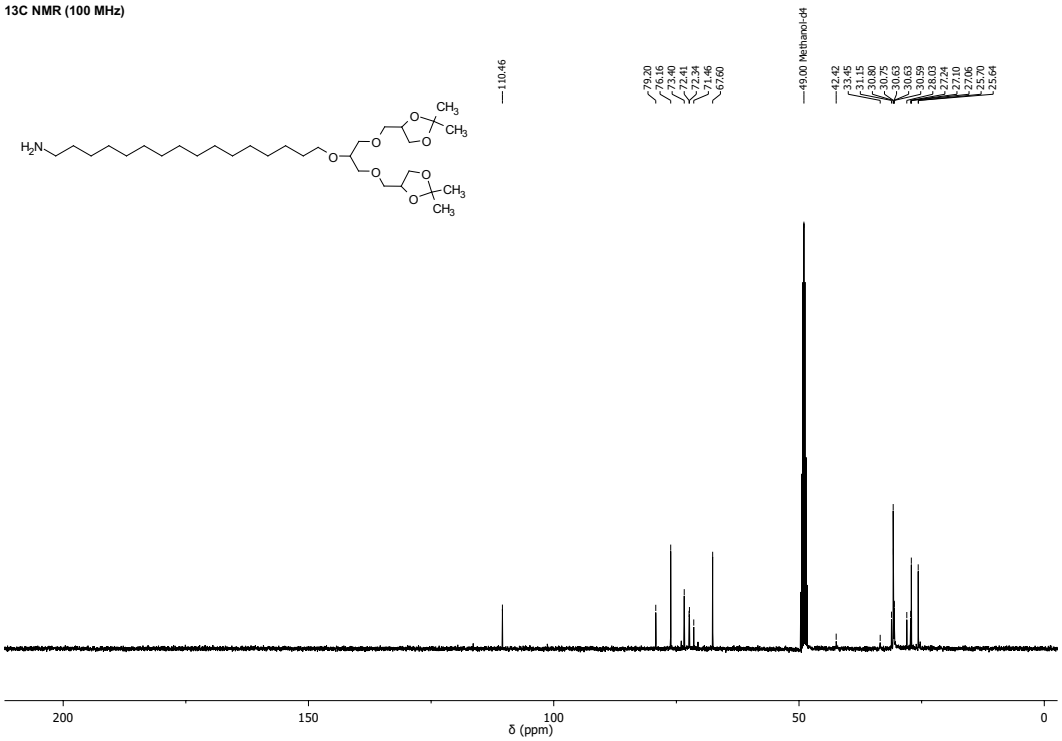

Figure D.19.: ^{13}C-NMR (100 MHz, Methanol-*d4*) of NH_2-C16-pG1 **4c**.

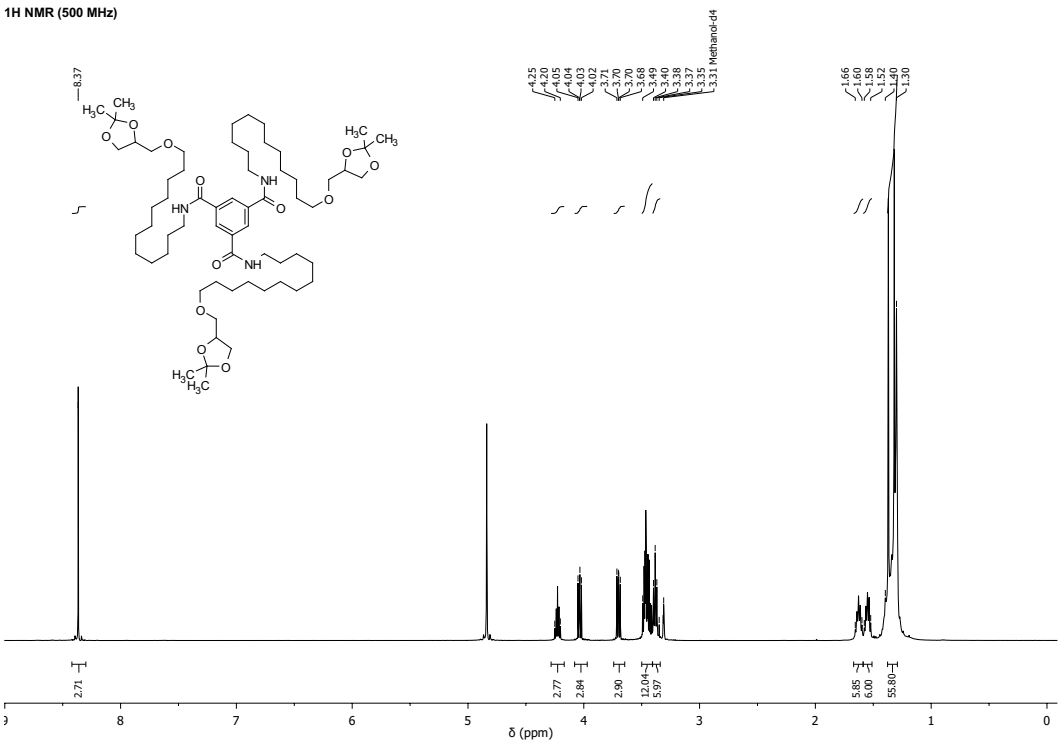

Figure D.20.: ^{1}H-NMR (500 MHz, Methanol-d_4) of BTA-C12-pG0 **5a**.

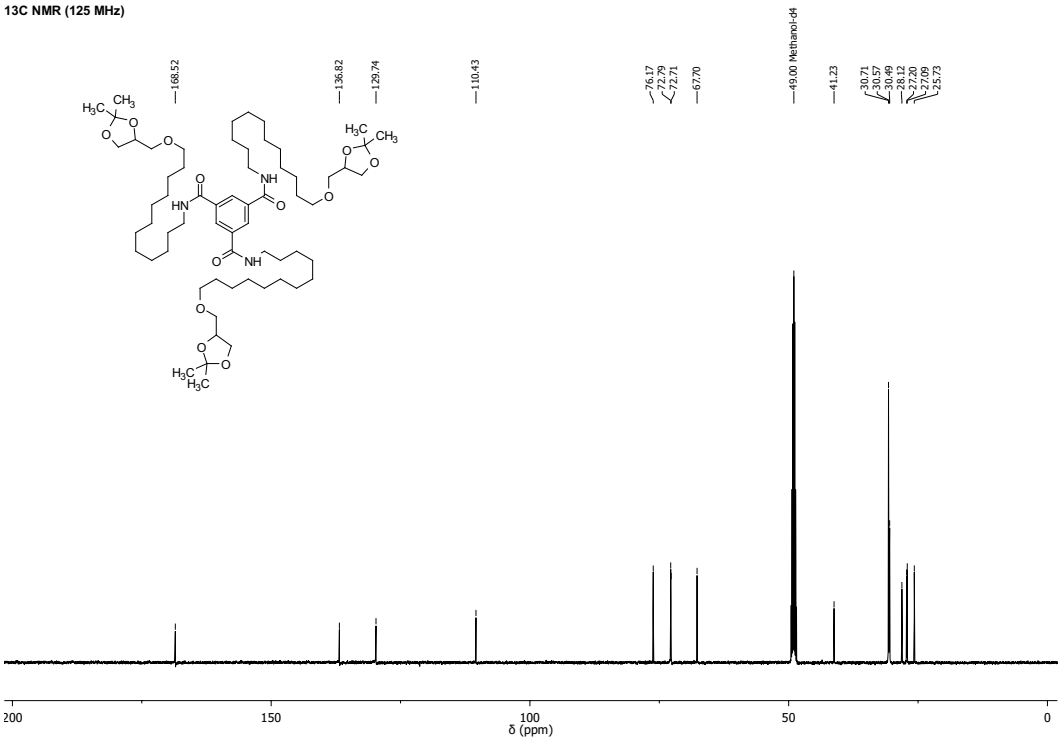

Figure D.21.: ^{13}C-NMR (125 MHz, Methanol-d_4) of BTA-C12-pG0 **5a**.

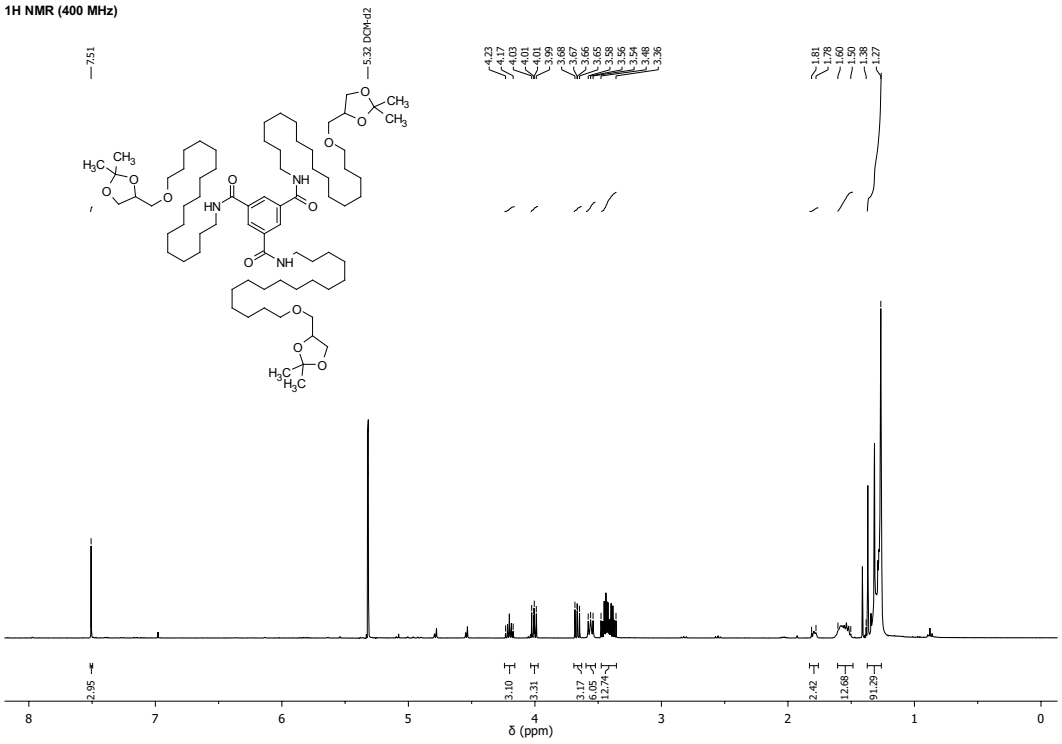

Figure D.22.: ^{1}H-NMR (400 MHz, DCM-d_4) of BTA-C16-pG0 **5b**.

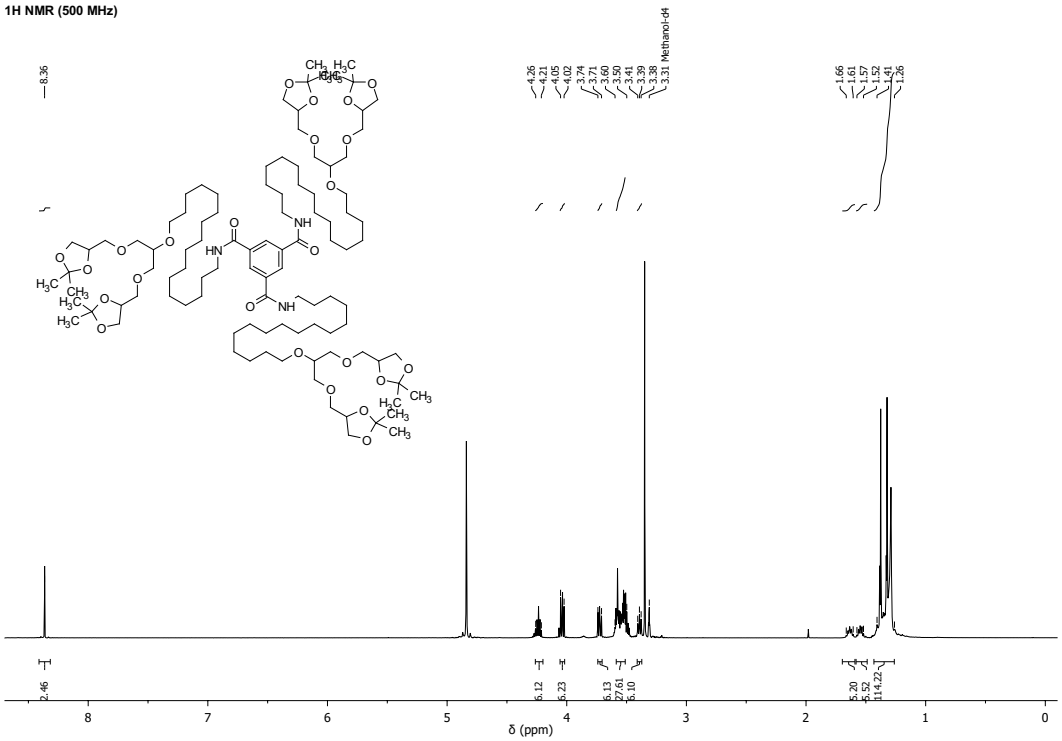

Figure D.23.: ^{1}H-NMR (500 MHz, Methanol-d_4) of BTA-C16-pG1 **5c**.

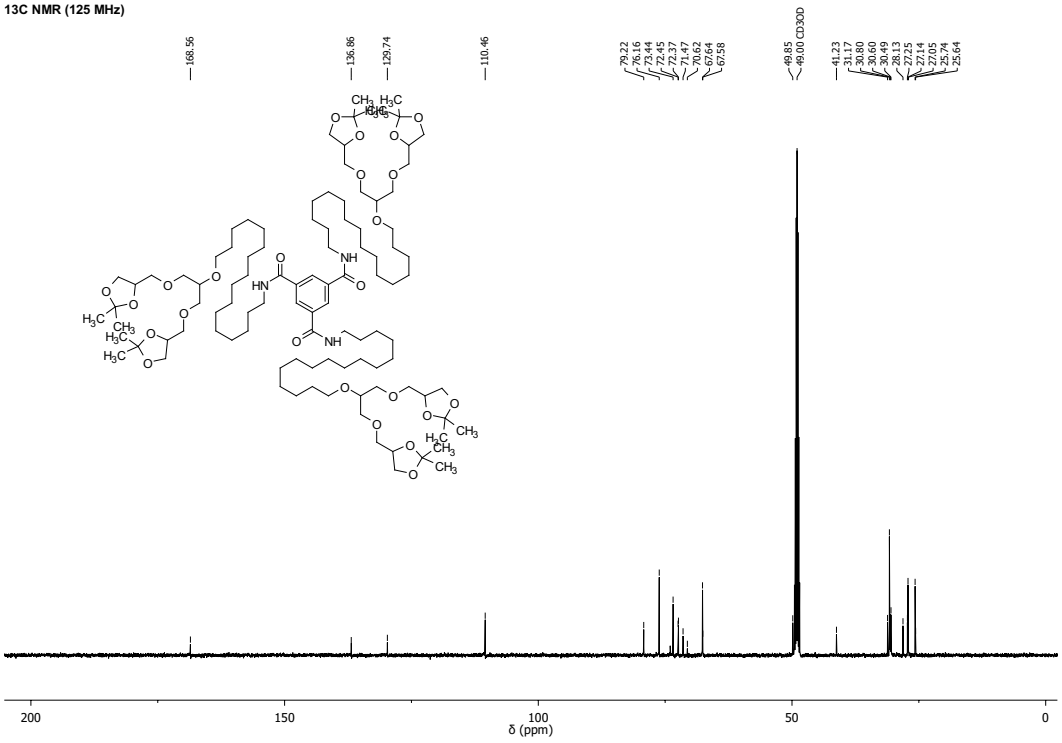

Figure D.24.: ^{13}C-NMR (125 MHz, Methanol-d_4) of BTA-C16-pG1 **5c**.

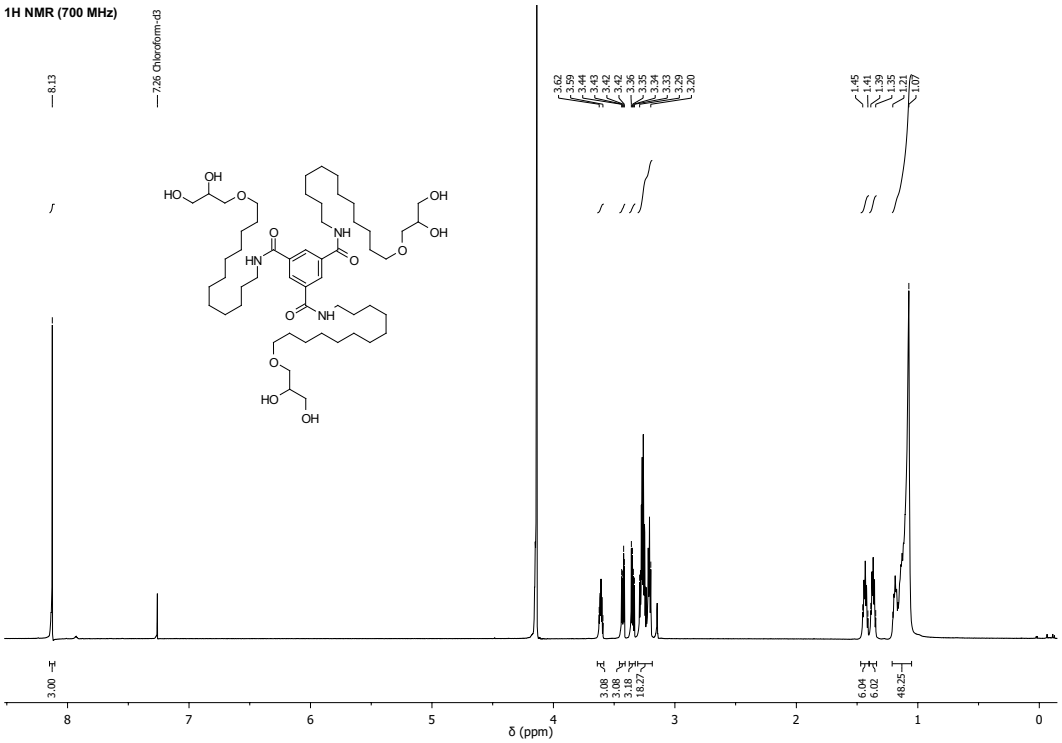

Figure D.25.: ^{1}H-NMR (700 MHz, Chloroform-d_3) of BTA-C12-G0 **6**.

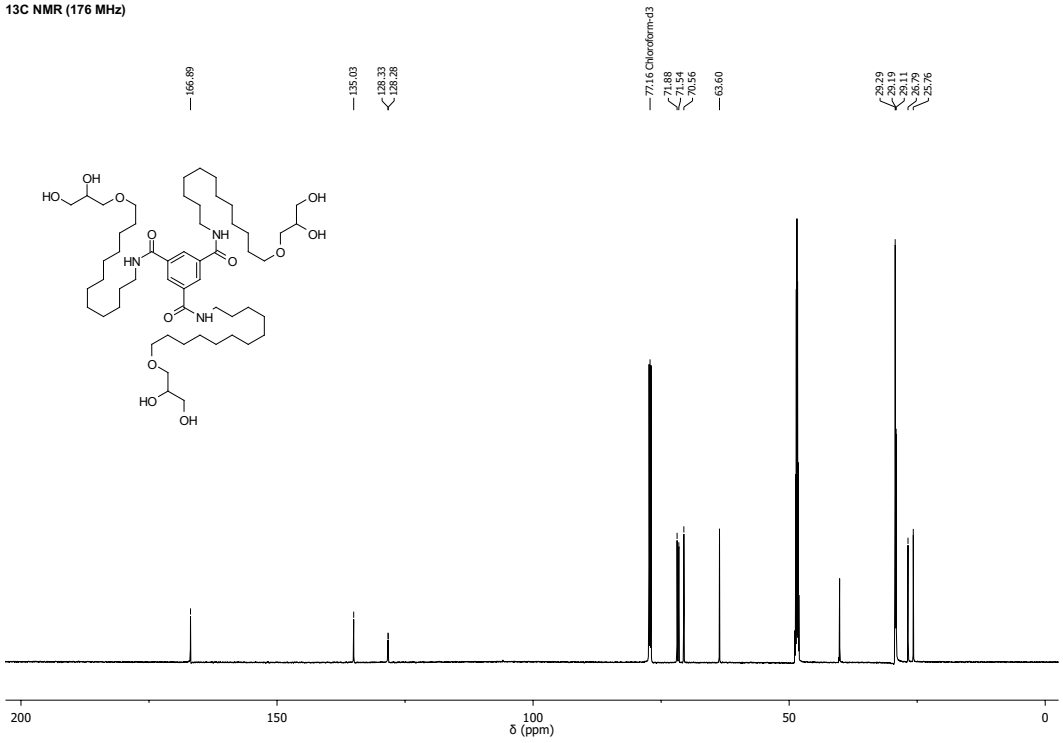

Figure D.26.: ^{13}C-NMR (176 MHz, Chloroform-d_3) of BTA-C12-G0 **6**.

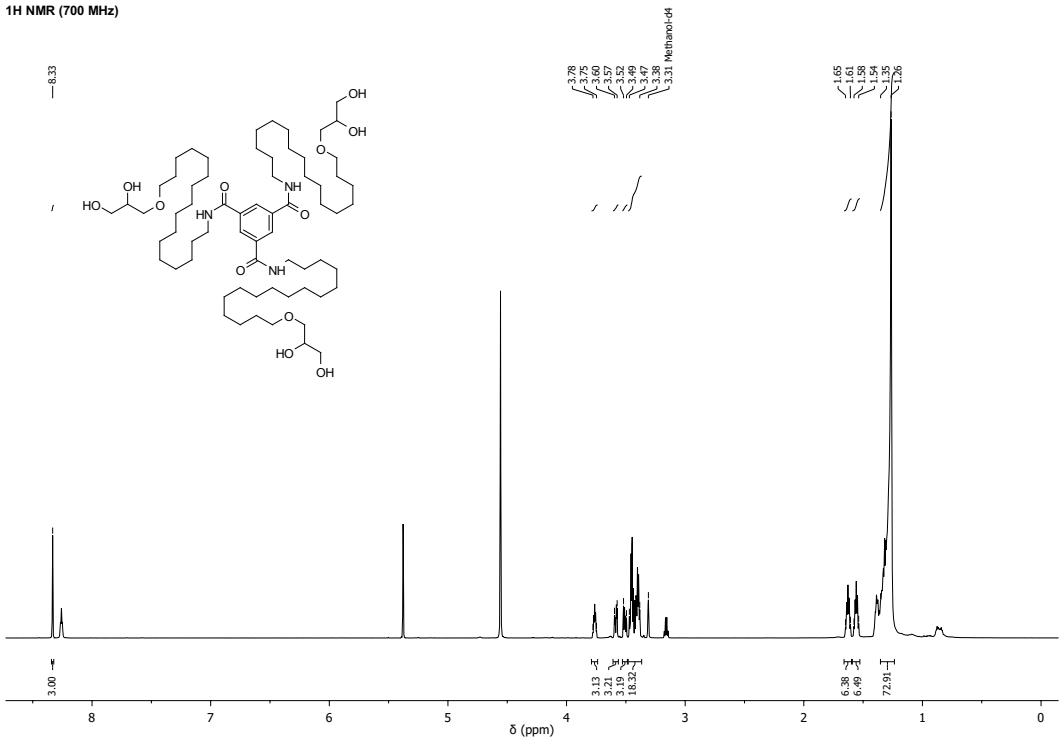

Figure D.27.: ^{1}H-NMR (700 MHz, Methanol-*d4* / DCM-*d2* 1:1) of BTA-C16-G0 **7**.

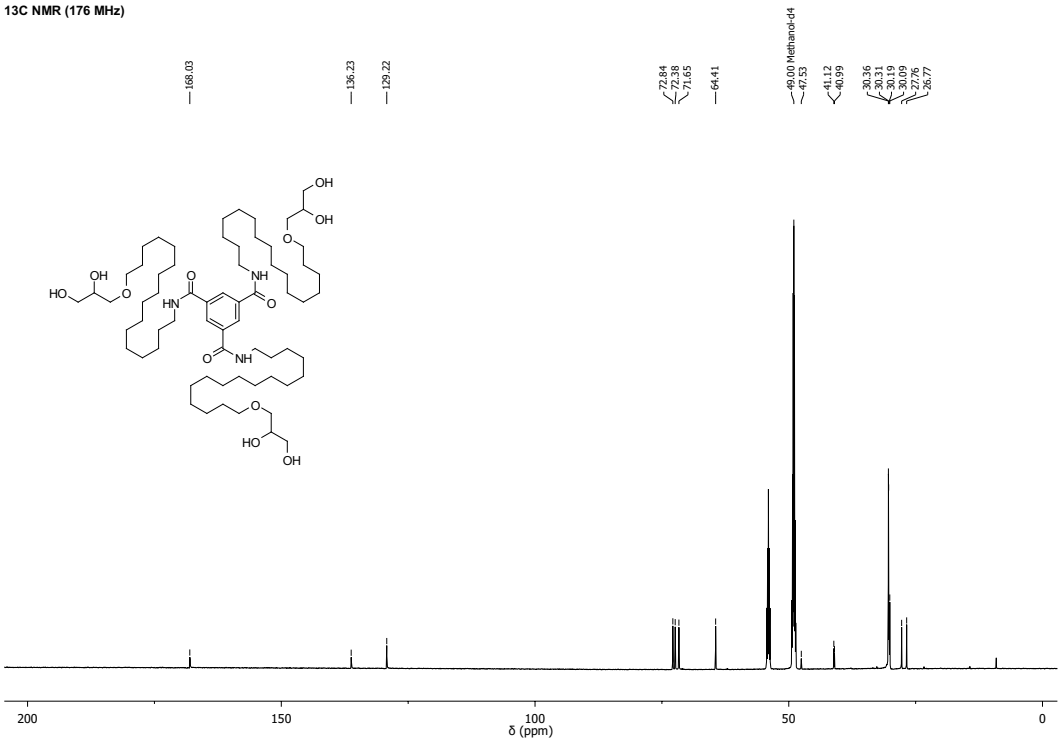

Figure D.28.: ^{13}C-NMR (176 MHz, Methanol-*d4* / DCM-*d2* 1:1) of BTA-C16-G0 **7**.

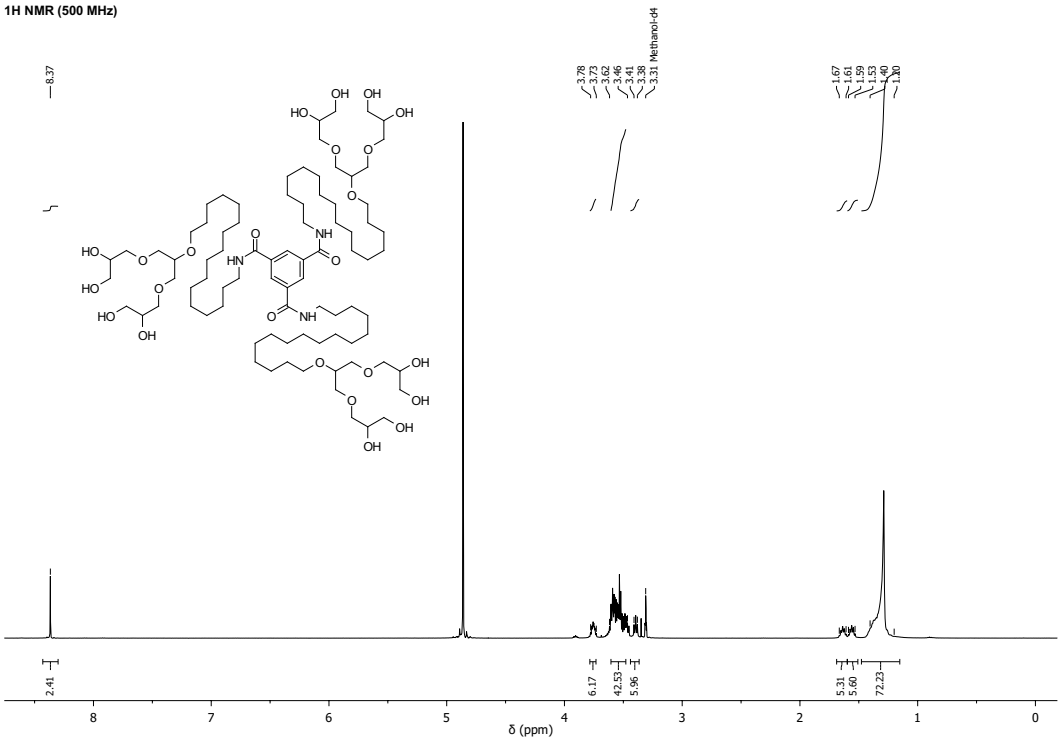

Figure D.29.: ^{1}H-NMR (500 MHz, Methanol-*d4*) of BTA-C16-G1 **8**.

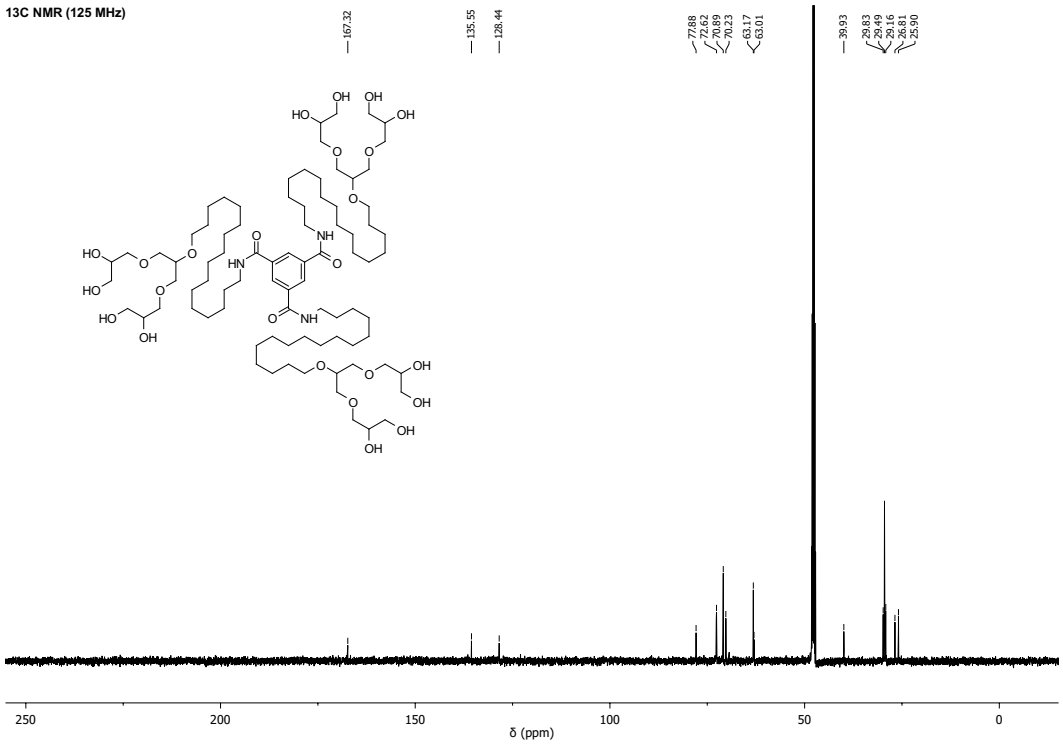

Figure D.30.: ^{13}C-NMR (125 MHz, Methanol-*d4*) of BTA-C16-G1 **8**.

Bibliography

[1] C. Tanford, *The hydrophobic effect: Formation of micelles and biological membranes*, John Wiley & Sons, New York, 2nd ed., **1980**.

[2] E. E. Meyer, K. J. Rosenberg, J. Israelachvili, *Proc. Natl. Acad. Sci. U.S.A.* **2006**, *103*, 15739–15746.

[3] E. Krieg, M. M. C. Bastings, P. Besenius, B. Rybtchinski, *Chem. Rev.* **2016**, *116*, 2414–2477.

[4] T. H. Rehm, C. Schmuck, *Chem. Soc. Rev.* **2010**, *39*, 3597–3611.

[5] J. D. Watson, F. H. C. Crick, *Nature* **1953**, *171*, 737–738.

[6] C. Fonseca Guerra, F. M. Bickelhaupt, J. G. Snijders, E. J. Baerends, *J. Am. Chem. Soc.* **2000**, *122*, 4117–4128.

[7] L. Pray, *Nature Education* **2008**, *1*, 100.

[8] J. N. Israelachvili, D. J. Mitchell, B. W. Ninham, *J. Chem. Soc. Faraday Trans. 2* **1976**, *72*, 1525–1568.

[9] J. N. Israelachvili, D. J. Mitchell, B. W. Ninham, *Biochimica et Biophysica Acta (BBA) - Biomembranes* **1977**, *470*, 185–201.

[10] R. Nagarajan, *Langmuir* **2002**, *18*, 31–38.

[11] B. N. S. Thota, L. H. Urner, R. Haag, *Chem. Rev.* **2016**, *116*, 2079 – 2102.

[12] B. M. Rosen, C. J. Wilson, D. A. Wilson, M. Peterca, M. R. Imam, V. Percec, *Chem. Rev.* **2009**, *109*, 6275–6540.

[13] F. Zeng, S. C. Zimmerman, *Chem. Rev.* **1997**, *97*, 1681–1712.

[14] A. Sunder, R. MÃ¼lhaupt, R. Haag, H. Frey, *Adv. Mater.* **2000**, *12*, 235–239.

[15] M. Calderon, M. A. Quadir, S. K. Sharma, R. Haag, *Adv. Mater.* **2010**, *22*, 190–218.

[16] J. Khandare, A. Mohr, M. Calderon, P. Welker, K. Licha, R. Haag, *Biomaterials* **2010**, *31*, 4268–77.

[17] J. Khandare, M. Calderón, N. M. Dagia, R. Haag, *Chem. Soc. Rev.* **2012**, *41*, 2824–2848.

[18] M. Wyszogrodzka, R. Haag, *Chem. Eur. J.* **2008**, *14*, 9202–9214.

[19] M. Wyszogrodzka, K. Möws, S. Kamlage, J. Wodzińska, B. Plietker, R. Haag, *Eur. J. Org. Chem.* **2008**, *2008*, 53–63.

[20] R. Haag, M. Wyszogrodzka, A. Wiedekind, A. Mohr, H. Rehage, B. Trappmann, *Linear-dendritische Polyglycerol-verbindungen Verfahren zu ihrer Herstellung und ihre Verwendung* **2008**, WO 2010000713A1.

[21] M. Sutter, E. D. Silva, N. Duguet, Y. Raoul, E. Métay, M. Lemaire, *Chem. Rev.* **2015**, *115*, 8609–8651.

[22] A. Martin, M. Richter, *Eur. J. Lipid Sci. Technol.* **2011**, *113*, 100–117.

[23] M. Kellermann, W. Bauer, A. Hirsch, B. Schade, K. Ludwig, C. Böttcher, *Angew. Chem. Int. Ed.* **2004**, *43*, 2959–2962.

[24] B. Trappmann, K. Ludwig, M. R. Radowski, A. Shukla, A. Mohr, H. Rehage, C. Böttcher, R. Haag, *J. Am. Chem. Soc.* **2010**, *132*, 11119–11124.

[25] L. C. Palmer, S. I. Stupp, *Acc. Chem. Res.* **2008**, *41*, 1674–1684.

[26] L. H. Urner, B. N. S. Thota, O. Nachtigall, S. Warnke, G. von Helden, R. Haag, K. Pagel, *Chem. Commun.* **2015**, *51*, 8801–8804.

[27] B. N. S. Thota, H. v. Berlepsch, C. Böttcher, R. Haag, *Chem. Commun.* **2015**, *51*, 8648–8651.

[28] B. N. S. Thota, X. Lou, D. Bochicchio, T. F. E. Paffen, R. P. M. Lafleur, J. L. J. van Dongen, S. Ehrmann, R. Haag, G. M. Pavan, A. R. A. Palmans, E. W. Meijer, *Angewandte Chemie-International Edition* **2018**, *57*, 6843–6847.

[29] A. C. Rodrigo, S. Malhotra, C. Böttcher, M. Adeli, R. Haag, *RSC Adv.* **2014**, *4*, 61656–61659.

[30] L. Brunsveld, B. J. B. Folmer, E. W. Meijer, R. P. Sijbesma, *Chem. Rev.* **2001**, *101*, 4071–4098.

[31] T. Aida, E. W. Meijer, S. I. Stupp, *Science* **2012**, *335*, 813.

[32] T. F. A. De Greef, M. M. J. Smulders, M. Wolffs, A. P. H. J. Schenning, R. P. Sijbesma, E. W. Meijer, *Chem. Rev.* **2009**, *109*, 5687–5754.

[33] A. W. Bosman, L. Brunsveld, B. Folmer, R. P. Sijbesma, E. W. Meijer, *Macromol. Symp.* **2003**, *201*, 143–154.

[34] L. Yang, X. Tan, Z. Wang, X. Zhang, *Chem. Rev.* **2015**, *115*, 7196–7239.

[35] T. F. A. de Greef, E. W. Meijer, *Nature* **2008**, *453*, 171.

[36] T. D. Pollard, J. A. Cooper, *Science* **2009**, *326*, 1208.

[37] T. P. J. Knowles, M. Vendruscolo, C. M. Dobson, *Nat. Rev. Mol. Cell Biol.* **2014**, *15*, 384.

[38] A. W. P. Fitzpatrick, G. T. Debelouchina, M. J. Bayro, D. K. Clare, M. A. Caporini, V. S. Bajaj, C. P. Jaroniec, L. Wang, V. Ladizhansky, S. A. Müller, C. E. MacPhee, C. A. Waudby, H. R. Mott, A. De Simone, T. P. J. Knowles, H. R. Saibil, M. Vendruscolo, E. V. Orlova, R. G. Griffin, C. M. Dobson, *Proc. Natl. Acad. Sci. U.S.A.* **2013**, *110*, 5468.

[39] N. Carulla, G. L. Caddy, D. R. Hall, J. Zurdo, M. Gairí, M. Feliz, E. Giralt, C. V. Robinson, C. M. Dobson, *Nature* **2005**, *436*, 554–558.

[40] K. Liu, Y. Kang, Z. Wang, X. Zhang, *Adv. Mater.* **2013**, *25*, 5530–5548.

[41] R. P. Sijbesma, F. H. Beijer, L. Brunsveld, B. J. B. Folmer, J. H. K. K. Hirschberg, R. F. M. Lange, J. K. L. Lowe, E. W. Meijer, *Science* **1997**, *278*, 1601.

[42] P. Y. W. Dankers, T. M. Hermans, T. W. Baughman, Y. Kamikawa, R. E. Kieltyka, M. M. C. Bastings, H. M. Janssen, N. A. J. M. Sommerdijk, A. Larsen, M. J. A. van Luyn, A. W. Bosman, E. R. Popa, G. Fytas, E. W. Meijer, *Adv. Mater.* **2012**, *24*, 2703–2709.

[43] O. J. G. M. Goor, S. I. S. Hendrikse, P. Y. W. Dankers, E. W. Meijer, *Chem. Soc. Rev.* **2017**, *46*, 6621–6637.

[44] P. Besenius, Y. Goedegebure, M. Driesse, M. Koay, P. H. H. Bomans, A. R. A. Palmans, P. Y. W. Dankers, E. W. Meijer, *Soft Matter* **2011**, *7*, 7980–7983.

[45] C. M. A. Leenders, L. Albertazzi, T. Mes, M. M. E. Koenigs, A. R. A. Palmans, E. W. Meijer, *Chem. Commun.* **2013**, *49*, 1963–1965.

[46] S. Cantekin, T. F. A. de Greef, A. R. A. Palmans, *Chem. Soc. Rev.* **2012**, *41*, 6125–6137.

[47] C. M. A. Leenders, G. Jansen, M. M. M. Frissen, R. P. M. Lafleur, I. K. Voets, A. R. A. Palmans, E. W. Meijer, *Chem. Eur. J.* **2016**, *22*, 4608–4615.

[48] D. Bochicchio, G. M. Pavan, *ACS Nano* **2017**, *11*, 1000–1011.

[49] M. Garzoni, M. B. Baker, C. M. A. Leenders, I. K. Voets, L. Albertazzi, A. R. A. Palmans, E. W. Meijer, G. M. Pavan, *J. Am. Chem. Soc.* **2016**, 13985–13995.

[50] X. Lou, R. P. M. Lafleur, C. M. A. Leenders, S. M. C. Schoenmakers, N. M. Matsumoto, M. B. Baker, J. L. J. van Dongen, A. R. A. Palmans, E. W. Meijer, *Nat. Commun.* **2017**, *8*, 15420.

[51] D. Bochicchio, M. Salvalaglio, G. M. Pavan, *Nat. Commun.* **2017**, *8*, 147.

[52] C. Fouquey, J.-M. Lehn, A.-M. Levelut, *Adv. Mater.* **1990**, *2*, 254–257.

[53] B. Adelizzi, N. J. Van Zee, L. N. J. de Windt, A. R. A. Palmans, E. W. Meijer, *J. Am. Chem. Soc.* **2019**, *141*, 6110–6121.

[54] B. Adelizzi, A. Aloi, A. J. Markvoort, H. M. M. Ten Eikelder, I. K. Voets, A. R. A. Palmans, E. W. Meijer, *J. Am. Chem. Soc.* **2018**, *140*, 7168–7175.

[55] M. Liu, L. Zhang, T. Wang, *Chem. Rev.* **2015**, *115*, 7304–7397.

[56] F. Biedermann, H.-J. Schneider, *Chem. Rev.* **2016**, *116*, 5216–5300.

[57] M. Szwarc, *The Journal of Physical Chemistry* **1958**, *62*, 568–569.

[58] M. C. T. Fyfe, J. F. Stoddart, *Acc. Chem. Res.* **1997**, *30*, 393–401.

[59] G. Vantomme, E. W. Meijer, *Science* **2019**, *363*, 1396.

[60] L. Albertazzi, F. J. Martinez-Veracoechea, C. M. A. Leenders, I. K. Voets, D. Frenkel, E. W. Meijer, *Proc. Natl. Acad. Sci. U.S.A.* **2013**, *110*, 12203–12208.

[61] L. Albertazzi, D. van der Zwaag, C. M. A. Leenders, R. Fitzner, R. W. van der Hofstad, E. W. Meijer, *Science* **2014**, *344*, 491–495.

[62] A. Das, G. Vantomme, A. J. Markvoort, H. M. M. ten Eikelder, M. Garcia-Iglesias, A. R. A. Palmans, E. W. Meijer, *J. Am. Chem. Soc.* **2017**, *139*, 7036–7044.

[63] C. Böttcher in *Transmission Electron Microscopy (TEM) of Radiation Sensitive Supramolecular Architectures - Strategies for a Comprehensive Structure Characterization* (Ed.: C. A. Schalley), John Wiley & Sons, Ltd, **2012**, book section 14.

[64] D. Danino, *Curr. Opin. Colloid Interface Sci.* **2012**, *17*, 316–329.

[65] R. Danev, B. Buijsse, M. Khoshouei, J. M. Plitzko, W. Baumeister, *Proc. Natl. Acad. Sci. U.S.A.* **2014**, *111*, 15635–15640.

[66] H. Engelhardt in *Elektronenmikroskopie* (Eds.: F. Lottspeich, J. W. Engels), Spektrum Akademischer Verlag, 3rd ed., **2011**, book section 20.

[67] L. Reimer, H. Kohl, *Transmission Electron Micrsocopy - Physics of Image Formation*, Springer-Verlag, New York, **2008**.

[68] R. Danev, K. Nagayama, *Ultramicroscopy* **2001**, *88*, 243–252.

[69] R. Danev, W. Baumeister, *Curr. Opin. Struct. Biol.* **2017**, *46*, 87–94.

[70] R. Danev, D. Tegunov, W. Baumeister, *eLife* **2017**, *6*, e23006.

[71] https://www.nobelprize.org/prizes/chemistry/2017/press release/, **2017**, `Lastaccess17.04.2019`.

[72] P. S. Shen, *J Analytical Bioanalytical Chemistry* **2018**, *410*, 2053–2057.

[73] J. Dubochet, A. W. McDowall, *J. Microsc.* **1981**, *124*, 3–4.

[74] J. Dubochet, M. Adrian, J.-J. Chang, J.-C. Homo, J. Lepault, A. W. McDowall, P. Schultz, *Q. Rev. Biophys.* **1988**, *21*, 129–228.

[75] R. Henderson, J. M. Baldwin, T. A. Ceska, F. Zemlin, E. Beckmann, K. H. Downing, *J. Mol. Biol.* **1990**, *213*, 899–929.

[76] J. Frank, *Ultramicroscopy* **1975**, *1*, 159–162.

[77] M. van Heel, J. Frank, *Ultramicroscopy* **1981**, *6*, 187–194.

[78] M. van Heel, *Ultramicroscopy* **1984**, *13*, 165–183.

[79] M. van Heel, G. Harauz, E. V. Orlova, R. Schmidt, M. Schatz, *J. Struct. Biol.* **1996**, *116*, 17–24.

[80] J. Frank, *Electron Tomography - Methods for Three-Dimensional Visualization of Structures in the Cell*, Springer-Verlag New York, 2nd ed., **2006**.

[81] Z. Su, C. Wu, L. Shi, P. Luthra, G. D. Pintilie, B. Johnson, J. R. Porter, P. Ge, M. Chen, G. Liu, T. E. Frederick, J. M. Binning, G. R. Bowman, Z. H. Zhou, C. F. Basler, M. L. Gross, D. W. Leung, W. Chiu, G. K. Amarasinghe, *Cell* **2018**, *172*, 966–978.e12.

[82] Y. Sugita, H. Matsunami, Y. Kawaoka, T. Noda, M. Wolf, *Nature* **2018**, *563*, 137–140.

[83] D. Sirohi, Z. Chen, L. Sun, T. Klose, T. C. Pierson, M. G. Rossmann, R. J. Kuhn, *Science* **2016**, *352*, 467.

[84] M. Sevvana, F. Long, A. S. Miller, T. Klose, G. Buda, L. Sun, R. J. Kuhn, M. G. Rossmann, *Structure* **2018**, *26*, 1169–1177.e3.

[85] H. v. Berlepsch, K. Ludwig, B. Schade, R. Haag, C. Böttcher, *Adv. Colloid Interface Sci.* **2014**, *208*, 279–292.

[86] H. Friedrich, P. M. Frederik, G. de With, N. A. J. M. Sommerdijk, *Angew. Chem. Int. Ed.* **2010**, *49*, 7850–7858.

[87] C. Böttcher, B. Schade, C. Ecker, J. P. Rabe, L. Shu, A. D. Schlüter, *Chem. Eur. J.* **2005**, *11*, 2923–2928.

[88] C. Böttcher, H. Stark, M. van Heel, *Ultramicroscopy* **1996**, *62*, 133–139.

[89] N. Sharon, H. Lis, *Science* **1989**, *246*, 227.

[90] C. Fasting, C. A. Schalley, M. Weber, O. Seitz, S. Hecht, B. Koksch, J. Dernedde, C. Graf, E.-W. Knapp, R. Haag, *Angew. Chem. Int. Ed.* **2012**, *51*, 10472–10498.

[91] M. Mammen, S. K. Choi, G. M. Whitesides, *Angew. Chem. Int. Ed.* **1998**, *37*, 2754–2794.

[92] G. Ercolani, C. Piguet, M. Borkovec, J. Hamacek, *The Journal of Physical Chemistry B* **2007**, *111*, 12195–12203.

[93] J. D. Badjić, A. Nelson, S. J. Cantrill, W. B. Turnbull, J. F. Stoddart, *Acc. Chem. Res.* **2005**, *38*, 723–732.

[94] T. K. Dam, R. Roy, D. Pagé, C. F. Brewer, *Biochemistry* **2002**, *41*, 1351–1358.

[95] Y. Kim, Z. Cao, W. Tan, *Proc. Natl. Acad. Sci. U.S.A.* **2008**, *105*, 5664.

[96] M. L. Talaga, N. Fan, A. L. Fueri, R. K. Brown, Y. M. Chabre, P. Bandyopadhyay, R. Roy, T. K. Dam, *Biochemistry* **2014**, *53*, 4445–4454.

[97] E. M. Munoz, J. Correa, R. Riguera, E. Fernandez-Megia, *J. Am. Chem. Soc.* **2013**, *135*, 5966–5969.

[98] T. K. Dam, C. F. Brewer, *Biochemistry* **2008**, *47*, 8470–8476.

[99] J. E. Gestwicki, C. W. Cairo, L. E. Strong, K. A. Oetjen, L. L. Kiessling, *J. Am. Chem. Soc.* **2002**, *124*, 14922–14933.

[100] J. Vonnemann, S. Liese, C. Kuehne, K. Ludwig, J. Dernedde, C. Böttcher, R. R. Netz, R. Haag, *J. Am. Chem. Soc.* **2015**, *137*, 2572–2579.

[101] S. Bhatia, L. C. Camacho, R. Haag, *J. Am. Chem. Soc.* **2016**, *138*, 8654–8666.

[102] M. E. Taylor, K. Drickamer, *Curr. Opin. Cell Biol.* **2007**, *19*, 572–577.

[103] C. Müller, G. Despras, T. K. Lindhorst, *Chem. Soc. Rev.* **2016**, *45*, 3275–3302.

[104] H. Lis, N. Sharon, *Chem. Rev.* **1998**, *98*, 637–674.

[105] J. J. Lundquist, E. J. Toone, *Chem. Rev.* **2002**, *102*, 555–578.

[106] M. Delbianco, P. Bharate, S. Varela-Aramburu, P. H. Seeberger, *Chem. Rev.* **2015**, *116*, 1693–1752.

[107] M. Touaibia, R. Roy, *Mini-Rev. Med. Chem.* **2007**, *7*, 1270–1283.

[108] S. Cecioni, A. Imberty, S. Vidal, *Chem. Rev.* **2015**, *115*, 525–561.

[109] L. L. Kiessling, J. E. Gestwicki, L. E. Strong, *Angew. Chem. Int. Ed.* **2006**, *45*, 2348–2368.

[110] D. A. Uhlenheuer, K. Petkau, L. Brunsveld, *Chem. Soc. Rev.* **2010**, *39*, 2817–2826.

[111] K. Petkau-Milroy, M. H. Sonntag, L. Brunsveld, *Chem. Eur. J.* **2013**, *19*, 10786–10793.

[112] Y.-b. Lim, K.-S. Moon, M. Lee, *Chem. Soc. Rev.* **2009**, *38*, 925–934.

[113] K. Petkau-Milroy, L. Brunsveld, *Org. Biomol. Chem.* **2013**, *11*, 219–232.

[114] L. Gao, M. Li, S. Ehrmann, Z. Tu, R. Haag, *Angew. Chem. Int. Ed.* **2019**, *58*, 3645–3649.

[115] Z. Qi, P. Bharate, C.-H. Lai, B. Ziem, C. Böttcher, A. Schulz, F. Beckert, B. Hatting, R. Mülhaupt, P. H. Seeberger, R. Haag, *Nano Lett.* **2015**, *15*, 6051–6057.

[116] B. J. Ravoo, R. Darcy, *Angew. Chem.* **2000**, *112*, 4494–4496.

[117] P. Falvey, C. W. Lim, R. Darcy, T. Revermann, U. Karst, M. Giesbers, A. T. M. Marcelis, A. Lazar, A. W. Coleman, D. N. Reinhoudt, B. J. Ravoo, *Chem. Eur. J.* **2005**, *11*, 1171–1180.

[118] R. V. Vico, J. Voskuhl, B. J. Ravoo, *Langmuir* **2011**, *27*, 1391–1397.

[119] U. Kauscher, A. Samanta, B. J. Ravoo, *Org. Biomol. Chem.* **2014**, *12*, 600–606.

[120] R. Dong, Y. Zhou, X. Huang, X. Zhu, Y. Lu, J. Shen, *Adv. Mater.* **2015**, *27*, 498–526.

[121] C. Guarise, S. Shinde, K. Kibler, G. Ghirlanda, L. J. Prins, P. Scrimin, *Tetrahedron* **2012**, *68*, 4346–4352.

[122] G. A. Silva, C. Czeisler, K. L. Niece, E. Beniash, D. A. Harrington, J. A. Kessler, S. I. Stupp, *Science* **2004**, *303*, 1352.

[123] J.-H. Ryu, E. Lee, Y.-b. Lim, M. Lee, *J. Am. Chem. Soc.* **2007**, *129*, 4808–4814.

[124] D.-W. Lee, T. Kim, I.-S. Park, Z. Huang, M. Lee, *J. Am. Chem. Soc.* **2012**, *134*, 14722–14725.

[125] M. K. Müller, L. Brunsveld, *Angew. Chem. Int. Ed.* **2009**, *48*, 2921–2924.

[126] D. Straßburger, N. Stergiou, M. Urschbach, H. Yurugi, D. Spitzer, D. Schollmeyer, E. Schmitt, P. Besenius, *ChemBioChem* **2018**, *19*, 912–916.

[127] S. M. C. Schoenmakers, C. M. A. Leenders, R. P. M. Lafleur, X. Lou, E. W. Meijer, G. M. Pavan, A. R. A. Palmans, *Chem. Commun.* **2018**, *54*, 11128–11131.

[128] A. Thomas, S. S. Müller, H. Frey, *Biomacromolecules* **2014**, *15*, 1935–1954.

[129] A. S. Abu Lila, K. Nawata, T. Shimizu, T. Ishida, H. Kiwada, *Int. J. Pharm.* **2013**, *456*, 235–242.

[130] I. An, H. Seong, K. H. Ahn, *Bull. Korean Chem. Soc.* **2004**, *25*, 420–422.

[131] M. C. A. Stuart, J. C. van de Pas, J. B. F. N. Engberts, *J. Phys. Org. Chem.* **2005**, *18*, 929–934.

[132] R. P. M. Lafleur, *doctoral thesis*, Technische Universiteit Eindhoven, **2017**.

[133] Y. Furusho, E. Yashima, *J. Polym. Sci. Part A: Polym. Chem.* **2009**, *47*, 5195–5207.

[134] J. M. Lehn, A. Rigault, J. Siegel, J. Harrowfield, B. Chevrier, D. Moras, *Proc. Natl. Acad. Sci. U.S.A.* **1987**, *84*, 2565.

[135] D. Haldar, H. Jiang, J.-M. Léger, I. Huc, *Angew. Chem. Int. Ed.* **2006**, *45*, 5483–5486.

[136] H. Ito, Y. Furusho, T. Hasegawa, E. Yashima, *J. Am. Chem. Soc.* **2008**, *130*, 14008–14015.

[137] H. Goto, Y. Furusho, E. Yashima, *J. Am. Chem. Soc.* **2007**, *129*, 109–112.

[138] D. Danino, Y. Talmon, R. Zana, *Colloids Surf. A* **2000**, *169*, 67–73.

[139] Y. Zheng, Z. Lin, J. L. Zakin, Y. Talmon, H. T. Davis, L. E. Scriven, *The Journal of Physical Chemistry B* **2000**, *104*, 5263–5271.

[140] S. Alpugan, G. Garcia, F. Poyer, M. Durmus, P. Maillard, V. Ahsen, F. Dumoulin, *J. Porphyrins Phthalocyanines* **2013**, *17*, 596–603.

[141] S. J. Ludtke, P. R. Baldwin, W. Chiu, *J. Struct. Biol.* **1999**, *128*, 82–97.

[142] S. Bhatia, D. Lauster, M. Bardua, K. Ludwig, S. Angioletti-Uberti, N. Popp, U. Hoffmann, F. Paulus, M. Budt, M. Stadtmüller, T. Wolff, A. Hamann, C. Böttcher, A. Herrmann, R. Haag, *Biomaterials* **2017**, *138*, 22–34.

[143] M. von Groning, I. de Feijter, M. C. A. Stuart, I. K. Voets, P. Besenius, *J. Mater. Chem. B* **2013**, *1*, 2008–2012.

[144] S. P. W. Wijnands, W. Engelen, R. P. M. Lafleur, E. W. Meijer, M. Merkx, *Nat. Commun.* **2018**, *9*, 1–9.

[145] M. A. Seelen, A. Roos, J. Wieslander, T. E. Mollnes, A. G. Sjöholm, R. Wurzner, M. Loos, F. Tedesco, R. B. Sim, P. Garred, E. Alexopoulos, M. W. Turner, M. R. Daha, *J. Immunol. Methods* **2005**, *296*, 187–198.

[146] M. A. Mulvey, S. J. Hultgren, J. D. Schilling, *The Journal of Infectious Diseases* **2001**, *183*, S36–S40.

[147] W. E. Thomas, E. Trintchina, M. Forero, V. Vogel, E. V. Sokurenko, *Cell* **2002**, *109*, 913–923.

[148] A. Ronald, *The American Journal of Medicine* **2002**, *113*, 14–19.

[149] H. J. Gabius, S. André, J. Jiménez-Barbero, A. Romero, D. Solis, *Trends Biochem. Sci.* **2011**, *36*, 298–313.

[150] J. Pizarro-Cerdá, P. Cossart, *Cell* **2006**, *124*, 715–727.

[151] A. M. Krachler, H. Ham, K. Orth, *Proc. Natl. Acad. Sci. U.S.A.* **2011**, *108*, 11614–11619.

[152] M. Hartmann, T. K. Lindhorst, *Eur. J. Org.Chem.* **2011**, 3583–3609.

[153] C. Svanborg, G. Godaly, *Infect. Dis. Clin. N. Am* **1997**, *11*, 513–529.

[154] J. R. Johnson, *Clin. Microbiol. Rev.* **1991**, *4*, 80–128.

[155] L. Hagberg, U. Jodal, T. K. Korhonen, G. Lidin-Janson, U. Lindberg, C. Svanborg Edèn, *Infect. Immun.* **1981**, *31*, 564–570.

[156] J. W. Wehner, M. Hartmann, T. K. Lindhorst, *Carbohydr. Res.* **2013**, *371*, 22–31.

[157] D. Deniaud, K. Julienne, S. G. Gouin, *Org. Biomol. Chem.* **2011**, *9*, 966–979.

[158] E. M. Munoz, J. Correa, E. Fernandez-Megia, R. Riguera, *J. Am. Chem. Soc.* **2009**, *131*, 17765–17767.

[159] W. Curatolo, A. O. Yau, D. M. Small, B. Sears, *Biochemistry* **1978**, *17*, 5740–5744.

[160] J. R. Kramer, A. R. Rodriguez, U.-J. Choe, D. T. Kamei, T. J. Deming, *Soft Matter* **2013**, *9*, 3389–3395.

[161] Q. Xiao, S. S. Yadavalli, S. Zhang, S. E. Sherman, E. Fiorin, L. da Silva, D. A. Wilson, D. A. Hammer, S. André, H.-J. Gabius, M. L. Klein, M. Goulian, V. Percec, *Proc. Natl. Acad. Sci. U.S.A.* **2016**, *113*, E1134–E1141.

[162] K. B. Li, N. Li, Y. Zang, G. R. Chen, J. Li, T. D. James, X. P. He, H. Tian, *Chem. Sci.* **2016**, *7*, 6325–6329.

[163] B. V. K. J. Schmidt, C. Barner-Kowollik, *Angew. Chem. Int. Ed.* **2017**, *56*, 8350–8369.

[164] J. Szejtli, *Chem. Rev.* **1998**, *98*, 1743–1754.

[165] J. Voskuhl, M. C. A. Stuart, B. J. Ravoo, *Chem. Eur. J.* **2010**, *16*, 2790–2796.

[166] U. Kauscher, B. J. Ravoo, *Beilstein J. Org. Chem.* **2012**, *8*, 1543–1551.

[167] H.-K. Lee, K. M. Park, Y. J. Jeon, D. Kim, D. H. Oh, H. S. Kim, C. K. Park, K. Kim, *J. Am. Chem. Soc.* **2005**, *127*, 5006–5007.

[168] A. Samanta, M. C. A. Stuart, B. J. Ravoo, *J. Am. Chem. Soc.* **2012**, *134*, 19909–19914.

[169] L. M. Coussens, Z. Werb, *Nature* **2002**, *420*, 860–867.

[170] R. P. McEver, K. L. Moore, R. D. Cummings, *J. Biol. Chem.* **1995**, *270*, 11025–11028.

[171] L. A. Lasky, *Annu. Rev. Biochem.* **1995**, *64*, 113–139.

[172] S. D. Rosen, C. R. Bertozzi, *Curr. Biol.* **1996**, *6*, 261–264.

[173] W. S. Somers, J. Tang, G. D. Shaw, R. T. Camphausen, *Cell* **2000**, *103*, 467–479.

[174] B. J. Graves, R. L. Crowther, C. Chandran, J. M. Rumberger, S. Li, K. S. Huang, D. H. Presky, P. C. Familletti, B. A. Wolitzky, D. K. Burns, *Nature* **1994**, *367*, 532–538.

[175] E. E. Simanek, G. J. McGarvey, J. A. Jablonowski, C. H. Wong, *Chem. Rev.* **1998**, *98*, 833–862.

[176] J. Fritzsche, S. Alban, R. J. Ludwig, S. Rubant, W. H. Boehncke, G. Schumacher, G. Bendas, *Biochem. Pharmacol.* **2006**, *72*, 474–485.

[177] J. Dernedde, A. Rausch, M. Weinhart, S. Enders, R. Tauber, K. Licha, M. Schirner, U. Zügel, A. von Bonin, R. Haag, *Proc. Natl. Acad. Sci. U.S.A.* **2010**, *107*, 19679–19684.

[178] A. Mulder, T. Auletta, A. Sartori, S. Del Ciotto, A. Casnati, R. Ungaro, J. Huskens, D. N. Reinhoudt, *J. Am. Chem. Soc.* **2004**, *126*, 6627–6636.

[179] A. Perl, A. Gomez-Casado, D. Thompson, H. H. Dam, P. Jonkheijm, D. N. Reinhoudt, J. Huskens, *Nat. Chem.* **2011**, *3*, 317–322.

[180] J. Huskens, A. Mulder, T. Auletta, C. A. Nijhuis, M. J. W. Ludden, D. N. Reinhoudt, *J. Am. Chem. Soc.* **2004**, *126*, 6784–6797.

[181] K. Petkau-Milroy, L. Brunsveld, *Eur. J. Org. Chem.* **2013**, *2013*, 3470–3476.

[182] N. Taulier, T. V. Chalikian, *J. Phys. Chem. B* **2008**, *112*, 9546–9549.

[183] B. Bertolotti, I. Sutkeviciute, M. Ambrosini, R. Ribeiro-Viana, J. Rojo, F. Fieschi, H. Dvorakova, M. Kasakova, K. Parkan, M. Hlavackova, K. Novakova, J. Moravcova, *Org. Biomol. Chem.* **2017**, *15*, 3995–4004.

[184] G. Goti, A. Palmioli, M. Stravalaci, S. Sattin, M. De Simoni, M. Gobbi, A. Bernardi, *Chem. Eur. J.* **2016**, *22*, 3686–3691.

[185] I. Morbioli, V. Porkolab, A. Magini, A. Casnati, F. Fieschi, F. Sansone, *Carbohydr. Res.* **2017**, *453-454*, 36–43.

[186] D. Diwan, K. Shinkai, T. Tetsuka, B. Cao, H. Arai, T. Koyama, K. Hatano, K. Matsuoka, *Molecules* **2017**, *22*, 157.

[187] M. Jerabek-Willemsen, C. J. Wienken, D. Braun, P. Baaske, S. Duhr, *Assay Drug Dev. Technol.* **2011**, *9*, 342–353.

[188] S. Duhr, D. Braun, *Proc. Natl. Acad. Sci. U.S.A.* **2006**, *103*, 19678–19682.

[189] S. A. Seidel, C. J. Wienken, S. Geissler, M. Jerabek-Willemsen, S. Duhr, A. Reiter, D. Trauner, D. Braun, P. Baaske, *Angew. Chem. Int. Ed.* **2012**, *51*, 10656–10659.

[190] S. D. Fihn, *N. Engl. J. Med.* **2003**, *349*, 259–266.

[191] R. H. Mak, H. J. Kuo, *Curr. Opin. Pediatr.* **2006**, *18*, 148–152.

[192] D. F. Sahm, C. Thornsberry, D. C. Mayfield, M. E. Jones, J. A. Karlowsky, *Antimicrob. Agents Chemother.* **2001**, *45*, 1402–1406.

[193] M. Kanai, K. H. Mortell, L. L. Kiessling, *J. Am. Chem. Soc.* **1997**, *119*, 9931–9932.

[194] D. M. Crothers, H. Metzger, *Immunochemistry* **1972**, *9*, 341–357.

[195] P. Bojarová, L. Petrásková, E. E. Ferrandi, D. Monti, H. Pelantová, M. Kuzma, P. Simerská, V. Křen, *Adv. Synth. Catal.* **2007**, *349*, 1514–1520.